DISS. ETH NO. 25927

Encoding a qubit in the motion of a trapped ion using superpositions of displaced squeezed states

A thesis submitted to attain the degree of
DOCTOR OF SCIENCES of ETH ZURICH
(Dr. sc. ETH Zurich)

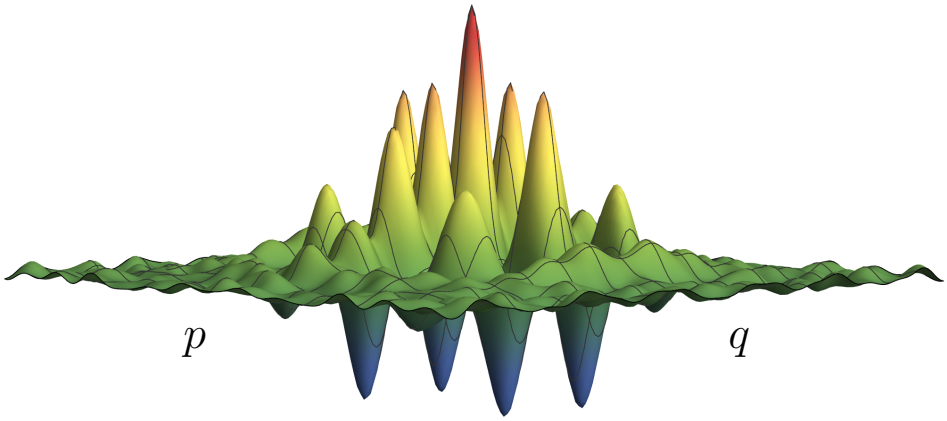

presented by

Christa Flühmann

MSc, ETH Zurich

born on 18.12.1989

citizen of Brienzwiler, Switzerland

accepted on the recommendation of
Prof. Dr. J. P. Home
Prof. Dr. P. O. Schmidt

2019

Abstract

Trapped-ions form a promising platform to realize a future large scale quantum computing device. Qubits are typically stored in internal electronic states, which are coupled using their joint motion in the trap potential. In this thesis this control paradigm is reversed. The harmonic motion of a trapped $^{40}Ca^{+}$ ion forms the main subject of studies, which is controlled via the internal electronic states.

A number of new techniques are introduced and examined, primarily based on the implementation of modular variable measurements. These are realized combining an internal state dependent optical dipole force with readout of the internal states. Modular measurements are used to investigate large "Schrödinger cat" states of the ion's motion, to violate Leggett-Garg tests of macroscopic realism, and finally to realize a logical qubit encoded in an error-correcting code based on the trapped-ion oscillator. The latter offers an alternative to the standard qubit based quantum information processing approach, which when embedded in systems of coupled oscillators could lead to a large-scale quantum computer.

Measurements of a particle's modular position and momentum have been the focus of various discussions of foundational quantum mechanics. Such modular measurements of the trapped-ion's motion are studied in depth in this thesis, in particular their ability to commute, which forms a key element for the latter work on error-correcting codes. Here we make use of the ability to investigate sequences of measurements on a single harmonic oscillator, and study correlations between their results, as well as quantum measurement disturbances between the measurements.

In order to achieve the major results of the thesis, it was necessary to characterize and control multiple wave packets in phase space. On the characterization side, the need to cope with states with high energy occupations led to the development of multiple new methods for quantum state tomography, including the use of a squeezed eigenstate basis, and the direct extraction of the characteristic function of the oscillator using state-dependent forces. These were used to analyze some of the largest oscillator "Schrödinger cat" states which have been produced to date.

The main result of this thesis is encoding and full control of a logical qubit in the motional oscillator space using a code proposed 18 years ago by Gottesman, Kitaev and Preskill. Logical code states are realized and manipulated using sequences of up to five modular measurements applied to an ion initially prepared in a squeezed motional state. Such sequences realize superpositions of multiple squeezed wave packets, which form the code words. The usage of the oscillator enables to encode and in principle correct a logical qubit within a single trapped ion, which when compared to typical qubit-array based approaches simplifies control and hardware.

While the discussion above focuses on the new physics in this thesis, in addition the work required technical upgrades to the system, improving control of both qubit and oscillator. These form important components which have impact on all experiments in our setup, beyond the bounds of the current thesis.

Zusammenfassung

Gefangene Ionen sind ein erfolgsversprechendes System um in Zukunft einen Quantencomputer zu realisieren. Quantenbits - kurz Qubits - werden typischerweise in internen elektronischen Freiheitsgraden der Ionen gespeichert, welche über die gemeinsame Schwingung im Fallenpotenzial gekoppelt werden. Dieser Ansatz wird in der vorliegenden Dissertation umgekehrt: Der Fokus liegt hierbei auf der Studie der harmonischen Schwingungsmode eines $^{40}Ca^{+}$ Ions, welche mithilfe der internen Zustände manipuliert und kontrolliert wird.

Neue Techniken die in erster Linie auf Messungen von modularen Variablen der Schwingungsmode beruhen, werden sowohl vorgeschlagen als auch experimentell untersucht. Eine solche modulare Messung wird durch eine vom internen Zustand abhängige optische Dipolkraft, gefolgt von einer Messung der internen Zustände realisiert. Modulare Messungen werden zur Studie grosser „Schrödinger Katzen“ des Ionenoszillators, wie auch für Makrorealismustests nach Leggett-Garg benutzt. Ausserdem erlauben modulare Messungen die Verschlüsselung eines fehlerkorrigierbaren logischen Qubits im Oszillator. Letzteres ist ein alternativer Ansatz zur Qubitregister basierten Quanteninformationsverarbeitung. Die Kopplung von mehreren logischen Qubits in Schwingungsmoden könnte in Zukunft die Realisierung eines Quantencomputers ermöglichen.

Darüber hinaus standen modulare Positions- und Impulsmessungen eines Teilchens im Fokus verschiedenster Diskussionen fundamentaler Aspekte der Quantenmechanik. Solche modularen Messungen werden ausführlich in der hier vorliegenden Arbeit studiert. Insbesondere wird die Kommutativität solcher Variablen untersucht, welche einen Kernbestandteil der Realisierung eines fehlerkorrigierbaren Qubits bildet. Dafür werden Sequenzen von modularen Messungen des Ionenoszillators genutzt, womit Korrelationen sowie quantenmechanische Messstörungen zwischen den Resultaten analysiert werden.

Um die Hauptresultate dieser Arbeit zu realisieren war es nötig, Überlagerungen aus mehreren Wellenpaketen im Phasenraum zu charakterisieren und zu kontrollieren. Für die Charakterisierung von Zuständen mit hohen Energieanregungen wurden neue Techniken zur Zustandsrekonstruktion entwickelt. Diese umfassen Analysen basierend auf gequetschten Energieeigenbasen sowie die direkte Messung der charakteristischen Funktion des Oszillators mittels zustandsabhängigen Kräften. Diese Techniken wurden zur Analyse von „Schrödinger Katzen“ benutzt, welche zu den grössten bisher in Oszillatormoden realisierten Zuständen gehören.

Das Hauptresultat dieser Dissertation ist die Verschlüsselung und vollständige Kontrolle eines logischen Qubits im Schwingungsraum eines Ions basierend auf der vor 18 Jahre von Gottesman, Kitaev und Preskill theoretisch vorgeschlagenen Methode. Sequenzen von bis zu fünf modularen Oszillatormessungen eines Ions in einem gequetschten Bewegungszustand erlauben die Herstellung und Kontrolle einer Überlagerung aus mehreren versetzten und gequetschten Wellenpaketen, welche die Codewörter realisieren. Die Nutzung der Schwingungsmode erlaubt die Verschlüsselung und im Prinzip die Fehlerkorrektur eines logischen

Qubits, das lediglich auf einem einzelnen gefangenen Ion basiert, welches im Vergleich zu qubitbasierten Ansätzen, einfachere Quantencomputer Hardware und Kontrolle ermöglicht.

Die bisherige Diskussion hat sich auf die neue Physik dieser Arbeit beschränkt. Darüber hinaus wurden dazu benötigte technische Verbesserungen, sowie verbesserte Kontrolle der internen Zustände und Schwingungsmoden umgesetzt. Diese repräsentieren Fortschritte welche die Qualität der präsentierten Ergebnisse ermöglichten und von denen künftige über diese Arbeit hinausgehende Experimente profitieren werden.

Acknowledgements

My PhD was very educative and time just flew by since there was always something to improve, fix or discuss.
My special thanks for this exciting time goes to:

Jonathan Home for giving me the opportunity to work in his group, his support and enthusiasm. I especially appreciated that he was always approachable and open to discuss any sort of question that arose and provided helpful input and guidance.

Peter Märki for his endless patience and knowledge during the desperate quest of hunting and eliminating magnetic noise sources. His collection of "educational" and fun toys makes working on the E floor a refreshing experience.

Daniel Kienzler for setting up a large part of the 3D trap setup, supervising my Master's project and later, while jointly taking data, teaching me a lot about running and maintaining the experimental system.

Matteo Marinelli, who started his PhD project simultaneously with me and also worked on the 3D trap setup, for always being a cheerful lab mate, helping to maintain the experimental system, especially for keeping Ionizer crashes low and fixing the beryllium lasers.

Vlad Negnevitsky, who was also part of the 3D trap team during the whole time I spent in the TIQI group. For his indispensable work on the control system and his support for any sort of related question. May he be proud that the present thesis is voluntarily backed up using git.

Thanh Long Nguyen for joining me to run some of my experiments before looking for further challenges in the cryo setup. I appreciated a critical discussion partner.

Mirjam Bruttin for removing any administrative obstacle and more, typically long before I even noticed it.

Frieder Lindenfelser for his contributions to the laser system, patiently helping me to debug electronic boxes and over-productive Christmas cookie sessions.

Christoph Fischer and Simon Ragg for being office table comrades typically answering my more or less witty questions and enduring the occasional disappearance of their sweets.

Lukas Gerster, Sebastian Saner and Chams Rutkowski for their Master and semester project work.

Christoph, Jonathan, Lucas, Maciej, Matt, Tanja and Vlad for feedback in the writing process.

Oliver Wipfli for ensuring high TIQI desktop background picture quality[1] and introducing the concept of the TIQI winter weekend.

Chiara Decaroli for helping HPF evolve to modern times by upgrading vital infrastructure.

The enthusiastic TIQI climbers for finally convincing me of this sport - The PhD truly made me stronger.

Robin Oswald for providing the complete Ice hockey experience including the smelly gear.

Ben, Daniel, Florian, Frieder, Hsiang-yu, Joseba and Ludwig for filling the laboratory with a nice set of experiments, electronic devices,

[1] at least one cub, kit of some animal species is a must.

lasers, optics and all other useful equipment "long" before I started my PhD project.

The current group members Brennan, Celeste, Chiara, Chi, Chris, Christoph, Daniel, Francesco, Karan, Maciej, Martin, Matteo, Matt, Nick, Oliver, Robin, Roland, Shreyans, Simon, Tanja, Thanh Long, Thomas, Tobias and Vlad for their contributions, help, discussions and shaping the nice group atmosphere.

I would like to thank Bernhard Lehmann who was my math teacher in 5th grade for sparking my interest in mathematics and later Robert Märki during high school for being an inspirational teacher.

My study colleagues and friends Aline, Andrea, Anja, Gian, Helga, Peggy, Samuel, Simon, Vera and many more... for an exciting time of studies and many joint adventures. Only much later did I realize how valuable our open discussion system was. Everyone contributed their list of open questions and we erased them one by one. Please come an help me erase some of my current open questions.

Aline Fluri and Peggy Schönherr for sharing each others mostly ups and few downs and being flatmates for about five years.

Andrea Hofmann for many long conversations over the years and for joining my long dreamed busking project in Ireland completing it with her music.

Last but not least my parents Peter and Silvia for their support throughout my life - it is good to know to have a home base. My brothers Andreas and Jonathan for a non boring childhood. Lucas for good laughs together, sharing similar passions especially for outdoor adventures, and tons of other things.

Contents

Chapter 1

Introduction

The potential building of a computer based on quantum systems raised the hope of solving problems intractable by classical computation [1, 2]. The challenge of building such a machine is nowadays not only tackled by academic research groups but also international companies, and numerous start-ups [3]. The race for the highest number of controlled quantum systems and operations is ongoing. Today's quantum machines use around 20 faulty physical qubits and are close to outperforming simulations on classical supercomputers for specifically designed problems [4]. Nevertheless these machines need to be scaled up and improved to work with thousands of perfect logical qubits in order to solve practically relevant problems [5]. In the following introduction we discuss relevant aspects for realizing a quantum computing device.

1.1 Qubit states and operations

Typical quantum computation uses the simplest quantum mechanical system - the two-state system - as their building blocks. The qubit computational basis states are often labeled $|0\rangle$ and $|1\rangle$ with the labels relating to the classical bit of information. Such a qubit can for example be realized using a spin, or a higher and lower energy level of an atom and thus $|\downarrow\rangle$, $|\uparrow\rangle$ are also commonly used labels[1]. In contrast to a classical bit, a qubit can be in a superposition state:

$$|\psi\rangle = \cos(\theta/2)\,|\downarrow\rangle + \sin(\theta/2)e^{i\phi}\,|\uparrow\rangle \tag{1.1}$$

with arbitrary real parameters θ and ϕ. In particular the two levels have a well defined phase relation defined by the phase ϕ. This larger state space of a qubit compared to a classical bit and the exponential scaling of state space size once multiple qubits are combined is thought to be an important factor for

[1] Here we used the "braket" notation introduced by Dirac [6] which provides an elegant way of representing quantum mechanical states. A short revision is given in Appendix (App.) A.1

the power of a quantum computing device. During a computation the machine can operate[2] in parallel on the state of all qubits [7]. Once the computation finishes the final superposition state of the qubits needs to be measured. The measurement provides us then with the computation result in form of familiar classical information.

Equation 1.1 gives a so called pure qubit state, which can be represented by a single element $|\psi\rangle$. More generally quantum systems are described using density operators $\hat{\rho}$. This formalism additionally allows to capture classical uncertainties in the states. For example a setup might be designed to prepare the target state $|\psi\rangle$ but with a small chance p_f a different state $|\psi_f\rangle$ is prepared. This is an example of a mixed state, which requires to be represented as the more general density matrix $\hat{\rho} = (1-p_\mathrm{f})|\psi\rangle\langle\psi| + p_\mathrm{f}|\psi_f\rangle\langle\psi_f|$. Pure states can be represented within the density matrix formalism, the ideal state preparation with $p_f = 0$ would for example read $\hat{\rho} = |\psi\rangle\langle\psi|$. Density operators are Hermitian operators as a consequence they can be expressed in terms of their eigenstates $|e_i\rangle$ and their real and positive eigenvalues[3] e_i.

$$\hat{\rho} = \sum_i e_i |e_i\rangle\langle e_i| \tag{1.2}$$

This form allows the interpretation of any state $\hat{\rho}$ as consisting out of a classical statistical mixture of pure states $|e_i\rangle$, where each state is present with probability e_i. The density matrix formalism thus in particular allows to represent imperfections when building the quantum computing device. Many noise processes convert pure superposition states to mixed states. Typically the impact of noise scales unfavorably with system size, which makes the extension of quantum control from one qubit to multiple qubits challenging [8]. Error correction and the theory of fault tolerance can be used to prevent this larger system to lose its quantum coherence due to noise.

One of the principal early results of quantum information processing is that a small discrete set of operations/gates can be universal. This means that the small gate set is able to approximate any unitary on a register of qubits to arbitrary precision [7]. A universal gate set is formed by the Hadamard operation $\hat{H} = |+\rangle\langle\downarrow| + |-\rangle\langle\uparrow|$, which interchanges the qubit states with $|\pm\rangle = (|\downarrow\rangle \pm |\uparrow\rangle)/\sqrt{2}$, the T-gate: $\hat{T} = |\uparrow\rangle\langle\uparrow| + e^{i\pi/4}|\downarrow\rangle\langle\downarrow|$, creating a relative phase of $\pi/4$ between the qubit states and a suitably chosen two qubit operation like the controlled not operation [7]. In practice, commonly used gates are formed from the Pauli gates:

$$\hat{X} = |\uparrow\rangle\langle\downarrow| + |\downarrow\rangle\langle\uparrow|, \qquad \hat{Y} = i(|\uparrow\rangle\langle\downarrow| - |\downarrow\rangle\langle\uparrow|), \qquad \hat{Z} = |\downarrow\rangle\langle\downarrow| - |\uparrow\rangle\langle\uparrow|. \tag{1.3}$$

$\hat{X}$ is called the bit flip operation since it interchanges the $|\uparrow\rangle, |\downarrow\rangle$ states. $\hat{Z}$ is called the phase-flip operator because it leads to a a sign change when acting on

[2] including entangling

[3] The eigenequation reads: $\hat{\rho}\,|e_i\rangle = e_i\,|e_i\rangle$

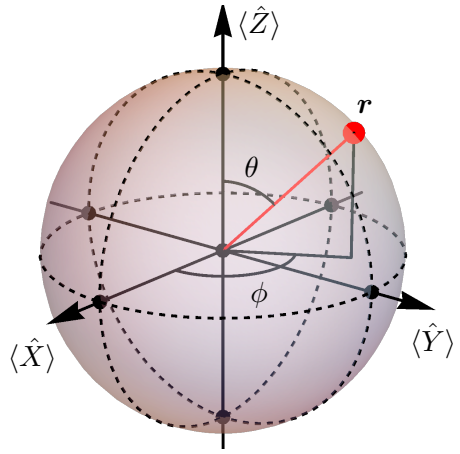

Figure 1.1: Bloch-sphere representation of a qubit state

a qubit superposition state represented by equation 1.1: $\hat{Z}\,|\psi\rangle = \cos(\theta/2)\,|\downarrow\rangle - \sin(\theta/2)e^{i\phi}\,|\uparrow\rangle$, while $\hat{Y}$ leads to the combination of the two operations.

The computational advantage of a quantum computer over a classical machine is subtle. Many remarkable quantum information protocols [9] can efficiently be simulated using classical machines. In particular protocols using computational basis state preparation and readout thereof together with operations only from the so called Clifford group can efficiently be simulated [10]. In the above list of operations only the T-gate is not part of the Clifford group and is thus vital for the computational power of the quantum machine.

The Pauli operations together with the identity $\mathbb{1} = |\downarrow\rangle\langle\downarrow| + |\uparrow\rangle\langle\uparrow|$ further form a basis for arbitrary Hermitian 2×2 operators. This allows to express an arbitrary qubit state including mixed states in this basis:

$$\hat{\rho} = (\mathbb{1} + \boldsymbol{\sigma} \cdot \boldsymbol{r})/2, \qquad \boldsymbol{r} = \mathrm{Tr}(\hat{\rho}\boldsymbol{\sigma}), \qquad \boldsymbol{\sigma} = \begin{pmatrix} \sigma_1 \\ \sigma_2 \\ \sigma_3 \end{pmatrix} = \begin{pmatrix} \hat{X} \\ \hat{Y} \\ \hat{Z} \end{pmatrix}. \tag{1.4}$$

Here the 3 dimensional real Bloch-vector $\boldsymbol{r}$ is given by the expectation value of the Pauli operators which we expressed using the vector of Pauli matrices $\boldsymbol{\sigma}$. We can graphically represent the qubit state by its Bloch-vector. All pure states span a unit sphere called Poincaré-Bloch sphere, which is shown in figure 1.1. The north and south pole of the Bloch sphere denote the computation basis states. Furthermore we can express the Bloch vector in spherical coordinates $\boldsymbol{r} = (|\boldsymbol{r}|\sin(\theta)\cos(\phi), |\boldsymbol{r}|\sin(\theta)\sin(\phi), |\boldsymbol{r}|\cos(\theta))$. Pure states represented by equation 1.1 are located on the surface of the sphere where $|\boldsymbol{r}| = 1$. While mixed states are located within the sphere. In this case

$|\boldsymbol{r}| < 0$ is a measure for how much the state is mixed. The maximally mixed state $\hat{\rho} = \mathbb{1}/2$ with $|\boldsymbol{r}| = 0$ is located at the origin of the sphere respectively.

1.1.1 Qubit realizations

Qubits are commonly stored in isolated two-state systems, like the internal states of an ion [11], atom [12], the spin of a nuclei [13], a solid state spin systems [12] or the states of an artificial atom realized using superconducting circuits[4] [14, 15]. But qubits can alternatively be encoded in bosonic degrees of freedom like a cavity- or traveling-field mode or the harmonic motion of an ion in the trapping potential [16]. We refer to such bosonic modes in the following as harmonic oscillators or simply oscillators.

The use of oscillators is natural for quantum computation based on traveling optical modes. In this case a simple encoding is provided by the absence or presence of a single photon (i.e. the two lowest energy states of the oscillator). In practice encoding based on the photon being present in one of two modes allows for simple gates [17]. These are provided by Gaussian operations, which include beam splitters, phase-shifters and squeezing. However universal quantum computation is only possible including a non-Gaussian resource, such as the non-linear interaction of photons. Non-linear Kerr media can provide such an interaction between photons but exhibits high photon absorption. A number of schemes were proposed to evade this problem by introducing the necessary non-linearity, either by using measurements [17, 18] and/or using non-Gaussian code states [19].

As an alternative to encoding two-state system qubits in an oscillator, it is also possible to store information in the continuous variables such as position and momentum. To examine universality, it is then possible to test the ability to simulate arbitrary oscillator Hamiltonians [20]. Similar to the qubit case this form of CV universality is only reachable having access to a non-linear element, either in the input state resources, the interactions or by using measurements [16].

A non-linear interaction between photons can be mediated via the coupling of the optical fields to the discrete energy levels of an atom [21]. In this case a strong atom-field coupling is needed, which typically requires embedding the atomic system within a high-finesse cavity [22]. Following early experiments of atom-photon coupling using Rydberg atoms, which will be described in the next section, similar physics was explored coupling "artificial" solid state atoms to superconducting microwave resonators. Encoding qubits in microwave modes is additionally motivated by the longer coherence times such modes exhibit when compared to typical qubits in the same experimental platform [23]. However optical modes are favorable for distributing qubits over large distances.

[4] In this case in some sense the two furthest down energy eigenstates of an anharmonic oscillator realized using the Josephson junction as non-linear circuit element are used.

1.2 Oscillator state engineering

Trapped ions, the system studied in this thesis, form a promising platform to realize a quantum computation device. Qubits are typically realized by suitably chosen internal energy states of the trapped ions, which are often manipulated using laser fields [11]. Multiple qubits can be coupled using the laser to manipulate their joint motion in the trapping potential [24].

In the present thesis this paradigm will be reversed: The internal state qubit will be used to manipulate the main system of interests provided by the motional mode. Control of the oscillator via the internal states allows for the required non-linearity for oscillator based quantum computation. The atom-oscillator coupling has historically been extensively studied in the field of quantum optics, where the state of a cavity field interacts with two levels of an atom. When the cavity field is tuned in resonance with the atom exchange of individual quanta of energy between the systems occurs. Such a coupling is referred to as Jaynes-Cummings interaction [25] and follows directly from the most fundamental light-matter interaction. The same fundamental physics can be explored coupling the trapped-ion qubits to the motional oscillator using classical laser fields [26]. Coupling via the strong lasers additionally allows to implement the so called Anti-Jaynes-Cummings interaction in which quanta are not exchanged between the systems but jointly added or subtracted [26]. In contrast such an operation is not possible in an isolated atom cavity system since it is energy non-conserving.

Oscillator-qubit couplings have allowed for ground state cooling of trapped-ion oscillators and subsequently allowed for a number of pioneering demonstrations of quantum state control [27, 28]. A variety of oscillator states have been prepared showing uniquely quantum features: Single higher excited energy quanta were put into the oscillators [29]; so called squeezed states were prepared [30], exhibiting less uncertainty in one degree than commonly believed possible and oscillators were put into superposition states of separated wave packets [31, 32]. A prominent example of a superposition state is a trapped ion which is, at one point in its periodic oscillation cycle, simultaneously at two distinct spatial locations. Such superpositions of macroscopically distinct possibilities have analogies to Schrödinger's famous thought experiment, in which he used a dead and alive cat to illustrate the absence of observed quantum behavior for macroscopic objects [33]. With the advances in creating such states their unique features needed to be determined and characterized, which lead to simultaneous development of full state reconstruction methods and analysis tools [29, 34]. In addition such states in particular allowed to study decoherence effects and their scaling with system size [35, 36]. In the context of trapped ions, these advances led to the award of the 2012 Nobel prize to David Wineland. He was awarded jointly together with Serge Haroche, who obtained a number of similar results using Rydberg atoms in microwave cavities. Following this seminal work superpositions of larger separations compared to wave packet extent were created [37, 38] and the control tools were further refined [39, 40].

1.3 Measurement

Building a quantum computer requires the combination of individual quantum systems to a large device still governed by the rules of quantum mechanics. Increasing the system size under quantum control provides a great engineering challenge. This border is sometimes referred to as the quantum-classical transition and so far it proved to be still mobile towards larger systems [41]. For example small mechanical systems have been cooled to the quantum regime and were put into superpositions [42, 43] or large molecules consisting of many atoms exhibited quantum interference [44].

At the same time a quantum computer requires measurements providing classical results of the computation. Measurements can additionally be used for error correction, which will be described in the following section. Measurements convert the system state into classical outcomes and thus provide the connection between quantum states and the classical world. A quantum computer thus requires precise control about when and where quantum coherence is maintained or converted to classical measurement results. This has to be achieved despite the fact that the greatest unsolved philosophical challenge is to understand quantum measurements [45]. Quantum systems can inherently be in superpositions of possibilities, which differ distinctively from classical statistical mixtures. Why is it that even if a quantum system is prepared in such a superposition a measurement reveals always only one definite outcome at a time? And why are we required to update the description of our quantum state in a non-unitary way [46, 47]?

To study the intrinsic quantum measurement back-action associated with the state update indirect measurements are beneficial [48, 49]. In these the system of interest is first coupled to a meter system, which in turn is read out. The simplest and best controlled meter system is given by a qubit. In the final readout of the meter qubit classical information is generated, which requires the qubit to be coupled to additional potentially less controlled meter systems. The indirect readout via the first well controlled meter stage thus in some sense separates this less controlled readout from the system.

Despite a lack of philosophical understanding of the state collapse associated with quantum measurement the mathematical description of it is accurate enough such that measurement can be used as an additional control tool. The initial coupling between oscillator and meter qubit creates an entangled state between the two. The qubit readout in turn removes this entanglement. Which in our case realizes, conditional on the measurement result, states analogous to "Schrödinger's cat" solely in the oscillator degree of freedom. This has been explored previously for optical [32] and microwave cavity modes [50] and provides a vital tool for the work presented in this thesis.

Also classical measurements can lead to disturbances of the measured system. But measurement strategies can be devised which are expected to lead to no disturbance [51]. Such strategies can be used to analyze

intrinsic measurement back-action, instead of more trivial effects of classical measurement disturbance. In this case measurement back-action can be used to discriminate if the system requires a quantum description or can be well described within our classical familiar world [52]. Additionally non-invasive measurements (NIM) were suggested to experimentally test realistic theories of physics [53]. This idea was first put forward by Leggett and Garg, who designed an inequality based on correlations between sequences of measurements [51]. Their aim was to reject realism at the macroscopic size scale (MR). The Leggett-Garg inequality has been violated using microscopic two level systems [54–65] and notably superpositions of an atom placed at distinct positions [66]. Furthermore a scheme to violate the inequality using mechanical oscillators has been proposed theoretically [67] and its implementation will be described in this thesis. Mechanical oscillators have a natural crossover from the quantum to the classical regime and thus allow to study this transition.

Using such techniques, we expect a continuation of the developments of the past few decades, in which quantum features have been observed in systems of ever increasing size. In the hypothetical case where we can push the quantum-classical border across the every day size scale of humans performing and observing measurements does it in this case still make sense to talk of such a thing as a measurement providing classical information? How do we think and reason while being in a superposition [33, 68, 69]?

1.4 Error correction

Like a classical computer a large quantum computing device will require error correction. In classical error correction information needs to be stored redundantly [70], which allows recovery of the original information even if part of the information is lost. Despite the no-cloning theorem [71], which forbids simple copying of quantum systems, redundant storage of information was found to be possible quantum mechanically [72]. Shortly after the discovery of first quantum codes [73, 74] the theory of fault-tolerance was developed [75, 76]. These techniques involve strategies which prevent the spreading and accumulation of errors across the quantum computing device. One of the well known results from this work is the production of threshold error rates [77, 78] which would allow a large-scale quantum computer to function in the presence of noise. This comes at the expense of a large overhead in system size and complexity.

A classical bit only exhibits one type of error - it can simply flip it's state. In contrast a quantum bit can be corrupted in a multitude of ways; the phase between the computational basis states can flip or the parameters ϕ and θ of equation 1.1 can change by an arbitrary amount. Quantum measurements of the qubits typically disturb their state and are thus expected to corrupt the stored information. In the following we will describe a method for the

detection of errors, which induces no disturbance of the encoded information and further shows how measurement back-action elegantly solves the problem of continuous errors. To do so we introduce the commonly used class of stabilizer codes [10, 79]. We use this formalism to discuss some of the basic concepts of quantum error correction. For a more complete discussion we suggest [7] and references therein.

1.4.1 Stabilizer codes

The main concept behind the stabilizer formalism are not the encoded qubit states themselves but the so called stabilizer operators. These define the code states indirectly, as the set of states which remain unchanged if a stabilizer operator acts on them. When an error occurs on a properly encoded qubit, then the encoded qubit state leaves the code space and the resultant state is no longer invariant under all stabilizers. The latter can be used for detection and correction of errors [80, 81].

In qubit array based codes the stabilizer operators can be defined generalizing the concept of Pauli operators to multiple qubits. Pauli operators together with the identity and pre factors of ± 1 and $\pm i$ form the Pauli group. The group generators in this case are given by the three Pauli operations themselves:

$$\hat{\sigma}_i \hat{\sigma}_j = \delta_{ij} \mathbb{1} + i \epsilon_{ijk} \hat{\sigma}_k \tag{1.5}$$

here δ_{ij} is the Kronecker delta and ϵ_{ijk} the Levi-Civita symbol.

All possible tensor products of n Pauli group elements form the Pauli group on n physical qubits. Stabilizer operators $\hat{S}$ are elements of the n qubit Pauli group, which themselves form a smaller group with the additional property that the stabilizer operators commute pairwise[5]. In particular being a tensor product of Pauli operators each stabilizer has eigenvalues ± 1.

The code space is then defined to be the set of all simultaneous $+1$ eigenstates of the stabilizer operators. Computational basis states are defined within the code space as eigenstates of the additional logical Pauli operation $\hat{Z}_L$ given by an additional element of the n qubit Pauli group. All operations within the logical code space must commute with the stabilizer operation otherwise their usage during computations leads to code states leaving the code space. Additional elements then realize the bit flip operation $\hat{X}_L$ and the $\hat{Y}_L$ operator.

Code states $|\psi\rangle_L = \cos(\theta/2)\,|0\rangle_L + \sin(\theta/2) e^{i\phi}\,|1\rangle_L$ are unchanged when a stabilizer is applied. This is different for states outside the code space $|\psi\rangle_L^f$ which will have eigenvalue -1 at least for one of the stabilizer operators: $\hat{S}\,|\psi\rangle_L^f = -\,|\psi\rangle_L^f$. Measurement of this eigenvalue is thus able to detect if an error has caused the encoded qubit state to leave the code space.

[5] It is sufficient to consider only a subset of stabilizer operators acting as generators of the stabilizer group (i.e. combinations of generators form the full group). Thus the word stabilizer refers to such a generator in this section.

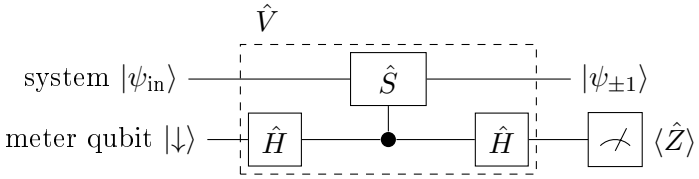

Figure 1.2: Circuit typically used in qubit array based error correction. $\hat{S}$ denotes a stabilizer operator, these have an eigenvalue spectrum of ± 1. Conditioned on the measurement result the input state is projected into the ± 1 eigenspace of the operator $\hat{S}$ while the statistics reads out the expectation of $\langle\hat{S}\rangle$.

The standard circuit to perform this measurement is given in figure 1.2. This is an example circuit of an indirect quantum measurement, in which a system is coupled to a meter qubit initialized to $|\downarrow\rangle$. In case of the stabilizer readout the system is given by the array of qubits realizing an encoded qubit state $|\psi_{\text{in}}\rangle = |\psi\rangle_L$. System and meter are coupled using the overall operation $\hat{V}$. This creates an entangled state between the two: $|\uparrow\rangle \otimes \hat{E}_- |\psi_{\text{in}}\rangle + |\downarrow\rangle \otimes \hat{E}_+ |\psi_{\text{in}}\rangle$ with $\hat{E}_\pm = (\hat{S} \pm \mathbb{1})/2$. The final readout measures the meter qubit in the $\hat{Z}$ basis, which provides us indirectly with information about the system. All aspects about this measurement can be described using the Kraus operators $\hat{E}_\pm$ which are thus sometimes referred to as measurement operators [48]:

- measurement probabilities: $P(\pm 1) = \langle\psi_{\text{in}}| \hat{E}_\pm^\dagger \hat{E}_\pm |\psi_{\text{in}}\rangle$
- system post-measurement state: $|\psi_{\pm 1}\rangle = \hat{E}_\pm |\psi_{\text{in}}\rangle / \sqrt{P(\pm 1)}$
- system observable: $\langle\hat{Z}\rangle = \langle\psi_{\text{in}}| (\hat{E}_+^\dagger \hat{E}_+ - \hat{E}_-^\dagger \hat{E}_-) |\psi_{\text{in}}\rangle = \langle\psi_{\text{in}}| \hat{O} |\psi_{\text{in}}\rangle$

The above formulas describing the measurement can readily be generalized to mixed input states $\hat{\rho}_{\text{in}}$ (App. E.1). A feature of quantum measurement is the resultant non-unitary update of the system state: Conditional on the measurement result ± 1 we change our description of the system from $|\psi_{\text{in}}\rangle \to |\psi_{\pm 1}\rangle$. This state can be compared to the case were we performed the circuit 1.2 but failed to record the result ± 1. In this case we would know that with probabilities $P(\pm 1)$ the system is in states $|\psi_{\pm 1}\rangle$ but would not know which of the scenarios has happened. Therefore the resultant state is described as a classical mixture $\hat{\rho} = P(+1)|\psi_{+1}\rangle\langle\psi_{+1}| + P(-1)|\psi_{-1}\rangle\langle\psi_{-1}|$[6].

Usage of the meter controlled stabilizer operation together with two Hadamard operations realizes the measurement operators $\hat{E}_\pm = (\hat{S} \pm \mathbb{1})/2$, while the observable reads $\hat{O} = \hat{S}$. $\hat{E}_\pm$ in this case are projection operators

[6]Note that the same state would be obtained when the final $\hat{Z}$ measurement is not performed, and we would just perform the partial trace over the meter qubit space.

onto the ± 1 eigenspaces of $\hat{S}$. A code state in this case leads to the result $+1$ with certainty, while the state update has no effect on this state. The faulty state $|\psi\rangle_L^f$ leads to a result -1 and the state update solely adds an irrelevant global phase. Thus we are able to tell if a state is in the code space or not but without learning information about the encoded state $|\psi\rangle_L$ i.e. the parameters θ and ϕ. The latter would necessarily disturb the encoded qubit state.

Measurement back-action due to projection of the system state from $|\psi_{\text{in}}\rangle$ to $|\psi_{\pm 1}\rangle$ is a key element in quantum error correction. Errors in quantum mechanics do not always move the state fully out of the code space, they can further be continuous i.e. they could slowly move the encoded state towards the faulty state $|\psi\rangle_L^f$. The stabilizer measurement with an input state $|\psi_{\text{in}}\rangle = \sqrt{1-p_f}\,|\psi\rangle_L + \sqrt{p_f}\,|\psi\rangle_L^f$ can yield either of the two results. The probability for these are $P(+1) = 1-p_f$, $P(-1) = p_f$, while the conditional post-measurement states are $|\psi_{+1}\rangle = |\psi\rangle_L$ while $|\psi_{-1}\rangle = |\psi\rangle_L^f$. The continuous/partial error before the measurement has become either no error at all or a complete error after the measurement, with the measurement result revealing which of the scenarios has happened.

Readout of all stabilizer operators allows to diagnose which type of error has occurred with the highest probability. But typically there is a chance of diagnosing the error wrongly, which happens when too many errors were present or an error has simply interchanged states in the code space [80, 81]. Error correction improves logical qubit fidelity, when the chances for undetectable and wrongly diagnosed errors are small.

In practice, multiple qubits are entangled in order to form an encoded state. This larger system is always harder to control than just a single physical qubit. The quality of the encoded state is first reduced, when comparing to the bare qubit. If the goal is to realize one higher quality qubit, then the error correction procedure is required to compensate for these reductions in fidelity and need to lead to an additional improvement. This places stringent demands on the operation fidelities required to successfully perform error correction.

1.4.2 Qubit based error correction

The implementation of error correction schemes and their essential building blocks for the protection of single and multiple quantum bits of information are explored nowadays [82–91].

Single internal state qubits in ion traps show extremely good performance. They exhibit coherence times of multiple tens of seconds [92, 93] while typical operations require few tens of micro seconds. Further, single qubit operations with average fidelities of around 99.9999% were reported [93], while for two qubit gates 99.9% was achieved [94]. Also in this platform experiments work on using multiple internal state qubits for error correction primitives [88–91]. The realization of a topologically encoded qubit using 7 ions [91] showed for example fidelities of 32.7(8) % for $|0\rangle_L$ state preparation. This illustrates that

control over the larger set of ions, despite high quality single qubit control is challenging [95][7]. This problem can be circumvented by using the larger state space provided by the motion of a single trapped ion in order to encode a correctable qubit. The use of a single oscillator system requires less resources and offers simplified control.

1.4.3 Bosonic codes

Various theoretical proposals for encoding correctable qubits in oscillators exist [19, 96–104], some of which have been realized experimentally in the optical platform using only Gaussian operations [84, 105]. In this case only errors which are non-Gaussian can be corrected. For Gaussian errors like photon loss in a transmission line no-go theorems exist [106, 107]. Non-Gaussian states have been used in superconducting microwave cavities to encode a qubit [87, 108] and have allowed for correction of the dominant photon loss error by feedback, which resulted in extension of qubit lifetimes [86].

A main result of this thesis is the implementation of a different powerful encoding, which has been proposed theoretically in 2001 by Gottesman, Kitaev and Preskill (GKP) [19]. GKP showed in their work how this encoding allows for universal fault tolerant computation in the optical platform. Their code benefits from simple gates i.e. Pauli operations are realized by Gaussian transformations, at the expense of complex non-Gaussian code states. Recent theoretical studies showed good error correction performance, when practically relevant regimes were considered [109, 110] and further work discussed how the GKP could in principle be concatenated to drive error rates down arbitrarily [107, 111].

[7] a qubit based error correction code requires at least five qubits [80].

1.5 Thesis layout

The remainder of this thesis covers trapped-ion oscillator control, state synthesis and reconstruction, as well as applications of this control to fundamental studies and quantum information processing:

Chapter 2 revises relevant aspects of the quantum harmonic oscillator formalism. Oscillator states and their description are introduced and discussed in connection to the Heisenberg uncertainty principle. Particular emphasis is put on discussing phase space representations and operators.

Chapter 3 introduces the necessary experimental control tools. Specifically the description of coherent interactions of the laser with the trapped ion including the physics of multi-chromatic control pulses.

Chapter 4 describes relevant upgrades and aspects of to the experimental setup. These include stabilization and compensation of magnetic fields as well as upgrades to the control laser system.

Chapter 5 describes characterization and calibration of the trapped-ion motional oscillator, which includes a fast and robust calibration scheme for the oscillator frequency.

Chapter 6 [112] presents a first set of results, which are concerned with the creation and analysis of "Schrödinger cat" states of the motional oscillator. Generalized energy eigenbases allow for Wigner function tomography as well as analysis of large cat states.

Chapter 7 [113] studies sequences of modular variable measurements. First the commutation of periodic position and momentum variables is explored. Second the quantum-classical transition is examined. Notably the Leggett-Garg inequality is violated based on oscillator superposition states.

Chapter 8 [114] describes encoding and full control of a qubit in the motional oscillator based on the GKP code.

Chapter 9 describes an efficient phase space tomography method and applies it to reconstruct a logical GKP code state.

Chapter 6 - Chapter 9 each end with a discussion of the performed measurements and describe relevant future extensions.

Chapter 10 concludes the thesis with a short summary and additionally provides an overview of possible future experiments.

Chapter 2

Harmonic oscillator

A large class of physical systems are approximately described by the physics of harmonic oscillators. One example are clocks based on pendulums. The properties of a single trapped ion are governed by the same oscillator physics but in contrast to the pendulum this system can be laser cooled to its quantum mechanical ground state giving rise to a multitude of counter-intuitive phenomena. The major results of this thesis involve the control of the trapped-ion mechanical oscillator. As a precursor to the later chapters, it is therefore important to establish the primary features of this system, as well as the methods which will be relevant to describing the evolution and the resulting quantum states. I place particular focus on different methods of representing quantum states of the oscillator, which is especially relevant for the quantum state reconstruction work of chapters 6 and 9.

2.1 Fock state ladder

A harmonically trapped particle with position $\hat{q}_r$ and momentum $\hat{p}_r$ is described by the Hamiltonian [115]:

$$\hat{H} = \frac{\hat{p}_r^2}{2m} + \frac{1}{2}m\omega^2\hat{q}_r^2. \tag{2.1}$$

Here ω is the angular frequency of the oscillator and m its mass. It is helpful to rewrite the Hamiltonian by defining dimensionless position $\hat{q}$ and momentum $\hat{p}$ and by introducing the energy quanta creation $\hat{a}^\dagger$ and annihilation $\hat{a}$ operators:

$$\hat{q} \equiv \sqrt{\frac{m\omega}{2\hbar}}\hat{q}_r = \frac{1}{2}(\hat{a}^\dagger + \hat{a}), \qquad \hat{p} \equiv \sqrt{\frac{1}{2m\omega\hbar}}\hat{p}_r = \frac{i}{2}(\hat{a}^\dagger - \hat{a}) \tag{2.2}$$

which transforms the above Hamiltonian to its second-quantization version:

$$\hat{H} = \hbar\omega(\hat{a}^\dagger\hat{a} + \frac{1}{2}). \tag{2.3}$$

Here we can identify the number operator $\hat{N} = \hat{a}^\dagger \hat{a}$. The eigenstates of $\hat{N}$ and thus also the oscillator Hamiltonian eigenstates are called Fock states $|n\rangle$, $n \in \{0, 1, 2, 3, ..\}$. The Fock state energy eigenvalues $(n + 1/2)\hbar\omega$ are equally spaced, running from $\hbar\omega/2$ to infinity. In the following we will typically omit the constant energy offset of $\hbar\omega/2$. The state $|n\rangle$ contains n energy quanta and the application of the creation (destruction) operator raises (lowers) the number of energy quanta by 1. The state ladder terminates by the application of the destruction operator onto the ground state $|0\rangle$, which yields zero. These relations are summed up below [115]:

$$\hat{N}|n\rangle = n|n\rangle \qquad \hat{a}|0\rangle = 0 \tag{2.4}$$

$$\hat{a}^\dagger|n\rangle = \sqrt{n+1}\,|n+1\rangle \qquad \hat{a}|n\rangle = \sqrt{n}\,|n-1\rangle \tag{2.5}$$

2.2 Oscillator phase space and displacements

Alternative to the description of the oscillator in terms of the energy eigenstates are descriptions based on the position-momentum phase space. A central concept in this case is given by the phase space shift operator:

$$\hat{\mathcal{D}}(\alpha) = e^{\alpha\,\hat{a}^\dagger - \alpha^*\,\hat{a}} = e^{-2i(\mathrm{Re}(\alpha)\hat{p} - \mathrm{Im}(\alpha)\hat{q})}. \tag{2.6}$$

Here α is a complex parameter denoting the induced shift of the oscillator state. The displacement operator $\hat{\mathcal{D}}(\alpha)$ will be used extensively throughout this thesis and we thus matched our definition of dimensionless position and momentum to correspond to the real and imaginary part of the complex parameter $\alpha = q + ip$. Note that this particular choice leads to the commutation relations $[\hat{q}, \hat{p}] = i/2$. A key property of the displacement operator is that in general it will not commute with a second shift operator [116].

$$\hat{\mathcal{D}}(\beta)\hat{\mathcal{D}}(\alpha) = e^{-i\Phi}\hat{\mathcal{D}}(\alpha + \beta) \text{ with } \Phi = \mathrm{Im}(\beta^*\alpha) \tag{2.7}$$

$$[\hat{\mathcal{D}}(\alpha), \hat{\mathcal{D}}(\beta)] = 2ie^{-i\Phi}\sin(\Phi)\hat{\mathcal{D}}(\alpha)\hat{\mathcal{D}}(\beta) \tag{2.8}$$

This leads to geometric phases of oscillator states dependent on their phase space trajectories. Such phases are exploited for multi-qubit gates in ion traps [117] and this mechanism is also key for many results presented in this thesis. Figure 2.1 shows the oscillator phase space parametrized by the complex number $\gamma = q + ip$. Displayed is in particular the geometric phase due to two consecutive shifts, which is minus twice the area subtended at the origin by the two displacements.

In classical physics the oscillator can be prepared in a state of well defined position and momentum (q, p). When considering imperfect preparation or incomplete state of knowledge of the classical system, it is possible to use a probability density function $P(q, p)$ to specify the oscillator [118]. In 1932 Wigner attempted to find a probability density for the description of quantum

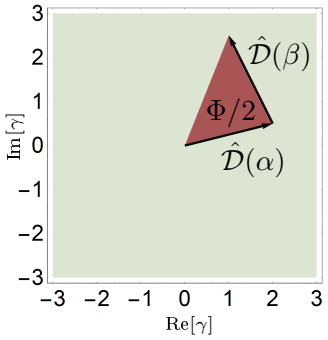

Figure 2.1: The oscillator phase space can be parametrized using a complex number $\mathrm{Re}[\gamma] = q$, $\mathrm{Im}[\gamma] = p$. The operator shifting states in phase space by the complex amount α is given by $\hat{\mathcal{D}}(\alpha) = e^{\alpha\,\hat{a}^\dagger - \alpha^*\,\hat{a}}$ and can be represented as an arrow. The quantum mechanical phase of an oscillator state depends on its trajectory in phase space. For example two consecutive shifts lead to a phase which is twice the size of the area subtended at the origin. This area is highlighted in red.

mechanical states [119]. He introduced the Wigner function $\mathcal{W}(q,p)$ for the complete description of quantum states. A useful definition of the Wigner function is given by the Fourier transform[1] of the expectation value of the phase space shift operator:

$$\mathcal{W}(\gamma) = \frac{1}{\pi^2}\int \chi(\beta) e^{\gamma\beta^* - \gamma^*\beta} d^2\beta \qquad \text{with } \chi(\beta) = \langle\psi|\,\hat{\mathcal{D}}(\beta)\,|\psi\rangle\,. \tag{2.9}$$

$\chi(\beta)$ provides also full state information and is called the characteristic function. Like a probability density the Wigner function is real valued and its marginals when integrating out the momentum or position are the probability density functions for position or momentum, respectively[2]. However, in contrast to a probability density the Wigner function can have negative values and is thus referred to as a quasi probability density.

2.3 Heisenberg relation and oscillator states

Innate to quantum mechanics is the non-commutativity of the position and momentum operators. This restricts the possible states a particle can be

[1] the connection to the conventional two dimensional Fourier transformation definition is given by identifying variables $\{\mathrm{Re}(\gamma), \mathrm{Im}(\gamma)\} \leftrightarrow \{-\mathrm{Im}(\beta), \mathrm{Re}(\beta)\}$

[2] i.e $P(q) = |\langle q|\psi\rangle|^2 = \int \mathcal{W}(q,p)dp$, $P(p) = |\langle p|\psi\rangle|^2 = \int \mathcal{W}(q,p)dq$

prepared in to fulfill the Heisenberg uncertainty principle [120, 121][3]

$$\Delta q \Delta p \geq \frac{1}{4} \left| \langle [\hat{q}, \hat{p}] \rangle \right|^2 \text{ with } [\hat{q}, \hat{p}] = i/2. \tag{2.10}$$

Here $\Delta q = \langle (\hat{q} - \langle \hat{q} \rangle)^2 \rangle$ denotes the variance of position (momentum). From classical physics we would expect the ground state of an oscillator to be given by $q = p = 0$. Quantum mechanically this is still true for the expectation value of position and momentum but as a consequence of the Heisenberg uncertainty relation these values need to have a certain spread. This can be seen calculating the Wigner function of the ground state $|0\rangle$ which is given by a Gaussian function centered around zero $\mathcal{W}(\gamma, |0\rangle) = 2e^{-2|\gamma|^2}/\pi$ with the variances along the axes of $1/4$ revealing the minimally allowed uncertainties.

Excitation to higher energies are required in order to obtain classical states of the oscillator. The action of the shift operator on the ground state $|0\rangle$ leads to such an excitation. The resulting states are called coherent states and are defined as:

$$|\alpha\rangle = \hat{\mathcal{D}}(\alpha) |0\rangle = e^{-|\alpha|^2/2} \sum_{n=0}^{\infty} \frac{\alpha^n}{\sqrt{n!}} |n\rangle . \tag{2.11}$$

The probability to find the oscillator in each energy eigenstate, given that it is initially in a coherent state is $\wp(n) = |\langle n| \hat{\mathcal{D}}(\alpha) |0\rangle|^2 = e^{-|\alpha|^2} |\alpha|^n / n!$, which follows a Poisson distribution. The displacement operator shifts the ground state wave packet to be centered at a different position in the phase space, but maintains its shape. Plots of the Wigner functions of the ground as well as an example coherent state are shown in figure 2.2 (a) and (b). The coherent state has the same uncertainties in position and momentum as the ground state. Thus classical states are obtained in the limit of very large α where these uncertainties become negligible compared to the size of α.

The Heisenberg relation puts a restriction only on the product of uncertainties in position and momentum. Thus we can trade less uncertainty along one axis for more uncertainty along the other axis, which is called squeezing. The relevant operator is given by:

$$\hat{\mathcal{S}}(\xi) = e^{(-\xi \hat{a}^{\dagger 2} + \xi^* \hat{a}^2)/2} \tag{2.12}$$

Applying this operator to the ground state leads to the Wigner function

$$\mathcal{W}(\gamma, \hat{\mathcal{S}}(\xi = re^{i\vartheta}) |0\rangle) = 2e^{-2|\gamma \cosh(r) + \gamma^* e^{i\vartheta} \sinh(r)|^2}/\pi \tag{2.13}$$

shown in figure 2.2 (c). The uncertainty along the axis enclosing the angle $\vartheta/2$ with the momentum axis is increased while the uncertainty along the

[3] Here we gave the uncertainty principle in its generalized version for any pair of hermitian operators $\hat{q}, \hat{p}$.

perpendicular axis is reduced. In this thesis we will often work with position squeezed states $|r\rangle = \hat{\mathcal{S}}(r)|0\rangle$ setting $\vartheta = 0$. In this case the limit of $r \to \infty$ leads to the position eigenstate $|q = 0\rangle$. The states $|q\rangle$ have well defined position i.e. $\hat{q}|q\rangle = q|q\rangle$ and completely uncertain momentum. Note that such a state can not be normalized and thus the limiting case is unphysical.

Shifts and squeezing of the oscillator can be combined leading to displaced squeezed sates $\hat{\mathcal{D}}(\alpha)\hat{\mathcal{S}}(\xi)|0\rangle$ with Wigner functions:

$$\mathcal{W}(\gamma, \hat{\mathcal{D}}(\alpha)\hat{\mathcal{S}}(\xi)|0\rangle) = e^{-|(\gamma-\alpha)\cosh(r)+(\gamma^*-\alpha^*)e^{i\vartheta}\sinh(r)|^2/2} \tag{2.14}$$

Note that here the order of the operation is relevant. In particular interchanging of the operators leads to:

$$\hat{\mathcal{S}}(\xi)\hat{\mathcal{D}}(\alpha')|0\rangle = \hat{\mathcal{D}}(\alpha)\hat{\mathcal{S}}(\xi)|0\rangle\,,\ \alpha' = \cosh(r)\alpha + e^{i\vartheta}\sinh(r)\alpha^* \tag{2.15}$$

2.4 Representations of the oscillator state

A complete basis of the oscillator space allows to fully describe any quantum mechanical oscillator state. The Fock state ladder forms an orthonormal basis[4] commonly used to express oscillator states:

$$\hat{\rho} = \sum_{n,m=0}^{\infty} b_{mn}|m\rangle\langle n| \qquad b_{mn} = \langle m|\hat{\rho}|n\rangle \tag{2.16}$$

$$|\psi\rangle = \sum_{n=0}^{\infty} c_n|n\rangle \qquad c_n = \langle n|\psi\rangle. \tag{2.17}$$

Even though any representation contains full information in practice choosing the basis cleverly facilitates greatly to calculate through a given problem. This idea is extended in chapter 6 to experimental state reconstructions where dependent on the state or feature of interests methods using a different analysis basis can be advantageous. Alternative Fock state bases can be obtained by applying any unitary operation to the original Fock states. In the experiments, we implement squeezing and displacement transformations, leading to reconstructions using displaced and squeezed Fock states $|n\rangle_{\alpha,\xi} = \hat{\mathcal{S}}(\xi)\hat{\mathcal{D}}(\alpha)|n\rangle$.

[4] $\langle n|m\rangle = \delta_{n,m}$, $\sum_n |n\rangle\langle n| = \mathbb{1}$

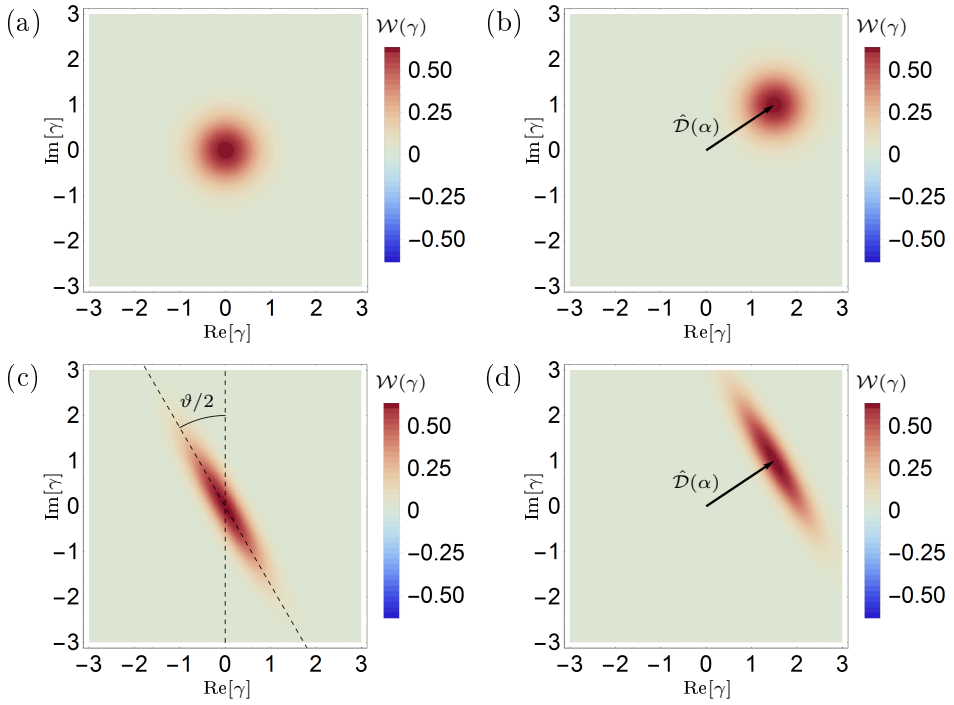

Figure 2.2: A sample of oscillator states in phase space. (a) The oscillator ground state $|0\rangle$, in this case $\Delta q = \Delta p = 1/4$ and the Heisenberg uncertainty relation is saturated. (b) Applying the shift operator to the ground state leads to a coherent state $|\alpha\rangle = \hat{\mathcal{D}}(\alpha)\,|0\rangle$. Shown is $\alpha = 1.4 + i$, the coherent state in particular has the same uncertainties as the ground state. (c) Squeezed vacuum state $\hat{\mathcal{S}}(\xi = re^{i\vartheta})\,|0\rangle$. The uncertainty (variance) along the direction enclosing the angle $\vartheta/2$ with the momentum axis increases by e^{2r} while the perpendicular direction has a reduced uncertainty by e^{-2r}. Shown is $r = 0.8$, $\vartheta = \pi/3$. (d) Combination of squeezing and displacement $\hat{\mathcal{D}}(\alpha)\hat{\mathcal{S}}(\xi)\,|0\rangle$ using the same shift and squeezing as (b) and (c). In case of the reverse order of operations the shift α would be squeezed accordingly and the wave packet would not be centered at $\alpha = 1.4 + i$.

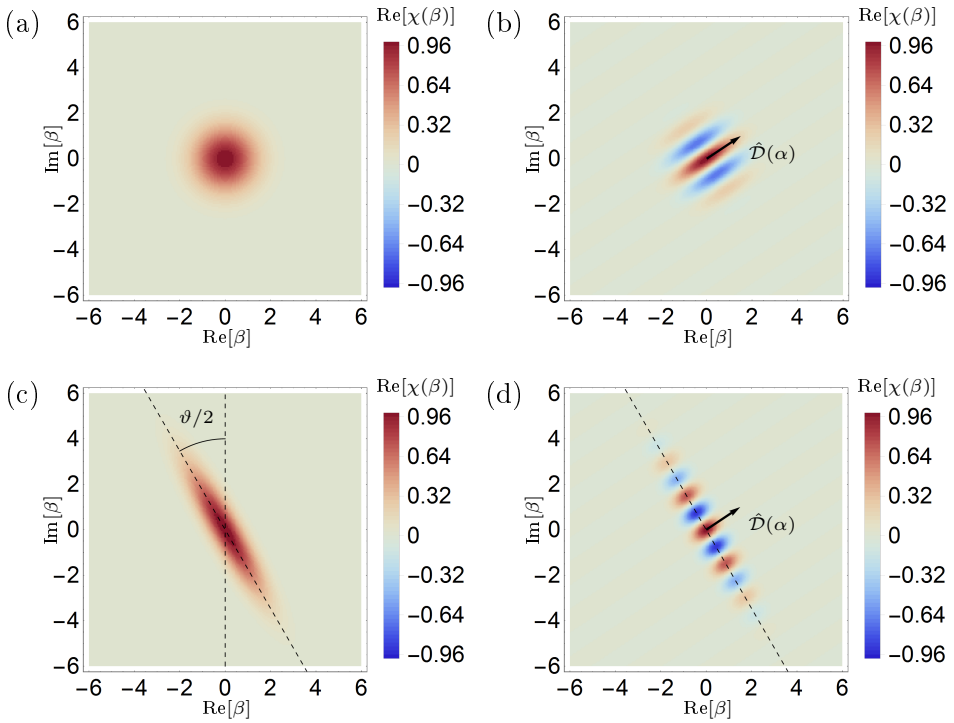

Figure 2.3: A sample of oscillator states in phase space represented by the real parts of their characteristic functions. (a) The oscillator ground state $|0\rangle$ for which $\chi(\beta) = e^{-|\beta|^2/2}$. (b) Coherent state $|\alpha\rangle = \hat{\mathcal{D}}(\alpha)\,|0\rangle$ with $\alpha = 1.4 + i$. (c) Squeezed vacuum state $\hat{\mathcal{S}}(\xi = re^{i\vartheta})\,|0\rangle$ with $r = 0.8$, $\vartheta = \pi/3$. (d) Combination of squeezing and displacement $\hat{\mathcal{D}}(\alpha)\hat{\mathcal{S}}(\xi)\,|0\rangle$ using the same shift and squeezing as (b) and (c). In case of the reverse order of operations the shift α would be squeezed accordingly and the frequency of the ripples would be changed.

2.4.1 Position and momentum representation

The position $|q\rangle$ (momentum $|p\rangle$) basis is often encountered during introductory quantum mechanics, since it bridges the description of a classical to a quantum particle. An oscillator state $|\psi\rangle$ can be written in the position basis as:

$$|\psi\rangle = \int_{-\infty}^{\infty} dq\psi(q)\,|q\rangle\,. \tag{2.18}$$

Here the weight of each position eigenstate is given by the complex valued wavefunction in the position representation $\psi(q) = \langle q|\psi\rangle$.

In addition the position representation is connected via Fourier transform to the momentum representation:

$$\phi(p) = \frac{1}{\sqrt{\pi}} \int_{-\infty}^{\infty} \mathrm{d}q e^{-i2pq}.\psi(q) \tag{2.19}$$

This Fourier relation directly implies the Heisenberg uncertainty relation for position and momentum. More generally any pair of perpendicular axes in the oscillator phase space are connected via a Fourier transform (see App. A.2) and thus exhibit an uncertainty relation. See for example [116] for a revision of position and momentum representation.

2.4.2 Quasi-probabilities and characteristic functions

We have already encountered the Wigner function in order to describe oscillator states in phase space, which we defined in terms of the two dimensional Fourier transform of the expectation value of the shift operator. The shift operator is an exponential function of non-commuting operators $\hat{a}$ and $\hat{a}^\dagger$ and therefore defined using its Maclaurin series[5] $\hat{\mathcal{D}}(\alpha) = e^{\alpha\,\hat{a}^\dagger - \alpha^*\,\hat{a}} = \sum_n (\alpha\,\hat{a}^\dagger - \alpha^*\,\hat{a})^n/n!$. In addition the operator ordering needs to be specified. The three most commonly used orderings are called normal, anti-normal and symmetric ordering. Normal (anti-normal) order refers to moving all $\hat{a}^\dagger$ ($\hat{a}$) operators to the left, while symmetric order refers to using the average of all possible orderings of $\hat{a}^\dagger$ and $\hat{a}$. Implicitly we have assumed symmetric order, which arises if we multiply each term in the exponential keeping the order of operators. For example the symmetrically order version of $(\alpha\,\hat{a}^\dagger - \alpha^*\,\hat{a})^2$ yields $\alpha^2\,\hat{a}^\dagger + (\alpha^*)^2\,\hat{a}^2 - |\alpha|^2(\,\hat{a}^\dagger\,\hat{a} + \hat{a}\,\hat{a}^\dagger)$ while the normal ordered version would give $\alpha^2\,\hat{a}^\dagger + (\alpha^*)^2\,\hat{a}^2 - 2|\alpha|^2\,\hat{a}^\dagger\,\hat{a}$. Using different operator orderings of the shift operator allows to define other quasi-probability distributions [122]:

$$\mathcal{W}_l(\gamma) = \frac{1}{\pi^2} \int \chi_l(\beta) e^{\gamma\beta^* - \gamma^*\beta} d^2\beta \quad \text{with } \chi_l(\beta) = \langle\psi|\,\hat{\mathcal{D}}(\beta)\,|\psi\rangle\, e^{l|\beta|^2/2} \tag{2.20}$$

The Wigner function is obtained in case of $l = 0$, which corresponds to symmetric order and in the following no subscript refers to the case of $l = 0$. In case of $l = -1$, corresponding to anti-normal order the Husimi- or $\mathcal{Q}$ function is obtained: $\mathcal{Q}(\gamma) = \mathcal{W}_{-1}(\gamma)$. The $\mathcal{Q}$ function has a particularly simple expression in terms of coherent states $\mathcal{Q}(\beta) = \frac{1}{\pi}|\langle\beta|\psi\rangle|^2$. The case of normal order $l = 1$ yields the Glauber-Sudarshan P-representation corresponding to representing the state $\hat{\rho}$ in terms of coherent states as $\hat{\rho} = \int \mathrm{d}\alpha^2 P(\alpha)|\alpha\rangle\langle\alpha|$.

The Wigner functions of a sample of relevant states are plotted in figure 2.2. The real parts of the corresponding characteristic functions i.e the Fourier transform of these states are given in figure 2.3. The Wigner function is real valued, thus as a consequence of the Fourier relation the characteristic function

[5] Taylor expansion around the origin

is a complex valued Hermitian function i.e $\chi^*(\beta) = \chi(-\beta)$. In other words the real part is given by an even function $\mathrm{Re}[\chi(\beta)] = \mathrm{Re}[\chi(-\beta)]$ while the imaginary part is and odd function $\mathrm{Im}[\chi(\beta)] = -\mathrm{Im}[\chi(-\beta)]$.

The characteristic function of the ground state is directly found using the overlap of two coherent states:

$$\langle\beta|\alpha\rangle = e^{-\frac{1}{2}(|\beta|^2+|\alpha|^2-2\beta^*\alpha)} \tag{2.21}$$

yielding $\chi(\beta, |0\rangle) = \langle 0|\,\hat{\mathcal{D}}(\beta)\,|0\rangle = e^{-|\beta|^2/2}$. Performing the Fourier transform leads then to the corresponding Wigner function $\mathcal{W}(\gamma, |0\rangle) = 2e^{-2|\beta|^2}/\pi$. The Gaussian of standard deviation $\sigma_\chi = 1$ is thus transformed to a Gaussian with $\sigma_\mathcal{W} = 1/2$. In this case the Wigner and characteristic function look qualitatively the same but their extent differs by a factor of two. If we think of the Wigner function giving the "real" extent of the wave packet then the characteristic function shows how far the wave packet needs to be displaced in order to lose overlap with itself. The latter takes double the extent of the wave packet. The rest of the presented states are connected to the ground state via phase space shifts $\hat{\mathcal{D}}(\alpha)$ as well as squeezing $\hat{\mathcal{S}}(\xi)$, both of which are unitary transformations. The relations for the Wigner and its characteristic function under these transformations are given by particular simple relations [122]:

$$\chi(\beta, \hat{\mathcal{S}}(\xi)\,|\psi\rangle) = \chi(\beta\cosh(r) + \beta^* e^{i\vartheta}\sinh(r), |\psi\rangle) \tag{2.22}$$

$$\mathcal{W}(\gamma, \hat{\mathcal{S}}(\xi)\,|\psi\rangle) = \mathcal{W}(\gamma\cosh(r) + \gamma^* e^{i\vartheta}\sinh(r), |\psi\rangle) \tag{2.23}$$

$$\chi(\beta, \hat{\mathcal{D}}(\alpha)\,|\psi\rangle) = \chi(\beta, |\psi\rangle) e^{\beta\alpha^* - \beta^*\alpha} \tag{2.24}$$

$$\mathcal{W}(\gamma, \hat{\mathcal{D}}(\alpha)\,|\psi\rangle) = \mathcal{W}(\alpha - \gamma, |\psi\rangle) \tag{2.25}$$

Under squeezing both functions χ and $\mathcal{W}$ transform identically. The transformation leads to an increased scaling by a factor e^r along the axis enclosing and angle $\vartheta/2$ with the momentum axis while phase space is scaled down by e^{-r} along the perpendicular axis. This can be seen comparing (a) to (c) in figures 2.2 and 2.3. In case of the phase space shift χ and $\mathcal{W}$ transform differently, which can be explored comparing (a) to (b) in figures 2.2 and 2.3. The Wigner function is simply shifted, by the corresponding amount which is in accordance with the intuition that the Wigner function is providing us with the information about the position and extent of the wave packet. The Fourier transform of this shift leads to a modulation in the characteristic function perpendicular to the direction of the shift. The characteristic function still shows us how far we need to shift the state to lose overlap with itself. The modulation of the signal provides us with information about where the wave packet is located in phase space. The combination of displacement and squeezing leads to the combination of the two transformations.

2.5 Cat states

So far we have analyzed single component states like the ground, coherent and squeezed states. Due to the Heisenberg uncertainty relation the states exhibited additional uncertainties, when compared to their classical versions. But the Wigner function of these states was always positive. In contrast superpositions of such wave packets, show additionally negative Wigner function points, which is a unique quantum feature. In this section we analyze the phase space representations of a superposition of two coherent states:

$$|\psi_\varphi\rangle = \frac{1}{\sqrt{N}}(|0\rangle + e^{i\varphi}|\alpha\rangle) \tag{2.26}$$

with the normalization $N = 2(1 + \cos(\varphi)e^{-|\alpha|^2/2})$. Such a state is simultaneously at two "locations" in phase space namely at 0 and α, while still being connected by the quantum phase φ. For α much larger than the coherent state wave packet extent, the locations become clearly separated. In this case the states are referred to as cat states, with the name relating to Schrödinger's famous thought experiment. Analysis of these highly non-classical states is the topic of chapters 6 and 9. Cat states will be analyzed using transformed Fock bases, while in chapter 9 full state reconstruction in phase space is described.

The expectation for reconstruction of the characteristic function and the $\mathcal{Q}$ function can be calculated using equations 2.7 and 2.21. Fourier transform of the characteristic function χ then leads to the Wigner function of the states. Using the same methods the phase space representations of arbitrary coherent state superpositions can be calculated, which are given in App. B.1.

$$\mathcal{W}(\gamma) = \frac{2}{\pi N}[\boxed{e^{-2|\gamma|^2} + e^{-2|\alpha-\gamma|^2}} + e^{-2|\gamma|^2-|\alpha|^2/2}(e^{-i\varphi+2\alpha^*\gamma} + e^{i\varphi+2\alpha\gamma^*})] \tag{2.27}$$

$$\mathcal{Q}(\beta) = \frac{1}{\pi N}[\boxed{e^{-|\beta|^2} + e^{-|\beta-\alpha|^2}} + e^{-|\beta|^2-|\alpha|^2/2}(e^{-i\varphi+\alpha^*\beta} + e^{i\varphi+\alpha\beta^*})] \tag{2.28}$$

$$\chi(\beta) = \frac{e^{-|\beta|^2/2}}{N}[\boxed{1 + e^{2i\mathrm{Im}(\beta\alpha^*)}} + e^{-|\alpha|^2/2}(e^{-i\varphi+\alpha^*\beta} + e^{i\varphi-\alpha\beta^*})] \tag{2.29}$$

Decoherence processes of the oscillator convert the pure cat state, equation 2.26 to the classical statistical mixture $\hat{\rho} = (|0\rangle\langle 0| + |\alpha\rangle\langle\alpha|)/2$. In particular the superposition phase φ is lost. In the following we analyze, which features of the phase space representations discriminate the quantum superposition from the classical mixture. The representations in case of the mixed states are given by keeping only the terms in the orange boxes in equation 2.27-2.29.

Figure 2.4 (a) shows a plot of the Wigner function of a cat state with $\alpha = 4$ and $\varphi = \pi/2$. The first term in the orange box in equation 2.27, leads to

the Gaussian located at 0. While the second term represents a Gaussian of equal width but located at α. For both the mixed and pure cat states these two indicate the position and sizes of the the two wave packets forming the states. The additional terms in case of the cat state $|\psi_\varphi\rangle$ have an amplitude close to zero unless $\gamma \approx \alpha/2$. The latter indicates the middle point on an imaginary line connecting the two wave packets. The addional terms lead to oscillations perpendicular to this imaginary line. The oscillation speed provides information about α while its phase is determined by φ. These ripples in the Wigner function discriminate the mixed state from the coherent quantum superposition and are thus often referred to as the "quantum interference" between the wave packets. In particular these lead to negative Wigner function values, which clearly lack an interpretation as classical probability density.

The $\mathcal{Q}$ function of the same cat state is shown in figure 2.4 (b). The two terms in the orange box in equation 2.28 again lead to two Gaussians at the positions of the wave packets. The standard deviations of the Gaussians have double the size, when comparing to the Wigner function. Similarly to the Wigner function the additional terms in case of the cat state lead to oscillations between the Gaussians. In case of the $\mathcal{Q}$ function the amplitude of oscillation scales with $e^{-|\alpha|^2/4}$, which for separated wave packets is close to zero. Hence the $\mathcal{Q}$ function is not a good tool to distinguish coherent superpositions from classical mixtures. Still it is well suited to study single component states.

In case of the characteristic function shown in figures 2.4 (c) and (d) the orange boxed terms in equation 2.29 together with the prefactor, no longer lead to Gaussians located around 0 and α. In contrast they generate the oscillations close to the origin. The oscillation speed is determined by α and thus indicates the extent of the state in phase space, independent of whether or not the state is mixed or has a coherent phase relation. The additional terms reminiscent of phase coherence lead to non-zero features for $\beta \approx \pm\alpha$. An intuition for this is provided by the definition of the characteristic function equation 2.20. Shifting the cat state either by α or $-\alpha$ and comparing the resultant state with itself leads to interference. Thus in contrast to the Wigner function these further out components are relevant when using the characteristic function for analysis of superposition states. Oscillations present in all features of the characteristic function indicate an average shift of the analyzed state in phase space. For example the shifted version of the cat state $(|-\alpha/2\rangle + e^{i\varphi}\,|\alpha/2\rangle)/\sqrt{N}$ would show no oscillations in the components at $\pm\alpha$.

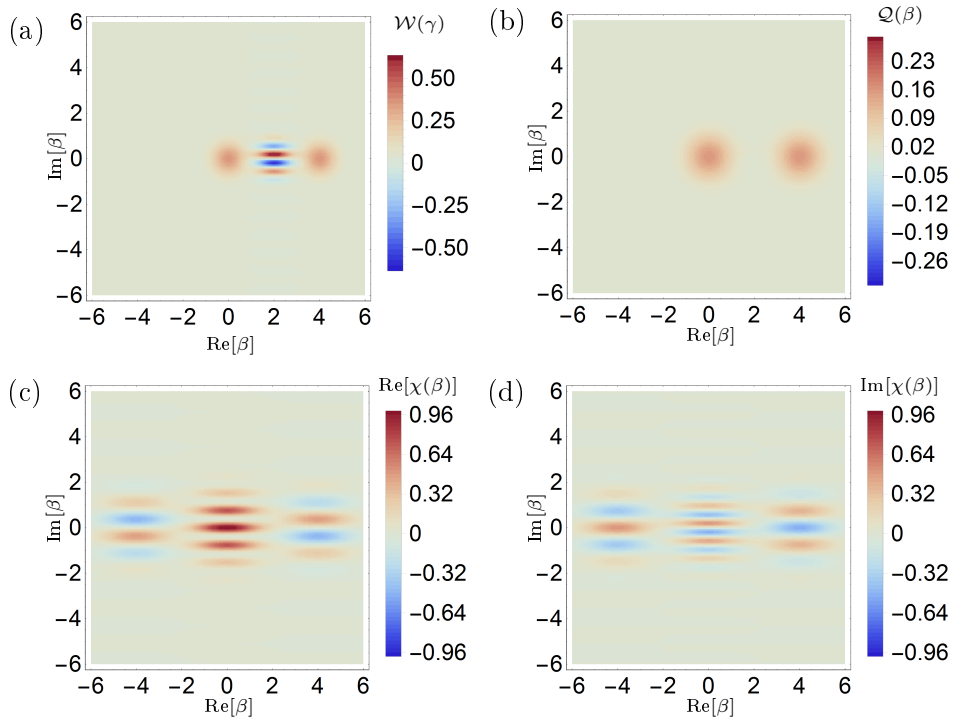

Figure 2.4: Superposition state $|\psi_\varphi\rangle \propto (|0\rangle + e^{i\varphi}|\alpha\rangle)$ with $\varphi = \pi/2$, $\alpha = 4$ represented in phase space. (a) Wigner representation the locations and extents of the wave packets are given by Gaussians while the coherence and the phase φ manifests itself in oscillations between the two wave packets. (b) $\mathcal{Q}$ representation again Gaussians are located at the locations of the wave packets but the interference rippels between them are exponentially suppressed. (c) and (d) Real and imaginary part of the characteristic function. Here oscillations close to zero provide information about the size of the state independent of its phase coherence. While components located at $\beta \approx \pm\alpha$ confirm the coherent superposition.

Chapter 3

Experimental techniques

This thesis is based on experiments using a single trapped $^{40}Ca^{+}$ ion. The ion motional state is cooled, controlled and read out by coupling it to multiple internal states using lasers. This chapter summarizes and introduces the required control tool box. This includes manipulations based on bi- and trichromatic laser beams allowing for versatile control of the oscillator.

3.1 The trapped calcium-40 ion

3.1.1 Motional harmonic oscillator

All experiments were performed in the room temperature TIQI 3D trap setup. This setup is based on a segmented Paul trap, realized using a stack of laser machined and gold coated wafers [123, 124]. The physics of Paul trapping can be found in [125]. For the purpose of this thesis the trapping potential is extremely well approximated by a 3 dimensional harmonic potential. The motion of the single trapped $^{40}Ca^{+}$ ion can be described by three independent modes of oscillation, with typical frequencies of around (1.9 MHz, 2.9 MHz, 3.6 MHz). The first frequency of around 1.9 MHz corresponds to oscillation along the trap axis, which will form our harmonic oscillator of interest, described theoretically using the methods presented in chapter 2.

3.1.2 Internal states and control laser systems

The experimental system is designed for quantum-information processing using both $^{40}Ca^{+}$ and $^{9}Be^{+}$ ions [127]. The vision for the experiment is to use $^{9}Be^{+}$ as a high fidelity qubit, while $^{40}Ca^{+}$ is used as an ancillary system, which for example can be used for sympathetic cooling of the joint motion [128, 129] or state readout [90]. At a magnetic-field of $\approx$ 119.45 G a qubit with a long coherence time is realized in $^{9}Be^{+}$, because two of the beryllium hyperfine levels have a zero first-order dependence on the magnetic field

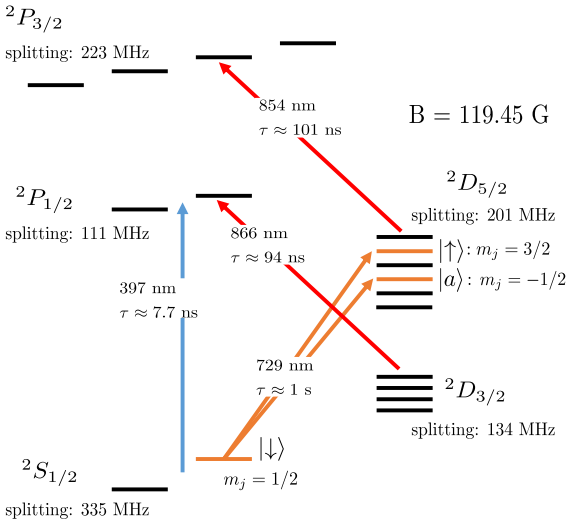

Figure 3.1: Relevant calcium electronic levels [124, 126]. Arrows represent available lasers, while τ gives the lifetime of the corresponding transition. Due to the intermediate magnetic field the Zeeman levels are split up by several 100 MHz as given at each state manifold. Each laser typically contains multiple frequency components separated on the order of the splitting and polarizations allowing to completely repump all states, see [123] for details.

strength [92, 124]. For the experiments of this thesis, this presents a challenge, since the $^{40}Ca^+$ levels are still first-order dependent on the field strength. The high field value therefore means that the fractional stability of the magnetic field must be rather high compared to typical ion trap experiments.

The relevant electronic levels of $^{40}Ca^+$ together with the used laser frequencies are shown in figure 3.1, while figure 3.2 provides an overview of the used laser beam lines with respect to the trap axis orientation and the magnetic field direction. Note that compared to other ion trap experiment operating at lower magnetic fields the lasers here contain multiple frequencies and polarizations to effectively address the required Zeeman sublevels.

The $^2S_{1/2} \leftrightarrow {}^2P_{1/2}$ transition is used for laser cooling of the ions motion. We typically use a sequence of precooling, Doppler cooling and Electromagnetically Induced Transparency (EIT) cooling [130]. For Doppler cooling we use two frequency components of the 397 nm laser beam, which are π and σ polarized respectively [123]. Precooling uses only the π beam, while EIT cooling requires an additional σ beam line [127]. Populations decaying into the $^2D_{3/2}$ manifold are recovered into the cooling cycle using the 866 nm re-pumper laser, which

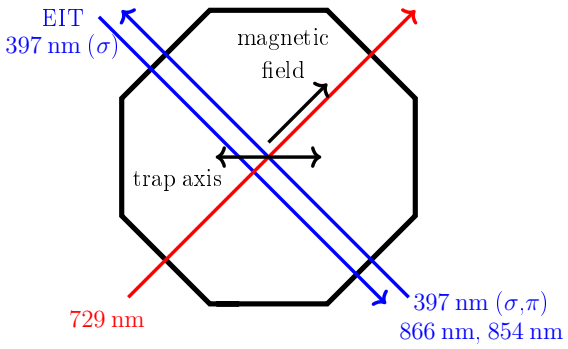

Figure 3.2: Calcium beam lines, trap orientation as well as magnetic field direction.

also contains multiple frequency components.

The dipole forbidden transition from ${}^2S_{1/2} \leftrightarrow {}^2D_{5/2}$ has a long lifetime of about $\approx 1\,\mathrm{s}$, while in our setup it currently decoheres in $\approx 1.5\,\mathrm{ms}$ and is thus suited to store quantum information. We choose the Zeeman sublevels $|\downarrow\rangle \equiv \left|{}^2S_{1/2}, m_j = 1/2\right\rangle$ and $|\uparrow\rangle \equiv \left|{}^2D_{5/2}, m_j = 3/2\right\rangle$ as our internal state qubit. The ion can be initialized in the state $|\downarrow\rangle$ using only the σ component of the 397 nm laser. The qubit transition can be coherently manipulated using a "clock" laser at 729 nm. The "clock" laser has a separate beam line, while 397 nm, 866 nm and 854 nm lasers are overlapped before entering the experimental vacuum chamber, see figure 3.2. We can also tune our 729 nm laser frequency to drive the transition $|\downarrow\rangle \leftrightarrow |a\rangle \equiv \left|{}^2D_{5/2}, m_j = -1/2\right\rangle$. The ${}^2D_{5/2}$ levels can be repumped via the short lived ${}^2P_{3/2}$ states using the 854 nm laser. From ${}^2P_{3/2}$ the state decays mainly back to the ${}^2S_{1/2}$ manifold. Usage of the 397 nm σ polarized laser prepares then again $|\downarrow\rangle$. Thus using the 854 nm and the 397 nm σ lasers we can implement an effective decay of our upper qubit state $|\uparrow\rangle$.

3.2 Internal state readout

The qubit is read out using the 397 nm laser for a duration of typically either 60 us or 200 us, while also repumping with the 866 nm laser. If the qubit is in $|\downarrow\rangle$ this will excite the state to ${}^2P_{1/2}$ from where it decays back to ${}^2S_{1/2}$ emitting a 397 nm photon. This process will repeat multiple times and 4.4% of the emitted photons are collected using in-vacuum lenses. The photons are counted by a photo multiplier tube (PMT) with a quantum efficiency of 26.5% [124]. In cases where the internal state is in $|\uparrow\rangle$ the detection laser does not drive any transition and no photons besides the background counts are detected. These contain contributions from the laser scattering off the electrodes as well as the dark count rate of the PMT. Both the background counts and the counts in case of fluorescence approximate a Poisson distribution, which is shown for the case

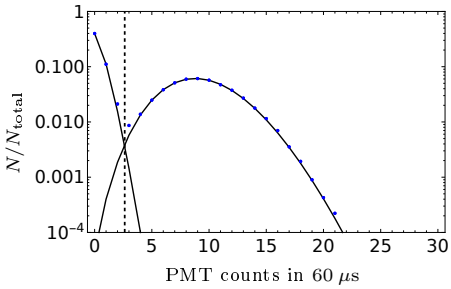

Figure 3.3: Fluorescence detection statistics for 280'000 short readouts (60 us) for a qubit prepared 47% in $|\uparrow\rangle$. Blue points show the observed histogram of counts, while the black lines show the two fitted Poissonian distributions. The found threshold is shown as the black dashed line. The fit matches very well in this case, for substantially longer detection times additional effects like decay of the $|\uparrow\rangle$ state need to be taken into account.

of a 60 us readout time in figure 3.3. From such data a threshold is calculated at the intersection of the two Poissonians and any following detection is classified as result $|\uparrow\rangle$ i.e. associated with the result -1, ($|\downarrow\rangle$, $+1$) if the number of counts is lower (higher) than the threshold. The error in this decision is given by the size of the areas of the Poissonians on the wrong side of the threshold. For the 60 us detection we expect the ion to scatter roughly 1000 photons for a bright result from which we collect about 10 leading to an error of around $\epsilon_{\mathrm{short}} \approx 4 \cdot 10^{-3}$. The error becomes substantially smaller for longer detection times, which separate the two Poisson distributions further apart.

3.2.1 Oscillator disturbance

Each photon absorption and emission cycle will induce at least two momentum kicks onto the oscillator, which is our primary system of interest. The momentum kick upon absorption will be in the direction of the laser while in case of emission the direction will be random. The average real-space kick will be on the order of $\Delta q_r \approx \hbar 2\pi/397\,\mathrm{nm}$. Converted to dimensionless units this leads to phase space shifts on the order of $\Delta q = 1/\sqrt{2m\omega_z\hbar}\Delta q_r \approx 0.13$. Multiple of these kicks will lead to substantial dephasing of our oscillator state.

The situation is different in case of a dark detection result. In this case we obtain information by a so called null measurement. We learn the qubit state via the absence of an interaction[1]. Since there is no interaction between the detection laser and our ion there will also be no momentum kicks onto the

[1] at least no measurable interaction

oscillator. Nevertheless we learn one bit of information and thus update our state description according to quantum theory.

If we wish to perform an experiment on the oscillator including multiple internal state readouts then we will only continue after a readout in case of a dark detection result. In order to be able to continue for both logical results, we will repeat the same measurements but will flip the qubit state just before detection. The decision whether or not to continue to further measurements is performed in real-time using a field-programmable gate array (FPGA) to save data acquisition time.

3.3 Coherent laser ion interactions

The joint system of the internal state qubit and the axial harmonic motional mode of oscillation is coherently manipulated using the 729 nm "clock" laser, which is tuned close to resonance with the internal state transition. We work in a regime where the laser drives only one motional mode, which is possible due to the frequency separation of the motional modes. This simplification further requires all modes to be cooled close to the ground state, which is experimentally achieved using the EIT cooling technique. The bare Hamiltonian of the internal states and the motional oscillator in the absence of the laser interaction is given by:

$$\hat{H}_0 = \hat{H}_a + \hat{H}_m = \hbar\omega_a(\hat{Z} \otimes \mathbb{1})/2 + \hbar\omega(\mathbb{1} \otimes \hat{a}^\dagger \hat{a}). \tag{3.1}$$

Here $\hat{H}_a$ denotes the internal state Hamiltonian with $\omega_a \approx 2\pi \times 411\,\text{THz}$ the angular transition frequency. $\hat{H}_m$ is the Hamiltonian of the motional mode harmonic oscillator where we typically use the axial mode with an angular frequency of $\omega \approx 2\pi \times 1.9\,\text{MHz}$. The joint eigenstates of this system are given by $|\downarrow\rangle|n\rangle, |\uparrow\rangle|n\rangle$ with $n \in \{0, 1, 2, ...\}$; a pictorial representation of the energies of these states is given in figure 3.4 (a).

The internal state qubit and the motional mode are coupled via a strong traveling wave electromagnetic field provided by the 729 nm laser. To describe this it is useful to move to an interaction picture with respect to the bare Hamiltonian $\hat{H}_0$. Terms oscillating at around twice the atomic transition frequency can be neglected from the Hamiltonian since their fast oscillation will average out their effect. The interaction Hamiltonian under this rotating-wave approximation reads [26]:

$$\hat{H}_I = \frac{\hbar\Omega}{2}\hat{\sigma}_+ \exp\left(i\eta(\hat{a}e^{-i\omega t} + \hat{a}^\dagger e^{i\omega t})\right) e^{i((\omega_a-\omega_l)t+\phi)} + \text{h.}c.\,. \tag{3.2}$$

Where ω_l is the laser angular frequency and ϕ the phase of the laser at the ion's position, $\hat{\sigma}_+ = |\uparrow\rangle\langle\downarrow|$ the internal state creation operator, Ω the Rabi frequency and η the Lamb-Dicke parameter. Definitions of these used in the rest of the thesis will be introduced in the following sections.

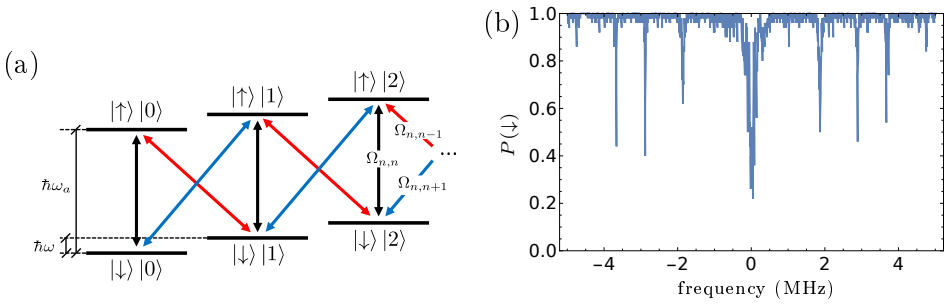

Figure 3.4: Joint internal and motional ion state ladder. (a) Uncoupled energy eigenbasis state ladder, spacing are not up to scale. Arrow indicate the following transitions: Black (carrier), red (red sideband), blue (blue sideband). (b) Excitation of the internal state as a function of laser frequency. Frequencies are given as detunings from the carrier transition at 0 MHz, to the left we find the red sideband transitions of the three independent motional modes, while on the right we find the three blue sideband transitions.

3.3.1 Rabi frequency

The Rabi frequency Ω depends on the specifics of the electro-magnetic interaction with the ion. For the $^{40}Ca^{+}$ qubit transition the electric dipole coupling vanishes leaving the electronic quadrupole coupling as the dominant term. In this case, for the calcium ion with one valence electron, the Rabi frequency is given by [131]:

$$\Omega = \frac{eE_0 k}{2\hbar} \langle\uparrow| (\boldsymbol{r_v} \cdot \boldsymbol{\kappa})(\boldsymbol{r_v} \cdot \boldsymbol{\epsilon}) |\downarrow\rangle \tag{3.3}$$

with E_0 the amplitude of the laser field, e the fundamental charge unit and $\boldsymbol{r_v}$ the position of the single valence electron relative to the nucleus of the $^{40}Ca^{+}$ ion. $\boldsymbol{k} = |\boldsymbol{k}|\boldsymbol{\kappa}$ is the laser wave-vector with $\boldsymbol{\kappa}$ denoting the unit vector along its direction and $\boldsymbol{\epsilon}$ denotes the laser polarization. The internal state wavefunctions are defined relative to the quantization axis given by the magnetic field. The quadrupole laser in our setup travels along the magnetic field direction. For this choice only transitions which change m_j by one have a non-zero Rabi frequency, which in particular is independent of the direction of polarization [132].

3.3.2 Lamb-Dicke approximation

The Lamb-Dicke parameter is given by $\eta = \cos(\theta)|\boldsymbol{k}|z_0$ with θ the angle between the direction of ion oscillation and the wave-vector $\boldsymbol{k}$. $z_0 = \sqrt{\frac{\hbar}{2m\omega}} \approx 8\,\text{nm}$ is the root-mean-square ground state wavefunction extent and

$m = 40\,\text{amu}$ is the ion's mass. The Lamb-Dicke parameter captures the effect of photon-recoil from the laser light onto the ion's motion. This can be seen rewriting the Lamb-Dicke parameter as $\eta = \cos(\theta)\sqrt{E_r/(\hbar\omega)}$ with $E_r = \hbar^2k^2/(2m)$ the photon-recoil energy of the ion and $\hbar\omega$ the energy of an oscillator phonon. In our setup the laser beam travels at an angle of 45 deg to the trap axis, which along with $\omega \approx 2\pi \times 1.9\,\text{MHz}$ yields $\eta \approx 0.05$.

Expanding the exponential containing the Lamb-Dicke parameter in the interaction Hamiltonian given in equation 3.2 leads to terms containing any number of phonon creation and annihilation operators. Thus it is in principle possible to drive transitions between $|\downarrow\rangle|n\rangle \leftrightarrow |\uparrow\rangle|n+s\rangle$ for any $s \in \mathbb{Z}$. If we consider a laser close to resonance with such a transition i.e $\omega_l = \omega_a + s\omega + \delta$ with $\delta \ll \omega$ then we find the following coupling strength for these transitions [26]:

$$\begin{aligned}\Omega_{n+s,n} &= \Omega_{n,n+s} = 2/\hbar|\langle\uparrow|\langle n+s|\hat{H}_I|\downarrow\rangle|n\rangle| \\ &= \Omega|\langle n+s|e^{i\eta(\hat{a}+\hat{a}^\dagger)}|n\rangle| \\ &= \Omega e^{-\eta^2/2}\eta^{|s|}\sqrt{\frac{n_{\min}!}{n_{\max}!}}L_{n_{\min}}^{|s|}(\eta^s), \\ n_{\min} &= \min(n, n+s), n_{\max} = \max(n, n+s)\end{aligned} \tag{3.4}$$

where $L_n^a(x)$ denotes a generalized Laguerre Polynomial:

$$L_n^a(x) = \sum_{k=0}^{n}(-1)^k\binom{n+a}{n-k}\frac{x^k}{k!}. \tag{3.5}$$

At small values of n the coupling strength to transitions with larger s decreases with $\eta^{|s|}$. The strongest transition will be the carrier ($\hat{H}_c$) $s = 0$ followed by the red sideband ($\hat{H}_r$) $s = -1$ and the blue sideband ($\hat{H}_b$) $s = 1$. These three transitions are denoted by the arrows in the state-ladder of figure 3.4 (a).

Figure 3.4 (b) shows the spectrum from scanning the frequency of the qubit laser over the internal state transition resonance with a fixed duration pulse, followed by detection of the qubit state of the ion. If the laser is close to resonance with one of these transitions then there is probability to excite the qubit. In the center we observe the carrier transition and at a $\approx 1.9\,\text{MHz}$ lower (higher) frequency the red sideband (blue sideband) of the axial motional mode can be seen. The additional transitions correspond to blue and red sideband of the radial modes of oscillation and we see that by selecting the frequency of the laser, so long as the Rabi frequency is sufficiently small we can address only one motional mode.

A useful approximation can be made for $\langle\eta^2(\hat{a}+\hat{a}^\dagger)^2\rangle^{1/2} \ll 1$ which allows to only keep the leading order terms in η when expanding the exponential. This condition is satisfied as long as the oscillator stays close to the ground state. Since $\eta \ll 1$ this so called Lamb-Dicke approximation stays valid for oscillators of moderate energy occupations, which is the regime relevant for

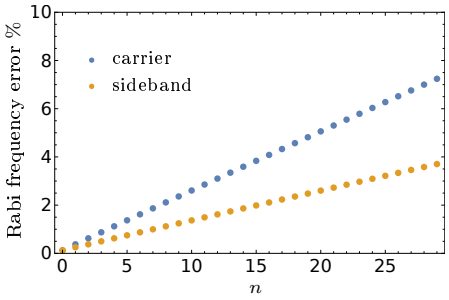

Figure 3.5: Plot of the Rabi frequency error as a function of phonon number n. Plotted is $|\Omega_{L;n,n+s} - \Omega_{n,n+s}|/\Omega_{L;n,n+s}$ in percent with Ω_L the Lamb-Dicke approximated Rabi frequency. Values are calculated using $\eta = 0.05$.

most of the experiments presented in this thesis. In the Lamb-Dicke regime we have the following coupling strength:

$$\Omega_{n,n} = \Omega \qquad \Omega_{n,n-1} = \Omega\eta\sqrt{n} \qquad \Omega_{n,n+1} = \Omega\eta\sqrt{n+1} \tag{3.6}$$

while the Hamiltonians read:

$$\begin{aligned}
\hat{H}_c &= \frac{\hbar\Omega_c}{2}(\hat{\sigma}_+ e^{-i(\delta_c t-\phi_c)} + \hat{\sigma}_- e^{i(\delta_c t-\phi_c)}) \\
\hat{H}_r &= \frac{\hbar i\eta\Omega_r}{2}(\hat{\sigma}_+ \hat{a} e^{-i(\delta_r t-\phi_r)} - \hat{\sigma}_- \hat{a}^\dagger e^{i(\delta_r t-\phi_r)}) \\
\hat{H}_b &= \frac{\hbar i\eta\Omega_b}{2}(\hat{\sigma}_+ \hat{a}^\dagger e^{-i(\delta_b t-\phi_b)} - \hat{\sigma}_- \hat{a} e^{i(\delta_b t-\phi_b)}).
\end{aligned} \tag{3.7}$$

For most of the experiments presented in this thesis the Lamb-Dicke regime is appropriate. Some experiments explore large motional states. In these experiments the Hamiltonians of equation 3.7 can be used but the Rabi frequencies Ω need to be modified in order to account for the full expansion in terms of the Laguerre-Polynomials. Figure 3.5 shows the error of the Lamb-Dicke Rabi frequencies as function of phonon number n and helps to asses the limitation of the Lamb-Dicke approximation.

3.4 Jaynes-Cummings physics

The red sideband Hamiltonian is historically very well known from the strong interaction of an atom with a cavity field mode. In this case it is referred to as Jaynes-Cummings Hamiltonian [133]. In ion traps we have naturally also access to its counterpart the anti-Jaynes-Cummings Hamiltonian (blue sideband). The ion control using these Hamiltonians has been developed in

the last 30 years. Below we summarize some of the main controls still used up to today and relevant for this thesis. The following section will be about how this control can be generalized to transformed motional bases.

3.4.1 Rotations

An arbitrary state of the ion can be expressed in the energy eigenbasis:

$$|\psi(t)\rangle = \sum_{n=0}^{\infty} d_n(t)\,|\downarrow\rangle\,|n\rangle + u_n(t)\,|\uparrow\rangle\,|n\rangle\,. \tag{3.8}$$

In the previous section we have seen that a single frequency near-resonant laser couples only pairs of levels $|\downarrow\rangle|n\rangle \leftrightarrow |\uparrow\rangle|n+s\rangle$ with the coupling strengths $\Omega_{n,n+s}$ dependent on n and s. Thus only transitions between pairs $d_n(t), u_{n+s}(t)$ of the complex normalized coefficients are induced. The full analytic solution of the time evolution under $\hat{H}_I$ (equation 3.2) keeping only resonant term is given by [26]:

$$\begin{pmatrix} u_{n+s}(t) \\ d_n(t) \end{pmatrix} = \hat{U}(t) \begin{pmatrix} u_{n+s}(0) \\ d_n(0) \end{pmatrix} \tag{3.9}$$

$$\hat{U}(t) = \begin{pmatrix} e^{-i\delta t}\left[\cos(\Omega_\delta t) + \frac{i\delta}{2\Omega_\delta}\sin(\Omega_\delta t)\right] & -\frac{i\Omega_{n+s,n}}{\Omega_\delta} e^{-i(\phi+\delta t)}\sin(\Omega_\delta t) \\ -\frac{i\Omega_{n+s,n}}{\Omega_\delta} e^{i(\phi+\delta t)}\sin(\Omega_\delta t) & e^{i\delta t}\left[\cos(\Omega_\delta t) - \frac{i\delta}{2\Omega_\delta}\sin(\Omega_\delta t)\right] \end{pmatrix}.$$

Here we have absorbed irrelevant phases into the laser phase and make use of the definition $\Omega_\delta = (\delta^2 + 4\Omega_{n+s,n}^2)^{1/2}/2$. Ω_δ is the effective Rabi frequency, which increases for higher detunings δ. For non-zero detunings also the off-diagonal prefactors $\frac{i\Omega_{n+s,n}}{\Omega_\delta}$ are less than 1, meaning that complete transfer does not take place between the two internal states. The dynamics can graphically be illustrated on the Bloch sphere as a rotation around a vector $\boldsymbol{W} = (\Omega_{n+s,n}\cos(\phi), \Omega_{n+s,n}\sin(\phi), -\delta)$ with a rotation rate $\Omega_\delta/2$. The evolution simplifies for $\delta = 0$. In this case the rotation will be around a vector on the equator $(\cos\phi, \sin\phi, 0)$, which allows to fully transfer the internal state populations. We can define the rotation angle $\theta = 2\Omega_{n,n+s}t$ and write the time evolution as:

$$\hat{U}(t) = \hat{R}(\theta,\phi) = \begin{pmatrix} \cos(\theta/2) & -ie^{-i\phi}\sin(\theta/2) \\ -ie^{i\phi}\sin(\theta/2) & \cos(\theta/2) \end{pmatrix}. \tag{3.10}$$

The times corresponding to rotations by an angle θ of π, $\pi/2$ are commonly referred to as π-time and $\pi/2$-time.

3.4.2 Preparing Fock state $|n\rangle$

If we apply a carrier π-pulse to an ion initially prepared in $|\downarrow\rangle|0\rangle$ then we excite the internal state while leaving the motion in the ground state $|\uparrow\rangle|0\rangle$ unchanged. If we instead apply a blue sideband π-pulse to the same input

pulse	duration	resultant state
blue sideband	T_π/η	$\|\uparrow\rangle\|1\rangle$
red sideband	$T_\pi/(\eta\sqrt{2})$	$\|\downarrow\rangle\|2\rangle$
blue sideband	$T_\pi/(\eta\sqrt{3})$	$\|\uparrow\rangle\|3\rangle$
red sideband	$T_\pi/(\eta 2)$	$\|\downarrow\rangle\|4\rangle$

Table 3.1: Pulse sequence and duration of pulses in order to transition from $|\downarrow\rangle|0\rangle$ to $|\downarrow\rangle|4\rangle$.

state then we add a motional phonon while exciting the internal state. Let's assume we would like to prepare Fock state $|4\rangle$ then we could after applying the blue sideband π-pulse continue with a red sideband π-pulse followed by an other blue sideband π-pulse and again a red sideband π-pulse. This sequence of pulses "walks" the state up the Fock state ladder according to: $|\uparrow\rangle|1\rangle \rightarrow |\downarrow\rangle|2\rangle \rightarrow |\uparrow\rangle|3\rangle \rightarrow |\downarrow\rangle|4\rangle$. If this sequence of operations is realized using constant laser power then the pulse times need to be adapted due to the dependence of the coupling strengths on the phonon number. Using the Lamb-Dicke approximation and defining T_π to be the carrier π-time results in the π-times given in table 3.1.

This example illustrates that it is possible to walk up and down the ion motional state ladder with suitable resonant sideband pulses thus allowing in principle to prepare Fock state $|n\rangle$ [134]. In case of higher Fock states the durations of the pulses need to include the full expansion in terms of Laguerre polynomials given in equation 3.10. It should be noted however that the dependence of the π-times on the phonon number makes it impossible to perform simultaneously a π-pulse on superpositions of different phonon levels. While this can not be achieved by resonant single frequency pulses it is possible using pulses where the frequency is slowly swept using so called rapid adiabatic passage [135].

3.4.3 Motional state analysis

The dependence of the Rabi frequency on the phonon number can be exploited to analyze the motional state. To do so the internal state is first initialized to $|\uparrow\rangle$ ($|\downarrow\rangle$), then the joint motional and qubit state $|\uparrow\rangle|\psi\rangle$ ($|\downarrow\rangle|\psi\rangle$) is subjected to a red (blue) sideband laser coupling for a variable time t, after which the internal state populations are measured. The internal state occupation varies as a function of time dependent on the Fock state populations of the oscillator state $\wp(n) = |\langle n|\psi\rangle|^2$ according to [29]:

$$\pm[P(\uparrow,t) - P(\downarrow,t)] = \gamma(t)\sum_{n=0}^{\infty}\wp(n)\cos(2\Omega_n t) \tag{3.11}$$

with the other sign for the blue sideband probe pulse instead of the red sideband pulse. For simplicity we use here and in the following $\Omega_n \equiv \Omega_{n,n+1}$.

We have additionally included $\gamma(t)$ accounting for decay in the coherence of the whole system during the probe pulse. By fitting the functional form of equation 3.11 to the measured spin populations it is possible to extract the relative probabilities of the energy eigenstates $\wp(n)$. However this does not confirm the coherent nature of the superposition. This method has been the standard method for characterizing quantum states of the oscillator throughout the work performed in this thesis. This includes for analysis of experimental results (section 6.2), as well as for characterizing the result of calibration experiments.

3.4.4 Sideband cooling

Combining the red sideband with induced decay of the internal state allows for resolved-sideband cooling of the trapped calcium ion [123]. In this case the effective decay rate of the qubit is implemented via the 854 nm coupling. The decay strength can be controlled via the 854 nm laser power and frequency. Additionally the 866 nm re-pumper needs to be switched on and 397 nm is used to optically pump the $^2S_{1/2}$ manifold into $|\downarrow\rangle$. Typically we sideband cool in a pulsed manner alternating between coherent red sideband pulses of variable length with 854 nm pulses inducing the incoherent decay. Further details can be found in [123]. This process leads to successive pumping of the state down the energy state ladder eventually ending up in $|\downarrow\rangle|0\rangle$. Since the red sideband is not able to drive any transition from $|\downarrow\rangle|0\rangle$ population will be trapped in this state and accumulate the longer sideband cooling is performed. This state is dark i.e. no transition is possible, which is captured by $\hat{a}|0\rangle = 0$.

3.5 Displaced squeezed Jaynes-Cummings physics

The toolbox of coherent manipulations, motional state analysis and cooling described in section 3.4 can be generalized to motional state ladders of transformed bases $\hat{U}|n\rangle$. We will consider transformations given by the combination of phase space displacements and squeezing $\hat{U} = \hat{\mathcal{S}}(\xi)\hat{\mathcal{D}}(\alpha)$. The generalizations of coherent manipulations and cooling were demonstrated in earlier work from our group in order to prepare squeezed and coherent states [40, 123]. In chapter 6 the generalization of motional state analysis will prove essential to characterize large "Schrödinger cat" states of the oscillator. Oscillator states transform as $\hat{U}|\psi\rangle$ while oscillator operators $\hat{A}$ transform to $\hat{U}\hat{A}\hat{U}^\dagger$. The novel basis states are given by $|n\rangle_{\alpha,\xi} = \hat{\mathcal{S}}(\xi)\hat{\mathcal{D}}(\alpha)|n\rangle$ while the annihilation operator transforms to [122]:

$$\hat{K} \equiv \hat{\mathcal{S}}(\xi)\hat{\mathcal{D}}(\alpha)\,\hat{a}\hat{\mathcal{D}}(\alpha)^\dagger\hat{\mathcal{S}}(\xi)^\dagger = \cosh(r)\,\hat{a} + e^{i\vartheta}\sinh(r)\,\hat{a}^\dagger - \alpha\mathbb{1}. \tag{3.12}$$

The commutation relations for the transformed operators $\hat{K}, \hat{K}^\dagger$ are preserved relative to the original operators $\hat{a}$, $\hat{a}^\dagger$. In particular we find:

$$\begin{aligned}
\hat{K}\,|n\rangle_{\alpha,\xi} &= \hat{U}\,\hat{a}\hat{U}^\dagger\hat{U}\,|n\rangle = \sqrt{n_{\alpha,\xi}}\,|n-1\rangle_{\alpha,\xi} \\
\hat{K}\,|0\rangle_{\alpha,\xi} &= 0 \\
\hat{K}^\dagger\,|n\rangle_{\alpha,\xi} &= \sqrt{n_{\alpha,\xi}+1}\,|n+1\rangle_{\alpha,\xi} \\
\hat{N}_{\alpha,\xi}\,|n\rangle_{\alpha,\xi} &= n_{\alpha,\xi}\,|n\rangle_{\alpha,\xi}\,.
\end{aligned} \tag{3.13}$$

The red sideband analog Hamiltonian $\hat{H}_-$ coupling directly $|\downarrow\rangle\,|n\rangle_{\alpha,\xi}$ to $|\uparrow\rangle\,|n-1\rangle_{\alpha,\xi}$ can be found transforming the creation and destruction operator in the red sideband Hamiltonian accordingly

$$\hat{H}_- = \frac{\hbar\widetilde{\Omega}i\eta}{2}\hat{\sigma}_+\left[\cosh(r)\,\hat{a} + e^{i\vartheta}\sinh(r)\,\hat{a}^\dagger - \alpha\mathbb{1}\right] + \text{h.c.}\,. \tag{3.14}$$

Inspection of this equation shows that this Hamiltonian can be implemented by using a laser containing three frequency components which are simultaneously resonant with the carrier, the red and the blue sideband transition. The relative Rabi frequencies $\eta\widetilde{\Omega}\alpha$, $\widetilde{\Omega}\cosh(r)$ and $\widetilde{\Omega}\sinh(r)$ of carrier, red and blue sideband together with their laser phases determine the implemented basis transform defined by the parameters $\xi = re^{i\vartheta}$ and α. We can readily implement such control pulses by simultaneously driving an acousto optic modulator (AOM) controlling our 729 nm laser frequency with multiple radio frequency (RF) tones [123] which is described in section 4.3.5. In a similar manner we can implement Hamiltonians $\hat{H}_+$ which are analogous to the blue sideband transition. We will call $\hat{H}_+$ the anti-Hamiltonian in the following. $\hat{U}$ only affects the motion thus within the Lamb-Dicke approximation the carrier is unaffected by the transformation. Furthermore the coupling strength of $\hat{H}_\pm$ in the Lamb-Dicke regime follows the same square root-dependence as a function of transformed quanta as the sideband Hamiltonians. This follows directly from the basis transformation as:

$$\begin{aligned}
\Omega_{n_{\alpha,\xi+1},n_{\alpha,\xi}} =& 2/\hbar|\,\langle\uparrow|\,\langle n+1|_{\alpha,\xi}\,\hat{H}_+\,|\downarrow\rangle\,|n\rangle_{\alpha,\xi}\,| \\
=& \widetilde{\Omega}\eta|\,\langle n+1|\,\hat{U}^\dagger\hat{U}\,\hat{a}^\dagger\hat{U}^\dagger\hat{U}\,|n\rangle\,| \\
=& \sqrt{n_{\alpha,\xi}+1}\widetilde{\Omega}\eta.
\end{aligned} \tag{3.15}$$

3.5.1 Reservoir engineering

Replacing the red sideband Hamiltonian in sideband cooling with $\hat{H}_-$ allows to dissipatively prepare $\hat{U}\,|0\rangle = \hat{\mathcal{S}}(\xi)\hat{\mathcal{D}}(\alpha)\,|0\rangle$ since this is the transformed dark state i.e. $\hat{K}\hat{\mathcal{S}}(\xi)\hat{\mathcal{D}}(\alpha)\,|0\rangle = 0$. This is the main topic of the PhD thesis by Daniel Kienzler [40, 123]. The Method has proven very reliable and robust in the laboratory and is used in this work to readily create moderately

squeezed states of around 9 dB of squeezing. In [40] levels of up to 12.5 dB were demonstrated. Squeezing is a key ingredient for the preparation of the logical grid qubit states discussed in chapter 8, additionally squeezed states were used for improved calibrations or as input states to some of the other experiments.

3.5.2 Preparing $\hat{U}|n\rangle$

Using the generalized couplings allows for coherent Rabi flopping between displaced squeezed Fock states. For example an anti-Hamiltonian $\pi/2$-pulse applied to $|0\rangle_{\alpha,\xi}|\downarrow\rangle$ can be used to create a superposition $(|0\rangle_{\alpha,\xi}|\downarrow\rangle + |1\rangle_{\alpha,\xi}|\uparrow\rangle)$. Further alternating Hamiltonian and anti-Hamiltonian π-pulses can be used to walk up the transformed state ladder. This allows the preparation of displaced and squeezed Fock states $\hat{U}|n\rangle$. The squeezed Fock state ladder has been explored in [39, 123].

3.6 Oscillator phase space shifts

Classical electric forces can be used to implement controllable displacements of the oscillator state. In turn so called optical state-dependent force (SDF) pulses displace the motional oscillator dependent on the internal states.

3.6.1 Electrical force

Application of an oscillating voltage to one of our trapping electrodes leads to an oscillating electric field[2] $E \propto (e^{i(\omega+\delta_t)t+i\phi_t} + e^{-i(\omega+\delta_t)t-i\phi_t})$ at the position of the ion. Here ϕ_t is the phase of the electric field, while $\omega + \delta_t$ its angular oscillation frequency. The potential energy of the ion in this field is given by eEq with q denoting the ions position and e the unit charge. The interaction Hamiltonian is then given by replacing q with the position operator $\hat{q}_r \propto \frac{1}{2}(\hat{a}^\dagger + \hat{a})$. In addition we move to the rotating frame of the oscillator[3] and keep only resonant terms giving

$$\hat{H}_t \propto (e^{i(\omega+\delta_t)t+i\phi_t} + e^{-i(\omega+\delta_t)t-i\phi_t})(\hat{a}^\dagger e^{i\omega t} + \hat{a}e^{-i\omega t}) \tag{3.16}$$

$$\approx \frac{i\hbar g}{2}(\hat{a}e^{i\phi_t+i\delta_t t} + \hat{a}^\dagger e^{-i\phi_t-i\delta_t t}). \tag{3.17}$$

Here we introduced the coupling strength g, which is determined by the applied voltage and the trapping geometry, while ϕ_t is controlled via the phase of the applied electrical signal. The time propagator under this Hamiltonian can be

[2] which is constant across the size of excursion of the ion, due to the larger size scale of the electrodes.

[3] defined by: $\hat{a} \to \hat{a}e^{-i\omega t}, \hat{a}^\dagger \to \hat{a}^\dagger e^{i\omega t}$

analytically calculated to be:

$$\hat{U}(t) = \hat{\mathcal{D}}(\alpha(t))e^{-i\beta(t)} \tag{3.18}$$

$$\alpha(t) = -\frac{ig}{\delta_t}e^{-i(\delta_t t+\phi_t)}\sin(\delta_t t/2),\ \beta(t) = \frac{g^2}{4\delta_t^2}(\delta_t t - \sin(\delta_t t)). \tag{3.19}$$

We will refer to the oscillating electrical drive as a tickling pulse in the remainder of the thesis. The evolution of an oscillator state under the tickling pulse with a constant detuning and using a fixed phase ϕ_t, follows the circular trajectory given by $\alpha(t)$ in equation 3.19. The diameter of the circle is given by g/δ_t and the oscillator periodically returns to the origin for times which are multiples of $T = 2\pi/\delta_t$. Additionally the state acquires a phase according to $\beta(t)$ with $\beta(T) = \frac{g^2\pi}{2\delta_t}$. This phase corresponds to twice the area subtended by the trajectory at the origin $\beta(t) = -\mathrm{Im}\int \alpha^*(t)d\alpha$ and is thus given by minus the integration of infinitesimal geometric phases as defined in equation 2.8. A more close analysis of the phase reveals that the origin of this phase is not only of geometric nature ϕ_G but has also a dynamical component ϕ_D i.e. due to varying energy of the state during the evolution [117]. The relation between the two phases is fixed $\phi_D = -2\phi_G$ such that the total phase $\beta = \phi_D + \phi_G = -\phi_G$. The fixed relation between ϕ_G and ϕ_D means that we will refer to the total phase as a geometric phase throughout the rest of this thesis [117, 136].

On resonance the radius of the trajectory approaches infinity thus the components move out on straight lines and will never return to the origin. The propagator in this case is given by:

$$\hat{U}(t) = \hat{\mathcal{D}}(\alpha(t)), \qquad \alpha(t) = -\frac{igte^{-i\phi_t}}{2}. \tag{3.20}$$

3.6.2 Optical state-dependent force

SDF pulses are realized by the simultaneous drive of red and blue sideband with equal strength $\Omega = \Omega_r = \Omega_b$ and detunings $\delta_{b/r} = \pm\delta$ [137]. This laser pulse is also commonly used in trapped-ion two-qubit Mølmer-Sørensen gates [24, 127, 138–142]. The Hamiltonian for the SDF is given by

$$\hat{H}_{SDF} = \frac{i\eta\hbar\Omega}{2}\hat{\sigma}_{\overline{\phi}}(\hat{a}e^{i\Delta\phi/2+i\delta t} + \hat{a}^\dagger e^{-i\Delta\phi/2-i\delta t}). \tag{3.21}$$

Where $\sigma_{\overline{\phi}} = \hat{\sigma}_+ e^{i\overline{\phi}} - \hat{\sigma}_- e^{-i\overline{\phi}}$ and the phases $\overline{\phi} = (\phi_r + \phi_b)/2$ and $\Delta\phi = \phi_r - \phi_b$ are given by the average and difference of the blue and red sideband laser phases respectively. Identifying $\eta\Omega \to g$, $\Delta\phi/2 \to \phi_t$ and $\delta \to \delta t$ in the SDF Hamiltonian shows its similarity to the coupling under tickling. The SDF Hamiltonian only differs by the additional operator $\hat{\sigma}_{\overline{\phi}}$ acting on the internal qubit states. The time propagator under the SDF Hamiltonian can thus be

written as:

$$\hat{U}(t) = \hat{\mathcal{D}}(-i\alpha(t)\hat{\sigma}_{\overline{\phi}})e^{-i\beta(t)\hat{\sigma}_{\overline{\phi}}^2} \tag{3.22}$$
$$\alpha(t) = \frac{\eta\Omega}{\delta}e^{-i(\delta t+\Delta\phi/2)}\sin(\delta t/2),\ \beta(t) = \frac{\eta^2\Omega^2}{4\delta^2}(\delta t - \sin(\delta t)).$$

On resonance, $\delta = 0$, giving

$$\hat{U}(t) = \hat{\mathcal{D}}(-i\alpha(t)\hat{\sigma}_{\overline{\phi}}),\ \alpha(t) = \frac{\eta\Omega t e^{-i\Delta\phi/2}}{2},\ \beta(t) = 0. \tag{3.23}$$

The effect of the additional $\hat{\sigma}_{\overline{\phi}}$ is to perform phase space displacements of the oscillator dependent on the internal qubit state. As an example consider an oscillator in an arbitrary state $|\psi\rangle$ and the qubit initialized in $|\uparrow\rangle$ and $-i\hat{\sigma}_{\overline{\phi}=\pi/2}^{-} = \hat{X}$, while $\delta = 0$. Since $|\uparrow\rangle = (|+\rangle - |-\rangle)/\sqrt{2}$ is a superposition of the eigenstates of $\hat{X}$ with eigenvalues ± 1 the SDF will split up the motion into two components and displace them in opposite directions. An illustration is given in figure 3.6 (a). This behavior follows directly from the definition of the operator exponential via its expansion:

$$\begin{aligned}\hat{\mathcal{D}}(\alpha\hat{X})\,|\pm\rangle\,|\psi\rangle &= e^{(\alpha\,\hat{a}^\dagger - \alpha^*\,\hat{a})\hat{X}}\,|\pm\rangle\,|\psi\rangle \\ &= \sum_{n=0}^{\infty}\frac{(\alpha\,\hat{a}^\dagger - \alpha^*\,\hat{a})^n\hat{X}^n}{n!}\,|\pm\rangle\,|\psi\rangle \\ &= |\pm\rangle\sum_{n=0}^{\infty}\frac{(\alpha\,\hat{a}^\dagger - \alpha^*\,\hat{a})^n(\pm 1)^n}{n!}\,|\psi\rangle \\ &= |\pm\rangle\,\hat{\mathcal{D}}(\pm\alpha)\,|\psi\rangle\,.\end{aligned} \tag{3.24}$$

In case of a constant detuning and using a fixed phase the state $|\pm\rangle\,|\psi\rangle$ splits up into two parts, which follow the circular trajectories of $\pm\alpha(t)$ given in equation 3.22 and shown in figure 3.6 (b).

In the laboratory we have full control over the phases $\overline{\phi}$ and $\Delta\phi$ via control of the blue and red sideband laser phases. The former controls the dependence of the displacement on the internal state, while the latter allows to control the direction of the displacement α. We typically fix $\overline{\phi} = \pi/2$ and change instead the internal state with resonant carrier pulses. As an example the motional state is split up into two equal weight components, when the SDF with $\overline{\phi} = \pi/2$ is applied to a $\hat{Y}$ eigenstate. This is because $-i\hat{\sigma}_{\overline{\phi}=\pi/2}^{-} = \hat{X}$. In order to displace all population to the same direction we can now (i) change the state to a $\hat{X}$ eigenstate using carrier pulses or (ii) use $\overline{\phi} = 0$ realizing $-i\hat{\sigma}_{\overline{\phi}}^{-} = \hat{Y}$.

In the following we will often make use of the sequence

$$\hat{R}(\pi/2)\hat{\mathcal{D}}(\alpha(t)\hat{X})\hat{R}(-\pi/2) = \hat{\mathcal{D}}(\alpha(t)\hat{Z}) = \text{SDFz}, \tag{3.25}$$

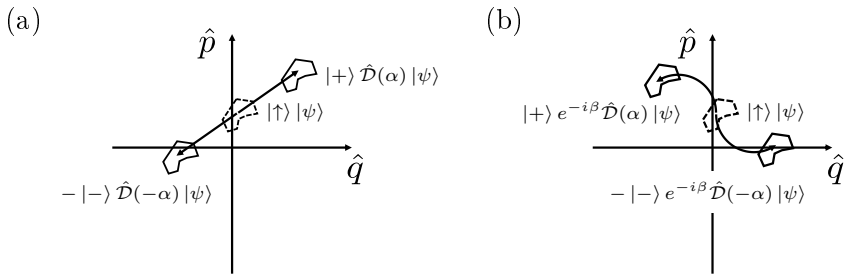

Figure 3.6: Evolution of the input state $|\uparrow\rangle\,|\psi\rangle$ under the SDF Hamiltonian with $\overline{\phi} = \pi/2$. The arbitrary motional state is represented by the polygon where the dashed polygon represents the state before the laser pulse. (a) The SDF on resonance $\delta = 0$, the motional state splits up into two components entangled with the internal qubit state. The components move outwards into opposite directions with the direction controlled via $\Delta\phi$ the size of the displacement is determined by the duration and coupling strength of the pulse. (b) The case of a detuning δ where again the state splits up into two components, which now follow circular trajectories and acquire phases β given by twice the magnitude of the subtended areas at the origin.

here $\hat{R}(\phi) = \hat{R}(\pi/2, \phi)$ are carrier $\pi/2$-pulses of laser phase ϕ. In this block the two rotations around the SDF pulse effectively rotate the state-dependence from $\hat{X}$ to $\hat{Z}$. Applying this sequence to an ion prepared in $|\uparrow\rangle$ or $|\downarrow\rangle$ allows to displace the oscillator effectively independent of the internal state and thus additional tickling pulses do not extend the laser control tool box. Nevertheless state independent shifts based on tickling have a simpler pulse sequence and additionally have an order of magnitude higher coupling strength. In the experiments of chapter 7 we used shifts based on SDFz, while in chapter 8 and 9 we replaced SDFz by tickling pulses. However SDFz is still used to calibrate the tickling pulse to the laser force as described in section 5.5.1.

Chapter 4

Extension of internal state coherence

The experiments in this thesis manipulate the state of the calcium motional oscillator via coupling to the internal states and hence rely on sufficiently long internal state coherence. The latter is determined by the joint effect of the magnetic field fluctuations defining the energy splitting of the qubit and fluctuations of the laser system used for driving transitions. In the following two sections I report on upgrades to the experimental setup improving both the magnetic field noise characteristics as well as the control laser spectrum. Together these changes allowed an improvement of the calcium coherence by roughly an order of magnitude.

4.1 Internal state coherence

We use the Ramsey method in order to quantify decoherence of our internal states. A superposition of $|\downarrow\rangle - i\,|\uparrow\rangle$ is prepared using a $\pi/2-$pulse, $\hat{R}(\pi/2, 0)$ applied to $|\downarrow\rangle$. During the following wait time of duration T the superposition is susceptible to decoherence. Neglecting internal state decay the decoherence can be modeled as an accumulation of relative phase $\phi_f + \phi_0 = \int_0^T (N_f(t) + N_0)\mathrm{d}t$ between $|\downarrow\rangle$, $|\uparrow\rangle$. Here $N_f(t)$ denotes temporal fluctuations of the laser and the magnetic field, while N_0 gives a constant offset. The accumulated relative phases due to $N_f(t)$ and N_0 are given by ϕ_f and ϕ_0 respectively. N_0 can arise due to a constant miscalibration or a deliberate detuning. A second $\pi/2$-pulse $\hat{R}(\pi/2, \phi_l)$ is followed by fluorescence detection of the internal states. For one realization of the Ramsey experiment we find a bright or dark detection result according to the probabilities $\langle\hat{Z}\rangle = 2P(\downarrow) - 1 = -\cos(\phi_f + \phi_0 - \phi_l) = -\mathrm{Re}[e^{-i(\phi_l - \phi_0)}e^{i\phi_f}]$ [123]. In order to find the measurement probabilities the ensemble average over the realization of the noise needs to be calculated. The laser control phase ϕ_l and the phase due to the detuning ϕ_0 are constants thus the relevant ensemble average $\langle e^{i\phi_f}\rangle_{\mathrm{real.}}$ captures the reduction in contrast

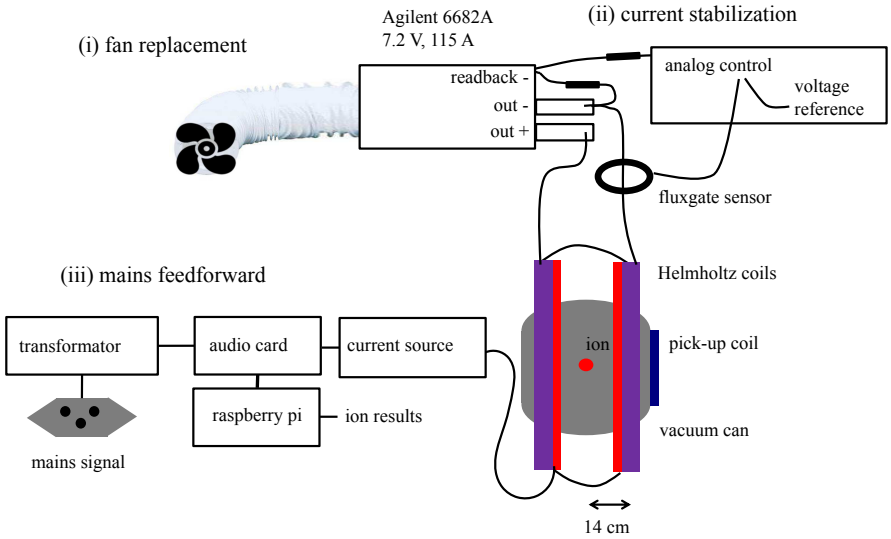

Figure 4.1: Summary of magnetic field system. A pair of coils in Helmholtz configuration are driven with a current of 115 A using an Agilent 6682A power supply. (i) The fan speed control leaks into the output of this model of power supply, which leads to 10 Hz noise. This noise source was removed by replacing the fan. (ii) The power supply output current is further stabilized using a fluxgate sensor. (iii) Line cycle noise is compensated by a feedforward system calibrated from measurements at the ion.

$C(T)$ if the cosine $\langle \hat{Z} \rangle$ is measured as a function of ϕ_l. ϕ_0 leads to a phase offset in the respective oscillation.

$C(T)$ can be calculated for different relevant noise models. For example fast (compared with the wait time T) white noise would lead to an exponential decay: $C(T) = e^{-T/\tau}$ [143]. At the other extreme, slow noise realizes in each experimental run a different but constant detuning δ, with the detuning sampled from a probability density $P(\delta)$. In this case the contrast follows the Fourier transform of the probability density $C(T) = |\int_{-\infty}^{\infty} P(\delta) e^{-i\delta T} d\delta|$. For detunings sampled from a normal distribution of standard deviation σ then the contrast follows a Gaussian $C(T) = e^{-\frac{1}{2}(\sigma T)^2}$. In case of a Lorenzian distribution an exponential decay is found [143].

Additional information about the noise spectrum can be obtained using so called dynamical decoupling pulse sequences [144]. In such sequences additional π-pulses during the wait time interchange the qubit states, which leads to a sign change in the integration of the noise. Using a single π-pulse in the middle of the wait time is called Hahn- or spin-echo [145], which completely cancels the phase shift due to ϕ_0 while further reducing sensitivity to slow noise frequencies (i.e. below $f < 2/T$) [146].

Coherence measurements using the additional level $|a\rangle$, see figure 3.1 can be used in order to discriminate decoherence due to the laser from contribution due to magnetic noise. Ramsey measurements between each pair of levels are considered. These are defined as follows and have different magnetic field sensitivities τ:

$$T1 : |\downarrow\rangle \leftrightarrow |\uparrow\rangle : \tau \approx 1.1\,\mathrm{kHz/mG}, \quad T2 : |\downarrow\rangle \leftrightarrow |a\rangle : 2\tau, \quad T3 : |\uparrow\rangle \leftrightarrow |a\rangle : 3\tau. \quad (4.1)$$

The Ramsey measurement on T2 is implemented analogous to the Ramsey measurement on the qubit transition T1. The laser frequency for the two $\pi/2$-pulses is just shifted in order to be resonant with T2. In contrast the creation of a superposition state in T3 requires an additional pulse. The superposition is created using first a $\pi/2$-pulse on transition T1 followed by a π-pulse on T2. Both pulses are implemented using the same laser thus the dependence on the laser phase drops out in the superposition state between $|a\rangle$ and $|\uparrow\rangle$. After the wait time the pulses are applied in reverse order; first the π-pulse on T2 followed by the $\pi/2$-pulse on T1. The independence of the superposition state on the laser phase renders the Ramsey measurement on T3 independent of laser noise. This was confirmed experimentally by injecting laser noise while performing this particular experiment.

4.2 Stabilization and compensation of magnetic fields

All experiments are operated at a magnetic field of 119.4 G, which is produced by a 115.61 A current through a pair of Helmholtz coils (diameter 0.29 m, 20 windings) located around the vacuum can hosting the ion trap [123]. This field realizes a first order magnetic field insensitive hyperfine qubit for beryllium, which allows for coherence times of multiple of seconds [92]. In our experimental system early measurements realized values of $\approx 3.9 \pm 0.8$ s [124]. In contrast, the relevant qubit transitions in calcium are sensitive to magnetic field fluctuations. Therefore fluctuations and noise in the 115.61 A current output of the Agilent 6682A power supply cause decoherence of the calcium internal states. Additionally, there is magnetic noise in the laboratory due to other electronics present in the vicinity of the setup. This noise is dominant at the mains frequency of 50 Hz and at multiples of this frequency.

The magnetic noise sources are either diagnosed outside the experimental vacuum chamber using a self-made pick-up coil [147] or directly at the ion's position using the ion itself as a sensor. In the latter case the Ramsey and spin echo experiments described above are used.

The magnetic field noise was improved by implementing the following modifications: (i) replacement of the cooling fan of the power supply, (ii) addition of a slow stabilization of the current output to the power supply and (iii) setting up a feedforward (FF) compensation for line noise calibrated from the ion signal. Figure 4.1 summaries these three changes. The magnetic field

work is based on the conclusion drawn in my master's project [147] and all three listed improvements were realized with close support from Peter Märki.

4.2.1 Power supply modification

The pick-up coil signal measured a dominant frequency component at 10 Hz. The source of this signal could be tracked down to the pulse-width modulated (PWM) signal at 10 Hz controlling the cooling fan speed of the Agilent 6682A power supply. Additionally, magnetic coupling from the fan produced a $90 - 110$ Hz peak, with the frequency dependent on the fan speed. Therefore the power supply fan was replaced with an external fan connected via an air flow pipe and the harmful PWM signal tracks were cut such that they no longer leak into the current output of the power supply. Please see App. C.1 for schematics of the electronics and details on the modification.

The leakage of the 10 Hz component into the output is specific to the 6682A model of Agilent power supply, the very similar model 6671A does not have this problem[1]. In figure 4.2 (a) the pick-up coil signal before the replacement of the fan is shown, while in (b) the same readout signal is shown after the replacement. In (a) and (b) noise peaks at 50 Hz and multiples of this frequency are visible. These peaks are due to the line noise. In (a) additional peaks at 10 Hz and around 100 Hz due to the fan are visible, which are clearly removed in the signal shown in (b).

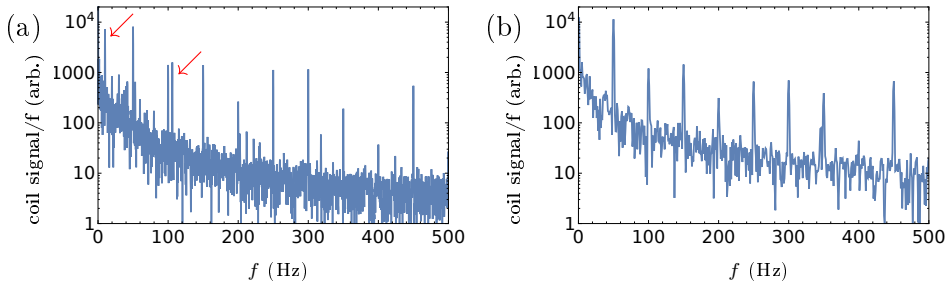

Figure 4.2: Measurements of magnetic noise spectrum using the pick-up coils close to the setup. Peaks at 50 Hz and multiple of this frequency are due to line noise. (a) Noise spectrum before replacement of the power supply fan. A dominant 10 Hz and an additional component at $90 - 110$ Hz are visible and highlighted by the red arrows. These components are no longer visible in (b), which shows the same measurement after the power supply modifications.

[1] Schäfer, Vera, University of Oxford, private communication

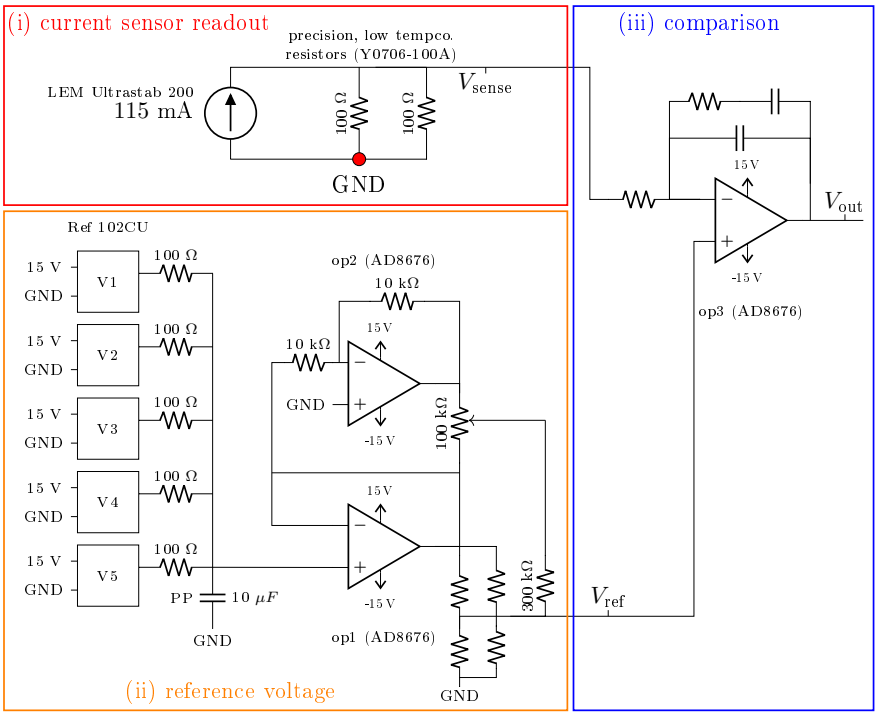

Figure 4.3: Output current stabilization circuit. (i) Conversion of the fluxgate sensor (LEM Ultrastab 200) current to a readout voltage using two precision resistors. The sensor current is guided via thick wire (indicated by the red dot) directly to the PCB 0 V input. (ii) Production of a stable adjustable reference voltage using the averaged output of five 10 V low noise references. (iii) Comparison and feedback of sensor voltage V_{sense} to the reference voltage V_{ref}. Not shown are 1 μF ceramic capacitors close to the power supply inputs of each Op. Amp. and voltage reference. Further not shown is input voltage filtering using 470 μF PET capacitors.

4.2.2 Current stabilization

The removal of the dominant 10 Hz noise component only led to a marginal improvement of the Ramsey coherence time. This was due to additional fluctuations of the Helmholtz coil current on slow timescales. These fluctuations can no longer be diagnosed with the pick-up coil sensor, since this sensor loses sensitivity for slower frequencies.

The stability of the Agilent power supply was improved by running it in constant voltage mode and performing the current stabilization with a self built low noise feedback loop. This self-built feedback loop consists of three main parts: (i) output current sensing, (ii) generation of a stable and adjustable reference voltage, (iii) slow feedback of the sensed current to the stable reference voltage.

Output current sensing

The power supply output current is measured using a fluxgate sensor[2], which is rigidly mounted around the Agilent output cable. A D-sub9 cable connects the sensor output to the DC stabilization box from where the sensor is also powered. The DC stabilization box contains a self etched printed circuit board (PCB) realizing the circuit depicted in figure 4.3. The sensor outputs a 1000 times smaller current than the primary current, which for the used 115 A amounts to 115 mA. The current is transformed into a voltage by two 100 Ω precision, low temperature drift resistors[3]. The sensor current of 115 mA is a relatively large current which is flowing across the PCB to ground. Thus a very short and thick cable connects the ground end of the readout resistors (see red dot in figure 4.3) to the 0 V input of the stabilization box. An additional thick cable is added in order to reduce the inductance of the cable.

Reference voltage

A stable reference is produced by averaging the voltage of 5 high precision voltage references[4] (see figure 4.3). Taking the average improves uncorrelated fluctuations between the individual references by a factor of $\sqrt{5}$ in the noise density which corresponds to a factor 5 in power. Further the noise characteristics of a batch of references was measured and only the best 5 references were chosen. The average is created using 100 Ω metal film resistors and is additionally filtered by a 10 μF polypropylene capacitor. The reference voltage is then buffered by an operational amplifier (Op. Amp.) op1[5] and the experimentally required voltage is roughly created by the following voltage divider network. The voltage can be adjusted by replacing the resistors on the board. Fine tuning of the reference voltage is performed by adding a variable voltage via the 300 kΩ resistor. The variable voltage is produced by a potentiometer between −10 V and 10 V. For 10 V the precise reference voltage is used. This voltage is inverted by an additional Op. Amp. op2 in order to produce the −10 V. The adjustment is ±0.05 V which is 0.64 % of the absolute voltage ≈ 5.7 V. Here it is important to use a wire potentiometer because thick film potentiometers produce excess noise[6].

[2] LEM Ultrastab200

[3] Y0706-100A; with ±0.2 ppm°C temperature drift and ±0.01 % precision

[4] Ref102CU

[5] model AD8676

[6] according to noise study of a set of electronic components by Märki, Peter, private communication

Voltage comparison and feedback

The reference voltage is compared to the sensor voltage using Op. Amp. op3. The elements in the Op. Amp. feedback are exchangeable in order to match the controller to the experimental system. Here in particular styroflex capacitors are used due to their high insulation properties. We output this feedback signal V_{out} via two BNC connectors. One is used for the feedback onto the power supply and the other for monitoring of the controller via an oscilloscope. The monitor output is not connected to the stabilization PCB ground in order to avoid ground loops, still it can be used to monitor the feedback voltage roughly.

Like a typical power supply the Agilent 6682A can either be operated in constant current or constant voltage control mode. We operate the Agilent power supply in constant voltage mode and provide the current stabilization via the self build slow control loop. In the voltage control mode the Agilent supply stabilizes its output based on the negative output voltage labeled "out -" in figure 4.4. This signal is connected via a short external cable to the "readback -" port of the Agilent supply.

Slow current stabilization is achieved by modifying the "readback -" signal. To do so a small resistance of $10\,\Omega$ is added in the cable connecting "out -" to the readback port. This resistance is small enough such that the Agilent supply is still working without the self built stabilization connected. The output of the DC stabilization box V_{out} is additionally connected to the "readback -" port via a $20\,\text{k}\Omega$ resistor. The two resistors form a voltage divider, which modifies the readback voltage by $\approx V_{\text{out}}/2000$.

Grounding

The grounding of the electronics is essential for the low noise stabilization and is shown in red in figure 4.4. The negative output "out -" of the Agilent supply is directly connected to the laboratory ground. This is the only laboratory ground connection of the whole slow stabilization system. The circuit given in figure 4.3 is contained in a shielding box, which is referenced to the laboratory ground via a cable from the housing to the Agilent "out -" port. The DC stabilization box is powered from a power supply unit (PSU) with a floating ground. Both housings are on ground and thus stand on plastic feet in-order to avoid ground loops.

The fluxgate sensor is connected to the DC stabilization box via the D-sub9 cable which serves two purposes. It routes the secondary sense current to the DC stabilization box ("sense in" in figure 4.4) furthermore the cable powers the fluxgate sensor. As described in the previous section an additional thick cable (given as the dashed red line) routes the relatively large secondary current to the ground of the floating PSU.

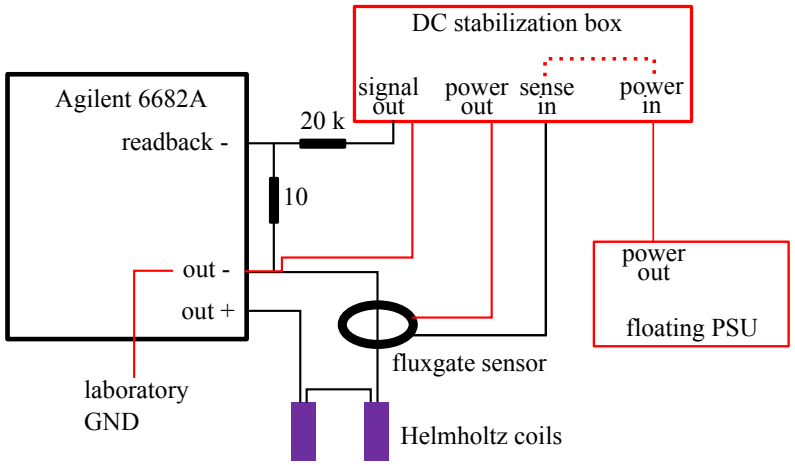

Figure 4.4: Grounding of current stabilization. Ground connections are given in red. The dashed line indicates that this connection is within the DC stabilization box. Solely the "out -" port of the Agilent supply is connected to the laboratory ground. This port provides then grounding to the DC stabilization box as well as the fluxgate sensor and the floating PSU as shown in the schematics. To avoid ground loops both the floating PSU and the DC stabilization box stand on plastic feet.

Characterization of the feedback electronics

In order to characterize the noise of the sensor readout and reference voltage a second almost identical feedback system is soldered and a second fluxgate sensor is used. Subtracting signals from the two independent systems allows to quantify their combined noise, which gives an upper bound on the noise of the individual systems. Any correlated noise is not captured. In order to create similar conditions as in the experiment but with a low 1 A current, 116 windings were put through both sensors. To avoid ground loops both electronic boxes were powered from individual power supplies. See App. C.2 for a photograph of the test setup. The measured noise characteristics are shown in figure 4.5 and the integration of the noise over selected frequency decade converted to magnetic field fluctuations is given in table 4.1. These measurements suggest that $O(10^{-7})$ relative magnetic field stabilities should in principle be possible. In addition using the same test setup it was confirmed that the potentiometer introduces negligible noise, and that fluctuations V_{ref} are independent of the sensed current. The board shows switch on characteristics as well as temperature drifts and thus for best stability it should be run continuously in a stable environment.

A similar stabilization system is used in the Oxford ion trapping group [148]. Their current feedback loop operates with a higher bandwidth which requires careful matching of the feedback circuitry to the transfer function of the coils. Our main motivation was to stabilize the slow noise components and thus the filter design was avoided by limiting the bandwidth of the controller. The NIST ion trapping group has built a similar feedback system based on and extending our work.

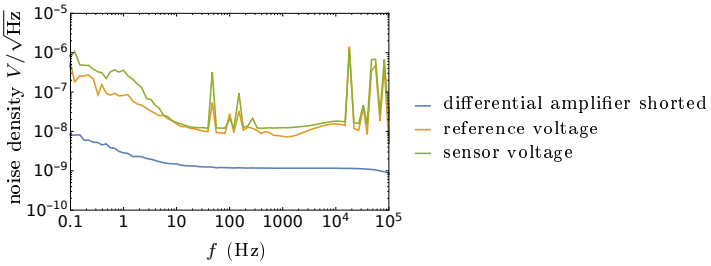

Figure 4.5: DC stabilization electronics noise analysis. Using a low noise differential amplifier the fluctuations of two magnetic field stabilization systems are subtracted. The blue line shows the noise characteristic of the differential amplifier itself, which confirms a low back ground noise due to the measurement. Yellow shows fluctuations in the two reference voltages V_{ref} before they are compared by op3 (see figure 4.3), green: fluctuations in the V_{sense} readouts of the 116 A current. Spikes at 50 Hz and multiples are due to the electronics in the vicinity of the test setup and do not reflect the situation in the experimental system. Spikes around $10^4 - 10^5$ Hz are due to the switching of the fluxgate sensor. These peaks should be filtered away by the integrating element of the feedback loop.

	$0.1 - 1$ Hz	$1 - 10$ Hz	$1 - 100$ Hz	$1 - 1000$ Hz
V_{ref} noise	3.2 μG_{rms}	2.2 μG_{rms}	3.9 μG_{rms}	7.3 μG_{rms}
V_{sense} noise	8.1 μG_{rms}	6.2 μG_{rms}	20.2 μG_{rms}	13.4 μG_{rms}

Table 4.1: Measured fluctuations of reference voltage as well as current sensing of 116 A using the fluxgate sensor. The sense V_{sense} and V_{ref} fluctuate on similar size scale with the references slightly better. Relevant are the first two (three) columns since the feedback loops bandwidth is ≈ 20 Hz, readout and current sensing limits the relative stability to $O(10^{-7})$.

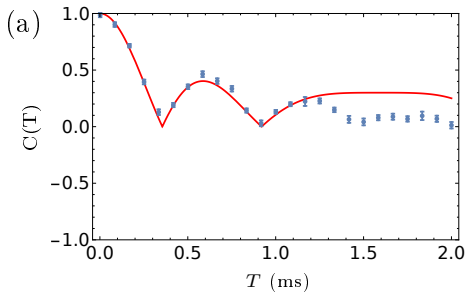

Figure 4.6: Ramsey contrast measurements. Decay and revival of Ramsey contrast after replacement of the fan as well as slow stabilization of the Helmholtz current. Blue points show the contrast extracted from the fits to the measured sinusoids where error-bars show errors of the fit. The red line shows the theoretical expectation for a single 50 Hz noise component with an amplitude of 1 mG according to equation 4.2. The curve agrees well for the shorter wait time, which indicates a dominant 50 Hz noise component. The discrepancy at longer times is explained due to additional decoherence mechanisms becoming more relevant.

Ion coherence time measurements

In order to assess how well the feedback loop operates we perform Ramsey coherence measurements at the ion. For each wait time T the second Ramsey pulse phase is swept between 0 and 2π. A fit to the resulting sinusoidal measurements trace extracts the Ramsey contrast C, with the fit parameter error providing the error bar. Results of these measurements are shown in figure 4.6. The signal decays quickly but revivals are visible up to longer timescales. Such revivals in the Ramsey contrast are a clear indication of dominant single frequency noise components $N(t) = \prod_k N_k \cos(\omega_k t + \alpha_k)$. In this case the Ramsey contrast is expected to follow:

$$C(T) = \prod_k J_0[i\frac{|N_k|}{\omega_k}(e^{-i\omega_k T} - 1)] \tag{4.2}$$

where J_0 is the zero order Bessel function[7] [149]. The expectation for a single 50 Hz noise component with an amplitude of 1 mG is shown in figure 4.6 and predicts similar collapses and revivals as the experimental result. Such noise is expected because of line cycle noise due to electronics in close vicinity of the setup. We thus postpone the performance characterization of the slow stabilization and describe first how we compensate for the 50 Hz noise.

[7] Here the ensemble average was taken further assuming that the noise frequencies are not synchronized to the experiment i.e. α_k is uniformly distributed between $[0, 2\pi]$

4.2.3 "Lullaby" feedforward compensation of mains noise

The influence of the line noise can be removed by synchronizing the Ramsey measurement with the mains noise cycle (line triggering). An ion trap experiment typically runs on a timescale of 1 ms where cooling of the ions take up a large fraction of the time. Therefore using line triggering make experiments roughly by a factor of 20 slower. Furthermore in a line triggered experiment the qubit transition frequency varies over the course of the experiment. Both of these problems can be avoided by applying an additional magnetic field canceling the mains noise components. In my master's thesis I designed an active control loop using pick-up coils outside the vacuum chamber. The controller canceled the sensed signal but led to no improvement in terms of ion coherence time [147]. Further studies during my PhD showed that the line noise which the ion experiences shows no correlation with the line noise measured outside the vacuum chamber using the pick-up coils. Therefore measurements of the line noise directly at the ion are required for effective compensation.

Line noise measurements

Line triggering the Ramsey measurement and varying a delay between the trigger and the start of the Ramsey measurement allows to map the line noise cycle. Dependent on the position of the Ramsey experiment in the line cycle the qubit angular transition frequency is detuned by $N_0 = \delta$. This leads to a constant phase shift ϕ_0 in the measured Ramsey sinusoid as a function of second pulse phase. Thus in order to map the line cylce noise a two dimensional scan of line trigger delay versus second Ramsey pulse phase can be used. However, such a scan is rather slow to run. The mapping time for the line noise cycle can be improved using an optimized sequence for determining the constant phase shift ϕ_0, which we call optimal Ramsey in the following. A real-time Bayesian update scheme was implemented by Vlad Negnevistky and is described in more detail in his PhD thesis [127]. In this scheme each shot of Ramsey measurement is run with a fixed wait time and the second $\pi/2$-pulse phase as variable parameter and leads to a bright or dark detection result. The phase setting for each Ramsey phase is calculated based on all the previous run settings and results, trying to maximize the knowledge gain in the current experimental shot. The accuracy of the estimated phase shift in this scheme scales as $\sqrt{n}$ with the number of measurement shots and thus does not provide a Heisenberg scaling, however in practice it reduces the number of required shots roughly by a factor of 25 and thus improves considerably the calibration speed.

Measurements of the line noise using the optimal Ramsey measurement with a fixed wait time of $T = 100\,\mu$s are shown in figure 4.7 (a) and show a dominating 50 Hz component of ≈ 1 mG. Here the 50 Hz amplitude of the magnetic field noise $A_m \approx \phi_0/(2\pi T\tau)$ is roughly estimated from the measured

phase shift ϕ_0 in radians assuming a constant detuning during the wait time T and using the qubit sensitivity to magnetic fields τ.

"Lullaby" feedforward system

The discussions about the typical mains line noise problems in the laboratory environment motivated Peter Märki together with his brother to develop an adaptive "hum canceler" system. The core components of his system are a Raspberry Pi communicating with a Cirrus Logic Audio Card programmed using C code. A voltage with an error signal can be put into the audio card, which is then Fourier transformed in order to extract the relevant 50 Hz and higher harmonic amplitudes and phases. In addition the audio card reads in the mains noise cycle via a transformer plugged into a wall socket. The audio card provides then an output voltage containing the relevant line frequencies of variable amplitude and phases synchronized to this wall socket signal. The output voltage can then be used to generate a current in order to drive feedback coils. In a first step the transfer function of the control system is measured. In addition the latency in the digital parts is monitored using the second in and output channels of the audio card. Dependent on the measured values of noise together with the measured transfer function the output amplitude and phases of the 50 Hz and higher harmonic components are calculated. The parameters of the output are slowly adapted in order to compensate the mains noise in a stable manner. This adaptive controller has a very low bandwidth since the latency in the audio card Raspberry Pi system is very long. This is typically no problem since the mains noise amplitudes and phases vary only slowly over the course of a day. The adaptive controller operates in a regime were amplitudes and phases can be updated slower than the actual frequency components present in the control output.

Because the generation of the error signal from the ion is slow, we simplified the adaptive control code to only provide feedforward on the main noise components. To do so we can specify amplitude and phase values in our experimental control system, which are sent to the Raspberry Pi and change the output voltage and phases of the audio card. This voltage is then fed to a current buffer soldered and provided by Peter Märki. The current output drives a field through two additional Helmholtz coils located next to the primary coils.

In order to find the right "Lullaby"[8] feedforward values randomized phases and amplitudes are output. The resultant combined field of laboratory noise and feedforward field is measured using the optimized Ramsey method. The measurement results are fitted with sinusoids of the relevant frequencies from which the optimal output parameters can be estimated. Brennan de Neeve wrote a Python script, performing the calibration of the feedforward parameters fully independently within 20 min.

[8] Naming under the cuteness requirement by Vlad Negnevitsky

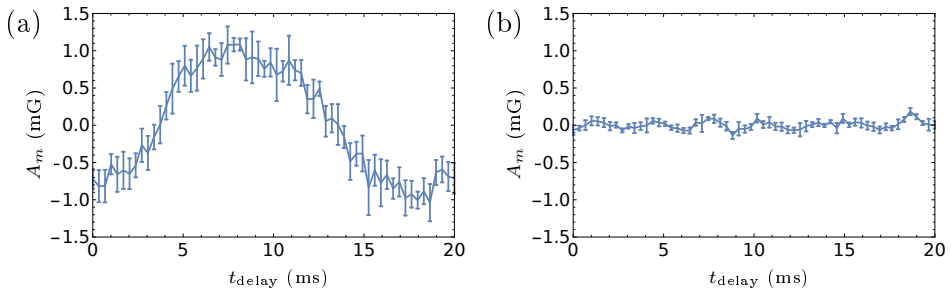

Figure 4.7: Line cycle noise measurement. Shown is magnetic noise as a function of delay time t_{delay} after the experimental line trigger. (a) Noise measured without FF compensation using a fixed wait time of 100 μs. The noise is dominated by a 50 Hz component of about ≈ 1 mG. (b) Noise measured with the calibrated FF compensation and using a wait time of 500 μs. Currently the system cancels multiples of 50 Hz up to frequencies of 250 Hz. The measurement shows residual 300 Hz fluctuations of about 25 μG.

Figure 4.7 (b) shows measurements of the line noise after the "Lullaby" system was calibrated. The measurements indicate a remaining 300 Hz component oscillating with an amplitude of about 25 μG. This is not surprising since the "Lullaby" compensates currently only frequencies up to 250 Hz. Extension of the system in order to include 300 Hz is straight forward and can be done in the future. At the time of implementing the "Lullaby" system the mains noise dependence on laboratory electronics was analyzed and very little dependence was found. Further the noise stayed constant on the timescales of weeks. More recently the influence of laboratory electronics[9] on the mains noise can be observed and the signal is less constant. In principle the system can be upgraded to run as a very slow adaptive controller. A calibration script could run an optimal Ramsey experiment every hour dependent on which the controller output could be updated. The dependence of the mains noise on specific laboratory electronics could also be used as a starting point in order to better understand the large mains noise the ion experiences.

4.2.4 Ion results

The qubit decoherence and the performance of the magnetic field FF compensation and DC stabilization are characterized using Ramsey and spin echo measurements. In addition, the effect of magnetic noise is discriminated from laser contributions using additional Ramsey measurements on all three transitions, see section 4.1. As a heuristic model, we take both the laser

[9] to be specific the Acopian power supply

angular frequency and the detuning due to magnetic noise to fluctuate on slow timescales with values sampled from two normally distributed probability densities $P_l(\delta)$, $P_m(\delta)$ of standard deviations σ_l and σ_m. The combined effect of these two uncorrelated sources is also normally distributed $P(\delta)$ with a standard deviation $\sigma = (\sigma_l^2+\sigma_m^2)^{1/2}$. Therefore we expect the Ramsey contrast to follow a Gaussian decay $C(T) = e^{-\frac{1}{2}(\sigma T)^2}$. A Gaussian fit to decay of a Ramsey measurement of T1 thus gives $\sigma_{T1} = (\sigma_l^2 + \sigma_m^2)^{1/2}$. The Ramsey measurement of T2 shows double the sensitivity on magnetic noise therefore $\sigma_{T2} = (\sigma_l^2 + 4\sigma_m^2)^{1/2}$ while the measurement on T3 is independent of the laser noise but three times as sensitive on the magnetic noise $\sigma_{T3} = 3\sigma_m$. Using a least square fit to these three equations provides an estimate of laser and magnetic noise. Table 4.2 provides measurement results alongside the estimation of laser and magnetic noise. Using FF and DC control, leads to a Ramsey (Spin echo) coherence time of around 1.71 ms (2.78 ms) respectively. The corresponding measurements are shown in figure 4.8 as blue points and can be compared to the same measurements when both compensation systems are off (red points). The latter shows coherence of about 0.248 ms (1.8 ms). The cooling fan is permanently removed and therefore comparison to the initial situation is no longer possible ($T_1 \approx 150\,\mu$s).

The laser is estimated to have a spectrum of $\sigma_l \approx 2\pi \times 99$ Hz while the magnetic field fluctuates with standard deviation $\sigma_m \approx 81\,\mu$G. The magnetic field fluctuations can be compared to the value with the DC control off: 452 μG. The noise measurements of the DC control electronic suggest that levels of at least half the amount of measured final fluctuations should be possible. The value of $\sigma_m \approx 81\,\mu$G relates to a relative field stability of $O(10^{-6})$ which is an upper bound on the current supply stability in the relevant frequency range. The latter is the case since there might be contributions due to other magnetic noise sources like the 300 Hz line noise. In addition, the performance of the FF control is compared to the line triggered experiment (given in purple in figure 4.8). The line triggered experiment required longer measurement times and might thus be affected from drifts on the longer timescales. The line triggered experiments show very similar coherence times, with only the spin echo experiment showing a slightly better result.

To summarize, the qubit coherence time was extended to a daily performance value of 1.71 ms, which is still low compared to other ion experiments with $^{40}Ca^{+}$ operated at low field, nevertheless an order of magnitude higher than previously in our system.

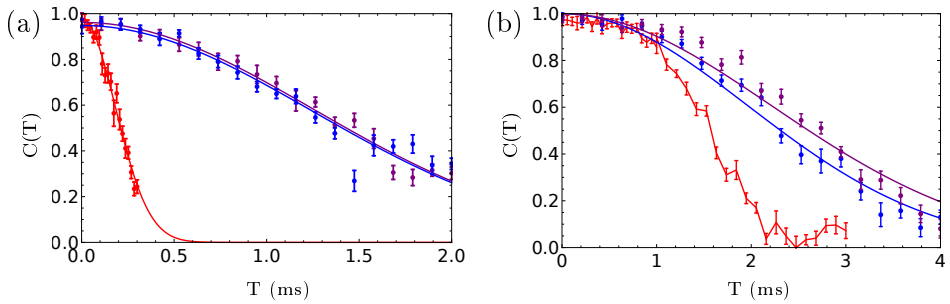

Figure 4.8: Decay of (a) Ramsey (b) spin echo contrast as a function of wait time T. Red points: all compensation systems off. Blue: "Lullaby" feedforward compensation and slow stabilization on, Purple: line triggered experiment and slow stabilization on. In the purple spin echo experiment, the calibrated feedforward was running additionally but this should not affect the results. Alongside the data fits to the Gaussian decays are shown leading to the coherence times given in table 4.2. In case of the spin echo experiments, the Gaussian fits match less well the data. Especially in the case of no compensation (red) where thus no fit is shown and coherence is extracted as the $1/e$ time of the data points.

	T_1 (ms)	T_{SE} (ms)	T_2 (ms)	T_3 (ms)	σ_l (Hz)	σ_m (μG)
DC+FF	1.71	2.78	1.06	0.83	$2\pi\times$ 99	81
DC+LT	1.73	3.13 (+FF)	-	-	-	-
FF	0.45	2.40	0.240	0.146	-	452
	0.248	1.8	-	-	-	-

Table 4.2: Summary of coherence measurements. DC: Slow DC stabilization, FF: Lullaby feedforward system, LT: Line trigger. T_1, T_2, T_3 coherence times of Ramsey measurements on transitions 1, 2, 3 fitted to Gaussian e^{-T/T_x}. T_{SE} spin echo 1/e time measured on transitions 1. In this case data shows discrepancies to the Gaussian model and thus T_{SE} was extracted as the 1/e time from the data. σ_l, σ_m are estimates of standard deviations of normally distributed noise of laser and magnetic field.

4.3 Quadrupole laser system

After decreasing the magnetic field noise the coherence time is now limited by magnetic field and laser to similar levels. Furthermore, the coherent qubit control described in the previous chapter 3 is based on the 729 nm laser. Thus I will summarize the laser stabilization system in order to understand the limitation in coherence due to the laser as well as the limits of the laser control. The current 729 nm laser system has been developed and changed by the TIQI group over the past few years.

The overall laser system currently used in the experiment is summarized in the schematics of figure 4.9. An extended cavity diode laser[10] is referenced to a spherical high finesse cavity[11] [150] made out of ultra low expansion (ULE) glass. The laser is locked to the cavity using the Pound-Drever-Hall (PDH) technique [151]. The lock references the laser diode output to the cavity and additionally narrows the laser spectrum. Due to the limited bandwidth of the lock electronics the noise background in the laser diode is amplified around ± 2 MHz detuned from the narrow central peaks. The locked laser diode is then used to seed a tapered amplifier (TA) providing the main laser output of 0.5 W. The spectrum of this output can be compared to the laser spectrum found in the 20 μW of light transmitted through the ULE cavity. In the latter case the narrow resonance of the cavity acts as an additional filter for the amplified background noise. At the beginning of my PhD work the setup was changed from using the main laser TA output to operate based on the transmitted light of the ULE cavity. To do so, the cavity transmission is used to inject a Fabry-Pérot (FP) diode[12] [152], which increases the laser power while preserving its spectral properties. The amplified light is guided to the experimental table using fiber noise canceled (FNC) optical fibers [153]. On the experimental table a second FP diode is injected and subsequently a TA[13] is seeded. The TA output is coupled through a short (≈ 1 m) uncompensated high power fiber from where it is guided through an AOM setup used for switching of the experimental beams as well as implementing multi-frequency control. From the AOM setup the light is delivered to the experiment via another ≈ 1 m uncompensated fiber.

Earlier experiments presented in this thesis were run using only the first diode injection stage and directly seeding the TA, while later the second injection was introduced. The additional fibers running via the neighboring laboratory B25 were installed very recently in order to allow the experimental systems in B25 also to benefit from the filtered laser light. These fibers were not present during the measurements presented in this thesis. The following sections motivate and summarize the key components of this chained laser system and point out relevant experimental parameters, references and concerns.

[10] Toptica, DL pro
[11] purchased from Advanced Thin Films
[12] Thorlabs, HL7302MG
[13] Toptica, BoostTApro

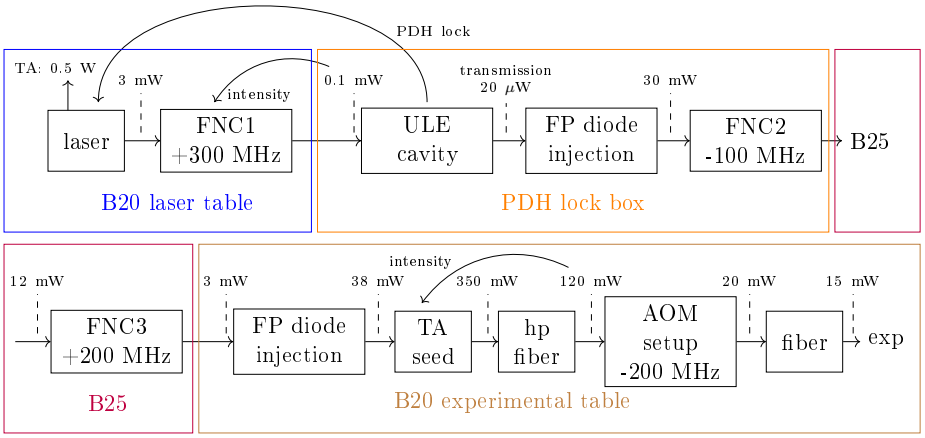

Figure 4.9: Chained 729 nm laser system. The diode laser is locked to the ULE high finesse cavity using the Pound-Drever-Hall (PDH) technique. To do so the laser light is guided via a fiber noise cancellation (FNC) fiber to the cavity. To improve stability, the cavity is hosted in an acoustic enclosure and the optical power onto the cavity is stabilized. In a next step the small cavity transmission is amplified injecting a Fabry-Pérot (FP) diode. Using two FNC compensated fibers the light is first guided to the laboratory B25 from where it returns to laboratory B20. A second FP diode is injected and a tapered amplifier (TA) is seeded. The TA output is coupled to a short uncompensated high power (hp) fiber after which the intensity is stabilized by controlling the TA current. After passing several AOMs (see figure 4.17) the light is coupled to a short uncompensated fiber which guides the light to the experiment.

4.3.1 Pound-Drever-Hall locking

A standard method of realizing a narrow "clock" laser is referencing the laser to the resonance of an optical cavity. Such optical cavities can exhibit very narrow (few kHz) and stable linewidths [154, 155]. To do so the PDH locking scheme [156] has several advantages. A PDH lock was initially designed and setup by Martin Sepiol and is described in detail in his master's thesis [151]. Since his implementation we have improved the stability of the lock and exchanged a fiber EOM with a free space model[14] and additionally stabilized the power going to the ULE cavity.

In the PDH scheme, see figure 4.10, the lock error signal is produced by modulating sidebands at a frequency of $\Omega \approx 30\,\mathrm{MHz}$ onto the laser. The sidebands and the main frequency component are coupled to the cavity and

[14] Qubig: EO-T38M3

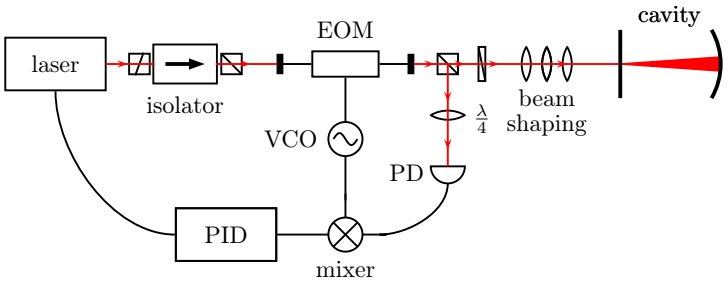

Figure 4.10: Pound-Drever-Hall locking scheme. An electro optic modulator (EOM) is driven by a voltage-controlled-oscillator (VCO) and modulates sidebands onto the laser. The light is coupled to a cavity from where the reflection is measured using a photodiode (PD). The PD signal is demodulated with the mixer and the resultant signal is input to a PID controller, which feeds back onto the laser current and piezo.

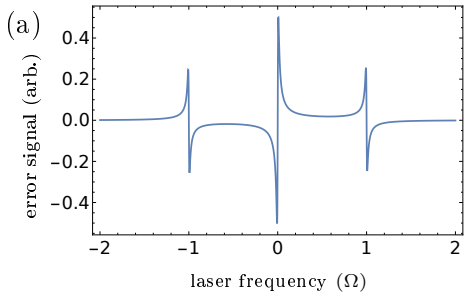

Figure 4.11: Typical PDH lock error signal. The laser frequency is given in units of the sideband frequency Ω. The signal is calculated using values reflecting the experimental system.

the cavity reflection is detected using a photodiode (PD). The PD detects the interference of the sidebands with the carrier component. The PD signal is then mixed with the same signal used to generate the sidebands. After this demodulation a suitable error signal is produced, which is shown in figure 4.11.

In particular the signal has odd symmetry across the cavity resonance, which allows to determine the sign of a laser frequency correction. The lock point of the error signal is at zero, independent of the laser intensity, which provides first order independence to laser power fluctuations. The detection of a signal oscillating at Ω further circumvents the larger noise present when detecting a constant signal. The signal has very high gain close to the resonance, while exhibiting a large lock range on the order of Ω. This error

signal is fed to a fast controller[15] which corrects the laser frequency by feedback onto the laser current and an additional slow feedback onto the laser piezo. The PDH lock shows bandwidths of around $1.5 - 2$ MHz below which the lock successfully suppresses noise. Above the bandwidth of the feedback noise in the laser diode becomes amplified. These unwanted frequency components are about 23 dB lower than the main laser peak and we refer to them typically as "servo bumps". They are roughly located at the $^{40}Ca^{+}$ motional frequencies, which limits achievable gate fidelities, due to off resonant carrier driving during SDF based gates. The servo bumps are suppressed in the transmission of the ULE cavity, since the narrow cavity resonance acts as a filter. A limit to the achievable PDH stability is given by thermal fluctuations in the cavity mirror substrates. To keep this at a low level only small amounts of power, in our case 0.1 mW are coupled to the cavity. Typical coupling efficiencies in our system are around 20 % leading to a transmission of only about 20 μw.

Ion getter pump monitor

The ULE cavity is mounted inside a small vacuum chamber, which was initially pumped to low pressures using a turbo pump. At low pressures the small ion getter pump[16] hosted in the vacuum system was turned on. The turbo pump was then disconnected using a pinch-off tube, which closes the vacuum system permanently [151]. In principle the ion getter pump has now operated longer than its specified lifetime[17]. The pump controller further showed unreliable behavior after power cuts, which switched off the pumping of the ion getter pump and caused the automatic restart feature of the pump controller to fail. If the pumping is off for too long then the pressure of the chamber raises above the required minimal pressure for the ion getter pump to operate. The chamber first needs to be turbo pumped in order to switch on the ion getter again. The latter is not straight forward due to the pinch-off tube. In order to avoid and flag problems with the ion getter pump an additional surveillance system was installed. The pump controller pressure is read out via serial communication from a Python script running on a Raspberry Pi. The readout values are sent to a data server and can be remotely accessed[18]. In case of a fault the script sends warnings via e-mail and tries to automatically restart the controller.

Second laser system in laboratory B18

Having a second narrow laser available allows for comparison of the two laser spectra using optical beat notes. This allows to find an upper-bound on the spectral properties of the laser system. A second PDH lock system was setup using a notched cavity[19] and using a commercial acoustic enclosure with

[15] Toptica, FALC-110
[16] 203S TiTanTM Ion Getter Pump, VACOM
[17] 50000 h $\approx$ 5.7 years at 10^{-6} mbar while we operate at about $6 \cdot 10^{-6}$ mbar
[18] http://hydrogen.ethz.ch:3000
[19] bought from stable laser systems

an active vibration stabilization table. This system uses a bigger ion getter pump and additionally the pinch-off tube is replaced with an all-metal valve. Nevertheless, the system uses the same pump controller and is thus monitored using the same Python script.

The beat note between the two laser systems can further be used to experimentally measure the zero crossing temperatures of the two cavities as described in [152]. The temperature dependence of the cavity resonances is designed to follow a parabolic shape. Operation at the vertex/zero crossing temperature provides first order insensitivity to thermal drifts. For completeness measurements for both cavities are shown in figure 4.12 and the two cavity key parameters are summarized in table 4.3. Currently this second laser system is being upgraded for amplification of cavity transmission light in order to supply the new setups built in the TIQI group.

	notched cavity B18	spherical cavity B20
length d:	100.045 mm	47.635 mm
free spectral range c/2d:	1.5 GHz	3.15 GHz
finesse $\mathcal{F}$:	300 000	270 000 (meas.)
linewidth $c\mathcal{F}/2d$:	5 kHz	11.5 kHz
coupling efficiency:	16 %	20-30 %
zero crossing temp (meas.):	29.29 °C	-4.4 °C

Table 4.3: cavity parameters

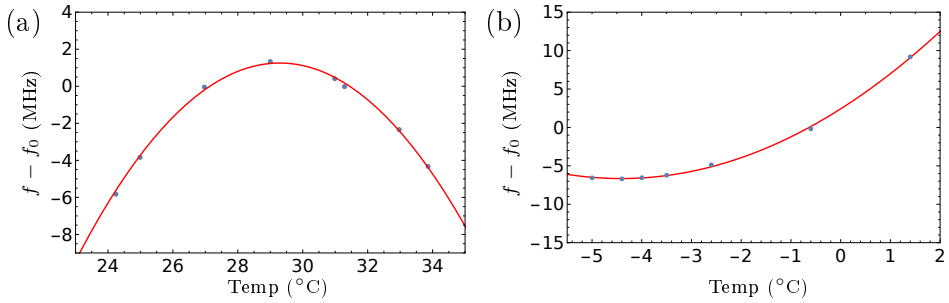

Figure 4.12: Measurements of "zero crossing" temperatures. Shown as blue points are measurements of the beat note frequency $f - f_0$ with error bars in both dimensions smaller than the dot size. Here f_0 denotes approximately the arbitrary difference in frequency of the two laser systems. The red line shows a fit to a parabola $(f - f_0)(T) = A(T - T_0)^2 + O$. T_0 defines the zero crossing temperature at which the dependence of cavity frequency is first order insensitive to temperature changes. (a) Notched cavity in B18. The fit gave $T_0 = 29.29 \pm 0.04\,°\mathrm{C}$. (b) The same measurement for the spherical B20 cavity where $T_0 = -4.4 \pm 0.1\,°\mathrm{C}$ is measured.

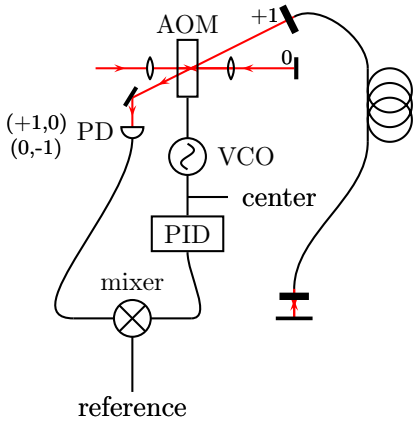

Figure 4.13: Principle of fiber noise compensation. A beat note is set up between a laser traveling twice through the fiber and a reference not traveling through the fiber. An AOM serves as a feedback element where the laser traveling through the fiber is first diffracted in to the +1st order and on its return path its non diffracted component is measured by the PD. The reference beam, is not diffracted in its first pass of the AOM and in its second pass it is diffracted into the −1st order. Mixing this beat note to DC and using it to feed back on to the AOM frequency allows for the compensation of slow fiber noise.

4.3.2 Fiber noise cancellation

Light delivery using optical fibers is very convenient, but typically the spectrum of a narrow laser broadens due to mechanical stress and temperature fluctuations. To avoid broadening of the spectrum FNC techniques can be used. The typical setup used in the TIQI group is shown in figure 4.13. For compensation of phase noise we install an AOM in front of the optical fiber. The AOM center frequency can be chosen freely in order to shift the laser frequency as required in the experiment. Further the RF power driving the AOM can be used to feedback onto the laser intensity. The diffracted order of the AOM is coupled to the optical fiber, shown in the figure is the +1st order. The light travels through the optical fiber, which induces phase fluctuations onto the beam. A small proportion of the light is reflected back through the fiber and experiences the fluctuations a second time. The back reflection is either realized using a window or a fiber with a flat polished end. Using the flat ended fiber has the advantage of not requiring to recouple the light into the fiber using the window. On the return path the non-diffracted zero order component of this beam is aligned to impinge onto a photo-diode. This light is overlapped with the part of the laser light initially not diffracted and directly

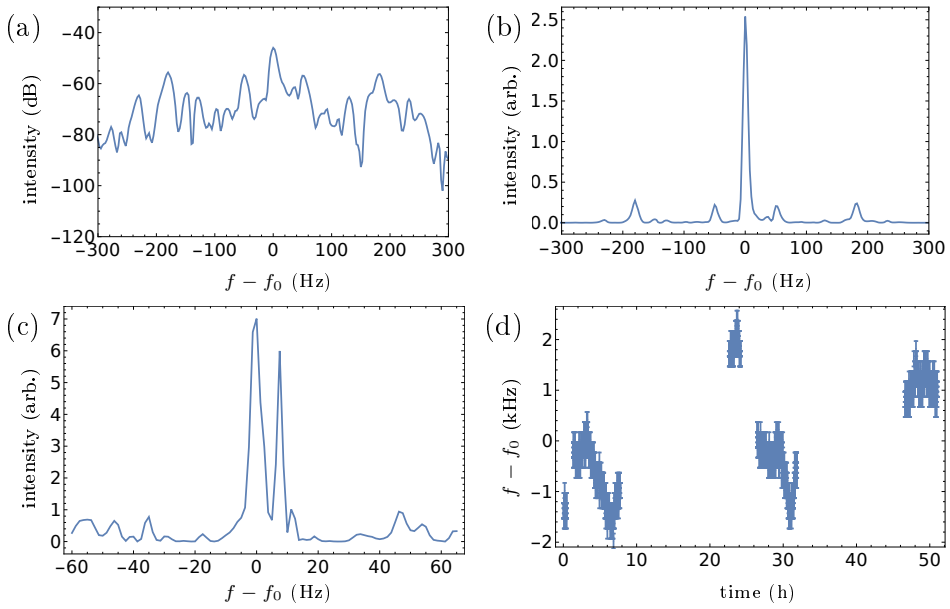

Figure 4.14: Beat note measurements between two narrow laser systems connected via phase noise compensated fibers. (a) The optical beat note measured with a sweep time of 480 ms and with a resolution bandwidth of 10 Hz shown in logarithmic scale. The spectrum shows a narrow center peak surrounded by additional noise peaks. (b) The same measurement plotted in linear scale. The width of the center peak is 10 Hz and therefore limited by the spectrum analyzer resolution. (c) Beat note measurement using a different spectrum analyzer model with a resolution bandwidth of 3 Hz, sweep time in this case was 780 ms. (d) Drift of beat note frequency over the course of 50 hours. Slopes are up to ≈ 0.4 Hz/s.

back reflected through the AOM without traveling through the fiber. A part of this beam is on its return path diffracted into -1st order, which naturally is aligned to the (+1st, 0th) beam which has traveled through the fiber. Here and in the following the notation $(+1, 0)$ is used to denote the diffraction orders of a beam passing through an AOM in double pass configuration. The photo diode measures an optical beat note at twice the AOM frequency, which is then demodulated to DC using a stable reference. This signal is input to a controller, which feeds back onto the voltage-controlled-oscillator controlling the AOM frequency.

Nelson Oppong has designed a suitable PCB for the necessary electronics, where he additionally included a voltage controlled attenuator in order to stabilize laser intensity [153]. This attenuator is used in order to stabilize the power onto the PDH lock cavity.

Only after such fiber noise compensation systems were installed was it possible to measure narrow beat notes between the two PDH locked laser systems located in different rooms. Measurements of these are given in figure 4.14 and show narrow central features of around 10 Hz. These are surrounded by further noise peaks within the next few 100 Hz. Measurements of the laser spectrum depend on the considered timescale. The beat note seems to be extremely narrow on short timescales (≤ 100 ms) but with the absolute frequency jittering around when longer times are considered. In part (c) of figure 4.14 the beat note seems to jitter on the timescale of one spectrum analyzer scan (780 ms). Fluctuations of the beat note frequency over several hours are shown in part (d) of figure 4.14 [152]. In this case fluctuations on the order of few kHz are measured, despite both cavities operating at their respective zero crossing temperatures. The measurement is still too short in order to extract a drift of the cavity frequencies over several months [157, 158]. Fluctuations of the beat frequency are either caused by the PDH lock system itself or by the FNC stabilization.

The beat notes confirm noise suppression by the fiber noise cancellation system. In addition they also show clear room for future improvements, which would include analyzing the noise bumps close to the central peak and determining the sources of jitter and slow fluctuations of the laser frequency. Furthermore in order to include imprecisions due to the injection setups and the uncompensated short fibers, the beat note could be set up between the PDH locked laser in B18 with the laser after the experimental chamber.

4.3.3 Diode injection

Under specific conditions a diode can be forced to lase with a spectrum of a reference beam which is coupled into its resonator. This is referred to as diode injection. To do so the injection beam, often of much less power than the typical diode output, is overlapped with the natural mode of the diode. Typically the diode is protected from back reflected light using an optical isolator. The isolator consist out of a Faraday rotor together with two polarizing beam splitter (PBS). The injection beam can be overlapped with the natural modes of the diode by entering the PBS of the isolator from its side port, see schematic in figure 4.15 for more details. At the right conditions of beam alignment, diode current, temperature and injection power all natural modes of the diode are suppressed and the diode starts to laser with the same frequency and spectrum as the injection beam.

Two types of red diodes were considered in the TIQI group. These are Fabry-Pérot (FP)[20] and anti-reflection (AR) coated diodes [21]. The AR diode showed less efficiency, thus the cavity transmission was not sufficient in order to inject an AR diode successfully [147]. Therefore the more efficient FP diode was

[20] Thorlabs, HL7302MG
[21] Toptica, LD-0730-0040-AR-2

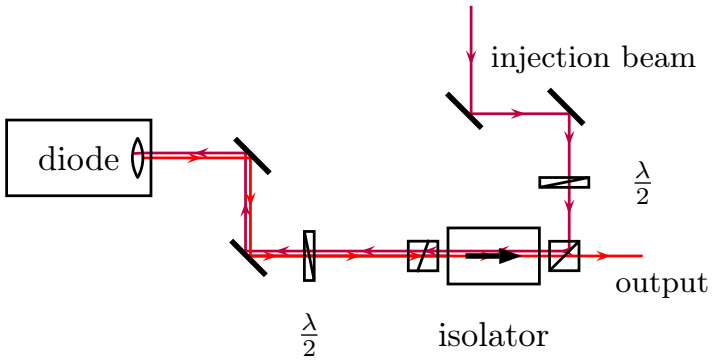

Figure 4.15: Injection setup principle. The diode is forced to lase at the frequency and spectrum of the injection beam. To do so the injection beam is overlapped with the natural mode of the diode entering the diode optical isolator from the side port [152].

installed and characterized in the setup (described in Lukas Gersters master's thesis [152]). This setup provided about 15 mW of power in order to directly seed the tapered amplifier on the experimental table. Figure 4.16 shows the ion internal state transition probabilities as a function of frequency either using amplified cavity transmission (b) or using the old spectrum provided by the PDH locked main laser TA output (a) [152]. Despite driving for long times with the laser the servo bumps were no longer visible in the new laser system.

While 15 mW just suffices to seed the TA, more power would be favorable. Therefore later a second FP diode injection system was installed on the experimental table. The second injection only requires few mW of injection power and thus the excess laser power can be further distributed to a second laboratory. The environment on the experimental table shows less stability compared to the PDH enclosed box but also more injection power is available, which partially mitigates this effect. The AR diode is less efficient but might offer better stability. A comparison of AR and FP diode at higher injection powers was performed in the semester project Sebastian Saner [159], which convinced the experiments in B25 to use AR diodes whenever more injection power is available. Currently the second injection needs to be realigned on timescales of few weeks, while the first injection shows much longer stability. This is assumed to be due to the less stable environment on the experimental table. In addition, typically every morning the second injection needs to be checked to operated at an optimal point of temperature, current and injection power. To improve the latter, a future setup could either actively stabilize the injection power or use an AR diode for higher tolerances of drifts.

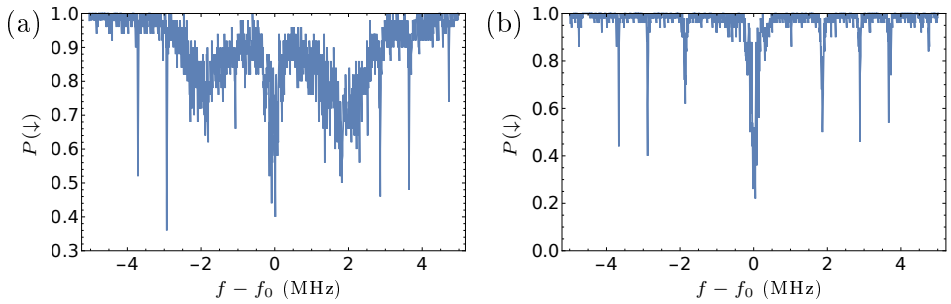

Figure 4.16: $^{40}Ca^{+}$ transition probabilities measured with (a) the unfiltered laser system (b) using the amplified ULE cavity transmission. The wide regions due to the servo bumps in the spectrum are removed.

4.3.4 Isolation

Optical isolation using Faraday rotors is a critical part in the overall laser system shown in figure 4.9. For diode injection the optical isolator is used in an unusual way where we are interested to couple a beam through the side port of the isolator. Dependent on the orientation of the polarizing beam splitters of the isolator, a part of the diode output light can exit through this side port. In fact misalignment of the PBS and therefore a larger diode component exiting through the side port can be used to overlap the injection beam over a longer distance with the laser natural mode and is thus a useful trick for initial alignment of diode injection. However, such a component is highly undesirable in operation of the laser system. In case of the first injection stage this component will directly couple back to the the ULE cavity, which makes the PDH lock less stable. In case of the second injection the side port beam will couple back through the fiber and contribute to the FNC3 beat note. Therefore the PBS are aligned in order to minimize the diode component through the side port and in case of the first low power injection an additional isolator is placed before the ULE cavity.

In typical applications the isolator is aligned for best extinction of back reflections into the diode. Now instead we are interested to suppress the diode output exiting the side port. The optimal alignment in the two cases are similar but not exactly the same. Therefore in both injection setups the first isolator is aligned to best suppress the diode output in the side port and an additional isolator is placed in the diode output before further components. This is particularly important before the TA seed since the TA always shows a small proportion of light exiting its back port. In other cases this isolator might not be strictly required.

4.3.5 729 AOM setup

The final AOM setup in order to switch on and off the laser beams as well as address the ion with the correct frequencies is shown in figure 4.17. Using this setup transition T1: $|\downarrow\rangle \leftrightarrow |\uparrow\rangle$ as well as T2: $|\downarrow\rangle \leftrightarrow |a\rangle$ can be addressed. To address the main qubit transition T1 the first double pass "master" AOM is driven with a frequency of around 200 MHz, while the second AOM "transition" is simply turned off. The laser beam is just reflected back through this AOM without being diffracted. After diffracting at the last single pass AOM the light is coupled to the fiber going to the experiment. The "master" AOM is used to pulse on and off the beam while additionally it enables a wider scanning range of the laser frequency. The single pass AOM can be driven with multiple frequency components, which is required in order to realize SDF forces and sideband pulses in transformed bases. For the coupling of all frequency components to the fiber and improved beam stability lenses are used to image the center of the AOM onto the fiber tip. Constant driving of the single pass AOM with a fixed frequency decreases power cycling issues.

In order to address transition T2 the "transition" AOM is switched on and used in double pass configuration in order to realize the approx. -400 MHz shift in frequency. The lens between the AOM and the back reflection mirror ensures that the $(0,0)$ beam is overlapped with the $(-1,-1)$ beam through the AOM. In the former case were T1 is addressed and the "transition" AOM is off, the beam only follows the $(0,0)$ path. Coupling of both beams is thus required in order to be able to switch between addressing T1 and T2. The frequency of the master AOM is changed to 190 MHz when driving transition T2 in order to move the $(0,0)$ beam off resonant with the first transition.

4.3.6 Laser stability measurements on the ion

The laser frequency is typically calibrated applying a long pulse (1.5 ms) with a low Rabi frequency ($\Omega \approx 630\,\mathrm{s}^{-1}$)[22] to the calcium ion, while sweeping the laser frequency across the carrier transition. For comparison, typical Rabi frequencies used to run 729 nm pulses are $\Omega \approx 0.5 \cdot 10^3\,\mathrm{s}^{-1}$ while the available laser power would in principle allow for more than double these values. The low Rabi frequency leads to a small Stark shift and thus provides roughly a measurement of the bare carrier transition frequency. Furthermore the low power leads to little power broadening of the calibration feature. The latter can be calculated using equation 3.10 and is expected to follow:

$$P(\downarrow) = 1 - \frac{\Omega_{n,n}^2}{\Omega_\delta^2}\sin^2(\Omega_\delta t) \text{ with } \Omega_\delta = (\delta^2 + 4\Omega_{n+s,n}^2)^{1/2}/2 \qquad (4.3)$$

[22] we use the unit s^{-1} for the angular Rabi frequency

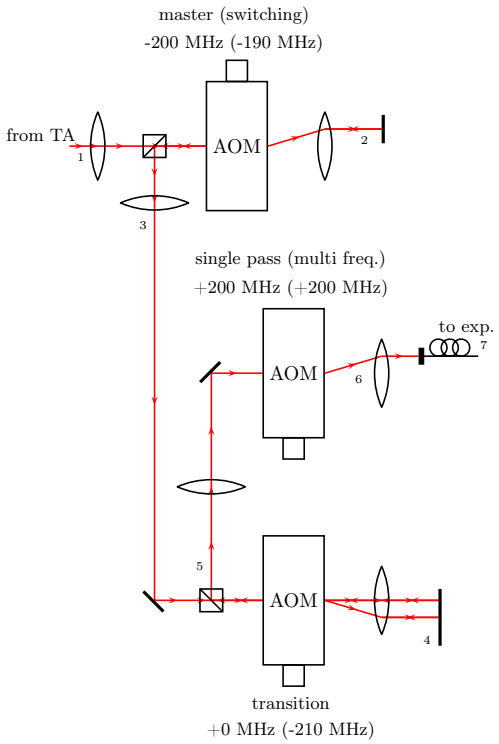

Figure 4.17: AOM setup used to drive transitions T1: $|\downarrow\rangle \leftrightarrow |\uparrow\rangle$ as well as T2: $|\downarrow\rangle \leftrightarrow |a\rangle$. The AOM frequency without brackets are used in order to drive the T1, while the values in the bracket are used for T2. The "transition" AOM is aligned in such a way that both the (0,0) order beam as well as the (-1, -1) order beam are coupled to the final fiber.

Figure 4.18 (a) shows this carrier frequency calibration. Blue points show the measurements, while the blue line provides the expectation according to equation 4.3. The dip of this feature is extracted in practice using a fit to a Lorentzian line shape. The corresponding fit is shown as red line in the figure. The width of the calibration feature is still larger than the expected shot-to-shot laser fluctuations estimated from the Ramsey coherence measurements $\sigma_l \approx 2\pi \times 99\,\mathrm{Hz}$.

Frequent recalibrations of this type show how the relative frequency of laser and transition drift. Measurements over a time span of 10 h are given in figure 4.18 (b). The observed fluctuations are on the same order of magnitude as expected from the beat notes between the two PDH locked lasers (see figure 4.14). Additional measurements indicated that the switch on characteristic of the slow magnetic field stabilization can also induce shifts

on the same order of magnitude. Furthermore non ideal injections can lead to shifts in the calibrated frequency.

The carrier π-time is calibrated using $\Omega \approx 0.5\,\mathrm{s}^{-1}$ and the calibrated bare carrier frequency as described above[23]. The pulse time is swept around five times the searched π-time value. Using multiple flops provides a narrower calibration feature. Figure 4.18 (c) shows results of repeated π-time measurements. The changes of the calibrated times T_π are given over the course of few hours. Shown is $\Delta\pi - \mathrm{time} = (T_\pi - \langle T_\pi \rangle)/\langle T_\pi \rangle$ in percent, here $\langle T_\pi \rangle$ denotes the mean over all calibrated values. The π-time fluctuates on the 1 % level. Therefore ≈ 2 % of laser power fluctuations are required to fully account for the measured fluctuations[24].

For many experiments not only the absolute laser power stability is important but also the relative stability of multiple frequency components, generated in the last single pass AOM. Drifts in the final laser coupling not only cause overall power changes but further lead to drifts in the relative powers. Calibrations of carrier and sideband components used for the results in chapter 6, show similar levels of 1 % relative Rabi frequency stability between the two components over a day.

[23] Note that in this scheme the ion is driven detuned by the stark shift, which causes a negligible error.

[24] the Rabi frequency scales with the square-root of the laser power.

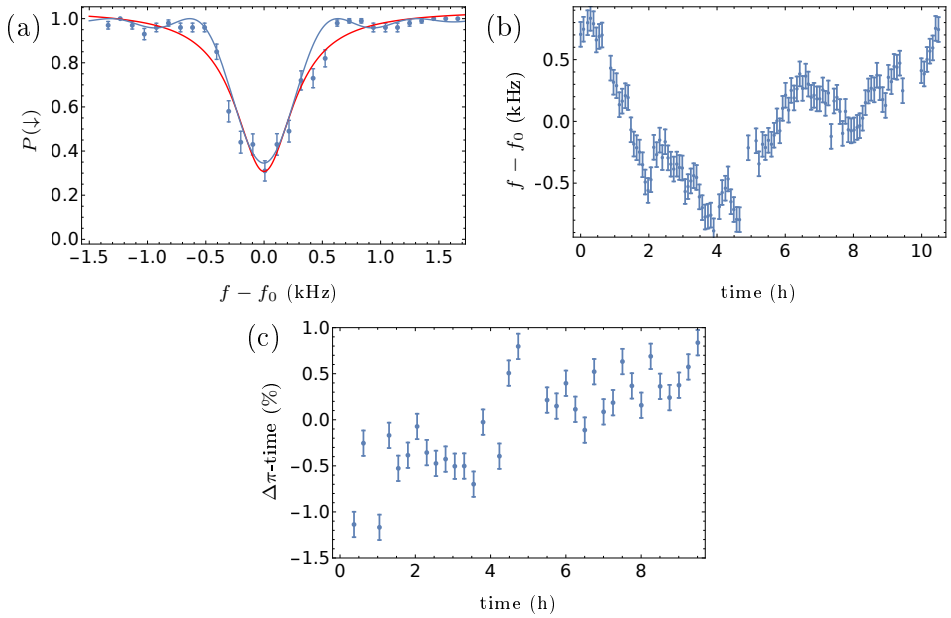

Figure 4.18: 729 nm laser calibrations and drifts. (a) Typical frequency calibration feature, when driving the calcium ion with a low Rabi frequency $\Omega \approx 630\,\mathrm{s}^{-1}$ and for a long time $t \approx 1.5\,\mathrm{ms}$ scanning the laser frequency. The blue line shows the expected signal using the above values. While in practice the dip is extract by fitting a Lorentzian to the measured signal, which is shown in red. Note that the laser linewidth $\sigma_l \approx 2\pi \times 99\,\mathrm{Hz}$ estimated from the coherence measurements is effectively smaller than the measured feature. (b) Repeated calibrations as described in (a) over the course of 10 h. In this figure error bars indicate the laser linewidth σ_l. Fluctuations are on a size scale as expected from the beat note measurements between the too PDH locked lasers. (c) π-time fluctuations on the order of $\pm 1\,\%$ over several hours.

Chapter 5

Oscillator calibration and characterization

The experiments presented in this thesis require a high level of stability of the trapped-ion oscillator. This chapter describes characterization of the coherence properties of the oscillator, as well as the calibration methods for control parameters. Together these determine the achievable experimental qualities and are thus important for understanding the limits of the experiments presented in the rest of the thesis.

5.1 Oscillator coherence and heating rate

The decoherence of the motional oscillations in our trapped-ion system is primarily thought to be due to noise in the trapping potentials. Such noise can fluctuate on various timescales, and to characterize the exact spectrum is a demanding experimental task [35, 160]. One type of fluctuation leads to heating of the ion's motion. This can differ dependent on the ion trap technology and even on the individual trap level. A clear understanding of the heating mechanisms is still investigated [160]. But low heating rates on the order of few quanta per second like in our setup are possible. Slow drifts in the trapping potentials can lead to additional dephasing of the motional oscillator. The scaling of heating and decoherence sources in case of larger motional states is still a topic of current studies [134, 161] and is vital for the results presented in this thesis.

5.1.1 Simulation of heating and dephasing

Dephasing and heating can be simulated using Lindblad master equations [115] to account for the coupling of the ion to the noisy environment of the trapping electrodes. Such a simulation captures the relevant physics as long as the Markov approximation is valid. In case of heating the resonant

frequency components of the fluctuations in the electrodes lead to addition and subtraction of quanta to the motion of the trapped ion. In this case the Markov approximation is well justified and we simulate heating using Lindblad operators $L_1 = \sqrt{\gamma(n_0+1)}\,\hat{a}$ and $L_2 = \sqrt{\gamma n_0}\,\hat{a}^\dagger$ where $n_0 = \frac{e^{-\hbar\omega T}}{1-e^{-\hbar\omega/k_B T}}$ with $T \approx 300\,\mathrm{K}$ the environment temperature and n_0 is the average number of quanta in the reservoir at the frequency of interest. The product $n_0\gamma$ determines the heating rate from the ground state [36], which can be assessed experimentally. Such heating rate measurements for the axial secular frequencies ω used in the following are describe in [123] and heating rates of $\approx 10\,\mathrm{quanta/s}$ were measured for the axial mode.

The addition and subtraction of quanta to the oscillator is not only expected to lead to heating of the ground state cooled ion but will also cause dephasing of motional superposition states. Additional sources of noise can cause dephasing. A phase reservoir, which only causes dephasing but no heating can be simulated using Lindblad operators $L = \sqrt{\Gamma}(\,\hat{a}\,\hat{a}^\dagger + \hat{a}^\dagger\,\hat{a})$ [36]. In this case the jump operators solely introduce frequency changes of the oscillator but do not introduce additional quanta.

Low frequency noise in the trapping potentials cause additional dephasing but in this case the noise starts to become correlated over the course of an experiment and the Markov approximation looses its validity. The timescale between subsequent experimental shots can be much longer than the duration of a single shot. Thus noise can be correlated or almost constant over the timescale of a single shot but uncorrelated between subsequent experimental realizations. In this case we can account for the noise by randomly sampling a different value of the relevant experimental parameter from a probability distribution. See for example the heuristic model we used to describe laser and magnetic noise in internal state Ramsey experiments in section 4.2.4.

Dephasing of motional superposition states can be measured extending the Ramsey coherence method [36], which is described in the next section. To simulate such experiments we first include dephasing due to the measured heating rate using the Lindblad master equation. Additionally we try to asses the size of less well understood additional dephasing sources using a simple phase reservoir in the Lindblad master equation.

5.1.2 Fock state superpositions

In order to measure the phase stability of a $(|0\rangle + |1\rangle)/\sqrt{2}$ Fock state superposition the ion is first ground state cooled. A modified Ramsey sequence is then used which includes two additional red sideband π-pulses before and after the Ramsey wait time in order to map the superposition from the internal states to the Fock states. The full motional Ramsey pulse sequence reads (right to left):

$$\hat{R}_c(\pi/2, \phi_l)\hat{R}_r(\pi, 0)\hat{U}_{\mathrm{free}}(T)\hat{R}_r(\pi, 0)\hat{R}_c(\pi/2, 0). \tag{5.1}$$

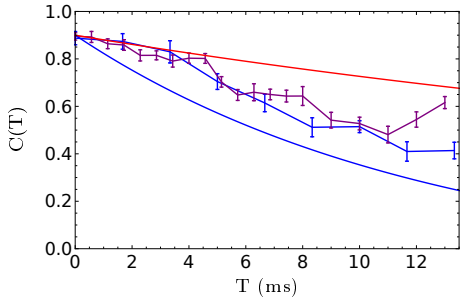

Figure 5.1: Motional coherence measurements. (a) Two sets of coherence measurements for a superposition of $|0\rangle, |1\rangle$ Fock states of the axial motional mode. Measurements were taken 06 October 2017 (blue) and 18 September 2018 (purple). For each data point ϕ_l was varied and the contrast was extracted from a fit to the resultant sinusoid. Error bars provide the parameter errors of the fit. The timescale for the loss of motional coherence is on the order of 10 ms. The newer data set indicates a revival in the contrast, which hints at to dominant frequency components in the noise spectrum. In addition the expected contrast decay due to the heating rate of 10 quanta/s is shown as the red line. A simulation of the decoherence during the wait time due to this heating rate together with a dephasing $\Gamma = 30s^{-1}$ is shown in blue.

Here the subscripts c and r relate to carrier and red sideband rotations respectively. First such measurements performed in our experiment are reported in [123], while figure 5.1 shows two more recent measurements for the axial motional mode. The recent experiments use only shorter wait times, which are roughly in agreement with the old measurement points at these timescales. Additionally the shorter times are now resolved with more detail, revealing decay of contrast at low wait times resembling Gaussian decay. The data shows that the relevant timescale is on the order of few 10 ms. Similar measurements were performed for EIT cooled radial modes, where the contrast decayed on timescales of about ≈ 1 ms.

The measured heating rate of 10 quanta/s is not enough to explain the decoherence of the Fock state superposition. The red line in figure 5.1 shows the expectation due to the heating rate. Identical curves were found from Lindblad master simulation as well as using the analytic formulas from [36]. The simulated curve is shifted down in order to match the imperfection at $T = 0$. The decoherence during the wait time was additionally simulated adding a dephasing term with $\Gamma = 30\,\mathrm{s}^{-1}$ to the heating. The obtained curve is shown in blue. The shape of the curve does not reproduce the functional form of the decay at shorter times but the slope of decay at longer timescales

appears similar. A quantitative comparison especially at shorter times would require the inclusion of imperfections in the pulse sequence and the initial ground state cooling. Nevertheless $\Gamma = 30\,\mathrm{s}^{-1}$ provides an upper bound on the additional dephasing experienced.

5.1.3 Separated wave packets

More relevant for this thesis is the coherence of superpositions of separated wave packets. Application of the SDF pulse to the oscillator $|\downarrow\rangle\,|\psi_0\rangle$ prepares:

$$|\psi\rangle \propto [|+\rangle\,\hat{\mathcal{D}}(\alpha/2) + |-\rangle\,\hat{\mathcal{D}}(-\alpha/2)]\,|\psi_0\rangle\,. \tag{5.2}$$

This is a joint superposition of the internal states $|+\rangle$, $|-\rangle$ with the initial oscillator state $|\psi_0\rangle$ displaced to two different phase space locations. During a free evolution time T decoherence effects in both systems will alter the state. For example the orientation $\arg(\alpha)$ of the coherent states in the rotating frame will fluctuate due to drifts in the motional frequency. A subsequent second SDF2 pulse of equal duration and strength but with opposite displacement direction probes the decoherence of the joint state. In the ideal case of no decoherence the internal states are expected to perfectly return to $|\downarrow\rangle$. Such experiments were explored by Hsiang-Yu Lo [37] using squeezed initial wave packets and setting the free evolution time to zero. The experiment were assumed to be limited by the poor qubit coherence time, which was around $150\,\mu\mathrm{s}$. Repeating these experiments after improving the qubit coherence showed only a marginal improvement, see App. D.1 for more details.

States solely in the oscillator degree of freedom can be prepared using readout of the qubit. These are given by:

$$|\psi\rangle \propto [\hat{\mathcal{D}}(\alpha/2) + \hat{\mathcal{D}}(-\alpha/2)]\,|\psi_0\rangle\,|\downarrow\rangle \tag{5.3}$$

Application of the second SDF2 pulse in this case also leads to a revival of the $P(\downarrow)$ population but of only half the size compared to the previous experiment. The details of this experiment will be discussed extensively in the following chapters. Decoherence of the state $|\psi\rangle$ is probed by letting it freely evolve for a duration T before the second SDF2 is applied. Figure 5.2 shows such coherence measurements for a superposition of squeezed states $|\psi_0\rangle = \hat{\mathcal{S}}(r)\,|0\rangle$ with $r \approx 0.984 \pm 0.03$ while the wave packets are separated along the squeezed axis by $\alpha \approx 4.3$. Figure 5.2 (a) shows the revival in $\langle\hat{Z}\rangle = 2P(\downarrow) - 1$ observed as a function of the second SDF2 duration. Part (b) shows the decay of the revival height as a function of wait time, alongside simulations of heating (red curve) and including additional dephasing (blue curve). The simulation curves were again shifted to match the imperfections at $T = 0$. In this case the heating together with the dephasing of $\Gamma = 30\,\mathrm{s}^{-1}$ (blue curve) accounts well for the observed decay. The relevant timescale for these larger superpositions compared to the Fock states is reduced to a few milliseconds. A more extensive

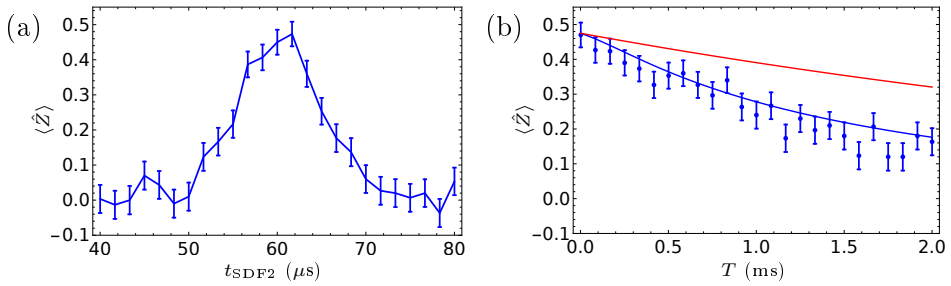

Figure 5.2: Coherence measurements for a superposition of displaced squeezed states $\propto [\hat{\mathcal{D}}(\alpha/2) + \hat{\mathcal{D}}(-\alpha/2)]\,|r\rangle$ with $r \approx 0.98$ and $\alpha \approx 4.3$. (a) Revival of qubit contrast $\langle \hat{Z} \rangle = 2P(\downarrow) - 1$ as a function of the second SDF time. (b) Decay of the revival for fixed $t_{\mathrm{SDF2}} = 60\,\mu$s as a function of a preceding free evolution time T. Displayed are the directly measured values and their standard error of the mean (s.e.m.). Alongside the data the Lindblad master equation simulation including heating of $n_0\gamma = 10\,\mathrm{s}^{-1}$ is shown as the red line. The simulation including additionally a dephasing term with $\Gamma = 30\,\mathrm{s}^{-1}$ is shown in blue.

experimental study of decoherence of squeezed superposition states is presented in App. D.2.

Imperfections in the experiments of this thesis are typically well-modeled using Lindblad equations whose heating and dephasing terms are of similar size to the ones observed in these motional coherence measurements. During longer SDF pulse sequences, which include only short free evolution times, the heating seems to have a marginal effect. Such experiments are typically simulated using a only a dephasing Lindblad term. We find that the simulations qualitatively match experimental data using terms in the range $\Gamma = 7\,\mathrm{s}^{-1} - 30\,\mathrm{s}^{-1}$. The dephasing in this case leads to a reduction of the observed revival heights. Most error sources, for example calibration errors, introduce almost identical reductions. Thus we can think of the dephasing term as phenomenologically accounting for all of these error sources, which might explain the differences in its size between different experiments.

5.2 Motional frequency calibration

One of the main sources of systematic errors is the calibration accuracy of the motional frequency. In addition frequent motional frequency calibrations allow us to estimate oscillator drift and stability.

5.2.1 Ground state tickle

In this method the ion is first cooled close to the ground state and its internal state is initialized to $|\downarrow\rangle$. Then a tickling pulse, described in section 3.6.1, is applied for time T, with strength g and detuning δ. Finally the state is probed using a red sideband pulse. The red sideband is only able to excite the internal state in case, where the tickling pulse had a low detuning δ and was able to excite the motional state. The excitation of the internal state is monitored as a function of the tickling frequency.

After tickling the ion is found in a coherent state with $|\alpha(\delta)| = |g/\delta \sin(\delta T/2)|$ where $|\alpha(0)| = \alpha_{\max} = gT/2$. In order to obtain a useful red sideband signal, the probe time must be chosen to be below a π-time at the relevant Rabi frequencies. In other words if the red sideband time is fixed to a short duration, then the maximal useful $|\alpha(0)|$ is finite. A certain difference in the coherent states is required in order to discriminate them: $|\alpha(0)| - |\alpha(\delta)| \approx 1$. Taylor expansion of the sine leads to the relation $\delta \approx \sqrt{6/\alpha(0)}2/T$ up to leading order in $1/T$. To enhance the accuracy a longer tickling pulse is required, while at the same time the coupling strength g needs to be reduced in order to maintain $\alpha(0)$ at an optimal value. For accuracies of around 20 Hz tickling pulses of durations of around 25 ms are required ($\alpha(0) = 3$), which makes such a calibration relatively slow. Many experiments presented in the following need frequent accurate recalibration of the motional frequency, thus a novel quicker scheme was used for most experiments.

5.2.2 Coherent state probe

For this method a first strong tickling pulse is applied, preparing a coherent state $|\beta\rangle$, which is then subjected to free evolution for a time T. A second strong tickling pulse with opposite phase inverts the initial shift. Figure 5.3 (a) shows this calibration in phase space; we assume that the tickling is strong and brief such that the detuning during this pulse plays a negligible role. For $\delta = 0$ no relative phase is accumulated between the oscillator and the control system during the long wait time T, and the state returns to the origin. Otherwise we find the state excited to $|\alpha(\delta)| = 2|\beta \sin(\delta T/2)|$. Using this together with the requirement $|\alpha(0)| - |\alpha(\delta)| \approx 1$ yields $\delta \approx 1/(|\beta|T)$ up to leading order in $1/T$. In ground state tickle $|\alpha(0)| = \alpha_{\max}$, while in the "coherent state probe" method $|\alpha(0)| = 0$. Therefore the red sideband probe time is no longer restricted to be short in relation to the relevant shifts. Thus we can reduce the required wait time T by increasing β. In practice oscillator decoherence limits the useful β size. Typically values around $\beta \approx 4.3$ were used, in which case the wait time required for a 20 Hz calibration is about 2 ms. Thus the "coherent state probe" method can be more than 10 times quicker than the previous method. A drawback of the novel scheme is that the signal is ambiguous since $\alpha(\delta)$ returns back to the origin for $\delta = 2\pi/T$ and

multiples of this detuning. Hence typically a hybrid scheme is used. At the beginning of the day the "ground state tickle" method is used to calibrate the motional frequency roughly; thereafter the fine calibration is performed using the "coherent state probe" method. In the following the motional frequency is tracked through frequent calibrations.

Figure 5.3 (b) shows a typical calibration scan measured in 20 s alongside a fit to a Lorentzian $o + 2A/(1 + (2(f - f_0)/w)^2)$ with $f_0 = 1.86030(5)$ MHz[1] and $w = 134 \pm 20$ Hz. The frequency needs to be recalibrated frequently as it drifts over the course of a day. The drifts over a 10 h time span are shown in figure 5.3 (c). The fit shown in red finds drifts on the order of 50 Hz/h, while the calibrations deviate from the fitted model with at most ± 40 Hz/h as shown in figure 5.3 (d).

5.3 SDF coupling strength calibration

The SDF pulse is calibrated by first roughly balancing blue and red sideband powers and applying it to an initial ground state cooled oscillator in the $|\downarrow\rangle$ internal level for a time t_{SDF}. The decrease in the probability $P(\downarrow, t_{\mathrm{SDF}})$ is observed and iteratively we find better balanced laser powers and a Stark-shift of our transition by flattening the $P(\downarrow, t_{\mathrm{SDF}})$ signal at 0.5 probability for the timescales required in the experiment. From the calibrated SDF pulse we extract the proportionality factor between pulse time and displacement size by fitting the qubit decay to its expected form $P(\downarrow, t_{\mathrm{SDF}})_{|0\rangle} = \frac{1}{2}(1 + e^{-2(ct_{\mathrm{SDF}})^2})$ with c the floated proportionality constant. The expected form for the ground state critically depends on the ion temperature since for a thermal state the expectation follows $P(\downarrow, t_{\mathrm{SDF}})_{\langle n\rangle} = P(\downarrow, t_{\mathrm{SDF}})_{|0\rangle} e^{-i(2ct_{\mathrm{SDF}})^2 \langle n\rangle}$, which leads to a quicker decay and thus leads to errors in extracting c. This problem can be mitigated by starting from the first Fock state, prepared with a blue sideband π-pulse after ground state cooling. In this case the expectation follows $P(\downarrow, t_{\mathrm{SDF}})_{|1\rangle} = \frac{1}{2}(1 - e^{-2(ct_{\mathrm{SDF}})^2})(1 - (2ct_{\mathrm{SDF}})^2)$ which shows an additional bump in the trace. The position of the bump is largely unaffected by an initial thermal state and is thus suitable for extracting the coupling c. Typical values of c obtained from these fits are $c \approx 36 - 28\,\mathrm{ms}^{-1}$. An example of this calibration in case of a Fock state is shown in figure 5.4.

For measurements on the order of several hours this calibration was repeated roughly every 20 min. The recalibrations had typical standard deviations from their mean value of about $1\,\mathrm{ms}^{-1}$. The recalibration in such a way makes sense if red and blue sideband powers fluctuated by the same amount and thus led to an overall change in the coupling strength of the SDF pulse. Laser power fluctuations were discussed in section 4.3.6 and relative fluctuations have been measured to be of similar size and thus the recalibration scheme should be improved in the future.

[1] the round brackets denote that the fit error is on the order of ± 1 Hz

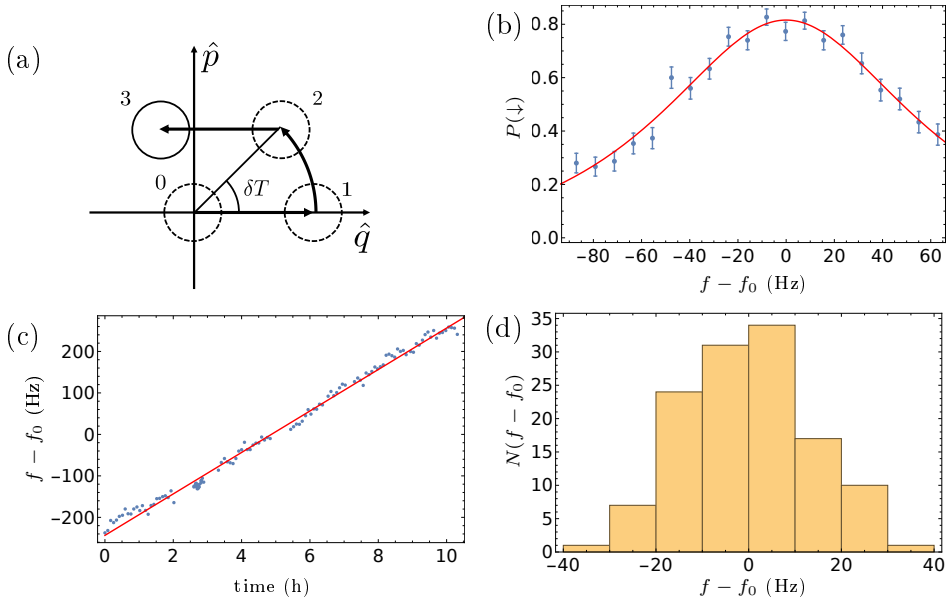

Figure 5.3: Motional frequency calibration using a coherent state probe. (a) Calibration explained in phase space. The ion is ground state cooled (see dashed state labeled 0), then a coherent state (1) is created by a first tickling pulse. The state evolves freely during the wait time T and rotates by an angle δT with δ the detuning from the angular motional frequency ω. A second tickling pulse reverses the inital displacement. In the case of a detuning the final state (3) does not return to the ground state, which can be detected using a red sideband probe pulse. (b) Typical calibration feature measured in 20 s alongside a fit to a Lorentzian (red line) $o+2A/(1+(2(f-f_0)/w)^2)$ with $f_0 = 1.86030(5)$ MHz and $w = 134 \pm 20$ Hz. (c) Frequent recalibration of the motional frequency for 10 h of the 9 of September 2018 fitted to a linear model (red) with slope 50 ± 0.4 Hz/h. (d) Histogram of the deviations of the calibration to the linear model.

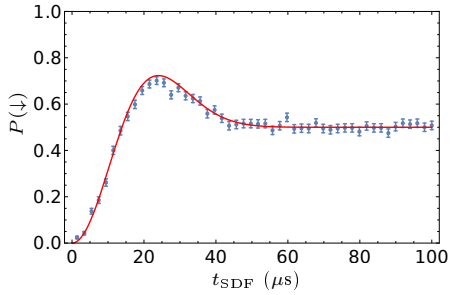

Figure 5.4: SDF coupling strength calibration. Shown is the evolution of the internal state probability for an SDF pulse applied to Fock state $|1\rangle$. A fit to the expected form $P(\downarrow, t_{\mathrm{SDF}})_{|1\rangle} = \frac{1}{2}(1 - e^{-2(ct_{\mathrm{SDF}})^2})(1 - (2ct_{\mathrm{SDF}})^2)$ yields $c = 36 \pm 0.4\,\mathrm{ms}^{-1}$.

5.4 Squeezing amount

The calibration of the squeezing parameter r is discussed in detail in [40]. After pumping into the squeezed ground state, we apply a blue sideband pulse and observe the internal state population as a function of pulse time. This follows the expectation of equation 3.11 with the Fock state populations determined by the squeezing amount r. Fitting the observed oscillations to this trace for a squeezed state using a floated variable r allows us to estimate the amount of squeezing r.

5.5 Relative phase space orientations

For all of the experiments presented it is important to be able to control the relevant phase space orientations. These are the SDF shift direction, the tickling shift direction and the squeezed state orientation. These can be referenced to each other via a multitude of possible sequences. The sequences used experimentally are summarized below.

5.5.1 Squeezed state orientation versus SDF direction

The SDF direction and the squeezed state orientation are both defined by the difference phase of the red and blue sideband components in the bi-chromatic laser pulses. The creation of the squeezed state and the SDF pulse use the exact same electronic and optical signal paths thus their directions stay fixed with respect to each other. Applying the SDF pulse to the squeezed state and monitoring the internal state populations $P(\downarrow, t_{\mathrm{SDF}})_{|\xi\rangle}$ for different displacement directions of the SDF allows us to confirm the fixed phase relation between the squeezed state and the SDF. In chapter 6 complete tomography of

squeezed state superpositions based on SDF pulses is discussed. These large data sets reveal a small tilt up to $\approx 5\,\mathrm{deg}$ between the orientation of the squeezed state and the SDF. The source of this tilt and whether it can be removed using an improved more accurate calibration is not well understood, and left for future studies.

5.5.2 SDF versus tickling

In order to match the tickle direction to that of the SDF laser force, a squeezed oscillator state $|\xi\rangle$ and a qubit initialized to $|\downarrow\rangle$ is used. As discussed in section 3.6.2 a carrier $\pi/2$-rotation before and after a SDF pulse implements the operation SDFz $= \hat{\mathcal{D}}(\alpha\hat{Z})$. We use this sequence in order to displace the squeezed motional state based on the laser force. Figure 5.5 shows a schematic of the calibration in phase space. We aim to invert this displacement using the tickling pulse. We probe whether we returned to the initially prepared squeezed state by using the squeezed version of the red sideband Hamiltonian as discussed in section 3.5. The laser will not induce a change of the internal qubit state if the motion is in the squeezed ground state. Thus in cases were we successfully invert the unconditional displacement due to the laser, we are not able to invert the qubit with the bi-chromatic pulse. We exploit the anisotropic nature of the squeezed state by displacing along the squeezed axis in order to calibrate the duration of the oscillating voltage (see figure 5.5 part (a)) and along the anti-squeezed axis in order to find its phase (part (b)).

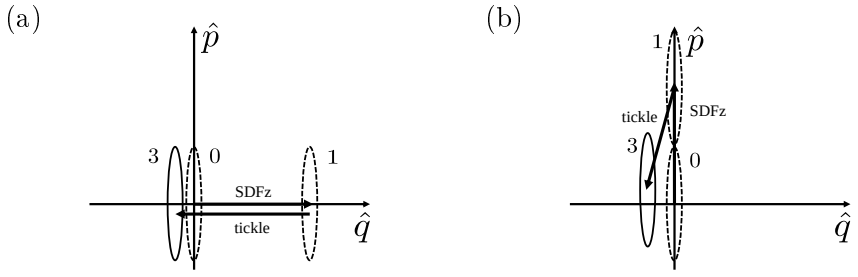

Figure 5.5: Matching of the tickling pulse to the SDF pulse. (a) The squeezed motional state (see dashed state labeled 0) is displaced using a SDF between two $\pi/2$ internal state rotations (SDFz). A subsequent tickling pulse is calibrated in order to revert the displacement implemented by the laser. Whether or not the squeezed state returns to the squeezed vacuum can be probed using the squeezed basis analog of the red sideband [40]. Shown is the case of a laser displacement along the squeezed axis, which enhances sensitivity for the tickling coupling strength. (b) Similarly a laser displacement perpendicular to the squeezed axis is used to calibrate the direction of the tickling pulse.

5.6 Rotating frames

Our control system [127] is currently operating in such a way, that before the experimental sequence starts a time $T_0 = 0$ is defined. This time is then used in order to calculate the phases of RF tones generated by our direct digital synthesis (DDS) cards. The current implementation is that a RF pulse programmed to begin at time T_{exp} with an angular frequency ω_p and offset phase ϕ will output a phase $\phi_{\mathrm{DDS}} = \phi + T_{\mathrm{exp}}\omega_p$.

This method of calculating the phase automatically implements a useful rotating frame in many cases. As an example we discuss addressing the axial motional mode using the SDF pulse given by equation 3.21. In the rotating frame of the bare oscillator Hamiltonian the operator $\hat{a}$ evolves according to $\hat{a}e^{-i\omega t}$. The SDF Hamiltonian with $\delta = 0$ contains the term $\hat{a}e^{i\Delta\phi/2}$ where $\Delta\phi/2 = (\phi_r - \phi_b)/2$. The red and blue sidebands are realized by two DDS channels outputting tones at angular frequencies $\omega_0 \pm \omega$. These simultaneously drive the last single pass AOM (see figure 4.17). In this case $\omega_0 \approx 200\,\mathrm{Hz}$ is the required laser frequency shift in order to drive the carrier transition. Calculating the phase $\Delta\phi/2$ for a pulse run at time T_{exp} and the DDS programmed to output ϕ_r and ϕ_b respectively leads to $\Delta\phi/2 = (\phi_r + (\omega_0 - \omega)T_{\mathrm{exp}} - (\phi_b + (\omega_0 + \omega)T_{\mathrm{exp}}))/2 = (\phi_r - \phi_b)/2 - \omega T_{\mathrm{exp}}$. The natural evolution of the oscillator is automatically tracked by the SDF pulse.

The internal state qubit phase evolution is governed by three different types of operation: (i) no pulse is run and the qubit evolves at its bare frequency; (ii) the qubit is addressed with a resonant carrier operation. In this case the qubit evolution includes a Stark shift of the qubit transition whose value is around $\delta/(2\pi) = 2\,\mathrm{kHz}$; (iii) the qubit is addressed using a bi-chromatic pulse, where we will consider mainly the case of the SDF laser. In this case the qubit evolution contains the Stark shift due to this laser pulse.

In the experiments presented throughout this thesis the carrier rotation is driven at a frequency calibrated using low laser powers and long pulses. This yields a frequency close to the bare internal qubit frequency. In the main experiment carrier rotations are run using high Rabi frequencies $\Omega \approx 0.5\,\mathrm{s}^{-1}$, thus we drive the qubit detuned by its Stark shift. But for the used settings this leads to a negligible reduction in Rabi oscillation contrast. The control system phase evolution in this case typically differs from the qubit evolution by the duration of carrier pulses multiplied by the Stark shift. This scheme is useful for example if a Ramsey sequence with a variable wait time T is run. In this case the phase is evolved correctly for the variable wait time and only a small constant phase mismatch due to the carrier pulse duration is induced.

In this thesis manipulations based on the internal state dependence of SDF are used and combined with carrier rotations. This type of control requires the SDF to address the internal states with the identical rotating frame as the carrier pulse. But when driving the SDF the internal qubit is addressed by the average frequency of blue and red sideband. This frequency differs by

the calibrated Stark shift to the bare frequency used in a carrier pulse. The control system thus evolves the qubit phase differently depending whether a SDF or a carrier pulse is run. In this case the arbitrarily chosen T_0 enters into relevant phases, which is highly undesirable as a change in i.e. cooling durations, changes the physics of the experimental run.

In principle these phases are known and a record of the executed pulses can be kept. The best way to implement phase tracking for arbitrary experiments including Stark shifts is left for future studies. In the experiments throughout this thesis some of the phases are evolved by additional phase calculations in the control software, while others are simply calibrated.

As an example we consider the SDFz $= \hat{R}(\pi/2)\hat{\mathcal{D}}(\alpha(t)\hat{X})\hat{R}(-\pi/2)$ sequence of operations, see section 3.6.2. Replacement of the SDF pulse in this sequence with a wait time leads to a Ramsey type experiment. For the Ramsey type experiment the control system evolves the phase during the wait time between the first $\pi/2$-pulse: $\hat{R}(\pi/2, \pi/2) = \hat{R}(-\pi/2)$ to the second pulse correctly. The control system evolution is unaffected, when the wait time is replaced by the SDF pulse. But the SDF pulse introduces an additional Stark shift, which now has to be included in the propagation of experimental phases. The Stark shift is known from the SDF calibration and can thus be used to propagate in the control code the phase from the first $\pi/2$ pulse to the second pulse for a variable duration of the SDF pulse. In addition these two pulses need to be referenced to the SDF absolute phase. In this case the carrier pulses realize a rotating frame of the bare qubit frequency and using the time T_0, while the SDF rotating frame includes the Stark shift. This introduces a phase mismatch of T_0 times the stark shift. Instead of correcting one of the rotating frames in software the mismatch is calibrated on the physics of the pulse sequence. In case of the correct aboslute phases the pulse sequence SDFz applied to $|\downarrow\rangle$ gives a constant probability $P(\downarrow) \equiv 1$ independent of the displacement size. An additional phase offset of the two $\pi/2$ pulses is then scanned jointly and set to the value where $P(\downarrow) = 1$. The successful phase propagation and calibration is confirmed when $P(\downarrow) = 1$ stays constant once the SDF duration is scanned.

The control system has the capability of resetting the $T_{\text{exp}} = 0$ during the sequence. This approach is useful in cases, where all experimental phases are reset [90]. It is not helpful for the experiments in this thesis, since the oscillator phase evolution needs to be tracked throughout the full duration of experiments.

Chapter 6

Generation and analysis of large cat states

This chapter describes experiments analyzing cat states using displaced and squeezed Fock state bases. All experiments have been performed jointly with Daniel Kienzler, while the results are published in [112]. We start by reporting on the first in-situ phase verification measurements for "Schrödinger's cat" states realized exclusively in the trapped ion's motion using the well-established technique of extracting populations in the Fock state basis [29]. Limitations of this method for larger cat states are overcome by using squeezed Fock state bases. Using a Fock basis with 8 dB of squeezing, we are able to observe quantum interference for a phase space separation of $\Delta\alpha = 15.6$, which corresponds to a direct measurement of interference between wave packets separated by 240 nm with a root-mean-square extent of 7.8 nm. Additionally displaced versions of both the energy eigenbasis and the squeezed energy basis can be used to reconstruct the Wigner function of cat states [112].

6.1 Creating cat states

The methods discussed in chapter 3 allow for the creation of a variety of interesting oscillator states. In this chapter, we focus our study on analyzing superpositions of two distinct oscillator wave packets sometimes referred to as "Schrödinger's cat" states. These are created by first applying an SDF pulse (section 3.6.2) to a ground state cooled oscillator $|0\rangle$, while the internal state qubit is initialized to $|\downarrow\rangle$,

$$|\downarrow\rangle|0\rangle \overset{\text{SDF}}{\rightarrow} (|+\rangle|\alpha/2\rangle + |-\rangle|-\alpha/2\rangle)/\sqrt{2} \tag{6.1}$$

$$= [|\downarrow\rangle(|\alpha/2\rangle + |-\alpha/2\rangle) + |\uparrow\rangle(|\alpha/2\rangle - |-\alpha/2\rangle)]/\sqrt{2}. \tag{6.2}$$

Such a state can be viewed as an analogy to the "Schrödinger's cat" thought experiment, where the macroscopic cat i.e. the oscillator wave packet $|\pm\alpha/2\rangle$

can be found in two distinct states (the different locations in phase space). Whether the cat is "dead" or "alive" depends if the radioactive atom, here represented by the internal qubit states, decayed ($|-\rangle$) or not ($|+\rangle$).

The oscillator is disentangled from the internal state using the fluorescence readout. Conditioned on the dark result the oscillator state is prepared in $|\uparrow\rangle(|\alpha/2\rangle - |-\alpha/2\rangle)$. Depending on the literature this disentangled superposition of the oscillator is referred to as "Schrödinger's cat" (instead of the state in equation 6.1). States of the form given in equation 6.1 have been prepared previously in trapped ions [31, 37, 162–165] while only for electromagnetic fields the entanglement with the microscopic degree has additionally been removed [50, 133].

In case of a bright detection, the motional superposition state is decohered due to the scattering of fluorescence photons. This problem is circumvented in order to create $|\uparrow\rangle(|\alpha/2\rangle + |-\alpha/2\rangle)$ by adding an additional carrier π-pulse in front of the fluorescence detection, which interchanges the bright and dark measurement results. The created cat states $|\psi_{\pm1}\rangle \propto |\alpha/2\rangle \pm |-\alpha/2\rangle$ have symmetric extent in phase space and are ±1 eigenstates of the parity operator. The parity operator reflects coherent states at the origin $\hat{\mathcal{P}}|\alpha\rangle = |-\alpha\rangle$ and can be defined in terms of the number operator $\hat{\mathcal{P}} = (-1)^{\hat{N}}$. Eigenstates of the parity operator $\hat{\mathcal{P}}$ with $+1$ eigenvalues are called even states while those with -1 eigenvalues are called odd states. These eigenstates contain only even or odd Fock states.

We prepare the mixed two-state superposition

$$\hat{\rho}_{\text{mix}} = |\alpha/2\rangle\langle\alpha/2| + |-\alpha/2\rangle\langle-\alpha/2| \tag{6.3}$$

by replacing the fluorescence detection with re-pumping of the internal state to the $|\downarrow\rangle$ level. The impact on the motional state by the repumping is estimated to be on the order of 2%.

6.2 Fock state reconstruction

All techniques presented in this chapter rely on indirect measurements of the oscillator via the internal state qubit. The oscillator is first coupled to the internal states, which are subsequently read out. Dependent on the coupling different information about the oscillator is obtained. A well-studied technique is the reconstruction of populations in the energy eigenbasis as discussed in section 3.4.3 [29, 34, 133]. In this case the internal state $|\uparrow\rangle$ ($|\downarrow\rangle$) is coupled to the motional state $|\psi\rangle$ using a red (blue) sideband pulse. The internal state readout then follows[1]:

$$\pm[P(\uparrow,t) - P(\downarrow,t)] = \gamma(t)\sum_{n=0}^{\infty}\wp(n)\cos(2\Omega_n t) \tag{6.4}$$

[1] for simplicity we repeat here equation 3.11

where $\wp(n) = |\langle n|\psi\rangle|^2$ and $\gamma(t)$ accounts for decay in the coherence of the whole system. The Rabi frequencies in the Lamb-Dicke regime are given by $\Omega_n = \Omega_{n,n+1} = \eta\Omega\sqrt{n+1}$ (see section 3.3.2).

The dynamics of the spin populations are governed by dephasing and rephasing of the various Rabi oscillations at frequencies Ω_n and with weight $\wp(n)$. In case of coherent states the spin populations follow characteristic collapse and revival dynamics [115]. In general the expected signal can be characterized qualitatively using properties of the distribution $\wp(n)$. These include the average phonon number $\langle n\rangle$ and standard deviation δn. In case of a coherent state $|\alpha/2\rangle$ the populations are given by a Poisson distribution $\wp(n) = e^{-|\alpha|^2/4}|\alpha|^{2n}/(4n!)$ for which $\langle n\rangle_{|\alpha/2\rangle} = \delta n^2_{|\alpha/2\rangle}$. The signal collapses on a timescale t_c governed by dephasing of frequencies separated by roughly the spread of the distribution. Narrower distributions thus show slower collapse. An estimate of the collapse time is given by $t_c \approx 1/[2(\Omega_{\langle n\rangle+\delta n} - \Omega_{\langle n\rangle-\delta n})]$. For a coherent state we find $1/t_c = 2\eta|\alpha/2|(\sqrt{1+1/|\alpha/2|} - \sqrt{1-1/|\alpha/2|}) \approx 2\eta$ with the latter approximation valid for sufficiently large α.

In case of distributions with small enough δn the signal revives after a time t_r. The revival occurs when neighboring frequencies rephase this happens around $t_r \approx \pi/(\Omega_{\langle n\rangle+1} - \Omega_{\langle n\rangle})$, which for a coherent state yields $1/t_{r2} \approx \eta\Omega/(\pi|\alpha|)$. More complete revivals are expected in case of narrower distributions, since a higher proportion of frequencies rephase.

Extraction of $\wp(n)$ is typically possible if either collapse is slow or if we are additionally able to measure the revival signal. Otherwise the short collapse time does not provide enough information about the state. Using a fit of the measurement trace to equation 6.4 allows us to infer the strength of each Fock state component $\wp(n)$ but not their relative phases $\arg(\langle n|\psi\rangle)$.

Experiments are limited in two ways. On one hand oscillator dephasing, the internal state coherence and the stability of the sideband coupling set a limit for the maximal duration of the measurement. In addition sideband Rabi frequency stability limits the maximal resolvable frequency.

6.2.1 Experimental results

Figure 6.1 shows collapse and revival for (a) a mixed cat $\hat{\rho}_{\text{mix}}$, (b) an odd cat $|\psi_{-1}\rangle$ and (c) an even cat $|\psi_{+1}\rangle$ all use settings $|\alpha| \simeq 6$. column (i) shows the measurement points, while column (ii) shows the motional populations obtained from fits of equation 6.4 to the data. In fitting the data we use a phenomenological exponential decay $\gamma(t) = e^{-\Gamma t}$ (more details regarding the fits can be found in [112]). The Fock state populations of the coherent state $|\alpha/2\rangle$ are independent of $\arg[\alpha/2]$. Therefore $\hat{\rho}_{\text{mix}}$ has the same Fock state population distribution as any other coherent state of size $|\alpha/2|$. In contrast the even (odd) parity cat states $|\psi_{\pm1}\rangle$ contain only even (odd) phonon numbers. The distribution $\wp(n)$ still shows the same mean and standard deviation as the populations of the state $\hat{\rho}_{\text{mix}}$. Direct calculation of the cat state populations

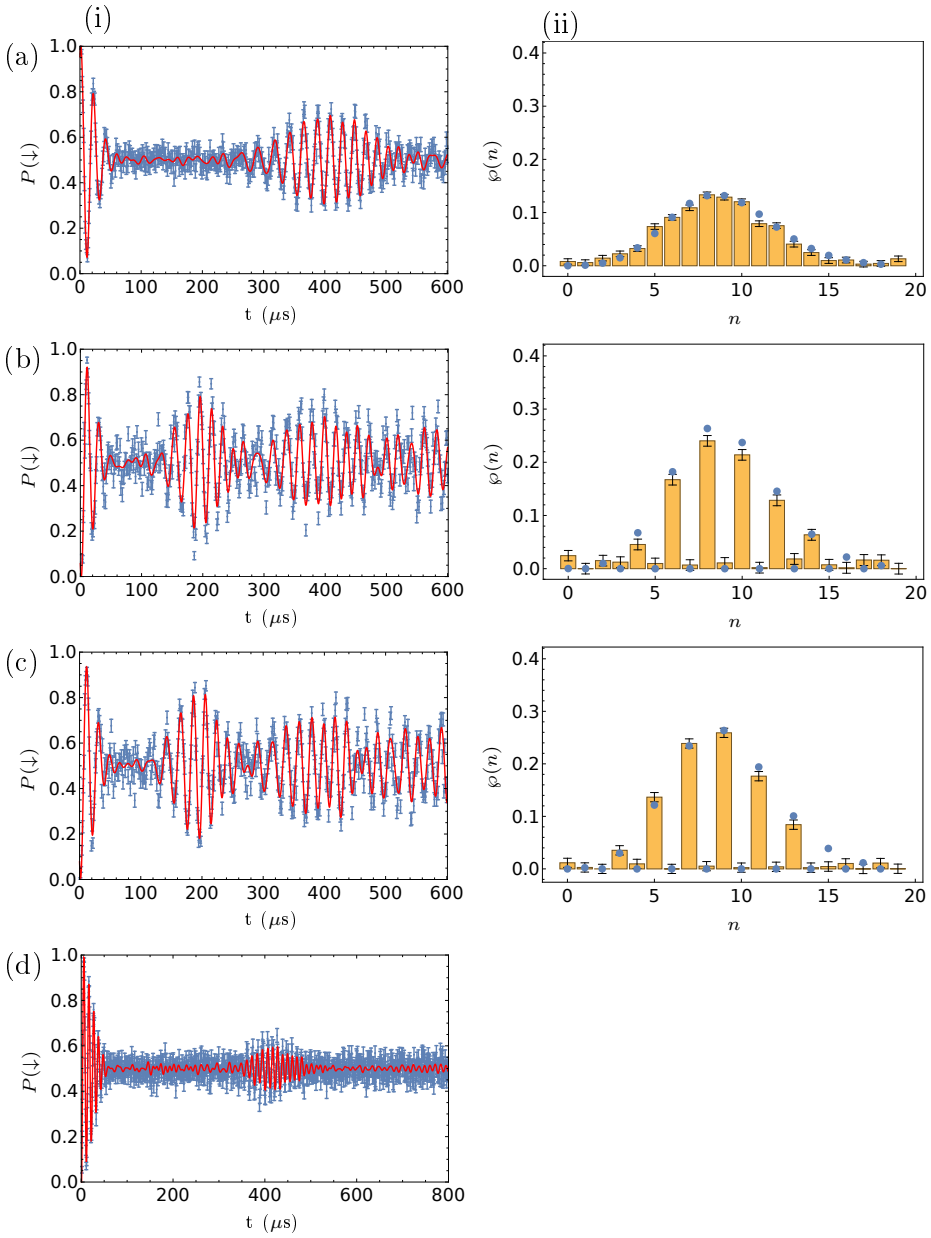

Figure 6.1: Fock state population reconstruction. The first column (i) shows the collapse and revival of the internal state flopping under the red sideband $\hat{H}_r$ (row (a) blue sideband $\hat{H}_b$) Hamiltonian. Data points are given in blue, while red represents a fit to equation 3.11 with the populations floated. column (ii) shows the fitted Fock populations as yellow bars together with the ideal populations of states with $\alpha = 6$. Row (a) shows $\hat{\rho}_{\text{mix}}$, while (b) shows the odd cat $|\psi_{-1}\rangle$ and (c) the even cat $|\psi_{+1}\rangle$. Part (d) shows the limitation of this method and displays data of an odd cat with $|\alpha| \simeq 11.6$. Spin populations are the result of 250 repeats of the full experimental sequence, which corresponds to roughly 125 analysis detections for the post-selected cases. Error bars are estimated from quantum projection noise. The population errors are given as s.e.m..

shows that contributions from the coherent states with opposite sign either add up constructively or destructively.

For all three states the collapse timescale is given by the corresponding time of the coherent state and a revival occurs at $1/t_{r2} \approx \eta\Omega/(\pi|\alpha|) = 386\,\mu$s for the settings $\eta\Omega/\pi = 31\,$kHz and $\langle n\rangle = |\alpha/2|^2 = 8.76$ used in the experiment. Since the odd and the even cat contain only every second frequency component an additional revival at approximately half the time $t_{\mathrm{r1}} = 198\,\mu$s is expected and confirmed by the measurements.

The populations extracted from the fit show that the odd and even cat states contain predominantly odd or even number states. We use these populations to extract the parity $\langle\hat{\mathcal{P}}\rangle \equiv \sum_n (-1)^n \wp(n)$ of the number state distributions, obtaining 0.029 ± 0.024 for the mixture, -0.88 ± 0.04 for the odd and 0.83 ± 0.05 for the even cat.

The limitation of this method is shown in part (d) of figure 6.1, which displays an odd cat signal for $|\alpha| \simeq 11.6$. In this case the time for the odd cat revival $t_{\mathrm{r1}} \simeq 400\,\mu$s and a second revival is expected around $t_{\mathrm{r2}} \simeq 800\,\mu$s. The first revival is still visible but the revival amplitude is decreased substantially. The second revival in turn is no longer visible. Due to the larger $\langle n\rangle$ the signal also oscillates at higher frequencies, which requires a much narrower sampling of the measurement trace. This illustrates the challenges of using this technique for characterizing larger cat states. Exceptional Rabi frequency stability and internal state coherence are necessary. In addition the amount of required data points becomes prohibitive. For this reason we extend the method to transformed energy bases allowing to measure the parity of cat states of increased size.

6.3 Interference of large cats using squeezed Fock states

To overcome this problem, we analyze larger cat states using a squeezed Fock state basis $|n\rangle_\xi \equiv \hat{\mathcal{S}}(\xi)\,|n\rangle$. The Hamiltonian required for this analysis is given by equation 3.14:

$$\begin{aligned}\hat{H}_- &= \frac{\hbar\widetilde{\Omega} i\eta}{2}\sigma_+\left[\cosh(r)\,\hat{a} + e^{i\vartheta}\sinh(r)\,\hat{a}^\dagger\right] + \text{h.c.} \\ &= \frac{\hbar\Omega_r i\eta}{2}\sigma_+\left[\hat{a} + e^{i\vartheta}\frac{\Omega_b}{\Omega_r}\,\hat{a}^\dagger\right] + \text{h.c.}\end{aligned} \tag{6.5}$$

Here the second line relates to the implementation of the squeezed Hamiltonian, realized by switching on the red sideband with a fixed Rabi frequency Ω_r and a blue sideband of variable Rabi frequency Ω_b. Without loss of generality the red sideband phase can be set to zero, since the initial internal state is $|\uparrow\rangle$ or $|\downarrow\rangle$, while the blue sideband has phase ϑ. The $\hat{H}_-$ pulse couples neighboring

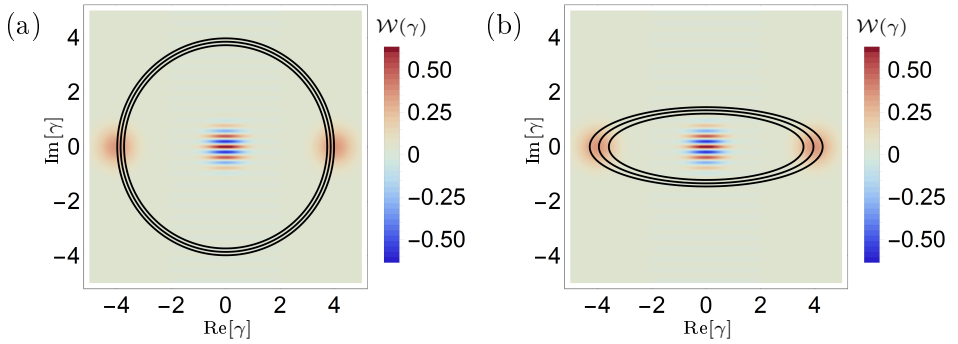

Figure 6.2: Reduction of $\langle n \rangle$ using the squeezed basis. (a) Wigner function of an even cat state of $\alpha = 8$ overlaid with the local maxima in the Wigner functions of the Fock state basis elements $|n\rangle = 15, 16, 17$. These elements lead to the highest populations $\wp(n)$ and shown are their local maxima located around $|\gamma| \approx 4$. (b) The same cat state together with the local maxima of the relevant basis elements in the squeezed basis $|n\rangle_\xi = 5, 6, 7$, with $\xi = 0.54$. These basis elements have substantially lower quantum numbers and their maxima cover a larger area of the cat state lobes.

squeezed Fock states $|n\rangle_{re^{i\vartheta}}$, where $\tanh(r) = \Omega_b/\Omega_r$ and the Rabi frequency $\Omega_{n_\xi} \approx i\eta\widetilde{\Omega}\sqrt{n_\xi + 1} \approx i\eta\Omega_r\sqrt{n_\xi + 1}/\cosh(r)$.

These relations allow to generalize the Fock state population extraction technique described in section 3.4.3 and used in section 6.2 directly to squeezed Fock state bases. The method can further be extended to bases including displacements. Replacing the sideband pulse with $\hat{H}_-$ ($\hat{H}_+$) in formula 6.4 leads to:

$$\pm[P(\uparrow, t) - P(\downarrow, t)] = \gamma(t) \sum_{n=0}^{\infty} \wp(n_{\alpha,\xi}) \cos(2\Omega_{n_{\alpha,\xi}} t) \tag{6.6}$$

In the current example $\alpha = 0$ but the experiments in the next section will involve $\alpha \neq 0$. The transformed basis is advantageous if the populations $\wp(n_{\alpha,\xi})$ in the new basis simplify. Analysis of a squeezed vacuum state $\hat{\mathcal{S}}(\xi)\,|0\rangle$ for example will only show populations in $\wp(n_{0,\xi} = 0)$, while in any other basis typically populations are spread over many quantum numbers. The squeezed basis is advantageous for motional states excited along one phase space axis, like the cat states. An intuition for $\wp(n_\xi)$ can be gained by plotting the Wigner function of $|\psi\rangle$ alongside features of the basis elements $|n\rangle_\xi$. Figure 6.2 provides this intuition for an even cat state of $|\alpha| = 8$ comparing the Fock basis to a squeezed basis with $r = 0.54$ where the anti-squeezing axis is aligned to the cat.

Since the squeezing operator preserves parity, the even (odd) cats $|\psi_{\pm 1}\rangle$ consist of only even (odd) squeezed number state populations. These can be

derived from the squeezed populations of the coherent state $|\alpha/2\rangle$. For the latter mean and variance are found to be [166]:

$$\langle n\rangle_\xi = \frac{\alpha^2}{4}|\cosh(r)e^{-i\vartheta/2} + \sinh(r)e^{i\vartheta/2}|^2 + \sinh(r)^2 \tag{6.7}$$
$$(\delta n_\xi)^2 = \frac{\alpha^2}{4}|\cosh(r)e^{-i\vartheta/2} + \sinh(r)e^{i\vartheta/2}|^2[e^{-2r}\cos^2(\vartheta/2) + e^{2r}\sin^2(\vartheta/2)] + \frac{\sinh(2r)^2}{2}$$

Here the parameter $\xi = re^{i\vartheta}$ defines the squeezed analysis basis and we fixed the cat to be aligned with position $\arg(\alpha) = 0$. This provides enough degrees of freedom, since only the relative orientation of the coherent states to the squeezing axis matter. Note that both $\langle n\rangle_\xi$, $(\delta n_\xi)^2$ depend on the orientation of the analysis basis.

In case of orientation of the anti-squeezing axis with $\mathrm{Re}(\alpha)$ i.e. inserting $\vartheta = \pi$, the formulas simplify to:

$$\langle n\rangle_\xi = |\alpha/2|^2e^{-2r} + \sinh(r)^2 \tag{6.8}$$
$$(\delta n_\xi)^2 = |\alpha/2|^2e^{-4r} + \frac{\sinh(2r)^2}{2}$$

The higher $\langle n\rangle_\xi$ due to the coherent state $|\alpha/2\rangle$ is suppressed via the squeezing at the expense of a constant increase due to the $\sinh(r)^2$ term. Moderate squeezings $r \leq 1$ thus allow for a reduction of mean and standard deviation of quanta in the new basis. However using a constant red sideband power (see equation 6.5) leads to reduced Rabi frequencies by a factor $1/\cosh(r)$ in the transformed basis[2]. This can limit the achievable reduction of experimental revival times. In fact we use this characteristic reduction of Rabi oscillation frequencies present in the signal to calibrate the orientation ϑ of the squeezed basis Hamiltonian. While the magnitude of squeezing is found by analyzing the motional ground state in the squeezed basis.

6.3.1 Experimental results

Measurements of the populations of larger cat states using the squeezed basis are shown in figure 6.3. In fitting the data we use higher order terms in the evaluation of equation 3.15 determining the Rabi frequencies. Data for cat states with $|\alpha| = 13.2, 14.3$ and 15.6 are shown in figure 6.3. The used values of $r = 0.74, 0.74$ and 0.9 differ from the optimal values which would minimize the revival time in the new basis including the effect of drop in Rabi frequency ($r_{opt} = 0.89, 0.91, 0.94$). The optimization does not include additional

[2] our formula underestimates this effect as we fix the Rabi frequency in such a way that we still have enough laser power in principle for an equally strong blue sideband. In practice blue and red sideband are generated by the same laser. In cases were the blue sideband power is not fully used then the additional power can be used to drive the red sideband more strongly. This in essence yields an even quicker decay of the Rabi rates for higher amounts of squeezing. Nevertheless our model captures the right qualitative drop in Rabi frequencies in higher squeezed bases for any experimental system with limited laser power.

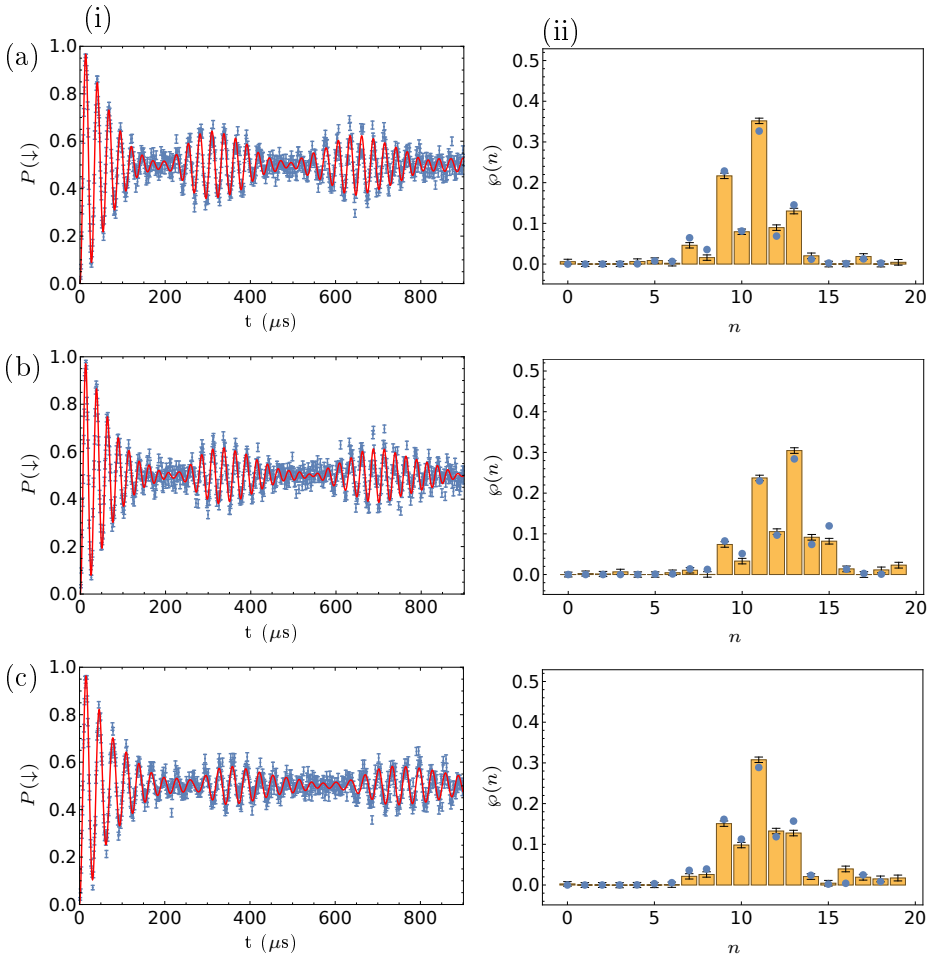

Figure 6.3: Squeezed Fock state population reconstructions. Column (i) shows the collapse and revival of the internal state populations under the $\hat{H}_-$ squeezed basis Hamiltonian. Data points are given in blue, while red represents a fit to equation 6.4 using floated populations. The fitted populations are shown in column (ii). Here the blue points are the Fock state populations obtained from a fit using a weighted mixture of an even and an odd cat. Part (a) shows a cat with $\alpha = 13.2$ analyzed using $r = 0.74$ for which we find a parity of $\langle\hat{\mathcal{P}}\rangle = -0.55 \pm 0.03$. The cat size is increased in part (b) to $\alpha = 14.3$ analyzed with the same amount of squeezing. Additional decoherence due to the larger cat reduces the parity to $\langle\hat{\mathcal{P}}\rangle = -0.48 \pm 0.03$. In (c) we push the cat size to an even higher value using $\alpha = 15.6$. This size requires a higher amount of squeezing $r = 0.9$ in the analysis in order to still resolve the revivals. We are still able to extract a clearly negative parity of $\langle\hat{\mathcal{P}}\rangle = -0.3 \pm 0.03$. Experimental data points are an average of 750 repeats of the full experimental sequence (1000 for (c)), which corresponds to roughly 375 (500) analysis detections for the post-selected cases. Error bars are estimated from quantum projection noise. Errors on population and parity estimates are given as the s.e.m..

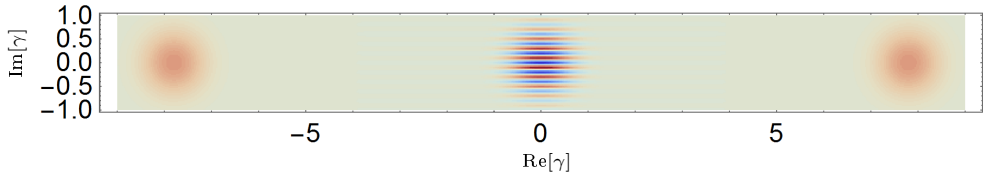

Figure 6.4: Theoretical Wigner function of an odd cat state with $\alpha = 15.6$. For a cat state of this size the squeezed basis allowed to confirm a clearly negative parity of -0.30 ± 0.03. The Wigner function shows how well the wave packets are separated.

dephasing of the Rabi oscillations at larger r impeding the signal. This is a consequence of the squeezed basis increased sensitivity to the dephasing of the motional state compared to the standard analysis. Nevertheless, for our largest cat, the number of Rabi oscillations at which the revival occurs is reduced from 60 to 11, which is essential for observing the interference. By fitting equation 3.11 with freely floated number state populations, we obtain the results shown in figure 6.3, from which we extract parities of $\langle \hat{\mathcal{P}} \rangle = -0.55 \pm 0.03$, -0.48 ± 0.03 and -0.30 ± 0.03. Also shown in figure 6.3 are the populations obtained from a fit to the experimental trace using a model of the motional populations which is derived from a weighted sum of the even and odd cats $\hat{\rho}_{\mathrm{p_{mix}}} = \mathrm{p_{mix}} \left|\psi_{-1}\right\rangle \left\langle\psi_{-1}\right| + (1 - \mathrm{p_{mix}}) \left|\psi_{+1}\right\rangle \left\langle\psi_{+1}\right|$. The close match between the theory and experiment indicate that the primary decoherence mechanism mixes the two cat states, which is compatible with heating and dephasing of the ion due to fluctuations in the electric fields [35, 36].

Thus the squeezed basis allowed us to confirm the creation of superposition states separated by $\alpha = 15.6$. Converted to real space variables this corresponds to a separation of about 240 nm where each wave packet has an extent of about 7.8 nm. Figure 6.4 shows a cat state of this size and provides an intuition for how well the wave packets are separated.

6.4 Wigner function reconstruction

Reconstruction of populations for states displaced away from the phase space origin would simplify using a displaced Fock basis. In the work described above we focused our efforts on analyzing the symmetric cat states, which do not exhibit such an advantage and thus this route is not explored. However displaced Fock bases can be used to perform full Wigner function tomography.

The Wigner function is related to the expectation value of the parity

operator for the populations of displaced number states $|n\rangle_\gamma \equiv \hat{\mathcal{D}}(\gamma)\,|n\rangle$ as

$$\mathcal{W}(\gamma) = 2/\pi\langle\hat{\mathcal{P}}_\gamma\rangle \text{ with } \langle\hat{\mathcal{P}}_\gamma\rangle = \sum_n (-1)^n \wp(n_\gamma). \tag{6.9}$$

This relationship has previously been used to experimentally reconstruct Fock, coherent and thermal states of a trapped-ion oscillator using a method that involves displacing the states by $-\gamma$ followed by extraction of the populations in the energy eigenstate basis [29]. Rather than taking this approach, we obtain the populations of the oscillator states directly in the displaced basis. The transformed basis Hamiltonian in this case is realized by simultaneously driving the carrier and the red sideband transition. The probed Wigner function point is determined by the ratio of the respective Rabi frequencies $|\gamma| = \Omega_c/(\eta\Omega_r)$, while $\arg(\gamma)$ is determined via their relative phase.

Note the general analogy between analyzing a transformed state $\hat{U}\,|\psi\rangle$ using the Fock basis compared to analyzing the bare state $|\psi\rangle$ and extracting populations in the transformed basis $\hat{U}^\dagger\,|n\rangle$. In both cases we find $\wp(n) = \wp(n_{\hat{U}}) = |\,\langle n|\,\hat{U}\,|\psi\rangle\,|^2$. This principle was also used for calibration of the transformed basis Hamiltonians. In the case of the coherent basis Hamiltonian, first the magnitude $|\gamma|$ is calibrated by preparing a ground state cooled ion and subsequently analyzing it with the coherent basis pulse. A fit using equation 6.6 to the Rabi oscillations as a function of time estimates $|\gamma|$ for a given AOM drive power. $|\gamma|$ is measured for three different AOM powers from which a linear dependence between power and coherent state size is extracted. Then the orientation of the basis $\arg(\gamma)$ is found by applying the coherent basis Hamiltonian to the superposition $|-|\gamma|/2\rangle + ||\gamma|/2\rangle$ and scanning the orientation of the basis. In cases where $\arg(\gamma) = 0, \pi$ we find half the population in the coherent basis ground state, which gives a characteristic trace of slow oscillations under the analysis pulse.

Reconstruction of one Wigner function point $\mathcal{W}(\gamma)$ involves recording a full trace of internal state time evolution according to equation 6.6 using the transformed basis $|n\rangle_\gamma$. Variation of the displaced basis leads then to reconstruction at a different point γ. The extracted Wigner function for an odd cat state with $\alpha \simeq 4.2$ is shown in figure 6.5. This reconstruction involved a grid of 17×21 values of γ. Figure 6.5 shows clearly the expected features, including the two separated peaks corresponding to the coherent state wave packets as well as the interference fringes close to $\gamma = 0$.

The two frequency components are generated using the single pass AOM driven with two frequency tones as described in 4.3.5. The laser spot when passing through the modulator is imaged onto the single mode fiber. This ensures that both frequency components are coupled to the fiber which delivers the light to the experiment. The main uncertainty in γ results from relative power fluctuations in Ω_r, Ω_c due to drifts in the fiber coupling. These can be estimated from repeated calibrations of the coherent state Hamiltonian as described above, which indicate 1 % of relative Rabi frequency fluctuations over

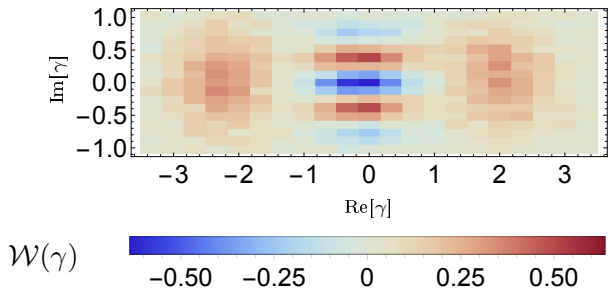

Figure 6.5: Reconstructed Wigner function for a cat with $\alpha \simeq 4$, extracted using 357 settings of the displaced Fock state basis

the course of a day. In case of no recalibrations and because $|\gamma| = \Omega_c/(\eta\Omega_r)$ this would lead to drifts of the basis on the order of 20 %. Such fluctuations set a limit on the smallest step, which we can perform faithfully during our reconstruction. For a drift of the Rabi frequencies by 0.1% between two consecutive recalibrations, a maximal error of $\delta\gamma = 0.04$ at $|\gamma| \approx 2$ would be introduced.

Usage of a displaced and squeezed basis reduces the resolvable step size along one phase space axis, while increasing it along the other. An increment in the carrier power either corresponds to a smaller or larger shift in γ compared to the non-squeezed case. Additionally as discussed in the previous section the squeezing either increases or decreases the number of transformed quanta dependent on the orientation of the squeezing term.

The fringes close to $\gamma = 0$ in the Wigner function contain the information about the stable phase relation and size of the cat state. The cut through the imaginary axis is expected to follow the functional form

$$f(x) = 2/\pi A e^{-2x^2} \cos(2\alpha x) \tag{6.10}$$

with $x = \mathrm{Im}(\gamma)$ ([115], App. B.1). The parameter A allows for a reduced contrast due to decoherence. Using a displaced and squeezed basis is especially advantageous for analyzing these cuts. Using the anti-squeezed axis aligned with the cat as in the previous section, benefits from both a lower number of transformed quanta as well as better resolution along the relevant direction.

Figure 6.6 shows Wigner function measurements along the imaginary axis of phase space. In (a) and (b) results for a cat with $\alpha \simeq 8.5$ are shown comparing measurements in the energy eigenbasis (a) to measurements in a squeezed basis with $r = 0.5$ (b). The fit to the expected fringes with a floating contrast A gives $\alpha = 8.42 \pm 0.02$ and $A = 0.90 \pm 0.02$ for the unsqueezed basis and $\alpha = 8.5 \pm 0.02$ and $A = 1.00 \pm 0.03$ for the squeezed basis. The data acquisition time per point is considerably longer for the non-squeezed basis, because extracting the multiple closely spaced high frequency components in the spin oscillations requires a higher sampling frequency and longer probe

times. Also shown is data for a cat with $\alpha \simeq 11.8$ (c) which was measured using a displaced-squeezed probe Hamiltonian with $r = 0.8$. In this case the fitted curve gives $\alpha = 11.72 \pm 0.04$ and $A = 0.57 \pm 0.01$. In all cases the interference fringes which result from the phase relationship of the quantum superposition are clearly visible.

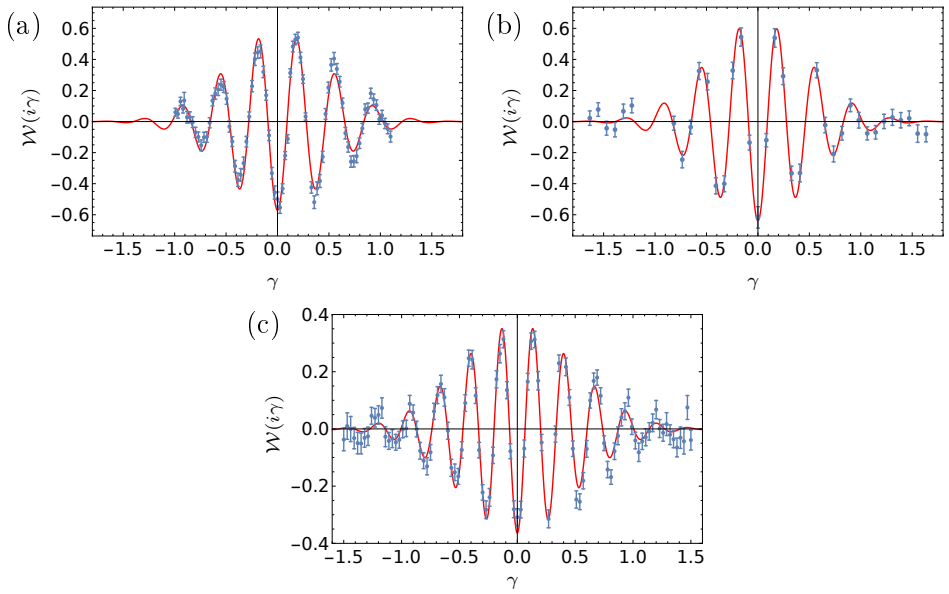

Figure 6.6: Extraction of Wigner function oscillations of cat states along the imaginary axis in phase space. (a) Cat with $\alpha = 8.5$ extracted using displaced bases. (b) Reconstruction for the same $\alpha \simeq 8.5$ performed using additional squeezing $r = 0.5$ of the basis . (c) Similar extraction for a cat with $\alpha \simeq 11.8$ performed using the squeezing amount $r = 0.8$. In (a)-(c), the red lines show fits to the form given in equation 6.10. Errors bars are given as s.e.m.. The $\mathrm{Im}(\gamma)$ axis is extracted from periodic calibration scans, and we observe drifts in the scaling at the 20% level over a day, resulting in some uncertainty in the values of $\mathrm{Im}(\gamma)$ due to drifts between calibrations.

6.5 Discussion and outlook

6.5.1 Efficient reconstruction

Usage of the transformed bases has allowed for extraction of the parity of large cat state as well as improved Wigner function tomography. The latter method requires measuring the full time evolution of internal state populations in order to extract one Wigner function point. This makes the method rather time-consuming. An extension of the work presented in this chapter would be to find and test more efficient ways to characterize the oscillator state.

Methods for efficient reconstruction of the oscillator density matrix in the energy eigenbasis basis instead of extracting the Wigner function have been considered previously [29]. These schemes are also based on shifting the oscillator state and subsequently extracting the Fock state populations. Using the transformed bases in the extraction process would again render the shift of the state obsolete. Instead of extracting the Wigner function the aim is to find the density matrix elements from sufficiently many measurement traces of different oscillator shifts. Which shifts and the minimal number required to estimate the density matrix elements faithfully is explored theoretically in [29, 167].

Reconstruction of the Husimi $\mathcal{Q}$ function is also possible using fewer fluorescence detections and has been explored previously [168]. The $\mathcal{Q}$ function can be expressed in terms of only the zero population in the corresponding displaced Fock basis: $\mathcal{Q}(\beta) = |\langle\beta|\psi\rangle|^2/\pi = \wp(n_\beta = 0)/\pi$. In order to readout the $\mathcal{Q}$ function the state is first displaced by $-\beta$ and then a blue sideband adiabatic passage can be used in order to flip the internal state conditional on starting in any of the Fock states except $|n = 0\rangle$ [169]. Fluorescence readout of the internal states then provides the desired population. Alternatively we can just use our collapse and revival traces in the coherent basis and treat all frequency components larger than $n_\beta > 0$ as noise. Using the appropriate sideband we can convert the zero population to a DC offset. This can be measured by randomly sampling time points t_i, which will average down

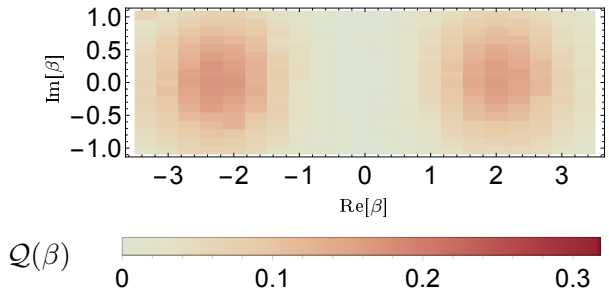

Figure 6.7: Reconstructed $\mathcal{Q}$ function for a cat with $\alpha \simeq 4$ using the measurements of the Wigner function reconstruction in figure 6.5

the non-zero frequency components. More sophisticated sampling might be employed to average down the higher frequency components more efficiently.

The Wigner function reconstruction shown in figure 6.5 required extraction of all relevant displaced Fock state populations. Extracting just the zero order component of these measurements provides a measure of the $\mathcal{Q}$ function which is shown in figure 6.7. This reconstruction closely follows the expectation for the $\mathcal{Q}$ function, see section 2.5. Shown are the two Gaussians at the locations of the wave packets but in contrast to the Wigner function there are no ripples close to the origin. The reconstruction for a mixed cat state would look identical, thus the $\mathcal{Q}$ function is not well suited for studying the stable phase relation in superposition states.

In the last chapter of this thesis we will describe a simple direct phase space reconstruction based on measuring the characteristic function of the states. We use this method to reconstruct states with isotropic extent in phase space. For such states using the squeezed basis leads to no advantage. We postpone further discussion of various reconstruction methods to chapter 9 where the novel method is compared to the transformed basis methods of the present chapter.

6.5.2 Mesoscopic cat states

The presented analysis tools allow for the verification of highly-non classical oscillator characteristics, where we gained an advantage over previous methods by using appropriate reconstruction basis. This is in some sense analogous to purely theoretical quantum optics calculations, where the right basis choice often simplifies a derivation considerably. This advantage allowed for the observation of large cat states where wave packets were separated by more than the diffraction limit of $\lambda/2 = 199$ nm of the fluorescence light from the ion. This could in principle allow to resolve fluorescence from the two different "locations" with an optical microscope.

The in-situ verification of such well separated superpositions allows for studying quantum features in the mesoscopic regime. The detailed understanding of how these features are lost as the size of the cat increases is interesting on one hand from an engineering point of view which has the goal of controlling larger and larger quantum mechanical states, but also from a fundamental perspective. Is it possible to put a truly macroscopic system into a quantum superposition and how can we verify this superposition beyond all doubt? These are the topics of the next chapter where we use our mesoscopic mechanical oscillator states in order to implement protocols devised for unambiguously confirming quantum superposition states.

Chapter 7

Sequential modular measurements

In quantum mechanics, measurements can show "spooky" correlations and often the measurement of one quantity influences a subsequent measurement of a different quantity. In this chapter we analyze such effects using sequences of periodic oscillator measurements. Heisenberg's uncertainty principle limits the ability to perform simultaneous position and momentum measurements [170–172]. However this is different for measurements of periodic position and momentum, which can commute. In a first set of experiments we test observable commutation of periodic position and momentum, from where we move on to using the sequential measurements to explore the quantum-classical transition. For the latter we consider two different quantum witnesses. The first is based on measurement disturbances, while for the second we use correlations between the sequential measurements. In particular we violate the Leggett-Garg inequality [51]. The results presented in this chapter are published in [113].

7.1 Modular measurement

The quantum mechanical state of a particle is restricted to fulfill the Heisenberg uncertainty principle discussed in section 2.3. The principle is also often used to describe restrictions onto the accuracies in simultaneous measurements. But due to quantum measurement back-action the relation in terms of measurements is more subtle [170, 171]. In order to gain a clearer understanding, indirect measurements, in which the system is first coupled to a well controlled meter, need to be used. In section 1.4.1 we discussed such an indirect measurement scheme in the context of error correction. Now we replace the system of interest by the ion motional oscillator. Using a sequence of two such measurements in order to represent a simultaneous measurement [173], allows one to precisely calculate the back-action when multiple variables are extracted. The back-action in this case is given by the change of the system state from $|\psi_{\text{in}}\rangle$ to $|\psi_{\pm 1}\rangle$, where $|\psi_{\pm 1}\rangle$ serves as the new input state for the second experiment in the sequence.

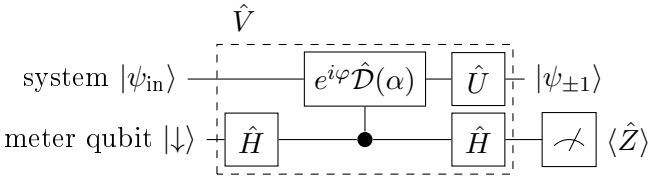

Figure 7.1: Modular measurement circuit. The oscillator system is coupled to the meter qubit with the total unitary $\hat{V}$. $\hat{V}$ consists out of two $\hat{H}$ Hadamard operations together with a meter qubit dependent shift and phase $e^{i\varphi}\hat{\mathcal{D}}(\alpha)$ and a general oscillator unitary $\hat{U}$.

Figure 7.1 shows such a measurement, where we inserted a system-meter coupling $\hat{V}$ given by meter-controlled oscillator shifts. Additionally we added the final unitary operation $\hat{U}$. In this case the measurement operators read $\hat{E}_{\pm} = \hat{U}(e^{i\varphi}\hat{\mathcal{D}}(\alpha) \pm \mathbb{1})/2$. The extracted information does not depend on the unitary transformation $\hat{U}$, although this does affect the state of the system after the measurement. The stabilizer considered in figure 1.2 had eigenvalues ± 1. In contrast, the shift operator $\hat{\mathcal{D}}(\alpha)$ has a continuous eigenvalue spectrum. The readout of the meter qubit only provides one bit of information, which is clearly insufficient for readout of the continuous eigenvalue. Likewise the measurement operators are no longer projection operators. For readout of the continuous eigenvalue and projection of the oscillator into the corresponding eigenspace, phase-estimation schemes need to be used. To do so, multiple rounds of measurements are required. Each round provides more accurate information about the continuous eigenvalue and increases the overlap of the oscillator state with the corresponding eigenspace [174].

The measurement observable of the circuit shown in figure 7.1 is given by:

$$\hat{O}(\varphi, \alpha) = \cos(\varphi + 2\text{Im}(\alpha)\hat{q} - 2\text{Re}(\alpha)\hat{p}) \tag{7.1}$$

$$= [e^{-i\varphi}\hat{\mathcal{D}}(\alpha)^{\dagger} + e^{i\varphi}\hat{\mathcal{D}}(\alpha)]/2, \tag{7.2}$$

which is connected to the characteristic function χ of the state $|\psi_{\text{in}}\rangle$ via:

$$\langle\hat{O}(\varphi, \alpha)\rangle = [e^{-i\varphi}\chi^*(\alpha) + e^{i\varphi}\chi(\alpha)]/2. \tag{7.3}$$

Measurements of the characteristic function based on this circuit are explored in chapter 9. The observable $\hat{O}$ is a periodic function of the position and the momentum operator. Such periodic variables are called modular position and momentum. These were first discussed in the context of the seminal Aharonov-Bohm effect [175] and provide new perspectives in the study of fundamental aspects of quantum mechanics [176, 177], which we will explore in the following.

7.1.1 Implementations of single measurements

In this chapter we will use two different implementations of the modular variable measurement, which are shown in figure 7.2. These circuits relate directly to the experimental pulse sequences since each circuit element is implemented by one experimental control pulse. The key ingredient in both implementations is provided by the SDF coupling, inducing internal qubit controlled shifts of the oscillator.

Symmetric implementation

A coupling just given by an SDF pulse together with the fluorescence readout can be used to implements the modular measurement with $\hat{U} = \hat{\mathcal{D}}(-\alpha/2)$ and $\varphi = 0$. In this case $\hat{E}_{\pm} = [\hat{\mathcal{D}}(\alpha/2) \pm \hat{\mathcal{D}}(-\alpha/2)]/2$. In case of a bright detection result the experiment differs from the ideal scenario. The post-measurement state in this case is decohered, due to the fluorescence photon scattering. In order to realize both post-measurement states a π-pulse can be included prior to the fluorescence readout, which interchanges the correspondence of internal qubit states to logical results. This sequence of operations has already been used in the previous chapter. There it was applied to the ground state cooled oscillator and conditional on the measurement result a cat state was prepared. In general the oscillator state after such a measurement consists of the superposition of two symmetrically displaced copies of the input state with a relative sign dependent on the measurement result. In order to gain control over the phase φ and also to be able to prepare asymmetric superpositions (i.e one wave packet has a larger separation from the origin than the other), we use additional control pulses on the internal states as well as on the oscillator.

Asymmetric implementation

One way of extending the control is to use the third internal energy state level $|a\rangle \equiv \left|D_{5/2}, m_j = -1/2\right\rangle$. In this case the measurement circuit is implemented with the sequence of operations shown in figure 7.2 (b) and given by (read right to left) $\hat{R}_2(\phi)\hat{R}_1(\pi/2)\hat{\mathcal{D}}(\alpha(t)\hat{X}_1)\hat{R}_1(-\pi/2)\hat{R}_2(0)$. Here $\hat{R}_k(\phi) = \hat{R}(\pi/2, \phi)$ are carrier $\pi/2$-pulses acting on $\{|\downarrow\rangle, |\uparrow\rangle\}$ basis for $k = 1$ and $\{|a\rangle, |\downarrow\rangle\}$ basis for $k = 2$, while the Pauli matrices $\hat{X}_1$ acts on the $k = 1$ transition.

If the pulse sequence is applied to an ion initially in the $|\downarrow\rangle$ level, then the first pulse puts half the population in the $|a\rangle$ state. This part of the population is then not affected by the following block of operations SDFz $\equiv \hat{\mathcal{D}}(\alpha(t)\hat{Z}_1) = \hat{R}_1(\pi/2)\hat{\mathcal{D}}(\alpha(t)\hat{X}_1)\hat{R}_1(-\pi/2)$ which acts on transition $k = 1$. In this block the two rotations around the SDF pulse effectively rotate the state-dependence from $\hat{X}_1$ to $\hat{Z}_1$. The final $\hat{R}_2(\phi)$ pulse then creates the state $-e^{-i\phi}|\downarrow\rangle \left|\psi_{(-,\phi)}\right\rangle + |a\rangle \left|\psi_{(+,\phi)}\right\rangle$ with $\left|\psi_{(\pm,\phi)}\right\rangle = (\mathbb{1} \pm e^{i\phi}\hat{\mathcal{D}}(\alpha))\,|\psi_{\text{in}}\rangle$.

This realizes the modular measurement given in figure 7.1 with $\hat{U} = \mathbb{1}$, $\varphi = \phi + \pi$. The computational basis prior to fluorescence detection is swapped

in this implementation by changing the last pulse phase $R_2(\phi)$ to $R_2(\phi + \pi)$ instead of adding an additional π-pulse. This implementation is used for the violation of the Leggett-Garg inequality as described in section 7.6, which requires control over the phase φ and a certain level of asymmetry in the displacement [67].

The symmetric implementation, besides its simpler pulse sequence, has several further advantages: The transition $k = 1$ has ≈ 6 times more laser power available and half the magnetic field sensitivity compared to relevant qubit in the asymmetric implementation given by transition $k = 2$. Therefore whenever possible we use the symmetric implementation. In chapter 8 we will use a simplified implementation of the asymmetric measurement, which avoids use of transition $k = 2$ but requires shifts based on tickling pulses.

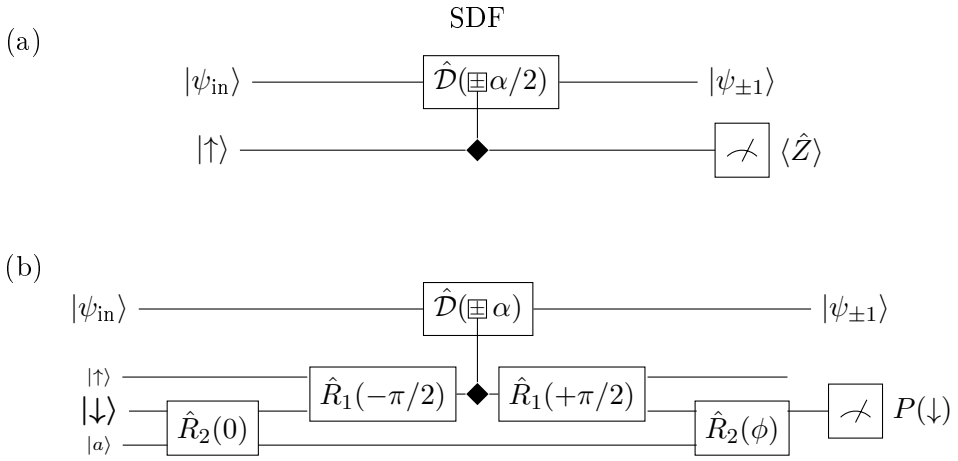

Figure 7.2: Different implementations of the modular measurement. In these circuits each element is realized by one control pulse. The internal state controlled shifts are implemented using the SDF pulse, which realizes the transformation $|+\rangle|\psi_{\text{in}}\rangle \to |+\rangle\hat{\mathcal{D}}(\alpha/2)|\psi_{\text{in}}\rangle$, $|-\rangle|\psi_{\text{in}}\rangle \to |-\rangle\hat{\mathcal{D}}(-\alpha/2)|\psi_{\text{in}}\rangle$. The diamond symbol is used in order to represent the control in the $\hat{X}$ basis. (a) Symmetric implementation, which is the simplest and experimental most robust implementation and realizes the modular measurement with $\hat{U} = \hat{\mathcal{D}}(-\alpha/2)$ and $\varphi = \pi$. (b) Asymmetric implementation based on using three internal levels, initialized to $|\downarrow\rangle$. The latter is highlighted by the larger label. Here the lines represent the individual levels instead of the full qubit. $\hat{R}_k(\phi) = \hat{R}(\pi/2, \phi)$ are carrier $\pi/2$ pulses acting on $\{|\downarrow\rangle, |\uparrow\rangle\}$ basis for $k = 1$ and $\{|a\rangle, |\downarrow\rangle\}$ basis for $k = 2$, while the SDF addresses basis $k = 1$. Shown is the sequence of operations (read right to left) $\hat{R}_2(\phi)\hat{R}_1(\pi/2)\hat{\mathcal{D}}(\alpha(t)\hat{X}_1)\hat{R}_1(-\pi/2)\hat{R}_2(0)$. The full circuit realizes the modular measurement with $\hat{U} = \mathbb{1}$ and $\varphi = \phi + \pi$.

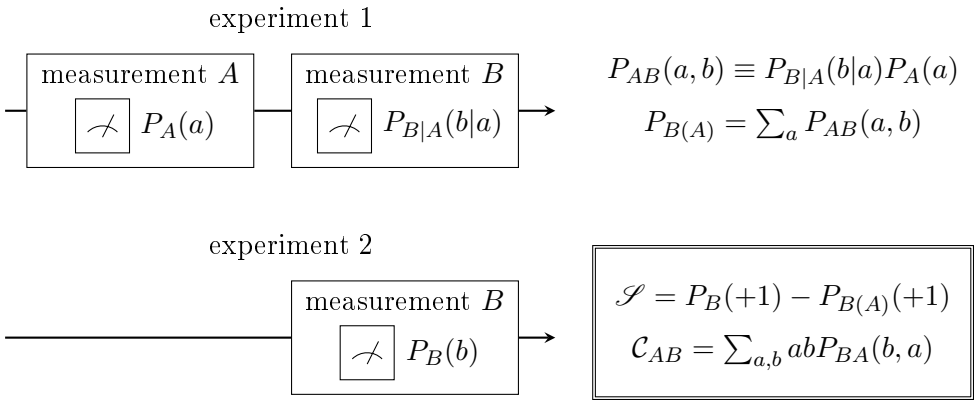

Figure 7.3: Statistical relations in a sequential measurement. Two experiments are performed to find out whether measurement A affects the result of measurement B or not. In the first experiment B is performed after A, while in a second experiment B is measured alone. The measured probabilities are then $P_A(a)$, $P_B(b)$ for measurements of A,B directly on the input states. For the measurement of B after A we find the conditional probability $P_{B|A}(b|a)$. From these probabilities we calculate the joint probability $P_{AB}(a,b)$ and the marginal distribution $P_{B(A)}(B)$. The statistics of the results can be related using correlations $\mathcal{C}$ as well as SIT captured by the parameter $\mathscr{S}$.

7.2 Sequential measurements

We next look to examine causation and correlation in sequences of modular measurements. To do so a sequence of two modular variable measurements A, B is considered. The post-measurement state of A serves as the input state for the following measurement B. The measurement outcomes are labeled $a, b \in \{+1, -1\}$ and figure 7.3 shows a schematic of the measurement sequence alongside measurement probabilities and derived quantities. The statistics of measurements A and B can be related to each other in two ways. On one hand, their results can be correlated, on the other hand, we can ask how much the statistics of the second measurement is influenced by the presence of the first measurement. The latter has previously been defined as signaling in time (SIT) [52, 53]. To measure SIT experimentally we perform measurement B either alone or subsequent to a measurement of A. Measuring A we obtain the probability $P_A(a)$, while the measurement of B after measuring A follows the conditional probability $P_{B|A}(b|a)$. From these two measurements we can find the joint probability distribution as $P_{BA}(b,a) \equiv P_A(a)P_{B|A}(b|a)$. Calculating the marginal of $P_{BA}(b,a)$ yields the probability distribution for the measurement B: $P_{B(A)}(b) \equiv \sum_a P_{BA}(b,a)$. Here the (A) in the subscript reminds us that this measurement B probability distribution is measured

following the measurement of A. This result is compared to the measurement of B alone, which yields $P_B(b)$. For the binary modular measurements the disturbance of measurement B due to the presence of measurement A is captured by the SIT parameter $\mathscr{S}$ defined as:

$$\mathscr{S} = P_B(b=+1) - P_{B(A)}(b=+1). \tag{7.4}$$

The correlator in contrast can be found from the sequence of measurements (experiment 1) alone as:

$$\mathcal{C}_{AB} = \sum_{a,b} abP_{BA}(b,a) = P(a=b) - P(a\neq b). \tag{7.5}$$

Note that extraction of all measurement probabilities requires two repetitions of experiment 1. In case of a bright detection result of measurement A, we abort the sequential measurement and restart the experimental sequence. The decision is done in real-time using an FPGA. Thus the first run is only able to measure $P_{B|A}(b|a=+1)$. We repeat experiment 1 with the additional π-pulse in order to extract $P_{B|A}(b|a=-1)$.

7.3 Signaling in time

Due to its simplicity, we use the symmetric modular variable measurement to analyze SIT. In this case the measurement settings are α_A, α_B, which control the internal state dependent shifts $\hat{\mathcal{D}}(\pm\alpha_i/2)$ and the $\mathscr{S}$ parameter reads (derivation in App. E.2):

$$\mathscr{S} = \frac{1}{2}\left(1-\cos(\Phi)\right)|\chi_{\alpha_B}|\cos(\arg[\chi_{\alpha_B}]). \tag{7.6}$$

Here $\chi_{\alpha_B} = \chi(\alpha_B) \equiv \langle\psi_{\text{in}}|\,\hat{\mathcal{D}}(\alpha_B)\,|\psi_{\text{in}}\rangle$ is the characteristic function of the input oscillator state $|\psi_{\text{in}}\rangle$. $\Phi = \text{Im}(\alpha_A^*\alpha_B)$ is the geometric phase which arises from the non-commutation of the displacement operators. If for some settings the statistics of measurement B do not depend on the presence of measurement A i.e. $\mathscr{S}=0$ then we say measurement A is non signaling in time (NSIT) to measurement B. From this expression we see that SIT will not occur for any state if either the geometric phase $\Phi = 2\pi k$, $k\in\mathbb{Z}$, or if the wave packet overlap: $|\chi_{\alpha_B}| = 0$. We analyze these dependencies in two experiments.

Wave packet overlap

We examine the effect of wave packet overlap using squeezed vacuum states $|\psi_{\text{in}}\rangle = \hat{\mathcal{S}}(\xi = re^{i\vartheta})\,|0\rangle$ with phase $\vartheta = 0$. Variation of r allows to control the extent of the oscillator state in phase space, which in turn affects the wave packet overlap. The squeezed states can be readily prepared using reservoir engineering [112]. We choose the measurement displacement

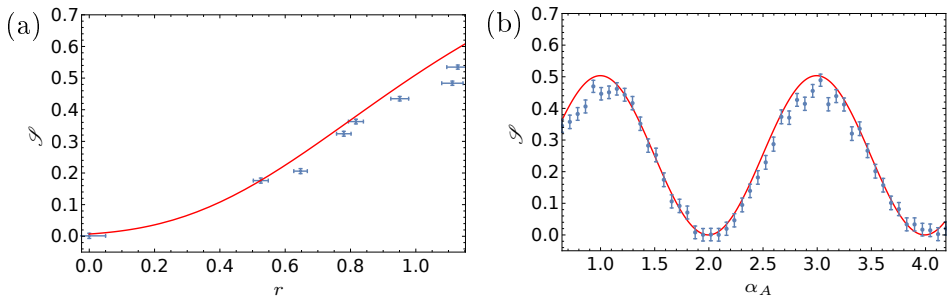

Figure 7.4: Dependence of SIT on (a) interference and (b) geometrical phases. Solid lines show the expectations for an ideal experimental system and the error bars of $\mathscr{S}$ are propagated from the shot noise standard error of the mean (s.e.m.) of the directly measured probabilities $P_B(b), P_A(a)$ and $P_{B|A}(b|a)$. (a) The SIT measurement settings $\alpha_B = 3.1i$, $\alpha_A = 3.02 \approx 3\pi/|\alpha_B|$ are applied to squeezed input states $\hat{\mathcal{S}}(r)\,|0\rangle$ where the squeezed axis is aligned with position. (b) The geometric phase is varied by sweeping the displacement amplitude α_A of measurement A, for a "Schrödinger's cat" input superposition $[\hat{\mathcal{D}}(-\alpha_B/2) + \hat{\mathcal{D}}(\alpha_B/2)]\,|0\rangle$ with $\alpha_B = i\pi$.

$\alpha_B = i|\alpha_B| = 3.1i$, which is aligned with the anti-squeezed axis of the squeezed input state. The wave packet interference in this case is given by $\chi_{\alpha_B} = e^{-|\alpha_B|^2 e^{-2r}/2}$ [37]. We choose $\alpha_A = 3.02 \approx 3\pi/|\alpha_B|$ to ensure that for a given overlap maximal SIT is observed. Experimental results are shown in figure 7.4 (a). For increased values of r the overlap χ_{α_B} increases, which causes higher amounts of SIT. The measurements agree with this ideal theoretical expectation. Deviations for large r are primarily due to imperfect squeezed state preparation.

Geometric phase

The input state $|\psi_{\text{in}}\rangle \propto [\hat{\mathcal{D}}(-\alpha_B/2) + \hat{\mathcal{D}}(\alpha_B/2)]\,|0\rangle$ exhibits a constant non-zero level of wave packet overlap $|\chi_{\alpha_B}| \approx 1/2$. Thus we use this state to illustrate the dependence of SIT on the geometric phase. This is done by varying α_A which is taken to be real. Data is shown in figure 7.4 (b) showing oscillations of $\mathscr{S}$ with amplitude $|\chi_{\alpha_B}|$. These oscillations illustrate the periodic effect of the geometric phase. NSIT is seen for this measurement when $\alpha_A = 2\pi k/|\alpha_B| \approx 2k$.

7.4 Commutation of modular variables

One of the fundamental notions of quantum mechanics is that position and momentum operators do not commute. However this is different for measurements of position and momentum modulo a characteristic length/momentum scale (i.e. $\hat{q}_r \bmod l_q$, $\hat{p}_r \bmod l_p$). These periodic variables are closely related to the periodic modular position and momentum observables $\cos(2l'_q\hat{q})$, $\cos(2l'_p\hat{q})$ with $l'_q, l'_p \in \mathbb{R}$ [178], which are studied in the current chapter. Dependent on their periodicities l'_q, l'_p these variables can either commute or anti-commute, which is in one to one relation with the commutation relations of the corresponding shift operators. The topic of this section is to experimentally verify the possibility of commutation of modular position and momentum. First we formalize a sufficient condition on the Kraus operators, in order to observe NSIT and further connect observable commutation to NSIT measurements. Using these relations we experimentally test for deviations from observable commutations.

7.4.1 Non signaling in time and observable commutation

If the order of measurements A, B does not matter, then for projective measurements, their observables commute. For the generalized measurements considered in this work this no longer holds. Still, there exists a general relation between Kraus operators and NSIT: $\langle[\hat{E}_a^A, \hat{E}_b^{\dagger B}\hat{E}_b^B]\rangle = 0 \Rightarrow$ NSIT. Here the bracket $\langle\hat{O}\rangle = \mathrm{Tr}\{\hat{O}\hat{\rho}_i\}$ relates to the expectation of the operator for a given input state $\hat{\rho}_i$. The relation between NSIT and Kraus operators is derived in the following:

$$\begin{aligned} P_{B(A)}(b) &= \sum_a P_{BA}(b,a) \\ &= \sum_a \mathrm{Tr}\left\{\hat{E}_a^{\dagger A}\hat{E}_b^{\dagger B}\hat{E}_b^B\hat{E}_a^A\hat{\rho}_i\right\}. \end{aligned} \tag{7.7}$$

Using $\langle[\hat{E}_a^A, \hat{E}_b^{\dagger B}\hat{E}_b^B]\rangle = 0$ this translates into

$$\begin{aligned} P_{B(A)}(b) &= \sum_a \mathrm{Tr}\left\{\hat{E}_a^{\dagger A}\hat{E}_a^A\hat{E}_b^{\dagger B}\hat{E}_b^B\hat{\rho}_i\right\} \\ &= \mathrm{Tr}\left\{\sum_a \hat{E}_a^{\dagger A}\hat{E}_a^A\hat{E}_b^{\dagger B}\hat{E}_b^B\hat{\rho}_i\right\} \\ &= \mathrm{Tr}\left\{\hat{E}_b^{\dagger B}\hat{E}_b^B\hat{\rho}_i\right\} \\ &= P_B(b). \end{aligned} \tag{7.8}$$

Calculation of the commutator $[\hat{E}_A^a, \hat{E}_B^{\dagger b}\hat{E}_B^b]$ for the symmetric and asymmetric implementations as well as the commutator of the modular observables $[\hat{O}_A, \hat{O}_B]$ leads to the conditions for NSIT or commutation of the observables

given bellow. Here α_A, α_B are the modular measurement A and B parameters:

$$\begin{aligned} &\text{Sym. :} && \mathrm{Im}(\alpha_B\alpha_A^*) = 2\pi k_1, && k_1 \in \mathbb{Z} \Rightarrow \text{NSIT} \\ &\text{Asym :} && \mathrm{Im}(\alpha_B\alpha_A^*) = \pi k_2, && k_2 \in \mathbb{Z} \Rightarrow \text{NSIT} \\ &[\hat{O}_A, \hat{O}_B] : && \mathrm{Im}(\alpha_B\alpha_A^*) = \pi k_3, && k_3 \in \mathbb{Z} \Rightarrow [\hat{O}_A, \hat{O}_B] = 0 \end{aligned} \tag{7.9}$$

Therefore if α_A, α_B are chosen such that $\mathrm{Im}(\alpha_B\alpha_A^*)$ is given by an odd multiple of π then the measurements observables commute and the asymmetric implementation is NSIT but the symmetric implementation is signaling in time. This is a general case for which the observables commute but the sequential measurements are SIT.

Note that NSIT $\not\Rightarrow \langle[\hat{E}_a^A, \hat{E}_b^{\dagger B}\hat{E}_b^B]\rangle = 0$. For states exhibiting no wave packet interference $\chi_{\alpha_B} = 0 \Rightarrow \mathscr{S} = 0$ independent of the setting α_A and thus independent of $\langle[\hat{E}_a^A, \hat{E}_b^{\dagger B}\hat{E}_b^B]\rangle$. In case of the symmetric measurements this can be seen from formula 7.6. In order to draw conclusions from NSIT measurements about the commutation of Kraus operators, we need to consider all possible oscillator states. In this case we can be certain to include states for which $\chi_{\alpha_B} \neq 0$. Expressed mathematically this reads:

$$\text{NSIT}, \forall\hat{\rho}_i, a, b \Rightarrow [\hat{E}_a^A, \hat{E}_b^{\dagger B}\hat{E}_b^B] = 0, \forall a, b \tag{7.10}$$

$$\Rightarrow [\hat{E}_a^{\dagger A}, \hat{E}_b^{\dagger B}\hat{E}_b^B] = 0, \forall a, b. \tag{7.11}$$

The second conclusion is given by Hermitian conjugate of the first line. Reshuffling of the Kraus operators shows, that in the case of NSIT for all possible input states, the underlying observables commute. To do so we first multiply equation 7.10 with $\hat{E}_a^{\dagger A}$ and then insert equation 7.11:

$$\Rightarrow \hat{E}_a^{\dagger A}[\hat{E}_a^A, \hat{E}_b^{\dagger B}\hat{E}_b^B] = 0, \forall a, b \tag{7.12}$$

$$\Rightarrow \hat{E}_a^{\dagger A}\hat{E}_a^A\hat{E}_b^{\dagger B}\hat{E}_b^B - \hat{E}_a^{\dagger A}\hat{E}_b^{\dagger B}\hat{E}_b^B\hat{E}_a^A = 0, \forall a, b \tag{7.13}$$

$$\Rightarrow \hat{E}_a^{\dagger A}\hat{E}_a^A\hat{E}_b^{\dagger B}\hat{E}_b^B - \hat{E}_b^{\dagger B}\hat{E}_b^B\hat{E}_a^{\dagger A}\hat{E}_a^A = 0, \forall a, b \tag{7.14}$$

$$\Rightarrow [\hat{E}_a^{\dagger A}\hat{E}_a^A, \hat{E}_b^{\dagger B}\hat{E}_b^B] = 0, \forall a, b \tag{7.15}$$

$$\Rightarrow [\hat{O}^A, \hat{O}^B] = 0 \tag{7.16}$$

7.4.2 Measurement results

From the above it follows that, if we test NSIT for all input states, we can verify commutation of the underlying observables. This is impossible to verify in practice given the infinite nature of the harmonic oscillator Hilbert space. As a reduced investigation, we examine this property using 150 input states of the form:

$$|\psi_{\text{in}}\rangle \propto [\hat{\mathcal{D}}(-|\alpha_B|e^{i\phi_I}/2) + \hat{\mathcal{D}}(|\alpha_B|e^{i\phi_I}/2)]\,|\phi\rangle\,, \tag{7.17}$$

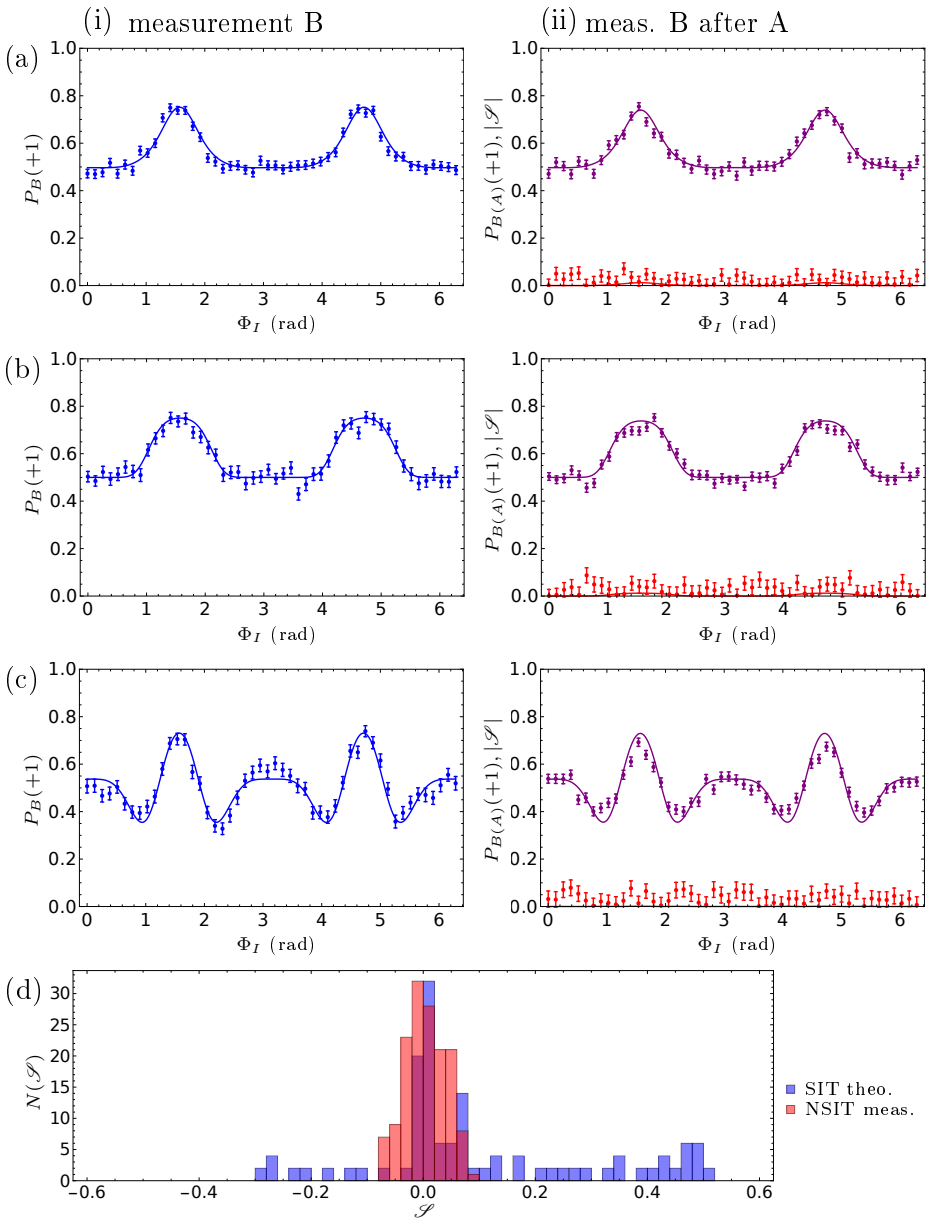

Figure 7.5: NSIT of modular position and momentum measurements for a variety of input states. Rows (a)-(c) show NSIT of A to B for the measurement settings $\alpha_B = i\pi$, $\alpha_A = 4.09 \approx 4\pi/|\alpha_B|$, and input superposition states $[\hat{\mathcal{D}}(-|\alpha_B|e^{i\phi_I}/2) + \hat{\mathcal{D}}(|\alpha_B|e^{i\phi_I}/2)]\,|\phi\rangle$ with the phase ϕ_I varied. $|\phi\rangle$ is chosen to be (a): the ground state $|0\rangle$, (b): a squeezed vacuum state $\hat{\mathcal{S}}(-0.82)\,|0\rangle$ or (c): the first excited state $|1\rangle$. We observe qualitative agreement between column (i), showing measurement of B alone and column (ii) showing B measured after A. Solid lines show the expectations for an ideal experiment, which are identical in both column s. Errors are given as s.e.m. and propagation of s.e.m.. The 150 measured $\mathscr{S}$ values are quantified in red in histogram (d) and compared to a theoretical histogram for the SIT settings $\alpha_A = 3$ and $\alpha_B = i\pi$ using the same set of input states.

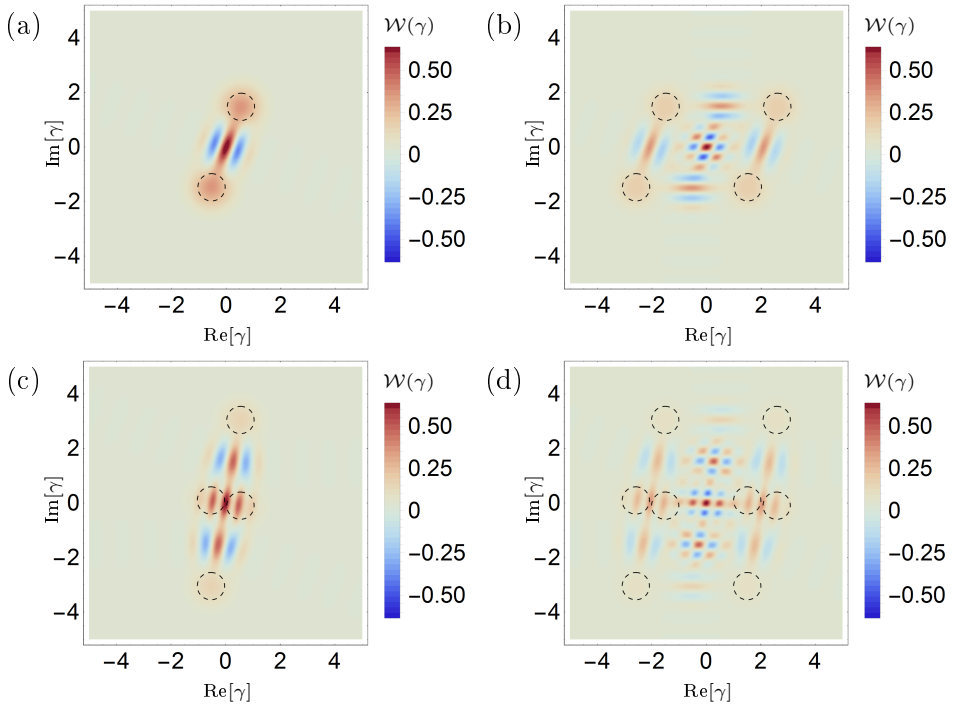

Figure 7.6: Theoretical Wigner function plots of the input state ($|\phi\rangle$=$|0\rangle$ and $\phi_I = 1.22$ rad) as well as its post-measurement states with result $+1$ during the experimental sequence. The dashed circles show the locations of the coherent state components, their radius denotes the r.m.s wave packet size. (a) Input state, (b) $+1$ post-measurement state after the measurement of A, (c) $+1$ post-measurement state after the measurement of B directly on the input state, (d) $+1$ post-measurement state of the measurement B using the state (b) as input. We clearly see how the sequential measurement prepare multi-component superpositions of the oscillator state. Measurements of NSIT mean that we cannot distinguish whether the measurement of B interferes the two-state superposition given in (a) or the four state superposition shown in (b).

where $|\phi\rangle$ is chosen to be one of (a) the ground state $|0\rangle$, (b) a squeezed state $\hat{\mathcal{S}}(-0.82)\,|0\rangle$ or (c) the first excited state $|1\rangle$, and for each $|\phi\rangle$ 50 values of ϕ_I evenly spaced between zero and 2π are used. We use the symmetric implementation and investigate the commutation of modular position and momentum for large displacements by choosing the NSIT geometric phase with $k_1 = 2$ ($\Phi \approx 4\pi$), which we implement using the measurement settings: $\alpha_B = i\pi$, $\alpha_A = 4.09$.

Data and a histogram of all measured values of $\mathscr{S}$ are shown in figure 7.5. For comparison, in histogram (d) we also plot theoretical calculations for $\alpha_B = i\pi$, $\alpha_A = 3$, resulting in $\Phi = 3\pi$ which corresponds to maximal SIT but with the same χ_{α_B} as used in the experiment. The theoretical histogram shows many values of $\mathscr{S}$ close to zero, which indicates that most of the probe states only exhibit a small value of wave packet interference χ_{α_B}. But a non-negligible amount of values show larger interference and thus higher values of $|\mathscr{S}|$. The absence of these values in the measurement results confirms that the measurement configuration was calibrated close to commutation of measurement observables. The maximal measured value of $|\mathscr{S}|$ is 0.087 ± 0.003, while the maximum calculated for the SIT settings is 0.5. Additionally, the standard deviation of the SIT theory histogram is 5.5 times larger than that of the experimentally measured NSIT distribution.

Theoretical Wigner function plots for one input state example ($|\phi\rangle$=$|0\rangle$ and $\phi_I = 1.22$ rad) sampled throughout the experimental sequence are shown in figure 7.6. The created states are superpositions of up to 8 displaced $|\phi\rangle$ states with separations of up to $\Delta\alpha \approx 8.3$. These measurements illustrate the high level of control for the implemented sequential modular measurements. The ability to tune them from SIT to (almost) NSIT demonstrates the quantum nature of the created states and additionally confirms the possibility of modular position and momentum measurements to commute. Nevertheless we see that experimentally due to limited accuracy in calibrations and projection noise measurements will never be perfectly NSIT. The latter is relevant for the discussion of quantum error correction schemes based on commutation of such observables. Such an error correction code is the topic of chapter 8.

7.5 Two-time correlator

The second means by which successive measurements can be related to one another is through the correlation function of the measurement results. The two-time correlator in the case of the symmetric modular measurements reads

$$\mathcal{C}_{AB} = \left[|\chi_{\alpha_A-\alpha_B}|\cos(\phi_-) + |\chi_{\alpha_A+\alpha_B}|\cos(\phi_+)\right]/2 \tag{7.18}$$

with $\phi_\pm = \arg[\chi_{\alpha_A\pm\alpha_B}]$ (derivation in App. E.2). This is independent of the geometric phase Φ, which was required to be non-zero in order to observe SIT.

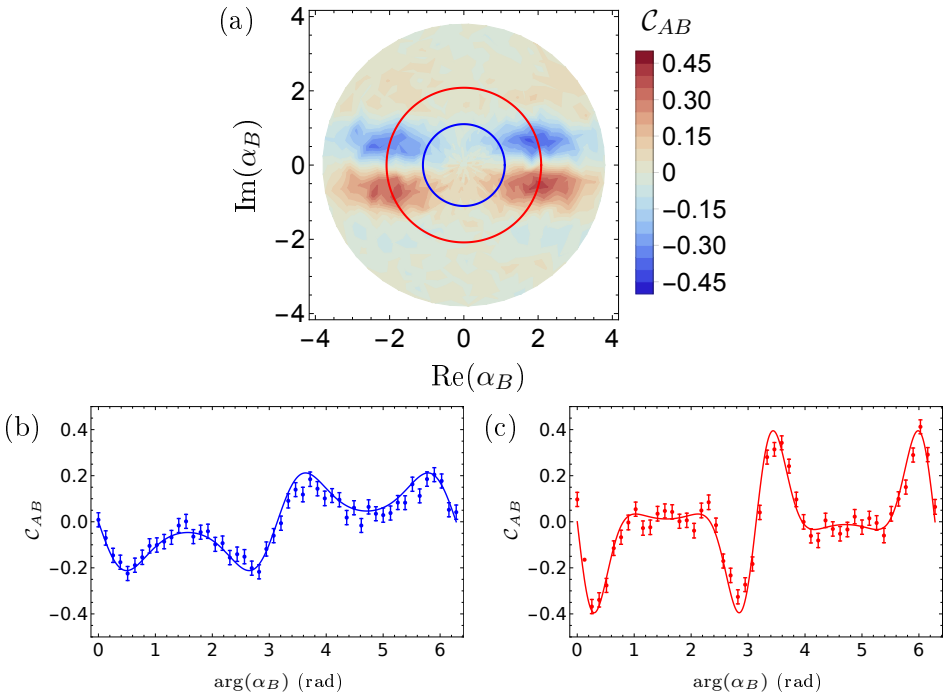

Figure 7.7: Two-time correlation measurement in the asymmetric implementation performed on an initial ground state cooled ion as a function of the second displacement α_B. The fixed experimental settings were: $\alpha_A = 2.1$, $\varphi_A = 0$, $\varphi_B = \pi/2$. The full data set is shown in the false-color plot (a). Two cuts through this data set with fixed $|\alpha_B|$ are indicated in this false-color plot and explicitly plotted in (b) $|\alpha_B| \approx 1.1$ and (c) $|\alpha_B| \approx 2.1$, where solid lines show the expectations for an ideal experiment.

In order to investigate the effect of the geometric phase on correlations we explore in the following the asymmetric modular measurement implementation (section 7.1.1) with measurement operators $\hat{F}_{\pm}(\varphi, \alpha) = \frac{1}{2}(\mathbb{1} \pm e^{i\varphi}\hat{\mathcal{D}}(\alpha))$. For this implementation we expect $\mathscr{S} = \sin(\Phi)|\chi_{\alpha_B}|\sin(\Phi + \varphi_B + \arg[(\chi_{\alpha_B}])$ and the correlation function is (App. E.2)

$$\begin{aligned} \mathcal{C}_{AB} &= \left[|\chi_{\alpha_A - \alpha_B}|\cos(\phi_-) + |\chi_{\alpha_A + \alpha_B}|\cos(\phi_+)\right]/2 \\ \phi_{\pm} &= \varphi_A \pm \varphi_B \pm \Phi + \arg[\chi_{\alpha_A \pm \alpha_B}]. \end{aligned} \tag{7.19}$$

This implementation thus reintroduces the geometric phase Φ to the correlator. The observables of the two implementations are the same but the post-measurement states differ. This changes the result of the second measurement and thus the time correlator and the signaling in time parameter $\mathscr{S}$.

A measurement of the correlation function using the asymmetric implementation as a function of α_B is shown in figure 7.7 (a), while two of the measurement traces with constant $|\alpha_B|$ building up this plot are given in (b) and (c). The experimental parameters were $\alpha_A = 2.1$, $\varphi_A = 0$, $\varphi_B = \pi/2$ and the input state was the ground state $|\psi_{\text{in}}\rangle = |0\rangle$. The correlation function then reads

$$\mathcal{C}_{AB} = -(e^{-|2.1-\alpha_B|^2/2} + e^{-|2.1+\alpha_B|^2/2}) \sin(\Phi)/2 \tag{7.20}$$

with the geometric phase $\Phi = 2.1\text{Im}(\alpha_B)$. The pre-factor is non-zero for $\alpha_B \approx \pm 2.1$. In this case wave packets overlap in the post-measurement state of B leading to interference effects during the measurement. The sign change of the correlator in this example is solely due to the geometric phase Φ. The extreme values of $\mathcal{C}_{AB}$ are reached as a compromise between the wave packet overlap and the geometric phase.

7.6 Leggett-Garg inequality violation

Correlation functions lie at the heart of many tests of the quantum nature of physical systems [51, 179, 180]. A Bell [181, 182] test for example is based on correlations between spatially separated entangled systems. For single systems measured at sequential times Leggett and Garg devised 1985 an inequality with the aim of certifying the existence of macroscopic superposition states [51]. To do so they considered a time sequence of three measurements A, B, C and considered the correlation between each pair of measurements:

$$\mathcal{L} = \mathcal{C}_{AB} + \mathcal{C}_{BC} - \mathcal{C}_{AC} \leq 1. \tag{7.21}$$

They derived the bound under two assumptions, which reflect our intuition about the macroscopic world:

1. measurements are of macroscopic quantities with pre-existing values (MR)
2. these values are unchanged by the act of measurement (NIM)

The first assumption is often referred to as macroscopic realism (MR) while the second is called the non-invasive measurement (NIM) assumption. Note the similarity to Bell's inequality, which is also about realism but in contrast combines the latter with locality [183]. Quantum mechanics violates both of the above assumptions, which has been studied previously in this thesis. Quantum system can be put into distinct superpositions of possibilities analogous to "Schrödinger's dead and alive cat", while quantum measurement back-action leads to signaling between the sequential measurements. In contrast using systems governed by classical physics allows to fulfill both assumptions.

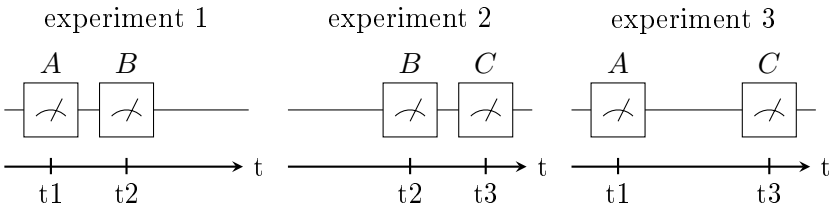

Figure 7.8: For the violation of the Leggett-Garg inequality three experiments each consisting of two of the three modular measurements A, B, C are run. We operate the experiment in the rotating frame of the oscillator, therefore time is implemented by the appropriate choice of measurement settings.

The first violation of the Leggett-Garg inequality was reported 25 years after the original proposal and used a superconducting qubit [54]. A qubit is far from being a macroscopic system, thus this violation can rather be viewed as a test of microscopic realism. A multitude of qubit based violations in a variety of systems followed [55–65], while more recently the inequality was violated using the position of an atom [66]. LGI violation implies that at least one of the two underlying assumptions has to be rejected. Therefore in order to exclude macroscopic or microscopic realism the NIM assumptions needs to be full filled. This is hard to ensure in practice [184] and led to debates among scientists [45, 185–189], while further motivated the detailed study of a variety of quantum measurement schemes [190].

In the next section we describe the experimental violation of the LGI using separated superpositions of the trapped-ion motional oscillator, while in the following we discuss the relation of our scheme to the NIM assumption.

7.6.1 Experimental results

A protocol for LGI violation using modular variable measurements of an oscillator has been proposed by A. Asadian an co-workers [67]. Their aim is to devise a feasible LGI protocol applicable to macroscopic mechanical oscillators. We implement their protocol using the motion of the single trapped-ion, which forms one of the smallest existing mechanical oscillators. Thereby realizing LGI inequality violations in a mesoscopic system exhibiting a natural cross over from the quantum to the classical regime.

In our implementation the protocol involves measuring the two-time correlations between each pair of three asymmetric modular measurements A, B, C while leaving out the third [67], see figure 7.8 for clarification. We typically operate the experiment in the rotating frame with respect to the oscillator natural evolution. This allows to implement time evolution by choosing the measurement settings appropriately. The modular displacement settings used

for the measurements are parametrized as $\alpha_A = |\alpha|e^{i\theta_A}$, $\alpha_B = |\alpha|e^{i\theta_B}$, $\alpha_C = |\alpha|e^{i\theta_C}$, with the respective angles $\theta_A = \omega t_1$, $\theta_B = \omega t_2$, $\theta_C = \omega t_3$ arranged to meet the constraints of successive measurements at times t_1, t_2, t_3. We violate the LGI as a function of $|\alpha|$ for three thermal input states with average occupations $\langle n\rangle \approx 0$, $\langle n\rangle \approx 0.23$ and $\langle n\rangle \approx 0.42$. This allows testing the robustness of the protocol with respect to finite thermal occupations, which is important to assess the applicability of the protocol to more macroscopic oscillators. For the latter ground state cooling still remains challenging [191, 192].

In order to find the measurement settings with which we violate the LGI we calculate the analytic expression for the value of $\mathcal{L}$ depending on the initial ion temperature and the displacement size $|\alpha|$ as well as the measurement settings A: (θ_1, φ_A), B: (θ_2, φ_B) C: (θ_3, φ_C). For each temperature and displacement $|\alpha|$ we maximize the analytic expression over $\theta_1, \theta_2, \theta_3$ and $\varphi_A, \varphi_B, \varphi_C$ using Mathematica. To do so, we first find a local maximum for a small displacement $\alpha = 0.2$, then we use the settings found from this analysis as an initial guess for the maximization for a slightly larger displacement $\alpha = 0.25$. Like this we find successively the settings for larger displacements. Figure 7.9 shows a raw data sample of $\mathcal{L}$ violation measurements together with the used settings.

The temperature of the oscillator is controlled by shortening the used cooling sequence. We extract the resulting $\langle n\rangle$ by reading out the Fock state populations of the oscillator and fitting them to a thermal state of the oscillator. All three correlators are measured based on an independent calibration of the SDFz sequence acting on transition 1 as described in section 5.6 and for each displacement size and temperature one additional phase calibration in order to reference the relative phase of the two $\pi/2$-pulses on transition 2 (section 7.1.1) is required. Based on this single additional calibration all three correlations are measured.

All LGI violation results are summarized and presented in figure 7.10, showing $\mathcal{L} > 1$ for displacements up to $\alpha = 3$. We notice that $\mathcal{L}$ is sensitive to noise in the experimental implementation, because it involves measuring three extremal correlations. The dashed lines in figure 7.10 show the expected violations for an ideal experiment and the solid lines show simulations including experimental imperfections. Spin decoherence limits the violation at small α, and the sharp drop in violation above $\alpha = 2$ is caused by motional dephasing. The motional dephasing is accounted for in the simulation by solving the Lindblad master equation during the SDF pulses with a dephasing operator $\sqrt{30}(\hat{a}\hat{a}^\dagger + \hat{a}^\dagger\hat{a})$ with 30 dephasing jumps/s. The linewidth of the transition 2 is known from Ramsey measurements to be $l \approx 665$ Hz FWHM[1]. The linewidth is included by averaging over 4000 randomly chosen phases φ from a normal distribution with $\sigma = \frac{l\pi t_{SDF}}{\sqrt{2\ln(2)}} + 0.087$. The last term accounts for phase calibration errors.

[1] Here the value is based on an older coherence measurement than the one presented in chapter 4.

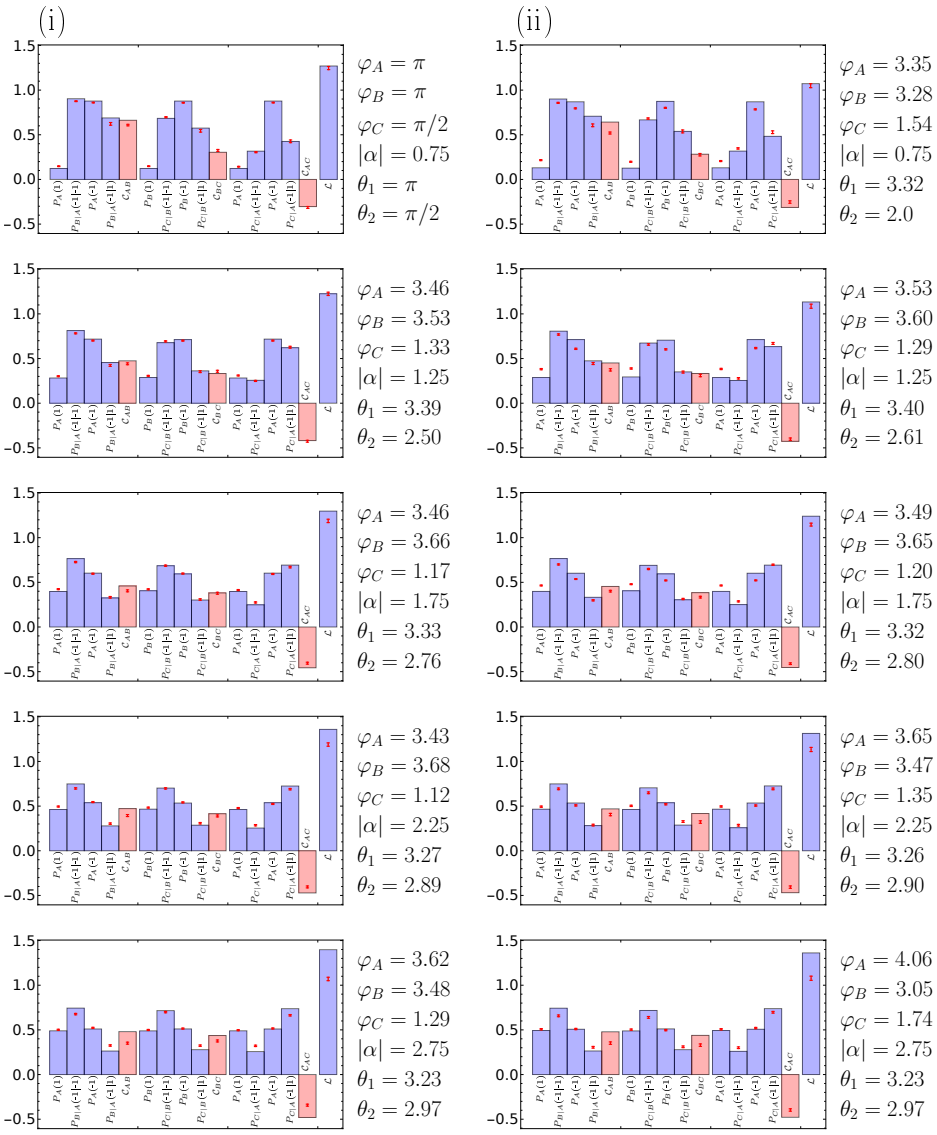

Figure 7.9: A sample of individual detection data and measurement settings for the Leggett-Garg violations presented in figure 7.10. Column (i) shows data with $\langle n \rangle \approx 0$ and column (ii) $\langle n \rangle \approx 0.23$. Data is shown as red points while the expectations for an ideal experiment are shown as bars. Blue bars are the detection data and the three red bars show the correlations calculated from these detections. We see qualitatively good agreement for smaller α which decreases for higher displacements, which is mainly due to dephasing noise in the experimental system. The settings θ_1 and θ_2 correspond to $\theta_1 = \theta_B - \theta_A$, $\theta_2 = \theta_C - \theta_B$.

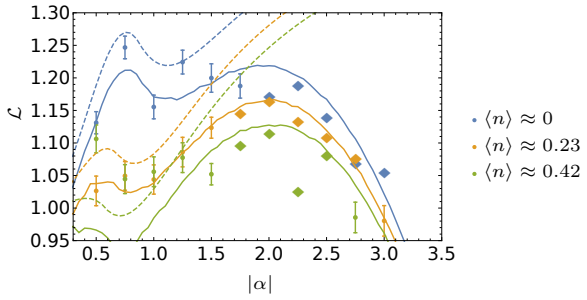

Figure 7.10: Violation of a Leggett-Garg inequality for increased modular measurement displacements $|\alpha|$ and three different initial temperatures. Solid lines show the expected violation including simulated qubit and motional dephasing as well as phase calibration errors. The dashed lines are the exceptions for an ideal experiment. Violations are observed over a wide range of α for all initial temperatures. With a ground state cooled ion violations are observed up to $\alpha = 3$. The points highlighted with a diamond violate the LGI when being corrected by the inbuilt theoretical amount of SIT, see section 7.7.4. The discrepancy between the data and the simulation at $\langle n\rangle = 0.42$ is due to additional experimental fluctuations in the preparation of this higher thermal occupation. All error bars are propagated from the s.e.m. errors due to quantum projection noise.

We experimentally violate the LGI using wave packet superpositions of the ion's motional states. For the larger displacements $|\alpha| \approx 3$ the two wave packets are separated and thus realize mesoscopic states. Do these violations now imply that we have to reject realism at the size scale of these oscillator states? To do so, we are required to fulfill the NIM assumption, which is discussed in the following sections.

7.7 Discussion and outlook

7.7.1 Definition of non-invasive measurements

A discussion of the non-invasive measurement assumption is challenging because different notions and definitions of NIM exist in the literature [190]. Two notions relevant to the implemented LGI protocol are given below.

NIM1: Non-invasive measurements as proposed by Leggett and Garg

To ensure NIM Leggett-Garg [51] considered not the quantum mechanical description of the measurement but its macroscopic version. Only for these macroscopic measurements did they discuss how to ensure non-invasivity. The

way they proposed to certify non-invasion is via so-called null measurements. In order to illustrate the concept of a null measurement, we consider a marble put in one of two boxes. By opening only one box we learn the location of the marble. If we open the box containing the marble (let's call it box one), we might reason that the measurement has been invasive. For example, the box could have been shaken during the process of opening. In case where we open the other box, which does not contain the marble, from its absence we still learn that the marble is in box one. But in contrast to the previous scenario we would be more confident that the act of measurement, which might have influenced box two, did not change anything about the marble in box one. We could gain even more confidence by using a large spatial separation of the two boxes. In this case, any information about the measurement at the second box would need a finite time to travel to the first box.

Ideal negative or null measurements are possible for quantum mechanical systems. For example the fluorescence readout of the internal states, where we only proceed to the next measurement conditional on the dark result constitutes one example of a null measurement. In this case the qubit is detected due to the absence of interaction with the fluorescence laser. Nevertheless the quantum mechanical description of this readout leads to state updated and is in this sense invasive. Thus we pretend to be ignorant about quantum theory, when we argue about NIM1 of the fluorescence readout, we simply say there is no interaction of the ion with the fluorescence laser taking place hence the measurement is non-invasive.

NIM2: non signaling in time

Instead of arguing about classical oscillators one might consider using $\mathscr{S} = 0$ as an experimentally testable definition of NIM2 also applying to quantum measurements. The use of NSIT as an experimental test of the non-invasive measurement condition has been discussed in the literature [53] and efforts have been undertaken to improve the LGI test by adding additional NSIT constraints and exploring their implications [193].

However a criticism of the NIM2 definition is that despite an observation of NSIT between A and B the measurements involve updating of the oscillator quantum state. Thus in general there are clear discrepancies between the final oscillator states dependent on whether measurement A has been performed or not. (See for example the states given in figure 7.6). This difference in post-measurement states could then in principle be detected by a latter measurement. Thus one might argue that also this novel definition is insufficient.

7.7.2 Quantum witnesses

The modular measurement consists out of both the SDF coupling together with the fluorescence readout. Thus we have to argue about NIM for both of these parts. The fluorescence readout can be viewed as an null measurement but for the SDF coupling we lack such a simple argument.

A. Asadian an co-workers [67] compared the modular measurement to its semi-classical analogue, where we keep the meter qubit description but replace the description of the oscillator using $\hat{q}$ and $\hat{p}$ operators with a classical variable. They further highlight the analogy of the modular measurement with the Ramsey measurement. The comparison is thus between a Ramsey measurement of a classical field with coupling $\hat{H} \propto |\uparrow\rangle\langle\uparrow| x(t)$ (as discussed in section 4.1) to a Ramsey measurement of a quantum field $\hat{H} \propto |\uparrow\rangle\langle\uparrow|(\hat{a}e^{i\Delta\phi/2} + \hat{a}^\dagger e^{-i\Delta\phi/2})$ as given by the modular measurement in the asymmetric implementation.

In the semi-classical measurement description the SDF laser coupling leads to a shift of the energy of the states of the meter qubit while the coupling has no back-action on the classical oscillator field state. The final readout of the internal states using only the dark detection events can be viewed as a null measurement, as discussed before. Thus in the semi-classical description neither the SDF laser nor the fluorescence readout change the classical field state. This argumentation about the non-invasivity is based on trusting the control of the experiment and does not constitute a simple argument as provided by ideal negative measurements alone.

In a sequence of two semi-classical measurements, the first measurement does not change the input classical field state and the two measurements are thus expected to be NSIT. Additionally in the supplemental material of [67] it is shown that violation of the LGI is not possible using the classical variable. Therefore both the observation of SIT or LGI violations can be used to confirm the presence of oscillator states showing quantum features [52, 53, 190], which is a weaker statement than to reject realism.

Advantage of quantum witnesses based on sequential measurements

In the following we compare the presented quantum witnesses based on the sequential measurements to measurements of quantum features in single time detections. In case of single time detections the semi-classical description would in principle allow to reproduce the measured characteristic traces as discussed in the supplemental material of [67]. Nature could thus be malicious and one could always just couple to a classical variable $x(t)$ giving rise to the observed oscillations and revivals.

Single time detections were used in previous trapped-ion experiments with superposition states (section 6, [31, 37, 38]) to confirm the creation of quantum mechanical states. In the following we discuss how nature could conspire to

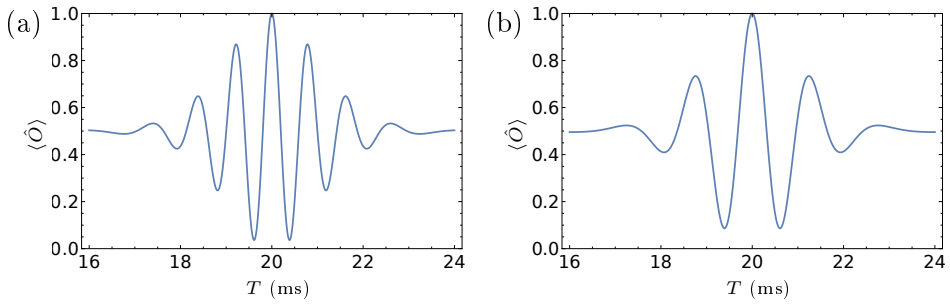

Figure 7.11: Expected results for a Ramsey measurement coupling to $x(t) = A\cos(2\pi ft)$ a classical single frequency noise source. The amplitude A of this single frequency noise fluctuates on timescales slower than an experimental shot with a Gaussian probability distribution $P(A) = \frac{1}{\sigma\sqrt{2\pi}}e^{-\frac{1}{2}(\frac{A-A_0}{\sigma})^2}$. The coupling constant is assumed to be 1: $\hat{H} = |\uparrow\rangle\langle\uparrow|x(t)$. Thus we find $\langle\hat{O}\rangle = -e^{\frac{1}{2}(\frac{\sin(2\pi fT)\sigma}{2\pi f})^2}\cos(\phi + \frac{A_0}{2\pi f}\sin(2\pi fT))$ with T given by the Ramsey wait time and ϕ the second Ramsey pulse phase. Shown are 2 different amplitudes A_0: (a) $A_0 = 8000$, (b) $A_0 = 5000$ of the noise with the noise frequency fixed to 50 Hz, $\sigma = 1000$, $\phi = 0$. The oscillations resemble characteristic traces of "Schrödinger cat" states, such as those found in [31].

reproduce the characteristic traces of these experiments.

A classical field $x(t)$ containing dominant frequency components leads to a variety of oscillations and revivals in the qubit probabilities. As an illustration of this we consider a simple example: $x(t) = A\cos(2\pi ft)$, which is given by a single frequency component f with a fluctuating amplitude A. The amplitude fluctuates on slow timescales compared to a single experimental shot and its probability distribution is given by the Gaussian $P(A) = \frac{1}{\sigma\sqrt{2\pi}}e^{-\frac{1}{2}(\frac{A-A_0}{\sigma})^2}$. Let us further assume that the experiment is synchronized with respect to the noise frequency (an example of such a noise source would be noise due to the mains lines measured in a line triggered experiment). For such a periodic noise source we find $\langle\hat{O}\rangle = -e^{\frac{1}{2}(\frac{\sin(2\pi fT)\sigma}{2\pi f})^2}\cos(\phi+\frac{A_0}{2\pi f}\sin(2\pi fT))$ where T is given by the Ramsey interaction time and ϕ is the phase of the second Ramsey pulse. $\langle\hat{O}\rangle$ is plotted in figure 7.11, where we can see that it exhibits very similar oscillations to those observed in experiments like [31]. Single measurements thus have a hard time proving that the experiments actually create Schrödinger cat like superpositions. However we note that the "conspiracy" theory is rather farfetched and could easily be falsified by additional measurements.

7.7.3 SIT measurements violating a Leggett-Garg inequality

In the previous section we have argued that both SIT or LGI can serve as quantum witnesses, while additionally SIT can be used as a definition of NIM2. Here we provide additional insight on the relation of these two quantum witnesses by showing that any experiment where SIT is observed can directly be used to violate a Leggett-Garg inequality. A procedure in order to violate the Leggett-Garg inequality $\mathcal{L} = \mathcal{C}_{AB} + \mathcal{C}_{BC} - \mathcal{C}_{AC} \leq 1$ having observed SIT between two modular measurements on an input state is given in the following. This procedure is equivalent to the one used and discussed in [66] and is briefly commented on in [190].

We consider two measurements B, C which we read out by coupling them to an ancilla qubit. Thus the measurement of the qubit has two possible outcomes, Up and Down, which we label U and D. The only assumption we make about the measurements B and C is that B is SIT to C when the input state $|\psi\rangle$ is measured. This means $P_C(c) \neq \sum_b P_{CB}(c,b) = P_{C(B)}(c)$. Thus one of the two probabilities is bigger than the other. Without loss of generality we choose $P_C(D) < P_{C(B)}(D)$ and we define $a \equiv P_{C(B)}(D) - P_C(D)$ to be the difference between the two. (In the case of $P_C(U) > P_{C(B)}(U)$ we can modify the protocol slightly). Measurement A is simply the state preparation or confirmation of the state preparation of $|\psi\rangle$. The key point of the protocol is to assign different measurement results to the outcomes U, D, which we denoted by $f_M(U/D) = \pm 1$. Here M labels one of the three measurements A, B, C. The assigned results are always $r = \pm 1$ which is compatible with the assumption $|r| \leq 1$ used in the proof of the LGI [190]. To be specific, the three measurements violating the LGI are given by:

t_0 Initial state preparation of $|\uparrow\rangle\,|\psi\rangle$

t_1 Measurement A: Readout of the qubit. We assign the result U the value $+1$ and -1 to D; $f_A(U) = +1, f_A(D) = -1$

t_2 Measurement B and both results D and U are identified with $+1$; $f_B(D) = f_B(U) = +1$

t_3 Measurement C. Result U: -1, result D: $+1$; $f_C(U) = -1, f_C(D) = 1$

Note that the assignment of a constant value for measurement B can be interpreted as performing the measurement but not looking at the result. We can now calculate the value of $\mathcal{L}$. $\mathcal{C}_{AB} = 1$ since measurement A always gives an Up result and in measurement B we assigned the constant value of $+1$. The correlator $\mathcal{C}_{AC} = \sum_c f_C(c) P_C(c)$ simplifies to be the expectation value of measurement C, since measurement A is only confirming the state preparation. $\mathcal{C}_{BC} = \sum_c f_C(c) \sum_b P_{CB}(c,b)$ simplifies since we assigned in measurement B

the constant value of +1 thus:

$$\begin{aligned}\mathcal{L} &= 1 + \left(\sum_c f_C(c) \sum_b P_{CB}(c,b) - \sum_c f_C(c) P_C(c)\right) \\ &= 1 + \sum_c f_C(c) \left(\sum_b P_{CB}(c,b) - P_C(c)\right) \\ &= 1 + 2a > 1.\end{aligned} \tag{7.22}$$

We can also see that in the case of $P_C(D) > P_{C(B)}(D)$ we can change the assignment of results in measurement C to $f_C(U) = 1, f_C(D) = -1$.

7.7.4 Correcting LGI violation for signaling in time

On might argue that it is trivial to violate the Leggett-Garg inequality using SIT measurements. SIT confirms experimentally, that the measurement A is violating the NIM2 assumption. The framework and arguments presented by J. Kujal and co-workers [194] suggest[2] to account for this trivial form of violation by simply subtracting the SIT between each pair of measurements from the $\mathcal{L}$ value:

$$\mathcal{L}_{\text{pen.}} = \mathcal{L} - 2(|\mathscr{S}_{AB}| + |\mathscr{S}_{BC}| + |\mathscr{S}_{AC}|) = \mathcal{L} - T\mathscr{S}. \tag{7.23}$$

They devise a formalism for contextuality inequalities, which can be formulated entirely in terms of measurement statistics, thus not requiring arguments about macroscopic measurements. They consider cyclic contextuality inequalities and consider some LGIs, for example $\mathcal{C}_{AB} + \mathcal{C}_{BC} + \mathcal{C}_{CA} < 1$, as special cases of their notion of contextuality. The paper addresses the problem that even if an experimenter intends to perform compatible measurements, then due to experimental fluctuations and imprecisions, there will still be a certain amount of SIT between the sequential measurements. The work derives penalized contextuality bounds to account for these imprecisions. The derived penalization is expressed in the notation of this work as $T\mathscr{S} \equiv 2(|\mathscr{S}_{AB}| + |\mathscr{S}_{BC}| + |\mathscr{S}_{CA}|)$ and can be interpreted as the total amount of SIT observed. Since they consider cyclic measurements, each measurement is performed once as the first measurement in the sequence and once as a second measurement. This allows the penalization to be extracted directly from the same measurements used to assess the contextuality bound.

In contrast, the inequality we considered in this work is not cyclic; $\mathcal{C}_{AB} + \mathcal{C}_{BC} - \mathcal{C}_{AC} < 1$. B is performed once as a first measurement and another time as a second measurement. But this is not the case for measurements A and C and thus we can not perform the suggested correction using our measurement data.

Our LGI measurement settings were solely optimized to maximize the value of the parameter $\mathcal{L}$ and are thus expected to contain some amount of SIT

[2] up to our current understanding

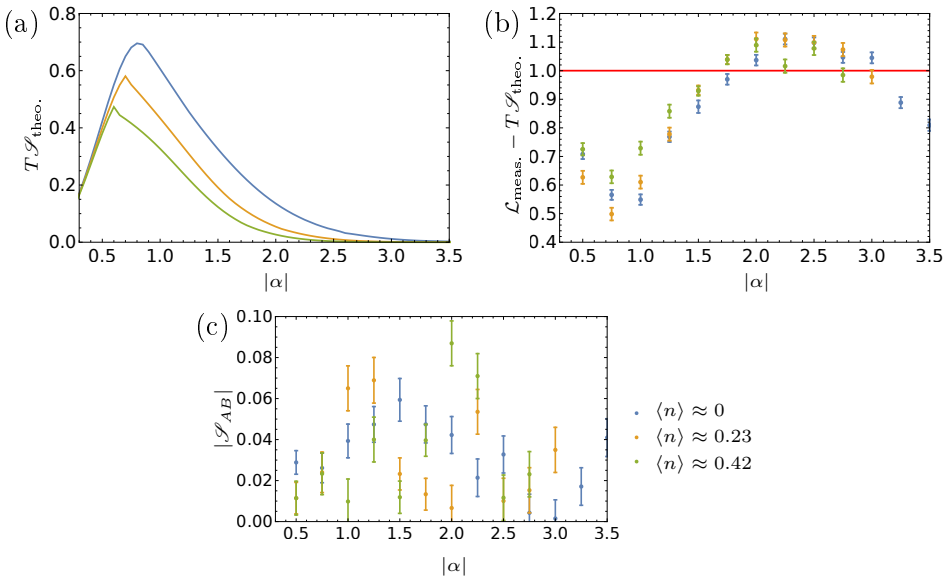

Figure 7.12: Penalization of $\mathcal{L}$ for inbuilt two-time SIT. (a) Analytic calculation of the total amount of SIT: $T\mathscr{S} = 2(|\mathscr{S}_{AB}| + |\mathscr{S}_{BC}| + |\mathscr{S}_{AC}|)$ due to incompatible settings used to violate the LGI. The $T\mathscr{S}$ approaches zero for the larger displacement α. (b) The measured data penalized by the theoretical amount of inbuilt SIT. Several points around alpha 2.25 are still able to violate the LGI in this penalized fashion. (c) $|\mathscr{S}_{AB}|$ extracted from the experimental data. The amount of SIT is higher than expected from the analytic calculation, which predicts values up to 0.02. But the values stay close to zero. Note that the total SIT is dominated by $|\mathscr{S}_{BC}|$ and $|\mathscr{S}_{AC}|$.

between the measurements. Analytic calculation of the amount of inbuilt SIT in our protocol, see figure 7.12 (a), shows that this is indeed the case for displacements of around $\alpha = 1$. But the amount of SIT approaches zero for larger displacements. From this we conclude that for large displacements the ideal protocol approaches $\mathcal{L} = 1.5$ with NSIT measurements at the two-time level.

We cannot correct the violation using our experimental measurement results, however we can still explore the reduction of $\mathcal{L}$ due to this theoretical amount of inbuilt SIT. This is shown in figure 7.12 (b). At our experimentally achieved size of displacements some points violate the LGI in this corrected fashion. These are the points highlighted with diamonds in figure 7.10. Furthermore, we can get an estimate for how close our experiment resembles the theoretical amount of inbuilt SIT, by extracting $|\mathscr{S}_{AB}|$ from our experimental data, see figure 7.12 (c). The theoretical expectation for $|\mathscr{S}_{AB}|$ is around zero and never exceeds 0.02. The amount of SIT we measure is close to zero but slightly

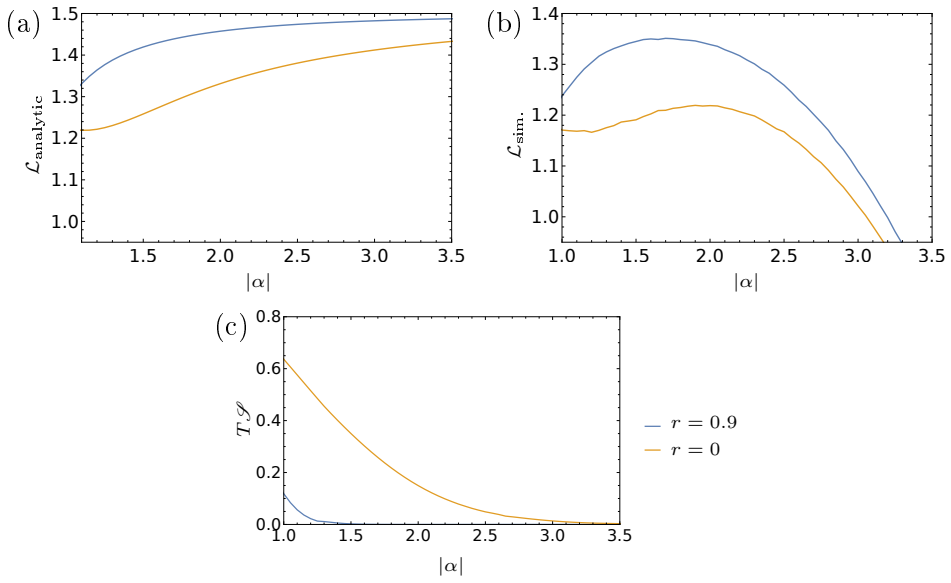

Figure 7.13: Theoretical comparison of a LGI experiment using a ground state cooled or a squeezed oscillator input state. Results are presented for a squeezing parameter $r \approx 0.9$. (a) Analytic calculation of the achievable $\mathcal{L}$ values. (b) Simulated $\mathcal{L}$ values including the same motional dephasing and linewidths as in the simulations of figure 7.10. (c) Analytic calculation of the amount of $T\mathscr{S}$.

higher than this theoretical expectation. The higher amount of SIT is expected given the accuracy with which we can calibrate and perform our experiments.

7.7.5 Future improved LGI protocols

Performing in the future an additional measurement of C directly on the input state would allow to extract $|\mathscr{S}_{BC}|$ and $|\mathscr{S}_{AC}|$ and then to calculated the corrected $\mathcal{L}$ value: $\mathcal{L}_{\text{pen.}}$. This is not fully equivalent to the cyclic inequality scenario. Since in our case measurement C would be performed alone, while in the cyclic scenario always a second measurement is following. Furthermore, there might be subtleties which we miss at this stage. A future experiment could find settings in order to violate the cyclic LGI inequality and process the data according to [194].

The use of squeezed input states would improve the LGI violation in two ways. These are an increased violation alongside a reduction in SIT for a given displacement size. We maximize the $\mathcal{L}$ value for squeezed initial oscillator states $\hat{\mathcal{S}}(re^{i\vartheta})\,|0\rangle$ using the method described in section 7.6.1. In addition we fix the setting r and allow the squeezed state orientation ϑ to vary. Results of the maximization are displayed in figure 7.13 (a), for comparison the

maximized values in case of the ground state $r = 0$ input are shown. At a fixed modular displacement higher violations are achieved in case of the squeezed state. The simulation of realistic dephasing noise, figure 7.13 (b) shows that this advantage is still present in a realistic scenario. The SIT in-built in the measurements further drops much quicker for the squeezed state compared to the ground state. Analytic calculations of the in-built SIT are shown in figure 7.13 (c). In addition the states created for a fixed $|\alpha|$ are in some sense more macroscopic since the ratio of separation to relevant wave packet extent (approximately the squeezed wave packet size) is larger. For $r = 0.9$ the ratio is improved by a factor of ≈ 2.5.

A number of methods have been proposed for performing a LGI test using NSIT measurements, see for example [53] where the key is to use mixed input states. In the work [193] a LGI test using two-time NSIT measurements is called a test of an intermediate form of macroscopic realism. Here the word intermediate relates to the understanding that two-time NSIT does not unambiguously confirm a non-invasive measurement, signaling at the three or higher time level might still occur.

7.7.6 Conclusion

The measurement techniques demonstrated here provide new tools for examining the quantum-classical divide with harmonic oscillators and could be applied in a range of experimental systems [67]. Both the Leggett-Garg correlation method and signaling in time provide quantum signatures using a small number of measurements. Extracting $\mathscr{S} \neq 0$ requires 6 data points, while $\mathcal{L} > 1$ needs 12 measurement points. This is much less than we typically need to extract, for example, a negative Wigner function point, as described in chapter 6. In chapter 9 we will show how to perform direct phase space reconstruction based on interference of wave packets. The scheme will be closely related to the $\mathscr{S}$ measurements. We find that measurements of $\mathscr{S}$ and $\mathcal{L}$ require excellent frequency stability of the oscillator mode. Extensions of modular measurements to multiple oscillators would allow for numerous foundational tests based on continuous-variable systems including tests of local realism and non-contextuality [195–199].

Alongside these fundamental applications, the combination of squeezed states and modular operator measurements demonstrated here will be used in the next chapter to prepare approximate oscillator-error-correction code states as proposed by Gottesman, Kitaev, and Preskill [19]. Ideal code states in particular would exhibit maximal signaling in time.

Chapter 8

Grid state qubit

This chapter reports on encoding and full control of a logical qubit in the motion of a trapped $^{40}Ca^{+}$ ion based on the scheme proposed in 2001 by Gottesman, Kitaev and Preskill (GKP) [19]. Code states are realized by multi-component superpositions of displaced squeezed states. These are prepared as well as analyzed using modular measurements. We prepare and reconstruct logical states with an average square fidelity of 87.3±0.7%. We also demonstrate a universal logical single qubit gate set, which we analyze using process tomography. For Pauli gates we reach process fidelities of ≈ 97%, while for continuous rotations we use gate teleportation, achieving fidelities of ≈ 89%. The chapter is based on the corresponding publication [114].

8.1 Bosonic codes

The work in the current chapter concerns one particular error correction code, which is called GKP code and has been devised for encoding a logical qubit in a single bosonic mode [19]. The GKP code has originally been proposed for a traveling optical mode. In the optical platform Gaussian operations, which include displacements, squeezing operations, and beam-splitters, are simple to implement. However codes solely based on Gaussian resources are not well suited for universal quantum computation [16] and further have been shown to only be able to correct certain types of errors [106, 107]. Their capabilities can be extended once non-linear resources are included, for example a non-linear interaction of two bosonic modes. Photons do not naturally interact [16], however a non-linear interaction can be realized by coupling an optical mode to the discrete energy levels of a trapped atom. This requires an optical cavity in order to enhance the interaction. Recently progress has been made using such systems to mediate the interaction of traveling photons [21]. Meanwhile alternative non-linear resources were considered including measurements [17, 18] or non-Gaussian code states [19].

Instead of using an optical mode we realize the bosonic encoding in the motional oscillator of the trapped-ion and introduce non-linearity via the laser mediated coupling to the internal qubit levels including measurements thereof. An alternative experimental approach examining similar physics has been built up using microwave superconducting cavities. There the non-linear element in early experiments were Rydberg atoms [115], but more recent advances have been driven by the use of non-linear superconducting circuits containing Josephson junctions [14, 86, 87]. This interest has arisen because coherence times for the microwave cavities were observed to be better than the non-linear Transmon qubits realized in the same experimental setting [23].

In the following, I provide a short overview of a number of different bosonic codes which have been considered, some of which have been experimentally implemented. These are then compared with the GKP code used for the experimental work in this thesis.

Cat codes

Superpositions of coherent states i.e. the previously discussed cat state (see section 2.5 and chapter 6) can be used for correction of boson loss. The symmetric cat states $|\psi_{\pm 1}\rangle \propto |\alpha/2\rangle \pm |-\alpha/2\rangle$ are ± 1 eigenstates of the parity operator. Additionally coherent states are also eigenstates of the boson destruction operator with eigenvalue α. Therefore the states $|\psi_{\pm 1}\rangle$ get interchanged under the destruction operator ($\hat{a}\,|\psi_{\pm 1}\rangle = \alpha\,|\psi_{\mp 1}\rangle\,/2$). Using $|\psi_{\pm 1}\rangle$ as the computational basis states, thus allows to transform boson loss into bit flip errors [99]. This is strictly speaking only true for $\alpha = \infty$. For realistic superpositions the remaining state overlap between the wave packets leads to small discrepancies.

A quantum error correcting code for boson loss can be realized by four state superpositions of even parity to realize arbitrary qubit states $|\psi\rangle_L = a\,|0\rangle_L + b\,|1\rangle_L$ with:

$$|0\rangle_L \propto |\alpha/2\rangle + |-\alpha/2\rangle \qquad |1\rangle_L \propto |i\alpha/2\rangle + |-i\alpha/2\rangle \tag{8.1}$$

$$\hat{a}\,|0\rangle_L \propto \alpha(|\alpha/2\rangle - |-\alpha/2\rangle)/2 \qquad \hat{a}\,|1\rangle_L \propto i\alpha(|i\alpha/2\rangle - |-i\alpha/2\rangle)/2. \tag{8.2}$$

In this case boson loss introduces a parity flip [98]. This scheme was used in order to experimentally correct for photon loss using only a single microwave cavity mode and allowed for lifetime extensions of the encoded qubit [86]. Cat qubits have been protected dissipatively [104] and the use of superpositions of equally spaced coherent states located on circles in phase space, has been shown to allow for correction of multiple boson losses or the encoding of qudits (multi-level systems) [200]. Such states in general realize eigenstates of the modular boson number operator: $(\hat{N} \bmod m)$ whith $m \in \mathbb{N}$. The case of $m = 2$ correspond to the described cat code.

Binomial code

Aside from multicomponent coherent state superpositions simpler superpositions of Fock states can be constructed which are eigenstates of the parity operator or have a well defined modular boson number [96, 97]. The amplitudes in these states are tailored such that boson loss does not lead to distortion of the states. This is necessary since different pre-factors arise when the destruction operator is applied to different Fock states: $\hat{a}\,|n\rangle = \sqrt{n}\,|n-1\rangle$. This is best illustrated considering the smallest code example allowing for the correction of a single boson loss:

$$|0\rangle_L = (|0\rangle + |4\rangle)/\sqrt{2} \qquad |1\rangle_L = |2\rangle \tag{8.3}$$

$$\hat{a}\,|0\rangle_L = \sqrt{2}\,|3\rangle \qquad \hat{a}\,|1\rangle_L = \sqrt{2}\,|1\rangle\,. \tag{8.4}$$

The boson loss transforms the two even parity code words into two odd parity error states. In particular such Fock state superpositions are orthogonal and thus in contrast to the cat code are not approximate codes. The mean boson number $\langle n\rangle$ is equal for the code states and smaller than in cat codes. The latter is favorable since typically decoherence sources scale with the size of the bosonic states. The code states given in equation 8.3 were analyzed experimentally in [201] and used in the context of communication protocols [87]. Binomial codes can be improved using superpositions of higher Fock states which allow for correction of errors represented by multiple $\hat{a}$ and $\hat{a}^\dagger$ operators and superpositions of these. In addition the larger state space can also be used to encode qudits.

8.2 GKP Encoding

An early proposal for a bosonic code based on non-Gaussian code words was due to Gottesman, Kitaev and Preskill [19]. This code has been shown to allow for fault tolerant universal computation [19, 202, 203]. In particular the GKP code can be expressed in the stabilizer formalism with stabilizer operations given by commuting phase space shifts, which further constitutes the error model under consideration. Other error channels, including amplitude damping, can be mapped onto the shift error model and thus be corrected as long as they are sufficiently weak. Theoretical code performance comparisons for the correction of boson loss for the various bosonic codes have shown best correction performance for the GKP code in practically relevant regimes [109]. Additionally the GKP code emerged in numerical searches for optimal boson loss codes [110]. These favorable properties come at the price of complex code states. Ideal code states are represented by infinite superpositions of displaced, infinitely squeezed states (i.e. position eigenstates). The Wigner function of the computational basis states is dominated by the quantum interference between each pair of shifted position eigenstates, which forms a two dimensional grid of delta peaks. This two dimensional grid exhibits perfect sensitivity to additional small phase space shifts representing errors.

These ideal code states are unphysical and therefore the implementation of this scheme requires the use of approximations to these states. Such approximations are given by superpositions of a finite number of displaced squeezed states. The error due to the use of these approximate states can be quantified and enters the overall error budget of the code [107]. Numerous theoretical proposals for the creation of approximate codes states have been made [174, 204–207]. After revising the technicalities of this encoding, we report on preparation and control of these code states.

8.2.1 Logical operations

In the stabilizer formalism a qubit code subspace is defined within a higher-dimensional Hilbert space by the action of a set of mutually commuting stabilizer operators [72]. These form the error-check operators which are measured in order to detect logical qubit errors. Such measurements should not disturb the stored information, therefore it is required that the stabilizer operators also commute with the Pauli operators, which generate the qubit subspace. In the previous sections we have seen that dependent on the shift sizes and directions, two displacement operators can either commute or anti-commute:

$$[\hat{\mathcal{D}}(\alpha), \hat{\mathcal{D}}(\beta)] = 2ie^{i\Phi}\sin(\Phi)\hat{\mathcal{D}}(\alpha)\hat{\mathcal{D}}(\beta), \text{ where: } \Phi = \mathrm{Im}(\beta\alpha^*).$$

Thus displacements satisfying $\Phi = k\pi, k \in \mathbb{Z}$ commute, while anti-commutation is found for $\Phi = (2k+1)\pi/2$. This allows to define GKP codes entirely based on phase space shifts [19]. Figure 8.1 shows a set of displacement operators defining such a code. The two stabilizer operators $\hat{S}_X \equiv \hat{\mathcal{D}}(l)$, $\hat{S}_Z \equiv \hat{\mathcal{D}}(i2\pi/l)$ span an area of $\Phi = 2\pi$ and thus commute. The Pauli operators $\hat{X}_L \equiv \hat{\mathcal{D}}(l/2)$, $\hat{Z}_L \equiv \hat{\mathcal{D}}(i\pi/l)$ are chosen with half the displacement sizes as compared to the corresponding stabilizer operators, while $\hat{Y}_L \equiv \hat{\mathcal{D}}(-l/2 - i\pi/l)$ ensures the correct Pauli commutation relations. The Pauli operators will commute with the stabilizer operators because the relevant geometrical phases $\Phi = \pi$ or 0. The simultaneous eigenstates of $\hat{Z}_L, \hat{S}_Z, \hat{S}_X$ are the computational basis states and are periodic with respect to the three phase space shifts. The displacement operators are non-Hermitian: $\hat{\mathcal{D}}(\alpha)^\dagger = \hat{\mathcal{D}}(-\alpha)$, nevertheless the action of $\hat{X}_L, \hat{Y}_L, \hat{Z}_L$ and their Hermitian conjugates are identical on the periodic code states. Furthermore the stabilizer operators act as the identity operation on the code states. Therefore we have:

$$\begin{aligned}
&\hat{\mathcal{D}}(l/2) = \hat{X}_L \approx \hat{X}_L^\dagger = \hat{\mathcal{D}}(l/2)^\dagger = \hat{\mathcal{D}}(-l/2) \\
&\hat{\mathcal{D}}(i\pi/l) = \hat{Z}_L \approx \hat{Z}_L^\dagger = \hat{\mathcal{D}}(i\pi/l)^\dagger = \hat{\mathcal{D}}(-i\pi/l) \\
&\hat{\mathcal{D}}(-l/2 - i\pi/l) = \hat{Y}_L \approx \hat{Y}_L^\dagger = \hat{\mathcal{D}}(l/2 + i\pi/l) \\
&\hat{S}_X = \hat{\mathcal{D}}(l) \approx \mathbb{1}_L \\
&\hat{S}_Z = \hat{\mathcal{D}}(2i\pi/l) \approx \mathbb{1}_L.
\end{aligned} \tag{8.5}$$

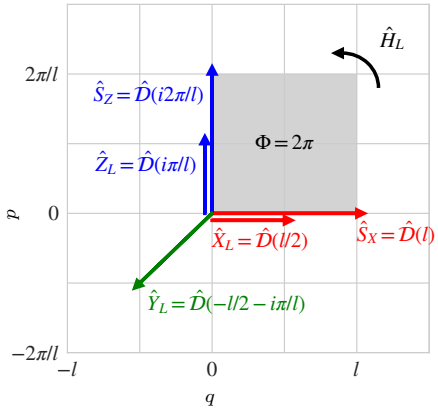

Figure 8.1: Grid state encoding logical operations. Phase space displacements for the two stabilizer operators $\hat{S}_X$, $\hat{S}_Z$ and the logical Pauli operators $\hat{X}_L$, $\hat{Y}_L$, $\hat{Z}_L$ shown is also the relevant phase space area Φ. The Hadamard operation is given by a $\pi/2$ rotation of phase space together with a rescaling of the phase space axis.

The logical Pauli operations should fulfill the relation $\hat{\sigma}_i\hat{\sigma}_j = \delta_{ij}\mathbb{1} + i\epsilon_{ijk}\sigma_k$ where δ_{ij} is the Kronecker delta and ϵ_{ijk} the Levi-Civita symbol. This is confirmed below using the relations given above:

$$\begin{aligned}
\hat{X}_L^2 &= \hat{\mathcal{D}}(l/2)^2 = \hat{\mathcal{D}}(l) = \hat{S}_X \approx \mathbb{1}_L \\
\hat{Y}_L^2 &= \hat{\mathcal{D}}(-l/2 - i\pi/l)^2 = \hat{\mathcal{D}}(-l - 2i\pi/l) = \hat{S}_X^\dagger \hat{S}_Z^\dagger \approx \mathbb{1}_L \\
\hat{Z}_L^2 &= \hat{\mathcal{D}}(i\pi/l)^2 = \hat{\mathcal{D}}(2i\pi/l) = \hat{S}_Z \approx \mathbb{1}_L \\
\hat{X}_L\hat{Y}_L &= \hat{\mathcal{D}}(l/2)\hat{\mathcal{D}}(-l/2 - i\pi/l) = i\hat{\mathcal{D}}(-i\pi/l) = i\hat{Z}_L^\dagger \approx i\hat{Z}_L \\
\hat{X}_L\hat{Z}_L &= \hat{\mathcal{D}}(l/2)\hat{\mathcal{D}}(i\pi/l) = -i\hat{\mathcal{D}}(l/2 + i\pi/l) = -i\hat{Y}_L^\dagger \approx -i\hat{Y}_L \\
\hat{Y}_L\hat{Z}_L &= \hat{\mathcal{D}}(-l/2 - i\pi/l)\hat{\mathcal{D}}(i\pi/l) = i\hat{\mathcal{D}}(-l/2) = i\hat{X}_L^\dagger \approx i\hat{X}_L.
\end{aligned} \tag{8.6}$$

All the commutation relations are independent of l, which can thus be chosen to suit experimental constraints.

8.2.2 Code states

The computational basis states in these codes consist of an infinite array of position eigenstates [19]. They can be chosen as:

$$|0\rangle_{L,\mathrm{id}} = \sum_{k=-\infty}^{\infty} \hat{\mathcal{D}}(kl)\,|q=0\rangle \tag{8.7}$$

$$|1\rangle_{L,\mathrm{id}} = \hat{X}_L\,|0\rangle_{L,\mathrm{id}} = \sum_{k=-\infty}^{\infty} \hat{\mathcal{D}}(kl + l/2)\,|q=0\rangle \tag{8.8}$$

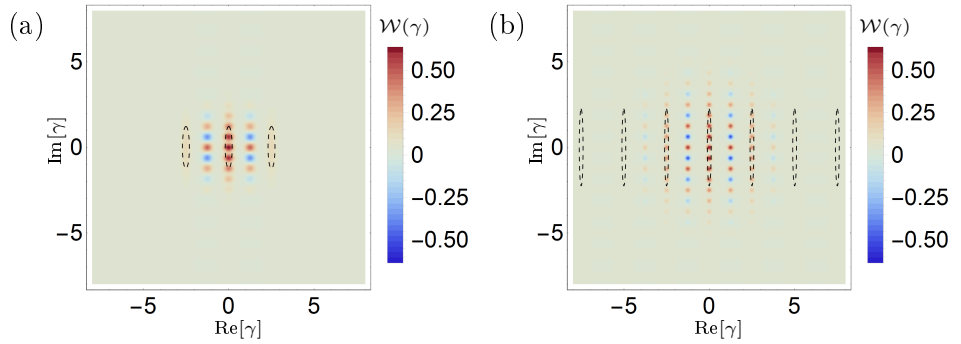

Figure 8.2: Two examples of approximate $|0\rangle_L$ states. (a) $r = 0.9$, $k_{\max} = 1$, $c_0/2 = c_{-1} = c_1$, (b) $r = 1.5$, $k_{\max} = 3$, $c_0 = 4c_{\pm1}/3 = 10c_{\pm2}/3 = 20c_{\pm3}$. The dashed ellipses help as a guide to the eye and show the r.m.s extent of the squeezed components used to built up the states. The interference between these components leads to the build up of the 2D grid in phase space. For more components and higher amounts of squeezing (b) the grid becomes larger while simultaneously the individual features become narrower. The limit of ideal code states is given by an infinite grid of delta peaks.

with $|q\rangle$ the dimensionless position eigenstates. These ideal code states are unphysical, since they cannot be normalized. Approximations to these states are given by finite superpositions of displaced squeezed states [19]:

$$|0\rangle_L = \sum_{k\in\mathbb{Z}}^{\pm|k_{\max}|} c_k \hat{\mathcal{D}}(kl)\,|r\rangle \qquad |1\rangle_L = \hat{X}_L\,|0\rangle_L \tag{8.9}$$

where $|r\rangle = \hat{\mathcal{S}}(r)\,|0\rangle$ is a squeezed vacuum state with the squeezed axis aligned with position. The weight of the displaced components is given by the real pre-factors c_k. This approximate form approaches the ideal states for larger r and $k_{\max}$. Using approximate logical code states leads to quantifiable logical qubit errors, which enter the overall error budget for the implementation of large scale computation based on this code [19, 107, 202].

Figure 8.2 shows two examples of logical $|0\rangle_L$ states. The first state (a) uses $r = 0.9$, $k_{\max} = 1$, $c_0/2 = c_{-1} = c_1$ while (b) shows $r = 1.5$, $k_{\max} = 3$, $c_0 = 4c_{\pm1}/3 = 10c_{\pm2}/3 = 20c_{\pm3}$. We see that the quantum interference between the various displaced squeezed components leads to a build up of a 2D periodic structure in phase space. The larger amount of squeezing and the higher number of components in (b) gives a larger extent of the structure alongside narrower individual features. Instead of expressing the code states in terms of the position eigenstates or position squeezed states, we can use the dimensionless momentum basis or momentum squeezed states. Using the Fourier

relation between position and momentum we find for the logical states [204]:

$$|0\rangle_{L,\mathrm{id}} \propto \sum_{k=-\infty}^{\infty} |q = kl\rangle \propto \sum_{k=-\infty}^{\infty} \left|p = \frac{\pi}{l}k\right\rangle \tag{8.10}$$

$$|1\rangle_{L,\mathrm{id}} \propto \sum_{k=-\infty}^{\infty} |q = kl + l/2\rangle \propto \sum_{k=-\infty}^{\infty} (-1)^k \left|p = \frac{\pi}{l}k\right\rangle. \tag{8.11}$$

From this we in particular find:

$$|+\rangle_{L,\mathrm{id}} \propto (|0\rangle_{L,\mathrm{id}} + |1\rangle_{L,\mathrm{id}})/\sqrt{2} = \sum_{k=-\infty}^{\infty} \left|p = \frac{2\pi}{l}k\right\rangle \tag{8.12}$$

$$|-\rangle_{L,\mathrm{id}} \propto (|0\rangle_{L,\mathrm{id}} - |1\rangle_{L,\mathrm{id}})/\sqrt{2} = \sum_{k=-\infty}^{\infty} \left|p = \frac{2\pi}{l}k + \frac{\pi}{l}\right\rangle. \tag{8.13}$$

$|+\rangle_{L,\mathrm{id}}$ and $|-\rangle_{L,\mathrm{id}}$ expressed in the momentum basis behave analogous to $|0\rangle_{L,\mathrm{id}}$ and $|1\rangle_{L,\mathrm{id}}$ in the position basis. This is an alternative way of deriving that the Hadamard operation $\hat{H}$ is given in this code by a rotation of phase space by $\pi/2$ together with scaling of the coordinates by factors of $l^2/2\pi$ and $2\pi/l^2$. In case of $l = \sqrt{2\pi}$ both stabilizer operator shifts have the same length and the Hadamard operation is just given by the phase space rotation.

8.2.3 Code variations

In the above we have chosen the stabilizer operators to be perpendicular to each other. This provides an intuitive encoding but is in principle not required. The choice of a 60 degree angle between the stabilizer operators constitutes another choice with special symmetry. In this case the three Pauli operations form a equilateral triangle. This so called hexagonal GKP code is analyzed in [110]. The authors find this encoding to be ideal for correcting the Gaussian loss channel in practically relevant regimes. The methods presented in the following could readily be adapted to implement such a modified code.

Once the angle between the stabilizer operators is fixed to 90 degrees a variety of choices still remain. These include the length scale l, the number of displaced squeezed components, the amount of squeezing as well as the prefactors c_k. The quality of an approximation can be quantified by the difference of $\langle \hat{S}_X \rangle$ and $\langle \hat{S}_Z \rangle$ to their ideal values of 1. A higher number of components and higher amounts of squeezing leads theoretically to better code states, however in practice due to the scaling of motional decoherence with larger state sizes, there exists a finite optimal size. Encoding with symmetric extents in position and momentum and with high weight close to the origin minimize the number of phonons in the states and are thus preferable for relevant error models [174].

The GKP code method can also be extended to encode a qudit or to codes using multiple oscillators [19]. This is not pursued in our current experiments.

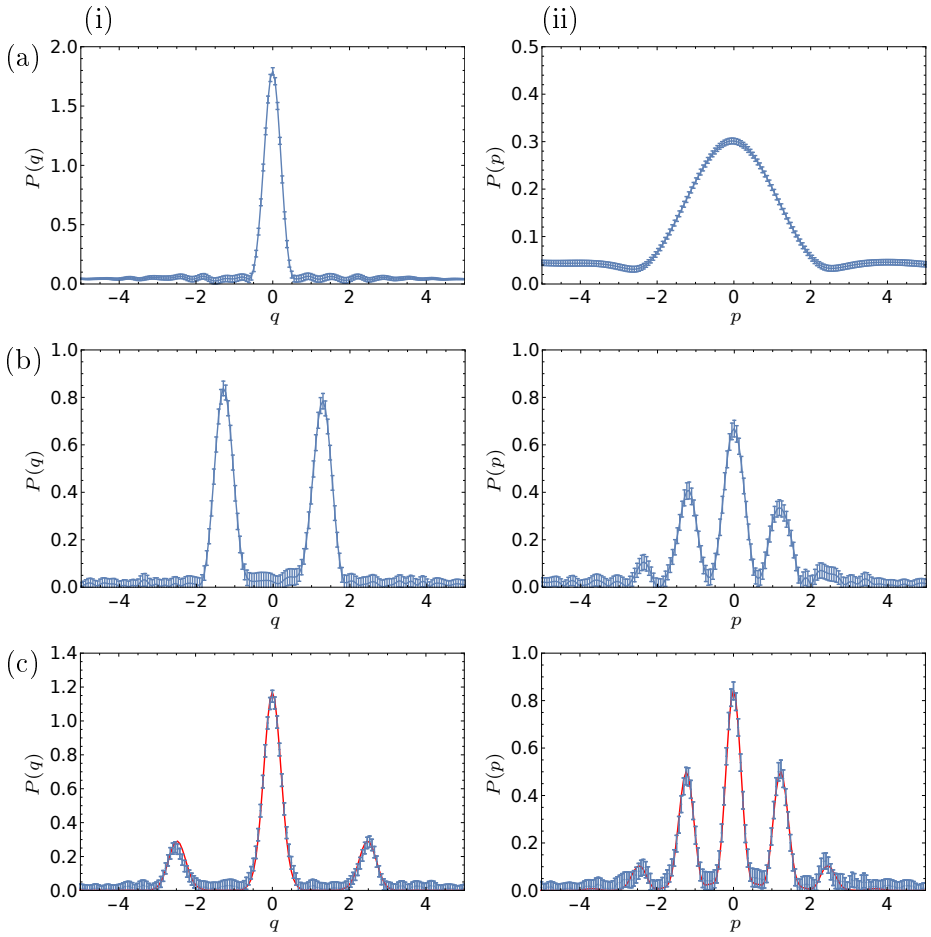

Figure 8.3: Preparation of a three-component grid state. (a) Shown are the dimensionless position $P(q)$ and momentum $P(p)$ probability densities for a squeezed state $\hat{\mathcal{S}}(r)\,|0\rangle$ with $r \approx 0.9$. The measurements are based on the characteristic function method using a one dimensional discrete Fourier transform, while error bars are obtained using bootstrapping (see chapter 9 for details). (b) The squeezed state serves as an input to a symmetric modular measurement of shift size $l \approx \sqrt{2\pi}$. Conditioned on the dark result a squeezed cat is prepared. (c) In a second round of measurement using the same shift a three-component state is created with a stronger center component. The red line here is obtained from a Lindblad Master equation simulation including motional dephasing and closely follows the blue measurements points.

8.3 Preparation of code states

In qubit array based stabilizer codes the $|0\rangle_L$ state can be prepared by measurement of a set of stabilizer generators as well as the $\hat{Z}_L$ Pauli operator. The relevant circuit to do so is given in figure 1.2 and is analogous to the modular measurements of figure 7.1. For the GKP code the relevant shift operators have a continuous eigenvalue spectrum, thus a single binary measurement cannot extract its eigenvalue, and the $\hat{E}_\pm$ are no longer projection operators. To obtain the eigenvalue of $\hat{\mathcal{D}}(\alpha)$ up to a given precision, phase estimation protocols using multiple measurement rounds are required [174]. In such protocols the initial system state in each round is the post-measurement state of the previous round and the back-action of each measurement pushes the system towards an eigenstate of $\hat{\mathcal{D}}(\alpha)$. Dependent on all measurement results most states can be corrected to become an approximate $+1$ eigenstate of the relevant operators [174]. This scheme works starting from an arbitrary oscillator state, but the number of measurements can be drastically reduced by starting in a position squeezed vacuum state, already providing an approximate eigenstate of $\hat{S}_Z \equiv \hat{\mathcal{D}}(i2\pi/l)$ and $\hat{Z}_L \equiv \hat{\mathcal{D}}(i\pi/l)$. Then only phase estimation of the second stabilizer $\hat{S}_X$ is required.

In our system the photon scattering in case of a bright measurement result destroys the oscillator superposition, thus we are required to post-select on dark measurement results and can not use the scheme proposed in [174]. A post-selected scheme for ions has been proposed by G.J. Milburn and co-workers [204] and our method closely follows their scheme.

We first prepare a squeezed vacuum state by reservoir engineering [40] and align the squeezed axis with position $|r\rangle = \hat{\mathcal{S}}(r)\,|0\rangle$ where $\vartheta = 0$. Figure 8.3 (a) shows the position $P(q)$ and momentum $P(p)$ probability densities of a typical squeezed vacuum state. These results are obtained using the characteristic function method, which will be described in detail in the next chapter. We use this state as input to a sequence of symmetric modular measurements (SDF + fluorescence readout). A first modular measurement with a shift of l produces a squeezed cat state conditioned on the dark detection result:

$$[\hat{\mathcal{D}}(-l/2) + \hat{\mathcal{D}}(l/2)]\,|r\rangle\,. \tag{8.14}$$

The relevant probability densities for $l \approx \sqrt{2\pi}$ are given in Figure 8.3 (b). Using this state as an input to a second modular measurement of shift l creates a superposition of three displaced squeezed components approximating the $|0\rangle_L$ state given as follows:

$$|0\rangle_L \propto [\hat{\mathcal{D}}(-l) + 2\cdot\mathbb{1} + \hat{\mathcal{D}}(l)]\,|r\rangle\,. \tag{8.15}$$

Measurements of the position and momentum probability densities in this case are given in figure 8.3 (c). A theoretical plot of the full Wigner function is shown in figure 8.2 (a). The middle component has double the weight since it

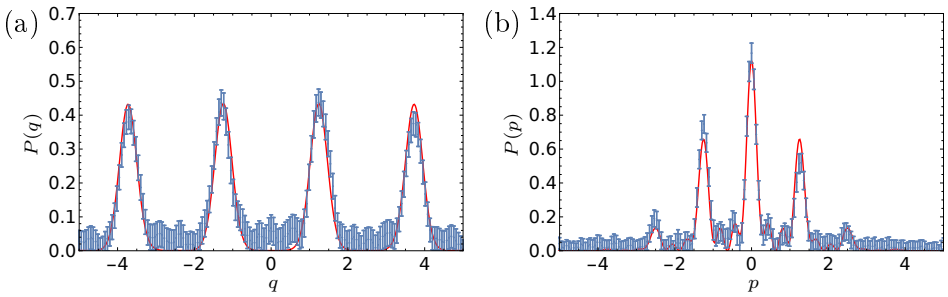

Figure 8.4: A four component displaced squeezed superposition is created applying a sequence of two modular measurements with shifts $\alpha_A = l$ and $\alpha_B = 2l$, $l \approx \sqrt{2\pi}$ to a position squeezed state $\hat{\mathcal{S}}(r)\,|0\rangle$ with $r \approx 0.9$. Blue are measurements obtained from the Fourier transform of characteristic function measurements, while the red line shows a Lindblad Master equation simulation of the experiment.

is created as the constructive interference of two squeezed components, which leads to a 4 times higher probability density. If we would continue with more measurement rounds, where each shift is fixed to l then in each round $|0\rangle_L$ or $|1\rangle_L$ is prepared in alternating fashion. The weights c_i follow Pascals triangle, and with each round we move to the next level in the triangle[1]. In this case the weights approximate a Gaussian envelope improving with more measurement rounds. The probability for a dark result in round k increases[2] due to the increase in constructive interference during the measurements.

Alternatively the shifts in subsequent rounds can be doubled. In this case the second modular measurement would use the shift $2l$ and prepare a four component version of $|1\rangle_L$.

$$|1\rangle_L \propto [\hat{\mathcal{D}}(-3l/2) + \hat{\mathcal{D}}(-l/2) + \hat{\mathcal{D}}(l/2) + \hat{\mathcal{D}}(3l/2)]\,|r\rangle \tag{8.16}$$

In this case all the components have equal weights. Measurements for such a state are shown in figure 8.4. If we would continue with more measurement rounds, then the number of components is doubled in each round, while all components will have the same weight. Therefore a box envelope is produced. The success probability in this case will roughly half with each round and states will approximate $|1\rangle_L$.

For both the three and the four component state $l \approx \sqrt{2\pi}$ is used which generates code states with similar modularities in q and p. In this case using $r \approx 0.9 \approx 7.8$ dB provides similar extent of the states in q and p. Using a Gaussian envelope is preferable to a box envelope because it leads to smaller $\langle n \rangle$ for

[1] hence they are given by the binomial distribution

[2] dark detection probability: $P_k(\uparrow) = \frac{1}{2}(1 + \frac{4knk(k-\frac{1}{2})!(k!)^2}{\sqrt{\pi}(2k)!(1+k)!})$

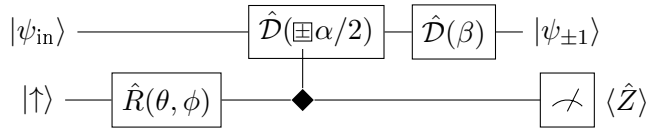

Figure 8.5: Typical grid state control circuit implemented using a carrier rotation $\hat{R}(\theta,\phi)$, an SDF pulse and a final unconditional displacement $\hat{\mathcal{D}}(\beta)$. The diamond symbol denotes control in the $\hat{X}$ basis. For the SDF the states $|\pm\rangle$ determine the sign of the displacement $\pm\alpha/2$. In case of $\phi = \pi/2$ this circuit implements a modular measurement with $\hat{U} = \hat{\mathcal{D}}(\beta)\hat{\mathcal{D}}(-\alpha/2)$ while $\varphi = \theta$.

the same quality of code states. Thus we will base our encoding in the reminder of this chapter on the three component state. $|0\rangle_L$ refers in the following to the state with $r \approx 0.9$, $l \approx \sqrt{2\pi}$ and $c_0 = 2c_{\pm 1}$ while the rest of $c_i = 0$.

8.4 Logical qubit control

In order to create eigenstates of the other Pauli operators as well as implement arbitrary logical control, we perform two types of operations on the logical states. Pauli operations are simple displacements $\hat{\mathcal{D}}(\alpha)$ with specific values of α. These are experimentally implemented by applying a tickling pulse (section 3.6.1). For continuous qubit rotations, we use an improved variant of the modular variable measurement, which we implement using the operations shown in the circuit 8.5. In case of $\phi = \pi/2$ the circuit implements the modular measurement given in figure 7.1 with $\hat{U} = \hat{\mathcal{D}}(\beta)\hat{\mathcal{D}}(-\alpha/2), \varphi = \theta$.

In particular we use ancilla controlled displacements $\hat{\mathcal{D}}(l_j\hat{X}/4)$ along variable directions $j = X, Y, Z$ defined using $l_X = l$, $l_Z = 2\pi i/l$ or $l_Y = -l_X - l_Z$. These are combined with an unconditional corrective displacement $\hat{\mathcal{D}}(\beta) = \hat{\mathcal{D}}(l_j/4)$, which ensures to remain within the code space. Combined with the carrier rotation $\hat{R}(\theta,\phi)$ this set of operations can be represented using the logical circuit shown in figure 8.6. Conditional on the dark detection event this circuit implements

$$\hat{U}_L^j(\theta,\phi) = \sqrt{2}(\cos(\theta/2)|+_j\rangle\langle+_j|_{L,\text{id}} - i\sin(\theta/2)e^{-i\phi}|-_j\rangle\langle-_j|_{L,\text{id}}) \qquad (8.17)$$

on the oscillator state, where $|\pm_j\rangle_{L,\text{id}}$ denotes the ± 1 ideal eigenstate of $\hat{\sigma}_L^j$.

Dependent on the carrier rotation settings a different logical operation is induced on the code space. In the context of error correction codes, this transformation is often referred to as teleportation of the gate onto the code[3] [77]. Typically quantum information processing is expressed in terms of arbitrary unitary operations. The $\hat{U}_L^j(\theta,\phi)$ operation is only unitary

[3]This is different to the standard teleportation protocol [9] where an arbitrary qubit

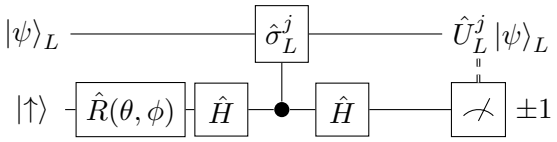

Figure 8.6: Implementation of continuous logical operations. Combining internal state dependent with unconditional shifts allows for the implementation of ancillary controlled logical Pauli operations. This combined with rotations $\hat{R}(\theta,\phi)$ allows to perform the operations $\hat{U}_L^j(\theta,\phi) = \sqrt{2}(\cos(\theta/2)|+_j\rangle\langle+_j|_{L,\mathrm{id}} - i\sin(\theta/2)e^{-i\phi}|-_j\rangle\langle-_j|_{L,\mathrm{id}})$ on the logical qubit space conditioned on the dark detection result. The performed logical gate is controlled via the settings of the rotation.

if we set $\theta = \pi/2$, resulting in a rotation $\hat{U}_L^j(\phi) = -ie^{-i\phi/2}R_L^j(-\phi) = -ie^{-i\phi/2}\exp(i\phi\hat{\sigma}_L^j/2)$ around the j-axis of the Bloch sphere [7]. For other settings non-unitary quantum channels are implemented. In the following we will use unitary as well as non unitary teleported operations in order to prepare eigenstates of the three Pauli operators.

8.5 Logical readout

The modular variable measurement provides readout of $\mathrm{Re}[\langle\hat{\mathcal{D}}(\alpha)\rangle]$. Thus using appropriately chosen complex displacements allows to measure the real part of the logical operators and stabilizers. The real part provides sufficient information since the shift operations are approximately Hermitian when acting on the code states. To analyze our states in more detail we give the readout as a function of the displacement amplitude along the three directions l_j, which are parametrized as $M_j(t) \equiv \mathrm{Re}[\langle\hat{\mathcal{D}}(tl_j)\rangle]$ with the real number t.

8.5.1 $\hat{Z}_L$ eigenstates

Figure 8.7 (a) shows the results of measurements performed on the three-component $|0\rangle_L$ state produced as described in section 8.3. $|1\rangle_L$ is obtained from $|0\rangle_L$ by applying an additional $\hat{X}_L = \hat{\mathcal{D}}(l/2)$ operation using a tickling pulse. Results for this state are shown in figure 8.7 (b). column (ii) provides theoretical Wigner function plots of the analyzed states. The two states are related by the phase space shift $\hat{X}_L$ and thus their Wigner functions show the same pattern but are shifted with respect to each other.

state is teleported from one place to another using a maximally entangled state together with a bit of classical communication. Here teleportation refers to the gate being applied to the ancillary system and then moved onto the code space using the joint coupling.

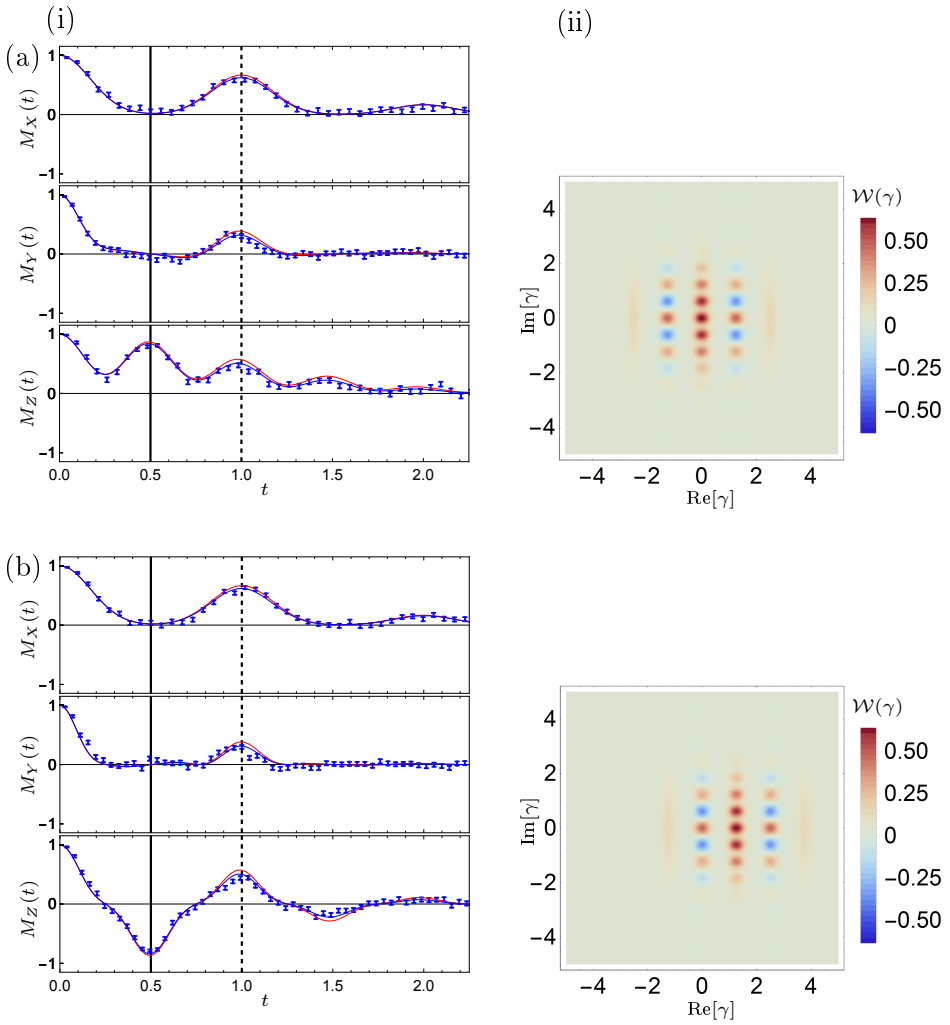

Figure 8.7: Analysis of $\hat{Z}_L$ eigenstates. column (i) shows the readouts $M_j(t) \equiv \mathrm{Re}[\langle \hat{\mathcal{D}}(tl_j)\rangle]$ along the three phase space axis l_j as a function of t. Blue points and error bars provide measurements and s.e.m errors, while the blue line shows a Lindblad Master equation simulation including motional dephasing. The red line shows an analytic calculation for the chosen approximation not including any dephasing. The vertical dashed (solid) line highlights readout of the stabilizer (logical Pauli) operations. In column (ii) the theoretical Wigner function of this approximate code state is shown. (a) Shows results for $|0\rangle_L$, while (b) shows measurements for $|1\rangle_L$.

In column (i) readout values of $M_j(t)$ are given as blue points with errors given as s.e.m. based on projection noise. The red line provides an analytic calculation of the expectation for the three-component state of the calibrated size l and squeezing r. The blue line is obtained from a Lindblad Master equation simulation including motional dephasing using the jump operator $\sqrt{\Gamma}(\hat{a}\hat{a}^\dagger + \hat{a}^\dagger\hat{a})$ with $\Gamma = 7\ s^{-1}$. The readouts collapse and revive. As expected we see a positive revival at $t = 1$ (dashed line) corresponding to stabilizer readouts along all three directions. Measurements at $t = 0.5$ (solid line) correspond to Pauli operator readouts. For both states the readouts of $\langle \hat{X}_L \rangle \approx \langle \hat{Y}_L \rangle \approx 0$. In contrast $\langle \hat{Z}_L \rangle$ provides a positive or negative revival in accordance with the logical states $|0\rangle_L, |1\rangle_L$. Better approximate code states would lead to higher and narrower revivals.

The readout probabilities are dependent on interference of the two displaced copies of the original state, which depends both on the state overlaps and on geometric phases. We explain this in the following for the l_Z readout direction and the $|0\rangle_L = \sum_k c_k \hat{\mathcal{D}}(kl)\,|r\rangle$ state. The modular measurement probability is given by $P(\pm 1) = \langle \psi_{\text{in}}|\, \hat{E}_\pm^\dagger \hat{E}_\pm\, |\psi_{\text{in}}\rangle$, which is given by the overlap of the un-normalized post-measurement state of the oscillator $\hat{E}_\pm\,|\psi_{\text{in}}\rangle$ with itself. This post-measurement state consists of two displaced copies of the input state $|0\rangle_L$. One copy is displaced down the momentum axis by $tl_Z/2$ while the other copy is displaced up. Only components originating from the same initial grid state component k i.e. $\hat{\mathcal{D}}(kl)\,|r\rangle$ have significant overlap. For these overlaps the non-commutativity of the displacement operators lead to different phase factors. Using these relations we find $P(+1) \approx 1/2\left(1 + \sum_k \cos(2l_Z tkl)\,\langle r|\,\hat{\mathcal{D}}(il_Z tkl)\,|r\rangle\right)$ from which $M_Z(t) = 2P(+1) - 1$ follows. We can observe this functional form shown in the bottom trace of figure 8.7 (a). The initial increase of t leads first to different phases between the various terms in the sum and the readout signal drops. At $t = 0.5$, which corresponds to readout of $\hat{Z}_L$ the terms have all phases of multiples of 2π and ideally would completely rephase. Due to the finite squeezing the overlap characteristic function $\langle r|\,\hat{\mathcal{D}}(tl_Z)\,|r\rangle = \exp(-|tl_Z|^2 e^{-2r})$ reduces which leads to a smaller revival. Note that for a squeezed vacuum state $|r\rangle$, the characteristic function is always real, which is in general not the case. The next revival occurs at $t = 1$ corresponding to readout of the stabilizer operator, where we see that the overlap dropped even further.

The squeezed components used to build up the state are shifted in the case of $|1\rangle_L$. This leads to changes in the geometric phase factors by $2\pi t$, which generate the negative revival at $t = 0.5$. Similar arguments can be made for the readouts in the other directions, for example in the l_X case components originating from neighboring grid state components will overlap. These overlaps add up constructively or destructively dependent on the initial relative phase between the components.

8.5.2 $\hat{X}_L$ eigenstates

The state $|+\rangle_L$ is created by first preparing $|0\rangle_L$ and then subsequently applying the teleported logical operation $\hat{U}_L^X(0, \text{arb.})$. For this teleported operation no resonant carrier operation is required on the ancillary qubit and thus the phase ϕ is not defined. The internal state controlled shift implemented using the SDF in this case is $\pm l/2$, which creates a superposition of six squeezed displaced components but misplaced from the origin relative to the desired code state. The corrective shift of $l/4$ removes this displacement and creates:

$$|+\rangle_L \propto [\hat{\mathcal{D}}(-l) + \hat{\mathcal{D}}(-l/2) + 2 + 2\hat{\mathcal{D}}(l/2) + \hat{\mathcal{D}}(l) + \hat{\mathcal{D}}(3/2l)]\,|r\rangle \tag{8.18}$$

conditioned on a dark readout. Additional application of $\hat{Z}_L = \hat{\mathcal{D}}(i\pi/l)$ creates $|-\rangle_L$. Measurement results alongside the theoretical Wigner functions are shown in figure 8.8. The Wigner functions in this case look like the $\pi/2$-rotated versions of the plots shown in figure 8.7. For both states $|\pm\rangle_L$, we find $\langle \hat{Z}_L \rangle \approx 0$. This is due to half the periodicity in these states, which leads to destructive interference at $t = 0.5$. As expected a positive (negative) revival is now visible in the $\langle \hat{X}_L \rangle$ signal of the state $|+\rangle_L$ ($|-\rangle_L$). These experiments were simulated using motional dephasing of $\Gamma = 30\ s^{-1}$, which is higher than for the $\hat{Z}_L$ eigenstates and indicates an incomplete understanding of the relevant dephasing mechanism for these more complicated states.

8.5.3 $\hat{Y}_L$ eigenstates

We create $|\phi_+\rangle_L = \hat{U}_L^X(\pi/2, \pi)\,|0\rangle_L$. The implementation of the teleported operation $\hat{U}_L^X(\pi/2, \pi)$ requires the ancillary carrier rotation and relies on control over both the phase ϕ as well as the angle θ. These define the relative weights and phases of the six components building up this state. $|\phi_-\rangle_L$ is then created using the additional $\hat{Z}_L$ shift. Results and theoretical Wigner functions are shown in figure 8.9. The periodicity of the states in the Wigner function is rotated by $\pi/4$ and additionally stretched by $\sqrt{2}$. Thus the readout of direction l_Y qualitatively behaves like the l_Z readout in case of the $\hat{Z}_L$ eigenstates. These two directions mark the same patterns in the Wigner functions. In this case again $\Gamma = 30\ s^{-1}$ was used in the simulation of the experiments.

8.5.4 State tomography

At $t = 0.5$ the measurements read out the logical Pauli operators which allows us to reconstruct the logical qubit density matrix

$$\hat{\rho}_L = \frac{1}{2}(\mathbb{1}_L + \langle \hat{X}_L \rangle \hat{X}_L + \langle \hat{Y}_L \rangle \hat{Y}_L + \langle \hat{Z}_L \rangle \hat{Z}_L). \tag{8.19}$$

Any measurement will yield an expectation value in the range [-1,1] and thus lead to a valid density operator. However it is worth noting that state

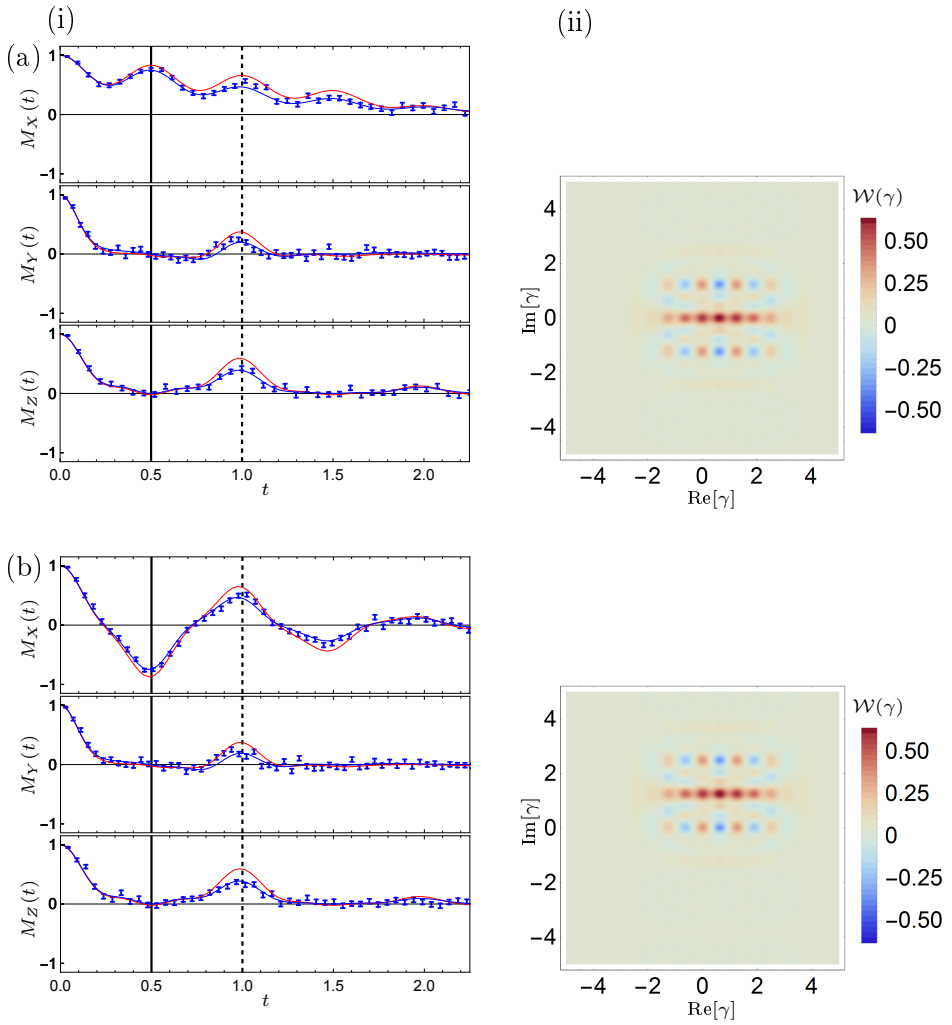

Figure 8.8: Analysis of $\hat{X}_L$ eigenstates. column (i) shows the readouts $M_j(t) \equiv \mathrm{Re}[\langle \hat{\mathcal{D}}(tl_j) \rangle]$ along the three phase space axis l_j as a function of t. Blue points and error bars provide measurements and s.e.m errors, while the blue line shows a Lindblad Master equation simulation including motional dephasing. The red line shows an analytic calculation for the chosen approximation not including any dephasing. The vertical dashed (solid) line highlights readout of the stabilizer (logical Pauli) operations. In column (ii) the theoretical Wigner function of this approximate code state is shown. (a) Shows results for $|+\rangle_L$, while (b) shows measurements for $|-\rangle_L$.

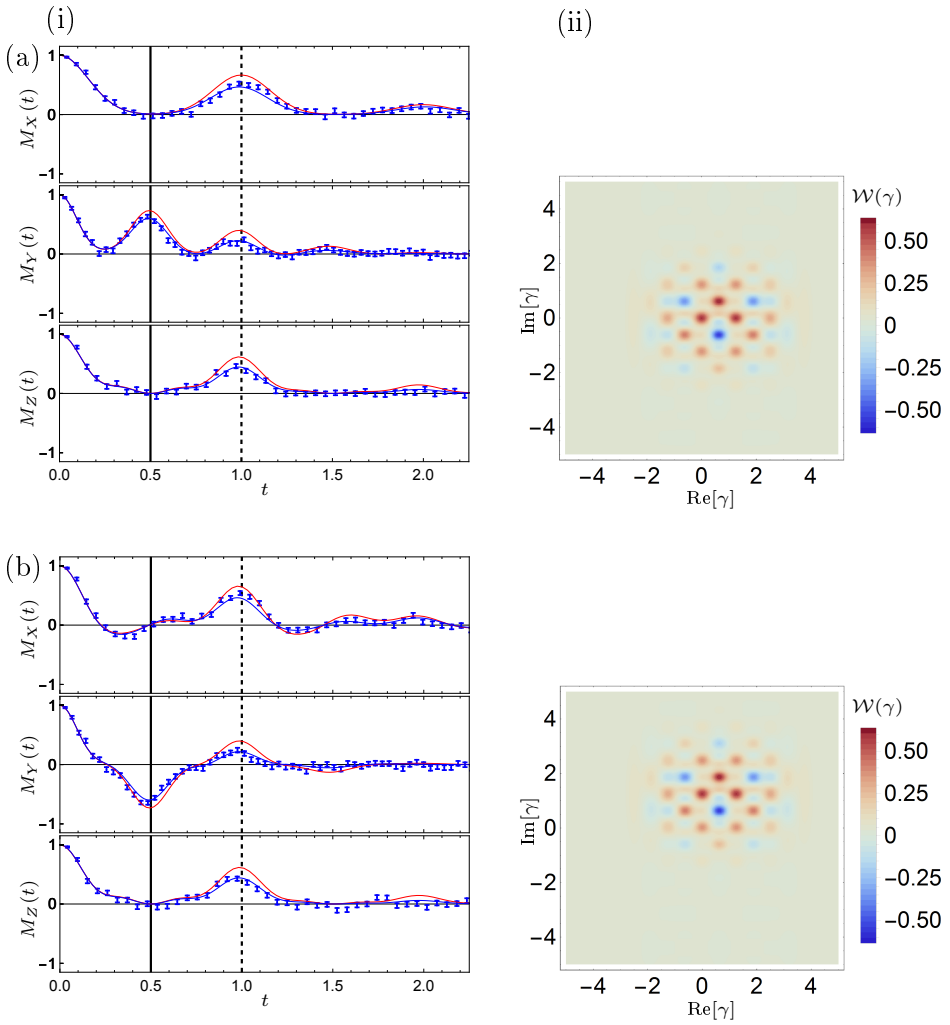

Figure 8.9: Analysis of $\hat{Y}_L$ eigenstates. column (i) shows the readouts $M_j(t) \equiv \mathrm{Re}[\langle \hat{\mathcal{D}}(tl_j)\rangle]$ along the three phase space axis l_j as a function of t. Blue points and error bars provide measurements and s.e.m errors, while the blue line shows a Lindblad Master equation simulation including motional dephasing. The red line shows an analytic calculation for the chosen approximation not including any dephasing. The vertical dashed (solid) line highlights readout of the stabilizer (logical Pauli) operations. In column (ii) the theoretical Wigner function of this approximate code state is shown. (a) Shows results for $|\phi_+\rangle_L$, while (b) shows measurements for $|\phi_-\rangle_L$.

tomography does not assess how well we are within the code space. An illustrative example would be the measurement of $\langle \hat{X}_L \rangle = \langle \hat{Y}_L \rangle = \langle \hat{Z}_L \rangle = 0$. This result could be obtained either from a fully mixed logical grid qubit state given by $\hat{\rho}_L = \frac{1}{2}\mathbb{1}_L$, or from a motional state which has fully decohered. In the first case the stabilizer values would both be $+1$ while for the latter the stabilizer readout would give zero.

The logical readout levels are limited by the underlying approximate code states. In particular they depend on how well the states are true eigenstates of the two stabilizer operators $\hat{S}_X$ and $\hat{S}_Z$. The readout of $\hat{S}_X$ and $\hat{X}_L$ improves with a higher number of squeezed components, while more initial squeezing improves the $\hat{S}_Z$ and $\hat{Z}_L$ readouts. We optimized the experimental code states in such a way that readouts of $\hat{Z}_L$ and $\hat{X}_L$ are limited at a similar level. In turn the $\hat{Y}_L$ readout is limited by both the number of components and the squeezing and is thus expected to be lower.

We quantify the logical qubit quality by calculating the fidelity between the reconstructed state and the ideal state $|\mathrm{id}\rangle$ on the surface of the Bloch sphere as

$$F(\hat{\rho}_L, |\mathrm{id}\rangle) = \langle \mathrm{id}| \, \hat{\rho}_L \, |\mathrm{id}\rangle \, . \tag{8.20}$$

The average state creation and readout fidelity of five data sets measured over several days was 87.3% with a standard deviation between the averages of 0.7%. In this case the finite approximation limits the achievable average fidelity to 90.8%. These five sets of data are shown as red points on the Bloch sphere in figure 8.12. Furthermore at $t = 1$ we measure the stabilizer operators for which we find an average over the six input states $\langle \hat{S}_X \rangle = 56 \pm 1\%$ (65.8%), $\langle \hat{S}_Z \rangle = 41 \pm 1\% (59.2\%)$. The value given in the parentheses is the expectation due to the approximate nature of the code states (red line).

8.6 Logical qubit lifetimes

Traditionally two-level qubits are characterized by two timescales T_1: the time over which the higher energy state decays and T_2: the time over which a superposition of the two levels dephases. The latter is typically measured using the Ramsey technique as described in section 4.1. For the logical grid state qubit the notion of these two timescales is blurred since the underlying physical states are not given by a two level system. In order to measure a timescale relating to T_1 we prepare $|0\rangle_L$ and wait for a variable time after which we measure $\hat{Z}_L$. Results of this measurement as a function of the wait time are shown in figure 8.10 row (a) column (i) alongside a fit using an exponential decay $Ae^{-t/T}$ with fitting parameters A and T. In this measurement we find $T = 3.7 \pm 0.2\,\mathrm{ms}$. Unlike an energy level qubit this measurement does not decay completely to the other level. Instead we end up in an equal superposition more like a traditional measurement of T_2.

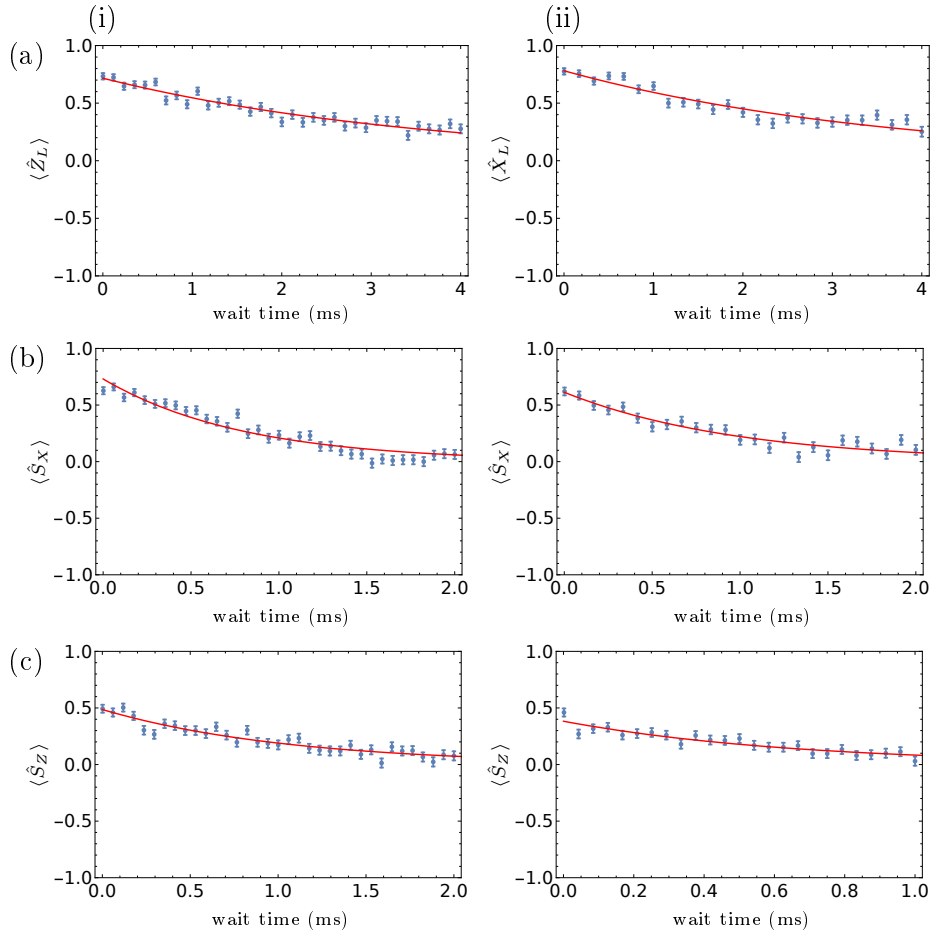

Figure 8.10: Grid qubit lifetime measurements. column (i) the state $|0\rangle_L$ (column (ii) the state $|+\rangle_L$) is prepared and after a variable wait time t the state is read out. The resulting measurement data (blue points with s.e.m. error bars) is fitted with an exponential decay $Ae^{-t/T}$ (solid line). (a) Shows readout of $\hat{Z}_L$ ($\hat{X}_L$) from which we find $T = 3.7 \pm 0.2$ ms ($T = 3.6 \pm 0.3$ ms). (b) Readout of $\hat{S}_X$ with $T = 0.8 \pm 0.1$ ms ($T = 1.0 \pm 0.1$ ms). (c) Readout of $\hat{S}_Z$ yielding $T = 1.1 \pm 0.1$ ms ($T = 0.7 \pm 0.1$ ms).

In the grid state encoding T_1 and T_2 are essentially the same parameters. This is seen by noting that the Hadamard operation can be implemented as a rotation of phase space by $\pi/2$ (and scaling if $l \neq \sqrt{2\pi}$). This is trivially implemented by updating the readout directions and scaling in our classical control system. In this sense the typical sequence to measure T_2, which involves preparing $|0\rangle_L$, applying the Hadamard operation, waiting for a fixed duration t and subsequently using an additional Hadamard operation followed by readout of $\hat{Z}_L$ simplifies to the previous experiment. Also note the close relation of the qubit lifetime measurements to the motional coherence measurements described in section 5.1.3.

However we can analyze the lifetime of our qubit with a second measurement. We prepare $|+\rangle_L$, wait for a duration t and readout $\hat{X}_L$. This can also be viewed as an analog of a Ramsey T_2 measurement[4]. The results of this measurement together with the exponential fit are shown in 8.10 row (a) column (ii). A similar timescale of $T = 3.6 \pm 0.3$ ms is extracted from the fit.

We can compare these logical qubit lifetimes to the decay of our averaged stabilizer readouts $\hat{S}_X$ and $\hat{S}_Z$, which we measure for both states $|0\rangle_L$ and $|+\rangle_L$. The results and timescales are given in 8.10 rows (b) and (c). We see that the stabilizer readouts decay on shorter timescales than the Pauli readouts. Thus the stabilizers have in some sense more sensitivity to errors than the Pauli operations. The functional form of these traces can not be simulated using a purely dephasing Lindblad Master equation simulation indicating multiple decoherence sources present in the experiments.

8.7 Universal single qubit gate set

8.7.1 Continuous operations

Readout of logical operators allows us to examine the teleported gates $\hat{U}_L^j(\theta, \phi)$ implemented using the ancilla qubit. First we set $\theta = \pi/2$ and use the controlled $\hat{X}_L$ operation. This implements a rotation around the X-axis $\hat{U}_L^X(\pi/2, -\phi) \propto R_L^X(\phi)$, with the choice of phase ϕ denoting the rotation angle. This operation applied to $|0\rangle_L$ is shown in figure 8.11 column (i). We see that the value of $\langle \hat{X}_L \rangle$ is largely unaffected, while a clear rotation is seen in the $\langle \hat{Y}_L \rangle$ and $\langle \hat{Z}_L \rangle$ signals. Figure 8.11 column (ii) shows similar data, obtained using $\phi = \pi/2$ while varying the value of θ again using the input state $|0\rangle_L$ and the controlled $\hat{X}_L$ operation. Although this transformation is useful in state preparation it is not unitary. The states produced using both operations are shown on the Bloch sphere in figure 8.12.

[4] In this case the Hadamard operations are replaced by preparation of $|+\rangle_L$ and analysis directly in the appropriate basis.

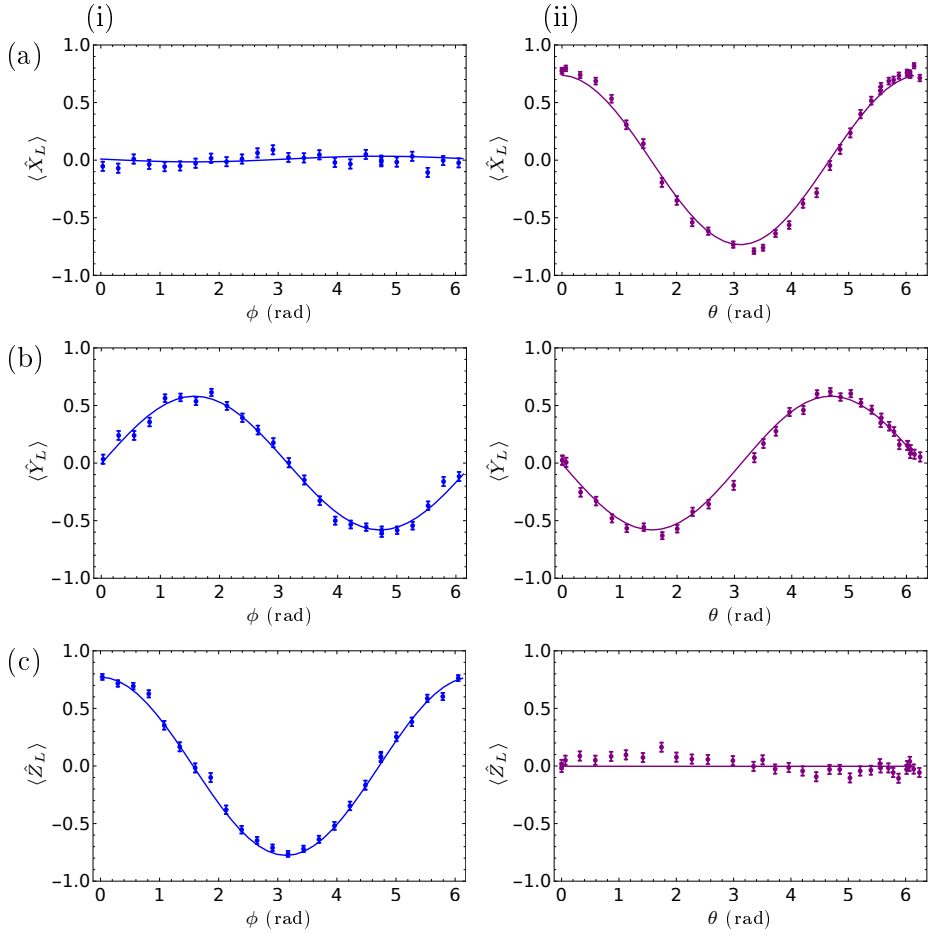

Figure 8.11: Continuous logical operations. column (i) shows $\hat{U}_L^X(\pi/2, -\phi)\,|0\rangle_L$ realizing a rotation around the X-axis of the Bloch sphere. column (ii) presents $\hat{U}_L^X(\theta, \pi/2)\,|0\rangle_L$. In both cases $|\psi_{\text{in}}\rangle = |0\rangle_L \propto [\hat{\mathcal{D}}(-l) + 2 + \hat{\mathcal{D}}(l)]\,|r = 0.91\rangle$ with l=2.36 and errors are given as s.e.m. while the solid line show the Lindblad Master simulation of the experiment.

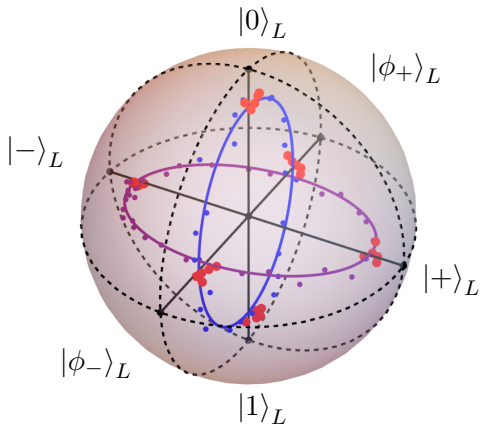

Figure 8.12: Logical state preparation, readout and continuous operations summarized on the Bloch sphere. Shown as red points are five sets of created states measured over several days. Their average fidelity was 87.3% with a standard deviation between the averages of 0.7%. In this case the finite approximation limits the achievable average fidelity to 90.8%. Blue and purple points show results of two continuous operations applied to $|0\rangle_L$ while the solid line show the Lindblad Master simulation of these experiments.

8.7.2 Process tomography

To characterize the performance of our qubit operations we use quantum process tomography. The six approximate eigenstates of $\hat{X}_L$, $\hat{Y}_L$ and $\hat{Z}_L$ are used as input states, which are then subjected to the process of interest. The states $|0\rangle_L$, $|1\rangle_L$, $|+\rangle_L$ and $|\phi_+\rangle_L$ were created as described in section 8.5. In contrast the states $|-\rangle_L$ and $|\phi_-\rangle_L$ where directly created from $|0\rangle_L$ using the operations $\hat{U}_L^X(\pi, \text{arb.})$ and $\hat{U}_L^X(\pi/2, 0)$ instead of shifting the corresponding $+1$ eigenstates using Pauli operations.

For each input state the three Pauli operators are measured: $\hat{\rho}_L^j = \sum_k o_{jk}\hat{\sigma}_k$. Here j labels the input state number, k the Pauli basis element and o_{jk} correspond to the readout results (where we added $o_{j0} = 1/2$ for the identity basis element). Then we apply the process of interest to each input state and reconstruct the output state in the same way with λ_{jk} the corresponding measurement results. An arbitrary physical process connecting input states to output states can be expressed in the Pauli basis introducing the process matrix Ξ:

$$\mathcal{E}(\hat{\rho}_L^{\text{in}}) = \hat{\rho}_L^{\text{out}} = \sum_{mn} \hat{\sigma}_L^m \hat{\rho}_L^{\text{in}} \hat{\sigma}_L^n \Xi_{mn}. \tag{8.21}$$

A linear set of equations for the matrix elements of Ξ_{mn} connects o_{jk} to λ_{jk}:

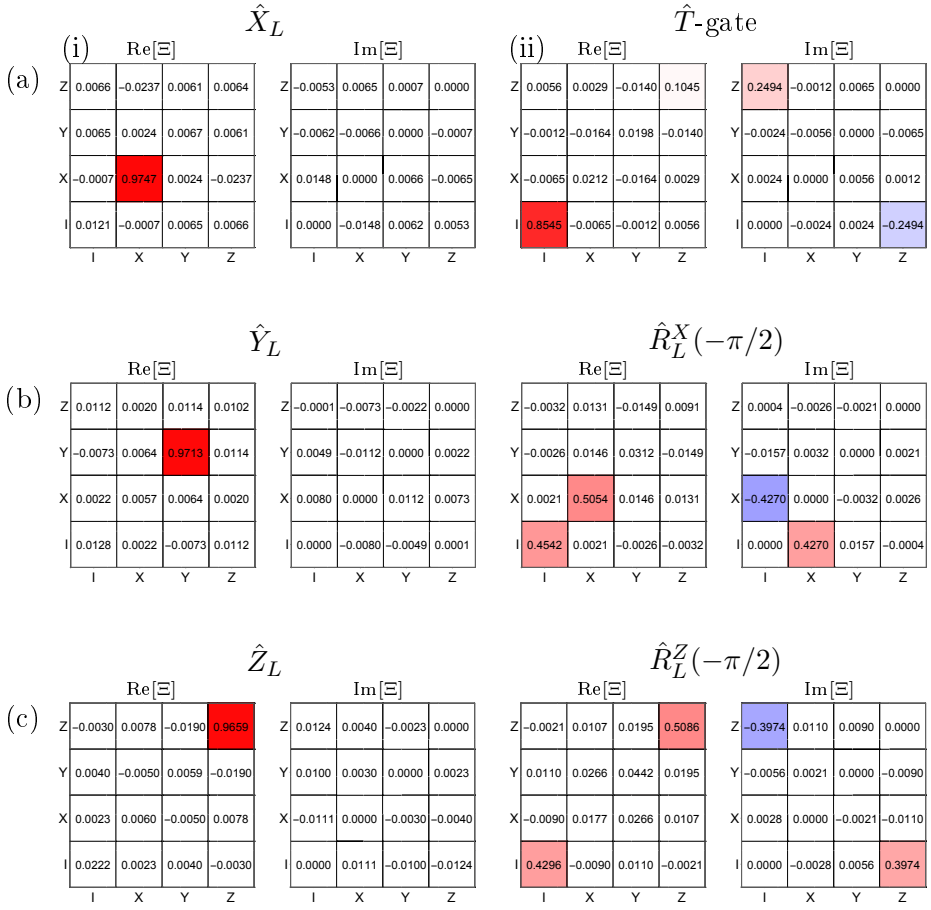

Figure 8.13: Process tomography of logical operations, characterized by the Ξ matrix. The reconstructed operations are column (i) Pauli gates, implemented by phase space displacements, and column (ii) continuous operations implemented using teleported gates these were $\hat{T}_L = \hat{R}_L^Z(\pi/4)$, $\hat{R}_L^X(-\pi/2)$ and $\hat{R}_L^Z(-\pi/2)$. The Hadamard operation $\hat{H}_L$ is given by an oscillator phase space rotation of $\pi/2$, which can be conveniently realized as an update to the readout direction in the classical control system. Such a permutation of readout results trivially leads to a perfect process tomography result. Each panel displays the real and the imaginary part of the experimentally reconstructed Ξ matrix. Each entry is colored where red (blue) colors indicate positive (negative) values.

	$\hat{X}$, $\hat{Y}$, $\hat{Z}$	$R_L^X(-\pi/2)$	$R_L^Z(-\pi/2)$	$\hat{T}_L$
F_{measured}	97%	91%	87%	92%
$F_{\text{approx.}}$	100%	94%	93%	96%
$F_{\text{simulation}}$	100%	91%	89%	93%

Table 8.1: Process fidelities $F = \text{Tr}(\Xi\Xi_{\text{id}})$. The first row evaluates the fidelity of the measured process matrix to the the ideal qubit gate. The second row provides an analytic calculation of the approximate code states transformed under the ideal gate. Input states and resultant output states were then evaluated using the numeric least square fit. The last row gives results from a Lindblad-Master simulation of the full experiment including input state preparation. The difference between simulated values and the experimental fidelities are likely due to miscalibration of the experimental parameters.

($\vec{\lambda} = \beta\ \vec{\Xi}$) with the matrix β calculated from the input state measurements o_{jk}. The process matrix Ξ is Hermitian and non-negative definite. To ensure these properties we parametrize $\Xi = \hat{T}^\dagger\hat{T}$ with

$$\hat{T} = \begin{pmatrix} t_1 & 0 & 0 & 0 \\ t_5 + it_6 & t_2 & 0 & 0 \\ t_{11} + it_{12} & t_7 + it_8 & t_3 & 0 \\ t_{15} + it_{16} & t_{13} + it_{14} & t_9 + it_{10} & t_4 \end{pmatrix} \tag{8.22}$$

a tridiagonal matrix [208]. We find 4 more constraints on the elements of $\hat{T}$ following from trace preservation of the logical process [209]. Ensuring these constraints we find the t_i elements which minimize $|\beta\ \vec{\Xi} - \vec{\lambda}\ |^2$ using the NMinimise function of Mathematica.

Results for a universal set of logical gates are shown in figure 8.13. The presented set of gates is given by all three Pauli operations $\hat{X}_L$, $\hat{Y}_L$ and $\hat{Z}_L$, together with the $\hat{T}_L$ gate ($R_L^Z(\pi/4)$), and two $\pi/2$-rotations $R_L^X(-\pi/2)$ and $R_L^Z(-\pi/2)$ about orthogonal axes. The latter three were performed by gate teleportation. The quality of each of these operations can be evaluated by calculating the process fidelity $F_{\hat{O}} = \text{Tr}(\Xi\Xi_{\text{id}})$ between the experimentally obtained Ξ and the ideal logical qubit matrix Ξ_{id}. Results of measured fidelities are summarized in table 8.1 and range between $\text{F}_{\hat{\sigma}_L^j} = 97\%$ for the Pauli operations to $\text{F}_{R_L^Z(-\pi/2)} = 87\%$ for the $\pi/2$ pulse around the Z-axis. The numerical optimization used for determining Ξ makes the evaluation of error bars non-trivial and we thus forego quoting error bars here. Additionally we note that the Hadamard gate can be implemented as an update of the readout directions. By definition, the process tomography routine then gives an ideal process matrix and a process fidelity of 1.

The presented method of process tomography is independent of the chosen grid state encoding. We solely specify the methods of input state creation, state tomography and analyze how well the implemented processes realize logical single qubit operations. Nevertheless we have additional knowledge about our code states and logical readout and see that a number of effects are not accounted for in process tomography. In order to understand the level of process fidelity decrease due to such effects we calculate the process matrix for the ideal process on the ideal approximate code states with the experimentally used number of components and parameters l and r. From this we calculate the fidelity due to the approximation. Results are given in the second row of table 8.1.

One effect related to the approximate nature of code states is that the readout levels differ for $\hat{X}_L$, $\hat{Z}_L$ and $\hat{Y}_L$. During gates these readout directions are interchanged for example the logical $\pi/2$-rotation around the Z-axis transforms logical $\hat{Y}_L$ readouts to $\hat{X}_L$ readouts. In this case we expect the readout levels to increase! Rescaling of the readout directions in order to account for such effects is not trivial since in the rotation implemented by gate teleportation typically the underlying states change (i.e more squeezed components or spread out squeezed states) which in general also changes the logical readout level. Furthermore in general gates rely on the interference of the squeezed wave packets building up the grid states. Due to their finite nature destructive interference in particular will not be complete.

To further assess susceptibility to dephasing of our oscillator we simulate the process tomography experiment using the typical level of dephasing present in our experiment, and once more estimate a fidelity, see the last row of table 8.1. We observe that for the Pauli operations all features related to the approximate code states drop out in the process tomography. Additionally since the displacement operation is relatively fast the effects of motional dephasing are minimal compared to that incurred during state preparation and thus this does not influence the process tomography result. For the teleported operations the duration is longer, which leads to lower expectations for the gate fidelities. The difference between the simulated fidelities and the measured fidelities are assumed to be due to mis-calibration of the experimental parameters.

8.8 Discussion and outlook

We have demonstrated encoding and control of a grid state qubit. Extensions to this work would include performing error correction or control of multiple encoded qubits. Furthermore quantum metrology based on the newly synthesized grid states can be explored. A discussion of some of these possibilities are listed below.

8.8.1 Grid states and the Heisenberg uncertainty relation

The Heisenberg uncertainty relation, equation 2.10, limits the product of uncertainties in position and momentum. Nevertheless the ideal grid state manages to have sharply defined values of modular position and momentum. Consider the superposition of infinitely many infinitely squeezed states given by:

$$|\text{grid}\rangle \propto \hat{\mathcal{D}}(ip_0) \sum_{k=-\infty}^{\infty} \hat{\mathcal{D}}(kl)\,|q_0\rangle \tag{8.23}$$

where $|q_0\rangle$ is a dimensionless position eigenstate and the variables $p_0 \in [0, \pi/l)$, $q_0 \in [0, l)$. The Wigner function of the state $|\text{grid}\rangle$ forms a two dimensional grid of delta peaks. These are indicated as dots in the schematic figure 8.14 where blue indicates peaks with negative signs while red stands for positive peaks. This state is an eigenstate of the two operations $\hat{\mathcal{D}}(l)$, $\hat{\mathcal{D}}(i\pi/l)$:

$$\hat{\mathcal{D}}(l)\,|\text{grid}\rangle \propto e^{-2ilp_0}\,|\text{grid}\rangle \qquad \hat{\mathcal{D}}(i\pi/l)\,|\text{grid}\rangle \propto e^{2i\pi q_0/l}\,|\text{grid}\rangle\,. \tag{8.24}$$

In other words the ideal grid state has precisely defined values for the modular observables $\text{Re}[\hat{\mathcal{D}}(l)] = \cos(-2l\hat{q})$ and $\text{Re}[\hat{\mathcal{D}}(i\pi/l)] = \cos(2\pi/l\hat{p})$.

The uncertainty relation still holds because these two observables commute. Nevertheless it is interesting that we can simultaneously learn precisely the two values of a periodic function of position as well as of momentum. Considering the grid in figure 8.14 we can express full information about dimensionless position and momentum by specifying both in which box the state is and where inside the box. The modular variables provide exact information only about the latter but leave completely uncertain in which of the boxes the state is. While the squeezed state traded uncertainty in one variable for the other, the grid state distributes the uncertainty across the full phase space allowing for precise values of modular variables.

8.8.2 Quantum metrology

Periodic states were considered already by von Neumann in his seminal book on foundations of quantum mechanics [49], where he thought about constructing measurements approximating simultaneous position and momentum measurements. More recent works propose to use the grid states for precise sensing of oscillator shifts due to small oscillating fields [210]. The key property of the grid state is that a single probe state provides "effective" squeezing along both directions. This is characterized by the effective squeezing parameter defined through the measurement of the stabilizer operator on the state [210]:

$$\Delta_j \approx \sqrt{\frac{1}{\pi} \ln\left(\frac{1}{\langle \hat{S}_i \rangle^2}\right)}. \tag{8.25}$$

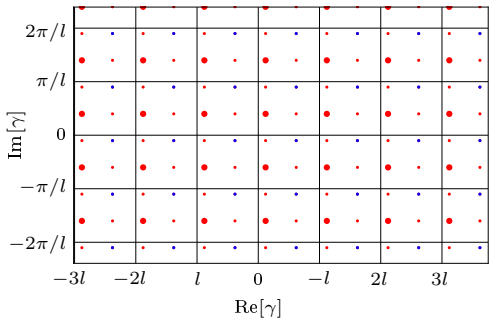

Figure 8.14: Schematics of the Wigner function of $|\text{grid}\rangle \propto \hat{\mathcal{D}}(ip_0)\sum_{k=-\infty}^{\infty}\hat{\mathcal{D}}(kl)\,|q_0\rangle$. The interference of the shifted position eigenstates $\hat{\mathcal{D}}(kl)\,|q_0\rangle$ leads to the build up of a two dimensional grid of delta functions. Blue point indicate delta functions with negative signs while red points show positive signs. The periodicity of the state is highlighted using the larger red points and the grid of lines. The position of this larger red point within one box of the grid is given by the bottom left corner of the box + (q_0, p_0).

If we consider the $\hat{S}_Z = \hat{\mathcal{D}}(\sqrt{2\pi}i)$ stabilizer acting on the vacuum state squeezed along the position direction, then we recover a relation to the standard squeezing parameter r as $\Delta_Z^2/2 = e^{-2r}$. Thus we more generally state the effective squeezing in dB for any state as $10\text{Log}_{10}(2/\Delta_j^2)$. The values of our stabilizer readouts on grid states are $\langle\hat{S}_X\rangle = 0.56 \pm 0.01$ and $\langle\hat{S}_Z\rangle = 0.41 \pm 0.01$ from which we calculate ≈ 7.3 dB and ≈ 5.5 dB of effective squeezing respectively.

Therefore use of sequential modular measurements on a single probe state is in principle able to provide a squeezing advantage for both directions. To do the same for example using squeezed states would require repetition of the experiment using two states squeezed along orthogonal directions. In the current system, where each bright result leads to decoherence of the motional state, we can only perform proof of principle experiments with short sequences of measurements. For example we could prepare the sense state and apply a small shift, which we will try to sense. Using this state we first perform one shot of phase estimation for the $\hat{S}_X$ stabilizer and conditioned on the dark detection we move on measuring $\hat{S}_Z$ using the post-measurement state of the first measurement as our input. Then we repeat the experiment preparing the same sense state and reading out a next bit of phase estimation. Like this it should be possible to measure the complete shift vector with higher accuracy than it is possible with a ground state cooled oscillator.

Using the real-time feedback control available in our experimental system allows to use Bayesian update for the choices of phase estimation settings in

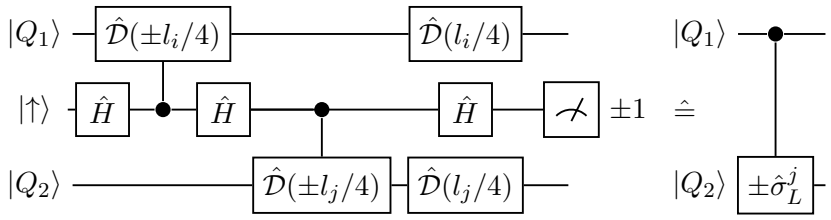

Figure 8.15: Two qubit gate implemented in two modes of a single trapped ion. This circuit implements $\hat{\sigma}_L^i$-controlled-$\pm\hat{\sigma}_L^j$ operations between two grid state qubits $|Q_1\rangle$ and $|Q_2\rangle$ mediated by one internal ancillary qubit $|\downarrow\rangle \leftrightarrow |\uparrow\rangle$. The sign of the operation is determined by the ancillary qubit readout.

each readout round. The best protocol in case of the reduced readout contrasts due to the approximate code states as well as our decoherence is currently under investigation. The multitude of motional states available in our system could allow comparison to other proposed sense states and sensing schemes like the compass states [210, 211], squeezed states [212], or Fock states [134, 213].

8.8.3 Two qubit gate mediated by internal state qubit

The tools presented in this chapter can be used to perform a two qubit gate on two logical qubits stored in two motional modes of a single ion. Let us assume we have a single ion and prepared logical grid qubit states $|Q_1\rangle$, $|Q_2\rangle$ in two of the three modes of oscillation. Let us further assume that we manipulated both these modes via the internal ancillary qubit levels $|\downarrow\rangle \leftrightarrow |\uparrow\rangle$. Then we can use the circuit given in figure 8.15 implementing a $\hat{\sigma}_L^i$-controlled-$\hat{\sigma}_L^j$ operation:

$$|-_i\rangle\langle -_i|_{L,\mathrm{id}} \otimes \mathbb{1}_L \pm |+_j\rangle\langle +_j|_{L,\mathrm{id}} \otimes \hat{\sigma}_L^j \tag{8.26}$$

with the sign $\pm$ determined by the readout result. This can best be derived by noting that the controlled shifts $\hat{\mathcal{D}}(\pm l_j/4)$ together with the unconditional shifts $\hat{\mathcal{D}}(l_j/4)$ can be replaced by controlled logical $\hat{\sigma}_L^j$ operations. The way we gave the circuit highlights that it can be implemented using carrier rotations, SDF pulses as well as unconditional displacements.

In our experimental system currently only the axial motional mode has sufficiently long coherence time in order to prepare and manipulate grid qubit states. The coherence time of radial modes is currently limited by trap RF potential stability, which in some way also affects multi-ion axial modes.

8.8.4 Coulomb coupling between neighboring wells for gates and error readout

An alternative method which is more applicable to performing quantum error correction would be to utilize the Coulomb coupling between local modes of two ions held in separate potential wells. This could be used in order to implement an exponential-SWAP gate (e-SWAP) [214–217]. The e-SWAP operation constitutes not only a two qubit gate for the GKP code it is further applicable to all bosonic encodings [217].

The e-SWAP operation could also be used to perform a non-destructive readout of error information from a grid state qubit in the following manner. First the encoded oscillator qubit is completely swapped to the (quasi-) local mode of the ion stored in the neighboring well by resonant exchange. A carrier rotation together with a SDF pulse are then applied to the second ion which transfers part of the syndrome information into that ion's internal state. This could for instance constitute one bit of information required for a phase-estimation protocol [174]. The SWAP operation is then repeated, transferring the encoded qubit back to ion 1. This procedure extracts one bit of relevant error information from the encoded grid qubit into the internal states of ion 2. The oscillations of the two ions are then detuned from each other such that fluorescence readout can be performed on ion 2 without destroying the encoded state in ion 1 (crosstalk of the internal states could be prevented by using ions of two species). For the next relevant bit of information the same procedure is repeated using a different carrier rotation setting. Multiple internal levels of the second ion could be used in order to readout more than one bit of information per SWAP cycle. The extracted information provides information on the oscillator shift up to a certain precision. Error recovery could then be performed by applying the opposite shift using an appropriate tickling pulse to the encoded qubit.

For this scheme excellent control over the trapping potentials are required, which is currently investigated in the TIQI group. First experiments on splitting and merging of wells are discussed in [127] and schemes for transporting wells with negligible heating are analyzed in theory [218] and practice [219]. All these are first steps towards the required control and will be developed further in the future.

8.8.5 Non-destructive readout based on cavity integration

Alternatively cavities integrated to ion traps could be used for non-invasive fluorescence readout. Using cavities could provide directional fluorescence readout with momentum kicks along the perpendicular direction of the mode of interests or other schemes could potentially be employed [220, 221]. The integration of cavities is also currently pursued in the TIQI group.

8.8.6 Repumping of internal states based on few scattering events

Measurement-free error correction schemes [222] could potentially be devised for the grid states. In this case corrections based on internal state dependent shifts combined with repumping of the internal state should be sufficient. The latter could potentially be done based on very few photon scattering events. One could for example use a narrow 854 nm laser selectively addressing the transition ${}^2D_{5/2}, m_j = 3/2 \leftrightarrow {}^2P_{3/2}, m_j = 3/2$ from where the main decay channel would be to ${}^2S_{1/2}, m_j = 1/2$. Careful simulation of the remaining disturbances and the best laser frequencies to use will be required to see if such schemes could be worth pursuing.

8.8.7 Stabilization of code states

Instead of performing full error correction we could aim to just extend the lifetime of a logical state. We could first prepare $|0\rangle_L$ by few rounds of post-selected modular measurements. Then we could investigate if it would be possible to extend the lifetime of such a state via further measurements of the stabilizers and the $\hat{Z}$ Pauli operator. After initial state preparation these measurements have a high chance of being dark results. Relevant questions to answer are: At what times should measurements be performed? And what happens to the larger states continuously projected in to the periodic states?

Related work is currently pursued for superconducting cavities in the group of M. Devoret at Yale. The superconducting platform compared to trapped-ions does not experience an intrinsic readout problem. Therefore code states can be prepared and stabilized using phase-estimation protocols of the stabilizers and the $\hat{Z}$ operator. This scheme has been proposed theoretically in [174]. Preliminary results show proof of principle preparation and stabilization of logical code states[5].

8.8.8 Optimized control pulses

Using optimized control pulses would allow to prepare grid states without post-selection. Motivated by the methods presented in [108], I supervised a study by Chams Rutkowski. He analyzed gradient ascent methods in order to find step wise constant blue and red sideband pulse amplitudes and phases which prepare a grid state directly from a ground state cooled ion [223]. In this scheme we have neglected off resonant effects. The calibration of this scheme will be hard in practice because the blue sideband power will depend on the present red sideband settings. Alternatively the control parameters could be taken to be a tickling phase and amplitude, together with one of the sideband parameters, while the others sideband is set to be constant. This will simplify

[5] private communications

a future calibration look-up table. Implementation of such pulses in practice is left for future experiments.

8.8.9 Concatenation

To successfully concatenate grid states with qubit stabilizer codes such as the surface [111] or Toric [107] codes an improvement in the approximation to ideal grid states would be required. Theoretical results indicate the need for squeezing levels on the order of $\approx 10 - 15$ dB in both phase space dimensions, with the exact value dependent on the chosen error-model, the architecture considered and the available quality of control.

We have previously prepared squeezed-vacuum states with ≈ 12.59 dB [40] but improvements in both trap stability and optimization of calibration techniques would be required to achieve this for both q and p of a grid-state qubit. Using numerical simulations we assess the required improvements to reach levels of 10 dB squeezing or better. As an example, we simulate the creation and stabilizer readout of a logical $|1\rangle_L$ using the following assumed conditions:

1. Doubling the current laser power, leading to a $\sqrt{2}$ improvement in our Rabi frequencies.
2. Shortening the FPGA decision time of each modular measurement from 50 us to 10 us
3. Adding one more round of modular measurement for the initial state preparation and increasing the squeezing to $r = 1.4$. This leads to the approximate preparation of the state $|1\rangle_L \propto [\hat{\mathcal{D}}(-1.5l) + 3\hat{\mathcal{D}}(-0.5l) + 3\hat{\mathcal{D}}(0.5l) + \hat{\mathcal{D}}(1.5l)]\,|r = 1.4\rangle$ with $l = \sqrt{2\pi}$.
4. Reducing our dephasing rate in the Lindblad operator $\sqrt{\Gamma}(\hat{a}\hat{a}^\dagger + \hat{a}^\dagger\hat{a})$ to $\Gamma = 2\,s^{-1}$.

This simulation leads to effective squeezing of ≈ 10.05 dB and ≈ 10.30 dB. However this does not include infidelities due to imperfect squeezed state preparation or mis-calibrations of the SDF pulse.

Chapter 9

Direct reconstruction of a grid state

Previously explored phase space reconstruction methods, as used for the results presented in chapter 6 have been indirect [29, 112]. They relied on several hundred of ion internal state detections for the reconstruction of a single phase space point. For reconstruction of oscillator states showing narrow features over a larger phase space extent, such as the logical grid qubit states explored in the previous chapter, these methods simply become too demanding. In the present chapter we resolve this limitation and perform tomography of a logical $|0\rangle_L$ grid state by implementing direct state reconstruction based on interfering wave packets. Using this technique a single measurement detection provides information about one phase space point of the symmetric characteristic function. We close this chapter with a comparison to the reconstruction methods discussed in chapter 6.

9.1 Measurement procedure

Performing a modular measurement as described in section 7.1 allows us to extract information about the characteristic function of the oscillator input state $|\psi_{\text{in}}\rangle$. We implement the modular measurement in this chapter by first applying a carrier rotation $\hat{R}(\theta, 0)$ to the internal state qubit initialized to $|\uparrow\rangle$. After this rotation we apply a SDF pulse, realizing $\hat{\mathcal{D}}(\beta\hat{X}/2)$, and end the measurement with the final fluorescence readout of the internal states. This sequence implements the modular measurement defined by the circuit 7.1 with $\varphi = -\theta$, $\hat{U} = \hat{\mathcal{D}}(-\beta/2)$ and for consistency the variable α is replaced by β. The readout of the internal states follows:

$$\begin{aligned}\langle\hat{Z}\rangle &= \langle e^{i\theta}\hat{\mathcal{D}}(-\beta) + e^{-i\theta}\hat{\mathcal{D}}(\beta)\rangle/2 \\ &= \cos(\theta)\text{Re}[\langle\hat{\mathcal{D}}(\beta)\rangle] + \sin(\theta)\text{Im}[\langle\hat{\mathcal{D}}(\beta)\rangle].\end{aligned} \tag{9.1}$$

Typically we perform a first measurement with $\theta = 0$[1], which reads out the real part of the characteristic function. This together with a second measurement with $\theta = \pi/2$, measuring the imaginary part, provides full information about $\chi(\beta) = \langle\psi_{\text{in}}|\,\hat{\mathcal{D}}(\beta)\,|\psi_{\text{in}}\rangle = \langle\hat{\mathcal{D}}(\beta)\rangle$. Note that any pair of angles differing by $\pi/2$ provide full information about the characteristic function.

9.1.1 Phase space sampling

Because the characteristic function is a Hermitian function $\chi(\beta)^* = \chi(-\beta)$ any half of the complex space covered by β is sufficient for measuring the full characteristic function. Thus using this scheme only a single fluorescence readout setting[2] is required to obtain one characteristic function point, which is two orders of magnitude fewer than in the Wigner function reconstruction method described in chapter 6.

The number of sampled points can be reduced further by optimizing the sampling pattern [224]. Various additional techniques can be exploited, including prior knowledge of the state under reconstruction or Bayesian methods based on choosing the next sampling point dependent on the already measured outcomes [167]. The latter may be interesting as measurements close to the origin of the characteristic function contain information about its extent in phase space. Nevertheless in testing and demonstrating the reconstruction method itself, we sample the state on an uniformly-spaced square grid in order to learn more about the method and obtain directly visually appealing pictures of the quantum mechanical oscillator states.

The physical control parameters for the sampled phase space points β are in polar coordinates. $|\beta|$ is proportional to the Rabi frequency and time of the SDF laser, while $\arg(\beta)$ is given by the laser phases as described in section 3.6.2. The Rabi frequency and laser phase are pre-calibrated using the methods discussed in chapter 5. The experimental control code then converts the desired phase space point in Cartesian coordinates $\{\text{Re}[\beta], \text{Im}[\beta]\}$ to the required physical parameters. In cases where the conversion leads to pulse times below 1.4 us (the shortest currently allowed pulse time) no pulse is run and the measurement corresponds to the origin. For typical laser powers a pulse duration of 1.4 us corresponds to roughly $\delta\beta = 0.05$. Time increments of 8 ns are possible at longer pulse times, and the sampling is limited by the SDF stability. Fluctuations and a calibration accuracy of 1 % in the overall coupling strength of the SDF lead to errors in $|\beta|$ of around 0.005 for $|\beta| \approx 1$, which linearly increases for phase space points with a larger distance from the origin. At $|\beta| \approx 7$ errors are on the order of 0.035 . Resolution and laser stability are sufficient for resolving the relevant features of the states presented in the following, thus we did not take additional care for measurements close to the origin. If the experimental interest is in resolving very small $|\beta|$ then the

[1] no carrier pulse is run

[2] which still is repeated few hundred times in order to extract a probability

laser power can be reduced in order to obtain a smaller innermost step $\delta\beta$ and additionally reduce effects related to the turn-on characteristics of the pulses.

9.1.2 Discrete Fourier transform

Wigner function and characteristic function are connected via the two-dimensional Fourier transform given in equation 2.20, which we repeat here for convenience:

$$\mathcal{W}(\gamma) = \frac{1}{\pi^2} \int \chi(\beta) e^{\gamma\beta^* - \gamma^*\beta} d^2\beta. \tag{9.2}$$

Integrating the Wigner function over one dimension yields its marginal, which relates to the probability density along the perpendicular direction [122]

$$P(\gamma^\lambda) = \int_{-\infty}^{\infty} \mathcal{W}(\gamma^\lambda, \gamma^{\lambda+\pi/2}) d\gamma^{\lambda+\pi/2}. \tag{9.3}$$

Here we used the quadrature variables $\gamma^\lambda \equiv \frac{1}{2}(\gamma e^{-i\lambda} + \gamma^* e^{i\lambda})$, $\gamma^{\lambda+\pi/2}$. Note that $\gamma^0 = \mathrm{Re}(\gamma)$, while $\gamma^{\pi/2} = \mathrm{Im}(\gamma)$. Inserting 9.2 into 9.3 and performing the integration over $\gamma^{\lambda+\pi/2}$ yields:

$$P(\gamma^\lambda) = \frac{1}{\pi} \int_{-\infty}^{\infty} \chi(0, \beta^{\lambda+\pi/2}) e^{2i\gamma^\lambda \beta^{\lambda+\pi/2}} d\beta^{\lambda+\pi/2}. \tag{9.4}$$

Thus the Fourier transform of a one-dimensional measurement of the characteristic function along $\beta^{\lambda+\pi/2}$ provides a measurement of the probability density in dimensionless phase space along the perpendicular direction. Such one-dimensional characteristic function measurements have been used previously in trapped-ion systems [225–227] in order to extract position probability densities. Additionally in [228] the authors used a sequence of 8 properly timed ultrafast laser pulses (not limited by the Lamb-Dicke regime) in order to extract 2D characteristic functions of hot thermal states. In our setup the pulse sequence for 2D extraction of the characteristic functions is much simpler, allowing us in particular to confirm more fragile stable phase relations of separated superposition states.

The measurements of the characteristic function are expected to drop to zero for shifts larger than the extent of the oscillator state. The discrete two-dimensional Fourier transform of the N_{meas} measured points is performed by zero-padding of the data outside of the measurement range with roughly $N_0 = 150$ additional points. We typically measure states over their whole extent, such that outside the measurement range a signal close to zero is expected. The amount of zero-padding sets the resolution of the Wigner function $\delta\gamma = \pi/[(N_{\mathrm{meas}} + N_0)\delta\beta)]$. Without zero-padding, typically not enough points lie in the relevant range of the Fourier transform, in order to resolve the features of the state. In cases where the characteristic function is

not sampled on an equidistant grid we re-sample the measurement points on such a grid by linearly interpolating between the measurement points. For the measurements performed this is expected to have a marginal impact on the Fourier transform result.

Internal state preparation infidelity leads to a small constant bias o in the measured characteristic function $\chi_{\text{meas.}} = \chi(1-o)+o$ (see App. F). In the Fourier transform such an offset o leads to a large component around the origin. Thus we first fit the large data set to its expected χ form including a floating bias o. We then remove the bias extracted from the fit before performing the discrete Fourier transform.

The real part of the Fourier transform provides a measure of the Wigner function of the state, while the imaginary part provides information about imperfections in our reconstruction method. In particular the imaginary part shows how non-Hermitian our characteristic function measurement was. This may be due to experimental drifts between the measurement of β and $-\beta$, a bias in the SDF leading to a difference in displacing to one side as compared to the opposite side, or due to fluctuations from projection noise.

Bootstrapping

To assess the sizes of non-systematic errors in the Fourier transform bootstrapping can be used [229]. To do so only a small part of the raw data is sampled and Fourier transformed. Comparing the mean and the standard deviation of multiple rounds of resampling provides an approximate measure of errors. For ion trap experiments the resampling could be performed at the level of bare photon counts, but resampling is also possible at later stages, for example after thresholding the bare counts. In the results presented in chapter 8, we first thresholded the bare counts and then estimate the bright state probability from around 20 thresholded shots. This process was repeated roughly $40-50$ times. The resampling was performed by randomly "choosing with repetition" ≈ 20 of the $40-50$ measured probabilities, which was repeated a few hundred times.

9.2 Measurement results

9.2.1 Squeezed vacuum

Figure 9.1 (a) and (b) show the reconstruction of the real and imaginary parts of the characteristic function of a squeezed vacuum state $\hat{\mathcal{S}}(re^{i\vartheta})\,|0\rangle$, which was independently calibrated to $r_{\text{calib}} = 0.93 \pm 0.02$ and its orientation is chosen to be $\vartheta_{\text{calib}} = 0$. The phase space results shown in figure 9.1 closely follow the expected signals discussed in section 2.4.2.

A closer look reveals small discrepancies. For example the imaginary part shows a small non-zero signal. To analyze such effects we fit the characteristic function data to the expectation for a displaced squeezed state

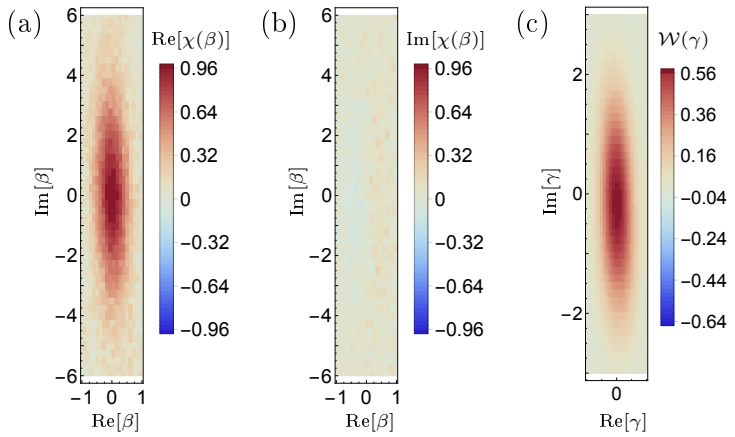

Figure 9.1: Reconstruction of a squeezed vacuum state $|\psi\rangle_{\text{calib}} = \hat{\mathcal{S}}(r)\,|0\rangle$ with $r_{\text{calib}} = 0.93 \pm 0.02$. (a), (b) Real and imaginary characteristic function measurements. (c) The Wigner function found via Fourier transforming the characteristic function data. In case of a squeezed vacuum both functions look qualitatively the same, neglecting the factor of 2 difference in phase space axis scaling. The large amount of data collected reveals small deviations from the calibrated state given by a slight tilt of the squeezing axis and a small shift of the state along the momentum axis.

$|\psi\rangle = \hat{\mathcal{D}}(\delta)\hat{\mathcal{S}}(re^{i\vartheta})\,|0\rangle$ with floating parameters δ, r, ϑ and additionally float the bias o, as described before. The best match is found for $\delta = -0.18i \pm 0.01i$, $r = 0.938 \pm 0.005$, $\vartheta = 0.04 \pm 0.003$ and $o = 0.035 \pm 0.001$. Before performing the discrete Fourier transform the bias o extracted from the fit is removed in the measurement data. Part (c) of figure 9.1 shows the plot of the resultant Wigner function of the state. The fit to the expectation reveals a barely measurable tilt of the squeezed state and an additional shift along the imaginary axis. The tilt is only visible in the large data set and indicates the potential for improving the SDF to squeezed state direction calibration in the future. The shift along the imaginary axis could be due to an off resonant carrier drive during the squeezed pumping. The transformed basis control and pumping pulse (section 3.5) is described in the $\hat{\mathcal{S}}(\xi)\hat{\mathcal{D}}(\alpha)\,|n\rangle$ basis, while in the present discussion we considered $\hat{\mathcal{D}}(\delta)\hat{\mathcal{S}}(re^{i\vartheta})\,|0\rangle$. Interchanging of the two operators leads to $\hat{\mathcal{D}}(-0.18i)\hat{\mathcal{S}}(0.94)\,|0\rangle = \hat{\mathcal{S}}(0.94)\hat{\mathcal{D}}(-0.07i)\,|0\rangle$ showing that a carrier with a Rabi frequency of only $0.07\eta\Omega_r$ is sufficient for the observed effect. Since the Rabi frequency is proportional to the electric field, this leads to a carrier laser power of only $O(10^{-5})$ times that of the sideband. Sources for this carrier component might be a non-ideal squeezed pumping pulse shape, noise in the quadrupole laser spectrum or coupling of wrongly diffracted frequency

components to the light-delivering fiber.

We calculate the reduced chi square value c_r to quantify how well a given model state is consistent with the measured data. The reduced chi square for a set of N measurement points $\chi(\beta_i)$ with s.e.m. errors σ_i and considering a model predicting the values $E(\beta_i)$ using ν different parameters is calculated as:

$$c_r = \frac{1}{\nu} \sum_{i=1}^{N} \frac{(\chi(\beta_i) - E(\beta_i))^2}{\sigma_i^2} \tag{9.5}$$

Values of $c_r \approx 1$ indicate a good match between data and model. Higher values indicate that the model is not able to capture the relevant features of the data or the errors σ_i have been underestimated. Lower values in turn indicate too many free parameters in the model.

Comparing the expectation of the calibrated state to the data yields a value of $c_r = 1.8$. After removing o from the data the value reduced to $c_r = 1.42$. The fitted state including all parameters yields $c_r = 1.09$, which is only slightly above 1. Furthermore we see that the measured data is already quite close to the calibrated state and only the large amount of data is able to reveal the slight differences, given by the barely measurable tilt and the additional shift of the state.

9.2.2 Displaced squeezed vacuum

Tomography of an intentionally displaced squeezed vacuum state $\hat{\mathcal{D}}(\delta)\hat{\mathcal{S}}(r)\,|0\rangle$ with $\delta_{\text{calib}} = 0.78 \pm 0.05$ and $r_{\text{calib}} = 0.93 \pm 0.02$ is shown in figure 9.2. The measurement results closely follow the expectations of the calibrated state ($c_r = 1.78$). A fit of the data to a displaced squeezed vacuum state model $\hat{\mathcal{D}}(\delta)\hat{\mathcal{D}}(re^{i\vartheta})$ finds $\mathrm{Re}[\delta] = 0.752 \pm 0.001$, $\mathrm{Im}[\delta] = 0.114i \pm 0.008i$, $r = 0.93 \pm 0.004$, $\vartheta = 0.05 \pm 0.003$ and $o = 0.026 \pm 0.001\,\%$. The discrepancy of the real part of the shift is within the accuracy of our calibration. Again we observe an additional shift along the imaginary axis together with a small tilt of the squeezed state. The inclusion of o reduces the chi square to $c_r = 1.43$ while the full fit yields $c_r = 1.07$, which is comparable to the case of the squeezed vacuum state.

9.2.3 Squeezed cat state

After confirming that the reconstruction method works well on the displaced squeezed vacuum, we move on analyzing the state of a squeezed cat $|\psi\rangle \propto [\hat{\mathcal{D}}(-\alpha/2) + \hat{\mathcal{D}}(\alpha/2)]\hat{\mathcal{S}}(re^{i\vartheta})\,|0\rangle$ with $\alpha_{\text{calib}} = 2.42 \pm 0.01$, $r_{\text{calib}} = 0.58 \pm 0.02$ $\vartheta_{\text{calib}} = 0$. Measurement results are shown in figure 9.3. The expectations for the phase space representations follow from straightforward analytic calculations using the methods given in App. B.1. Using these formulas the measured data is fitted to a squeezed cat functional form while floating the

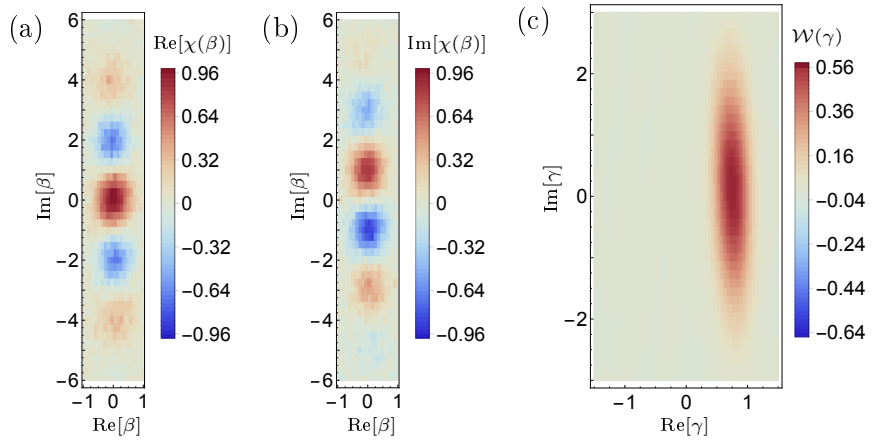

Figure 9.2: Reconstruction of a displaced squeezed vacuum state $\hat{\mathcal{D}}(\delta)\hat{\mathcal{S}}(re^{i\vartheta})\,|0\rangle$ where parameters were calibrated to be $\delta_{\text{calib}} = 0.78 \pm 0.05$, $r_{\text{calib}} = 0.93 \pm 0.02$, $\vartheta_{\text{calib}} = 0$. The characteristic function shown in (a) and (b) and the Wigner function given in (c) transform diffrently under the phase space shift. The Wigner function is simply shifted, while the characteristic function is still located around the origin and the shift manifests itself in oscillations perpendicular to the shift.

separation α, the initial squeezing $\hat{\mathcal{S}}(re^{i\vartheta})$, together with an additional phase space shift of the state, including o and a rescaling of the calibrated SDF coupling strength c (see section 5.3).

The fit result yields $\alpha = 2.396 \pm 0.004$, $r = 0.543 \pm 0.005$, $\vartheta = 0.111 \pm 0.007$, $o = 0.009 \pm 0.0001$ together with a negligible overall shift, and a rescaling of c by $4.8 \pm 0.1\%$. We expected the characteristic function of the squeezed cat state to be zero, therefore it was measured with lower resolution. A consequence of the lower resolution might be that a small overall shift is not well captured by the sampled points. The tilt of the squeezed state increased in this measurement, and the fit yields a smaller squeezing amount than calibrated. The calibrated state matches the data with $c_r = 2.15$, while the fitted state matches with $c_r = 1.41$. The higher discrepancy of the model to the data is most likely due to the longer measurement timescale ($\approx 6\,\text{h}$) during which the experimental parameters drifted. For comparison, tomography of the squeezed states took $\approx 1\,\text{h}$. The longer measurement timescale requires recalibration of the coupling strength c of the SDF laser pulse, which was tested for the first time during the data taking of the squeezed cat state. The SDF strength of both the analysis pulse and the cat state preparation pulse were updated dependent on the calibrations. In order to check for consistency of this recalibration scheme the complete data set was fitted allowing for a rescaling of c in the analysis pulse as well as the created cat size. The fit yields a rescaling of all calibrations by

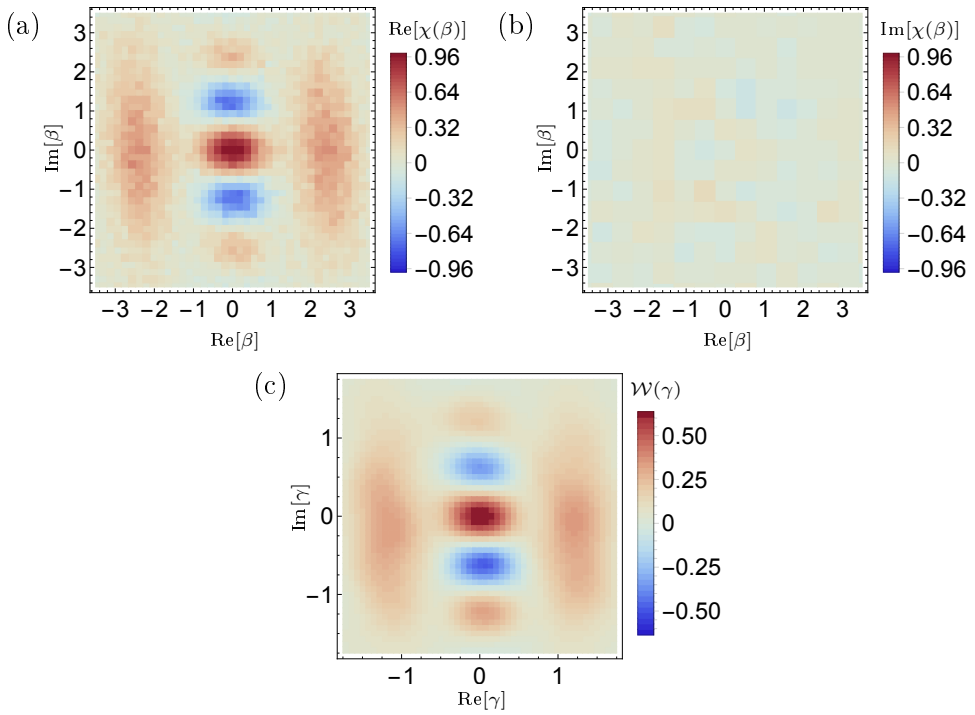

Figure 9.3: Reconstruction of a squeezed cat state $|\psi\rangle \propto [\hat{\mathcal{D}}(-\alpha/2) + \hat{\mathcal{D}}(\alpha/2)]\hat{\mathcal{S}}(re^{i\vartheta})\,|0\rangle$ with $\alpha_{\text{calib}} = 2.42 \pm 0.01$, $r_{\text{calib}} = 0.58 \pm 0.02$ $\vartheta_{\text{calib}} = 0$ closely following the expected signal. The similarity between characteristic function and Wigner function is misleading. For example the stable superposition phase manifests itself in the Wigner function oscillations along the imaginary axis, while in the characteristic function the information is present in the "wave packets" located at $\text{Re}(\beta) \approx \pm 2.42$.

$4.8 \pm 0.1\%$, which lead to the large error on the cat state separation calibration. The recalibration needs to be analyzed more closely in the future.

In chapter 6 the parity of the cat states was used in order to confirm the stable phase relation of the two separated wave packets. The parity relates directly to the Wigner function at the origin. This single point translates in the Fourier space to an integral over the full space, which is determined only by the real part of the characteristic function due to its Hermiticity.

$$\frac{2}{\pi}\langle\hat{\mathcal{P}}\rangle = \mathcal{W}(0) = \frac{1}{\pi^2}\int \chi(\beta) d^2\beta = \frac{1}{\pi^2}\int \text{Re}[\chi(\beta)] d^2\beta. \tag{9.6}$$

Similarly properties connected to integrals over the full phase space in the Wigner function transform to quantities related to the characteristic function around the origin. The most prominent of these are the symmetrically ordered

expectation of powers of creation and destruction operators [122]:

$$\langle \hat{a}^{\dagger m} \hat{a}^n \rangle_S = \int_{-\infty}^{\infty} \mathrm{d}\gamma^2 \mathcal{W}(\gamma) \gamma^{*m} \gamma^n \tag{9.7}$$
$$\langle \hat{a}^{\dagger m} \hat{a}^n \rangle_S = \left(\frac{\partial}{\partial \beta}\right)^m \left(-\frac{\partial}{\partial \beta^*}\right)^n \chi(\beta)|_{\beta=0}.$$

Thus information regarding, for example $\langle n \rangle$ or $\mathrm{g}^2(0)$ of the states is completely determined by a narrow region of the characteristic function around the origin. Nevertheless estimation of a derivative from a sparsely sampled noisy signal is not straightforward and requires filtering of the projection noise in an appropriate way [230, 231].

States with a parity $\langle \hat{\mathcal{P}} \rangle = \pm 1$ have purely real characteristic functions with a zero imaginary part. Examples of such states are the previously analyzed squeezed vacuum state or the squeezed cat analyzed in this section.

In case of the even cat the characteristic function looks qualitatively the same as the Wigner function, which is misleading as the information provided by the features differ. See the discussion in section 2.5. In particular the stable phase relation is confirmed in the characteristic function by the presence of the wave packets located around $\mathrm{Re}[\beta] \approx \pm 2.42$. The strength of these can be found via integration over the full space, in which the oscillations at the center average out, this integration corresponds to a measurement of the parity.

Performing the Fourier transform of the characteristic function measurements without accounting for the bias o yields $\pi/2\mathcal{W}(0) = \langle \hat{\mathcal{P}} \rangle = 0.90$. Removing the bias $o = 0.009$ before the Fourier transform leads to a parity of $\langle \hat{\mathcal{P}} \rangle = 0.98$, which shows that any constant offset in the data leads to large errors in this parity measure.

9.2.4 Grid state

As a final state we tackle the partial reconstruction of a three-component GKP state $|0\rangle_L \propto [\hat{\mathcal{D}}(-l) + 2 \cdot \mathbb{1} + \hat{\mathcal{D}}(l)]\hat{\mathcal{S}}(re^{i\vartheta})|0\rangle$, which has narrow features along both phase space directions. Reconstructing this state would simply be too time-consuming using the Wigner function reconstruction method. The state is calibrated to have parameters $l_{\text{calib.}} = 2.5 \pm 0.05$ and $r_{\text{calib.}} = 0.93 \pm 0.03$, $\vartheta_{\text{calib.}} = 0$. The probed grid state has even parity thus we only sample a few points in the imaginary part to confirm that it is close to zero. Furthermore we expect the state to be symmetric with respect to both phase space axes, therefore all relevant information is captured, by only sampling the positive quadrant of the characteristic function. The symmetry is checked by measuring the full imaginary and real phase space axes. Fitting of all data to a three-component state of variable displacement l, squeezing r, an additional overall phase space shift and including a bias o yields $\mathrm{Re}[l] = 2.471 \pm 0.005$, $\mathrm{Im}[l] = -0.022i \pm 0.008i$, $r = 0.892 \pm 0.008$, $\vartheta = 0.102 \pm 0.008$, no visible additional shift and a negligible bias of 0.0015 ± 0.001. Again a small tilt of the squeezed state

is observed. The fitted model matches with a reduced chi square of $c_r = 1.58$ to the data. The main limitation in the data taking is the recalibration and fluctuations of the SDF during the several hours timescale of the measurement. In contrast to the squeezed cat state the automatic calibration routine did not show a consistent bias. In figure 9.4 (a) the measured data (positive quadrant) together with 4 copies of itself mirrored at the phase space axes is shown. Part (b) shows the respective Fourier transform. The grid like structure of the state is clearly visible in both representations.

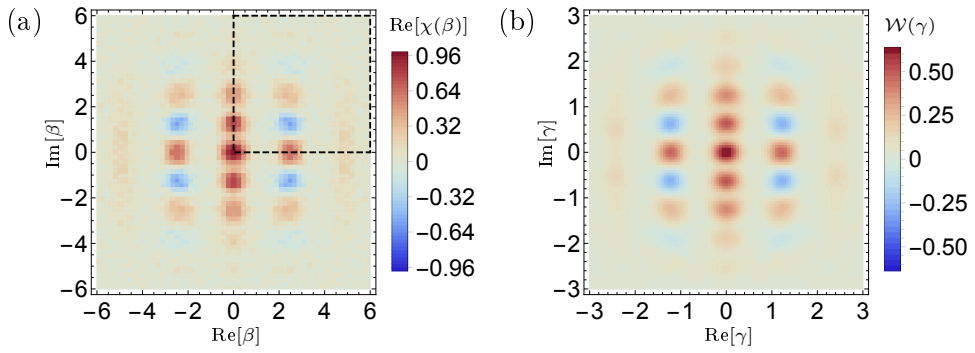

Figure 9.4: Reconstruction of a three-component superposition of displaced squeezed states $[\hat{\mathcal{D}}(-l) + 2 \cdot \mathbb{1} + \hat{\mathcal{D}}(l)]\hat{\mathcal{S}}(re^{i\vartheta})\,|0\rangle$ with $l_{\text{calib.}} = 2.5 \pm 0.05$, $r_{\text{calib.}} = 0.93 \pm 0.03$, $\vartheta_{\text{calib.}} = 0$. The measured quadrant is shown by the dashed box in part (a). Four copies of this quadrant are stitched together for the full plot and used in order to perform the discrete Fourier transform shown in part (b).

9.3 Discussion and outlook

9.3.1 Comparison to analysis in squeezed Fock state bases

Both the present chapter and chapter 6 cover state reconstruction methods of the oscillator based on bi-chromatic pulses. The analysis in a squeezed Fock basis as well as the characteristic function reconstruction rely on red and blue sideband drives. However our description of the two methods used different formalisms. The current section tries to bridge this gap by discussing analysis in an "infinitely squeezed Fock state basis".

Application of the squeezed basis Hamiltonian, equation 6.5:

$$\hat{H}_- = \frac{i\eta\hbar\Omega_r}{2}\sigma_+ \left[\hat{a} + e^{i\vartheta}\frac{\Omega_b}{\Omega_r}\,\hat{a}^\dagger\right] + \text{h.c.} \tag{9.8}$$

to an ion initialized to $|\uparrow\rangle|\psi\rangle$ leads to the measurement trace:

$$P(\uparrow,t) - P(\downarrow,t) = \sum_{n_s=0}^{\infty} \wp(n_\xi)\cos(2\Omega_{n_\xi} t). \tag{9.9}$$

Here $\wp(n_\xi)$ refers to the squeezed Fock state populations

$$\wp(n_\xi) = |\langle\psi|\hat{\mathcal{S}}(re^{i\vartheta})|n\rangle|^2 \tag{9.10}$$

with $r = \tanh(\Omega_b/\Omega_r)$ and the Rabi frequencies in the transformed basis scale as $\Omega_{n_\xi} = \frac{\eta\Omega_r}{\cosh(r)}\sqrt{n_\xi+1}$. We now consider the limit $\Omega_b \to \Omega_r$, while $\Omega_r =$ const.. In this case $r \to \infty$. Any physical oscillator state has a finite extent in phase space. Nonzero populations $\wp(n_\xi) \neq 0$ in the limit $r \to \infty$ are found for $n_\xi \to \infty$. Furthermore the frequencies Ω_{n_ξ} decrease with $1/\cosh(r)$, however as the relevant n_ξ increases, the limit can be finite.

An infinitely squeezed vacuum state is well known to be equivalent to the corresponding quadrature eigenstate $\hat{\mathcal{S}}(re^{i\vartheta})|0\rangle \to |q^{\vartheta/2}=0\rangle$, where the quadrature eigenstate is defined via $\hat{q}^\lambda|q^\lambda\rangle = q^\lambda|q^\lambda\rangle$ with the quadrature operator $\hat{q}^\lambda \equiv \frac{1}{2}(\hat{a}e^{-i\lambda} + \hat{a}^\dagger e^{i\lambda})$. From the symmetry of higher Fock states it is reasonable to assume[3], that even Fock states $\hat{\mathcal{S}}(re^{i\vartheta})|n_{\text{even}}\rangle \to |q^{\vartheta/2}=0\rangle$ while odd Fock states $\hat{\mathcal{S}}(re^{i\vartheta})|n_{\text{odd}}\rangle \to 0$. In the limiting case the state ladder collapses and does not provide a valid phase space basis anymore.

We can ad hoc complement the missing basis elements $|q^{\vartheta/2}\rangle$ and analyze the effect of the analysis Hamiltonian on the full basis. The transformed creation and destruction operators become $\hat{K} = e^{i\vartheta}\hat{K}^\dagger = 2\hat{q}^{\vartheta/2}e^{i\vartheta/2}$. These are up to a global phase the identical operator and thus these operators can no longer provide quanta creation or destruction operators. Instead the $|q^{\vartheta/2}\rangle$ basis is an eigenbasis of these operators. The arbitrary motional state can be expressed in the quadrature basis as:

$$|\psi\rangle = \int_{-\infty}^{\infty} \psi(q^{\vartheta/2})\left|q^{\vartheta/2}\right\rangle \tag{9.11}$$

$\hat{H}_-$ thus leads to flopping only on the internal state with frequencies proportional to the eigenvalues of the $|q^{\vartheta/2}\rangle$ states.

This is indeed the measurement trace obtained starting from the SDF Hamiltonian given in equation 3.21 with the laser phases $\overline{\phi} = \vartheta/2$, $\Delta\phi = -\vartheta$, $\delta = 0$:

$$\hat{H}_{SDF} = \frac{i\eta\hbar\Omega_r}{2}\hat{\sigma}_+(\hat{a} + e^{i\vartheta}\hat{a}^\dagger) + \text{h.c.} \tag{9.12}$$

Note that H_- transforms to H_{SDF} in the considered limit. From this the measurement as a function of time is calculated to be:

$$P(\uparrow,t) - P(\downarrow,t) = \text{Re}[\langle\hat{\mathcal{D}}(-i\eta\Omega_r t e^{i\vartheta/2}/2)\rangle] = \text{Re}[\langle e^{-i\eta\Omega_r t\hat{q}^{\vartheta/2}/2}\rangle]. \tag{9.13}$$

[3] at least from my understanding

Inserting the state expansion given in equation 9.11:

$$P(\uparrow,t) - P(\downarrow,t) = \int_{-\infty}^{\infty} dq^{\vartheta/2} \wp(q^{\vartheta/2}) \cos(2\Omega_{q^{\vartheta/2}} t)$$

Here $\wp(q^{\vartheta/2}) = |\psi(q^{\vartheta/2})|^2 = P(q^{\vartheta/2})$ and the oscillation frequency is proportional to the corresponding eigenvalue $\Omega_{q^{\vartheta/2}} = q^{\vartheta/2}\eta\Omega_r/2$. Note that this calculation corresponds to a direct calculation of the Fourier relation given in equation 9.4. This description complements the insights gained by expressing the characteristic function measurement in terms of the orthogonal quadrature basis $\left|q^{\vartheta/2+\pi/2}\right\rangle$, leading to a picture of interfering wave packets. To rigorously connect the $\hat{H}_-$ analysis to the $\hat{H}_{SDF}$ analysis is left for future work.

The above discussion motivates one to consider several variations and combinations of the protocols developed in the work throughout this thesis. One example is to consider the limit of a highly excited coherent basis, which has been proposed previously [232].

M. S. Kim and co-workers propose to measure the internal state flopping under the Jaynes-Cummings Hamiltonian for a highly displaced version $\hat{\mathcal{D}}(\beta)\,|\psi\rangle$ of the state under reconstruction given by $|\psi\rangle$. They consider the limit of the shift $\beta = |\beta|e^{i\phi}$ being much larger than the extent of the oscillator state. In this limit they derive the formula:

$$\langle \hat{Z}(\tau)\rangle \approx \mathrm{Im}[\chi(i\tau e^{i\phi})]\cos(2\tau\sqrt{|\beta|^2+1}) - \mathrm{Re}[\chi(i\tau e^{i\phi})]\sin(2\tau\sqrt{|\beta|^2+1}) \qquad (9.14)$$

Here $\tau = \Omega\eta t$ with t the duration of the Jaynes-Cummings coupling, Ω its Rabi frequency and η the Lamb-Dicke parameter. The formula shows that $\langle \hat{Z}(\tau)\rangle$ oscillates rapidly with a slower envelope determined by the characteristic function along the perpendicular direction of the shift.

In our ion trap setup the larger displacement would create a state outside the Lamb-Dicke regime and thus render this method inapplicable. However we can use the same mathematical approximation, replacing the large shift with an analysis pulse directly in a large coherent basis using the methods of section 6.4. Such an analysis pulse consists of a large carrier component together with a small red sideband component. The shape of the envelope in this case is determined by the red sideband Rabi frequency. The difficulty in this method might be laser intensity stability, as the signal critically depends on sampling the rapid oscillations at positions where they are maximized or minimized.

This method is interesting as it provides an example where the use of a coherent basis provides an additional advantage besides making a shift in the pulse sequence obsolete.

9.3.2 Conclusion

We demonstrated a relatively efficient phase space reconstruction method when comparing to the methods of chapter 6. The discussion in chapter 6 has

shown that for states with an isotropic extent in phase space extracting phonon populations becomes very involved due to fast oscillations and revivals at long timescales. Furthermore the estimation of the density matrix elements in the Fock state basis in optimized schemes, is connected to the raw measurements results in a mathematically complicated way. This makes it difficult for the experimenter to pinpoint experimental limitations and eventually improve the experiment. The characteristic function scheme on the other hand is mathematically very simple and relies on exactly the same control tools as used for the realization of a logical qubit in chapter 8. Thus the method is well suited for learning about the experimental limitations in realizing these oscillator qubits. These measurement revealed a small tilt and sometimes an additional shift of the squeezed state. Understanding and removing the cause of these effects would allow us to directly improve upon the logical qubit quality in the future.

Chapter 10

Summary and outlook

This thesis explored ion-trap motional oscillator physics and applications. All experiments were based on the same control tool box. The continuous-variable oscillator system was manipulated via coupling to the finite dimensional internal state qubit together with post-selected readout of the latter. Combination of internal state-dependent and independent oscillator shifts, initial squeezed state preparation, qubit rotations and fluorescence readout allowed for a surprisingly large variety of oscillator experiments. The results cover three main focus areas. These are oscillator state engineering and analysis, foundational studies and last but not least quantum information processing. Figure 10.1 provides a summary of the achieved advances in each of these areas and furthermore emphasizes relevant future research directions.

10.1 State engineering & analysis

The results presented in this thesis started and ended with the description of improved state engineering and analysis. The combination of SDF pulses and post-selected readout, defined as symmetric modular measurement, was used to synthesize "Schrödinger cat" states of solely the oscillator degree of freedom. Existing energy-basis analysis tools based on the fundamental Jaynes-Cummings interaction were successfully generalized to transformed energy bases. This allowed the in-situ confirmation of quantum features for large cat states. Furthermore the techniques were employed for full Wigner function tomography of a cat state.

Sequences of post-selected modular measurements were used for foundational studies but were also exploited to prepare multi-component superposition states throughout the thesis. In particular superpositions of position squeezed states, which realized the logical GKP code states. Despite the improved performance of oscillator analysis in the transformed energy bases these extended multi-component superpositions brought the novel techniques to their limit in terms of required time resources. Therefore an additional

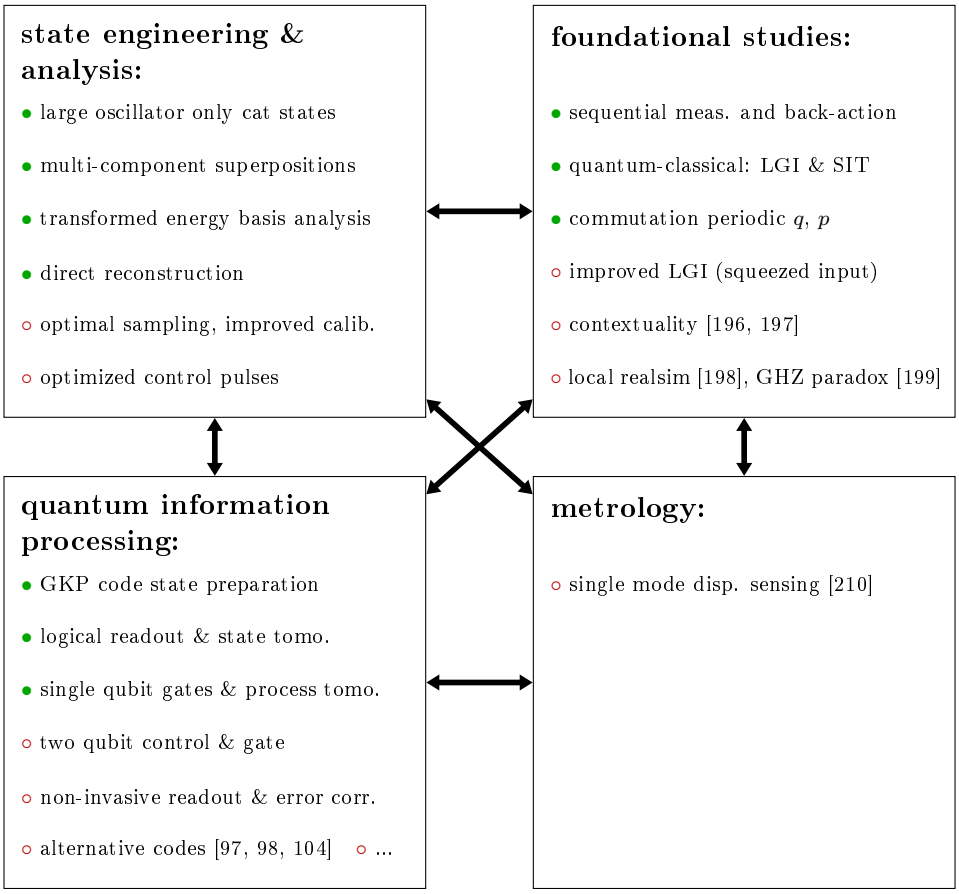

Figure 10.1: Summary and outlook. The major advances of this thesis can be attributed to three main areas. These include oscillator state engineering and analysis, applications of oscillator measurements for foundational studies as well as to quantum information processing. Metrology based on the novel oscillator control tools can additionally be explored in the future. Green filled bullets summarize results of this thesis, while red empty circle highlight suggested future research directions. The black arrows symbolize the close connection between the four given research areas.

direct and hence efficient state reconstruction technique was demonstrated, which allowed state tomography of a logical GKP code state.

This detailed analysis of the logical GKP code state was able to revealed several small discrepancies between the created states and the expectation. Hence the novel technique allows directly to improve upon the relevant GKP qubit control and could allow to augment code performance in the future. The reconstruction technique can in the future be further refined by optimizing the sampling pattern and automating and improving the SDF calibration techniques.

A future advance in state engineering would be to create multi-component superposition states without post-selection. This can in principle be achieved by carefully tailored step-wise constant control pulses. I supervised a first theoretical study towards this direction [223], while the experimental exploration is left for future work.

10.2 Foundational studies

Intrinsic quantum measurement back-action in sequences of modular measurements were quantified using signaling in time. A peculiarity of quantum theory is that despite the intrinsic incompatibility of the position and the momentum operator periodic versions of these operators can actually commute. We experimentally tested commutation of periodic position and momentum analyzing SIT between modular measurements. SIT can further be interpreted as a quantum witness, which can be used to quantify the "quantumness" of a system and can therefore be used to study the quantum classical-transition. The Leggett-Garg inequality based on correlations between sequential measurements, was originally devised to rule out macroscopic realism but such a conclusion relies on non-invasive measurements. We violate this inequality considering a sequence of three modular measurements and observe violations with measurement separations of up to $\alpha = 3$. The scheme tested in this thesis could in the future be applied to more macroscopic mechanical oscillators, therefore we analyzed the robustness of the protocol with regards to imperfect ground state cooling.

First we took a cautious perspective on our violation result and interpreted it as an alternative quantum witness. Second we theoretically assessed the SIT between our Leggett-Garg violation measurements. In our protocol SIT becomes smaller for larger separations of the modular measurements. Therefore multiple points are expected to still violate the LGI once the violation is corrected for this "obvious" form of measurement disturbance (i.e SIT). The vast majority of LGI violations so far were based on qubits [55–65] only one experiment[1] attempted the violation of the LGI with a more macroscopic system given by the position of an atom [66]. In this case the LGI violation was entirely based on SIT.

[1] up to my knowledge

In the future a cyclic version of the LGI test could be performed [194], which would allow to experimentally assess SIT between the measurements and correct the violation for this form of disturbance. To do so we suggest using a squeezed oscillator input state, which provides a higher violation for a given displacement size α, alongside smaller amounts of SIT between the measurements. Furthermore employing the control techniques used in the context of the GKP qubit a future experiment can use an improved version of the asymmetric modular measurement, based on only the primary internal state transition. This allows for lower qubit decoherence and faster measurements and thus reduces the susceptibility to experimental imperfections.

We find it instructive to explore the relations of the LGI as well as the SIT quantum witness [53], nevertheless we are bemused with the ambiguity of the NIM notion[2]. A related concept to the LGI test, which might improve the latter problem is given by measurement contextuality, which can in principle be tested using modular measurements of two oscillator modes [196, 197]. Modular variables are the observables of choice in order to generalize fundamental studies from microscopic qubit degrees to continuous-variable systems which exhibit a natural crossover to classical physics. Therefore numerous theoretical proposals for continuous-variable tests exist e.g. local realism [198] or a test of the GHZ paradox [199].

10.3 Quantum information processing

The demonstrated state engineering capabilities allowed the preparation of approximate GKP code states based on multi-component superpositions of squeezed states. The modular measurement techniques furthermore allowed for logical readout in all three Pauli bases, which enabled an assessment of logical qubit quality based on state tomography of a set of logical code states. State preparation and readout levels of $87.3 \pm 0.7\%$ were reached. Pauli operations were implemented by simple shifts of the oscillator and complemented with continuous operations performed using gate teleportation. The quality of a universal single qubit gate set was assessed using the method of process tomography and process fidelities in the range 87% - 97% were obtained.

A clear long term vision for extensions of this work exists, which include harnessing the error correcting capabilities of the GKP code alongside scaling of the code to multiple qubits and eventual code concatenation. However photon scattering in case of bright fluorescence detections in our system poses a challenge to such advances. We suggested multiple ways to overcome this limitation in the future, which included the integration of optical cavities to experiments or the Coulomb coupling of ions trapped in neighboring wells. Both of these are currently pursued in the TIQI group but require critical

[2] and share the opinion of the [66] authors that ideal negative measurements exhibiting SIT are sufficient to challenge MR.

technological developments. In case of cavity integration the problem of stray charges on optical components in close vicinity of the ion needs to be solved, while high fidelity fast exchange of oscillator modes based on Coulomb coupling requires small trapping structures alongside extraordinary control over the temporal shapes of the trapping potentials.

Using the GKP code states allows to study the decoherence sources in our system more closely and a different bosonic code tailored for the present error sources could be used in the future. Currently dephasing noise seems to be dominating, in this case cat codes form a promising alternative. The dissipative preparation of squeezed states was used as a resource for the work of this thesis. The control over the tailored dissipative reservoir could be explored in the future to stabilize bosonic code states, as has previously been explored in the superconducting platform for the cat code [104].

An additional area where the developed techniques and synthesized states find clear applications is quantum metrology. As an example usage of the GKP states has been proposed to precisely sense a 2D shift using a single probe state [210]. The same is not possible with alternative sense states including squeezed states.

In all three covered areas major advances were achieved and a multitude of intriguing future research directions and experiments were suggested. I hope to see many of these explored and realized in the future, especially the realization of GKP qubit error correction in trapped-ions.

Appendices

A State representation

A.1 Dirac Notation

Throughout this thesis we use the Dirac Notation [6] in order to describe quantum states. The symbol $|\psi\rangle$ is used as an abstract symbol representing a state, which is given by an element of a complex Hilbert space. The label ψ is used to give us some abstract information about the state. In case of a finite dimensional space and using a basis we can associate $|\psi\rangle$ with a column vector. The abstract form $|\psi\rangle$ has the advantage of not requiring a basis and defining the element solely on its properties. The symbol $\langle\psi|$ represents the conjugate transpose of the element $|\psi\rangle$. The inner product of two elements $|\psi_1\rangle$ and $|\psi_2\rangle$ can then simply be represented as $\langle\psi_2|\psi_1\rangle$. Operators are represented by matrices (in the finite dimensional case) and have the form $\sum_{i,j}|\psi_i\rangle\langle\psi_j|$. See for example [120] for a more complete introduction.

A.2 Position and momentum representation

The quantum mechanical state of a particle can be represented by its complex valued wavefunction in the position representation $\psi(q_r)$. The connection to the braket notation is then given by $\psi(q_r) = \langle q_r|\psi\rangle$ where $|q_r\rangle$ represents a position eigenstate $\hat{q}_r|q_r\rangle = q_r|q_r\rangle$. These position eigenstates form a set of continuous basis functions for which we in particular have $\langle q_r|q_r'\rangle = \delta(q_r - q_r')$ where δ denotes the delta function. In the position representation the position operator is $\hat{q}_r = q_r$ while the momentum operator is given by $\hat{p}_r = \frac{\hbar}{i}\frac{\partial}{\partial q_r}$. The probability density of the particles position is then given by $P(q_r) = |\psi(q_r)|^2$ and measurement expectations of observables as $\langle Q(q_r, p_r)\rangle = \int \psi^* Q(\hat{q}_r, \hat{p}_r)\psi \mathrm{d}q_r$.

The state of the system can equivalently be described using the momentum representation $\phi(p_r) = \langle p_r|\phi\rangle$. The momentum description is connected via Fourier transform to the position representation. This connection leads directly to the Heisenberg uncertainty relation for position and momentum.

In case of the harmonic oscillator we have introduced the raising $\hat{a}^\dagger$ and the lowering $\hat{a}$ operators, which we connected to the oscillators dimensionless position and momentum. Similarly we can define more general quadrature operators:

$$\hat{q}^\lambda \equiv \frac{1}{2}(\hat{a}e^{-i\lambda} + \hat{a}^\dagger e^{i\lambda}) \tag{A.1}$$

$$\hat{q}^0 = \hat{q},\ \hat{q}^{\pi/2} = \hat{p} \tag{A.2}$$

Note that typically dimensionless position and momentum is defined as $\sqrt{2}\hat{q}$ and $\sqrt{2}\hat{p}$, which leads to scaling factors when comparing to text books. The Fourier relation between position and momentum is generalized to a relation

between $\left|q^{\lambda}\right\rangle$ and $\left|q^{\lambda+\pi/2}\right\rangle$. For our dimensionless variables this reads:

$$\langle q^{\lambda+\pi/2}|\psi\rangle = \frac{1}{\sqrt{\pi}} \int_{-\infty}^{\infty} \mathrm{d}q^{\lambda} e^{-i2q^{\lambda+\pi/2}q^{\lambda}} \langle q^{\lambda}|\psi\rangle \tag{A.3}$$

B Phase space calculations

B.1 Coherent state superpositions

In the following the characteristic function and the Wigner function is derived for the arbitrary coherent state superposition:

$$|\psi\rangle = \frac{1}{\sqrt{N}} \sum_{\delta} c_\delta |\delta\rangle \tag{B.1}$$

$$N = \sum_{\delta,\epsilon} c_\delta^* c_\epsilon e^{-\frac{1}{2}(|\delta|^2+|\epsilon|^2-2\delta^*\epsilon)}. \tag{B.2}$$

Here the normalization can be found using equation 2.21. The characteristic function then reads:

$$\chi(\beta) = \langle\psi| \hat{\mathcal{D}}(\beta) |\psi\rangle = \frac{1}{N} \sum_{\delta,\epsilon} c_\delta^* c_\epsilon \langle\delta| \hat{\mathcal{D}}(\beta) |\epsilon\rangle \tag{B.3}$$

$$= \frac{1}{N} \sum_{\delta,\epsilon} c_\delta^* c_\epsilon e^{-\beta^*\epsilon+\delta^*\beta+\delta^*\epsilon} e^{-\frac{1}{2}(|\delta|^2+|\beta|^2+|\epsilon|^2)}. \tag{B.4}$$

Performing the Fourier transform equation 2.20 we find the Wigner function:

$$\mathcal{W}(\beta) = \frac{2}{N\pi} \sum_{\delta,\epsilon} c_\delta^* c_\epsilon e^{-\delta^*\epsilon+2\delta^*\beta+2\epsilon\beta^*-2|\beta|^2} e^{-\frac{1}{2}(|\delta|^2+|\epsilon|^2)}. \tag{B.5}$$

B.1.1 Cuts through cat states

The even (odd) cat state have coefficients $c_{-\alpha/2} = \pm 1$, $c_{\alpha/2} = 1$. If we insert these and only consider an imaginary beta $\beta = ix$ then we find $\mathcal{W}(ix) = \frac{\pm 2}{N\pi} e^{-2x^2} \cos(2x\alpha)$ with $N = 2(1 \pm e^{-x^2/2})$. This is the functional form used in section 6.5.

B.2 Extension to superpositions of squeezed states

Using the above formulas the Wigner and the characteristic function in case of superpositions of identically squeezed wave packets can be calculated using equations 2.22, 2.23 and 2.15.

B.3 Displaced squeezed Fock state populations

For the calculation of populations either in the Fock basis or displaced squeezed basis the overlap

$$\langle n| \hat{\mathcal{S}}(\xi)\hat{\mathcal{D}}(\beta) |m\rangle \tag{B.6}$$

is typically helpful. The general formula is rather long and I thus forgo repeating it here. It can for example be found in equation 38 of [233]. In chapter 6.3 we analyze superpositions of coherent sates in this case the overlap (see for example equation 2.48 of reference [234]):

$$\begin{aligned}\langle n|\,\hat{\mathcal{D}}(\beta)\hat{\mathcal{S}}(\xi)\,|0\rangle = &\exp\left(-\frac{1}{2}|\beta|^2-\beta^{*2}\frac{e^{i\vartheta}}{2}\tanh(r)\right) i^n\sqrt{\frac{e^{in\vartheta}}{n!\cosh(r)}}\left(-\frac{\tanh(r)}{2}\right)^{n/2}\\ &\times H_n\left[-\frac{i}{2}e^{-i\vartheta/2}\sqrt{\frac{2}{-\tanh(r)}}(\beta+e^{i\vartheta}\tanh(r)\beta^*)\right]\end{aligned} \tag{B.7}$$

together with equations 2.15, 2.8 are sufficient for the calculations of all populations. In the above formula H_n denotes the nth Hermite polynomial.

C Magnetic field work technical details

C.1 Agilent cooling fan replacement

The original fan (6224N Papst) had an air flow of 410 m^3/h and was replaced with the Wallair 20100262 model with only 320 m^3/h. The new fan is connected to the power supply via a half meter long air flow pipe, this further reduces the cooling power of the fan. The smaller cooling power is enough since we run the power supply at around 0.8 kW (115 A at 7 V), which is well below its maximal specifications of 5 kW. This change needs to be kept in mind in case the power supply will be used for a different purpose in the future.

The cooling fan is powered by the AC lines supplying the Agilent power supply. To do so the phase line is connected after the power on switch of the Agilent (see schematics in figure C.1). The neutral line is added additionally and taken into the supply via a new drilled hole and via a slow blow 1 A fuse. The power cable of the fan is routed inside the pipe so care needs to be taken when changing the pipe connection. Powering the fan in such a way assures running of the fan as soon as the Agilent is powered on and in particular independent on the output current size.

The old fan is disconnected and its interlock is bridged by shorting resistor R863 as shown in figure C.2. The coupling of the PWM signal into the output is removed by cutting the relevant track as shown in figure C.3. Furthermore an additional direct grounding wire is introduced which is also indicated in figure C.3.

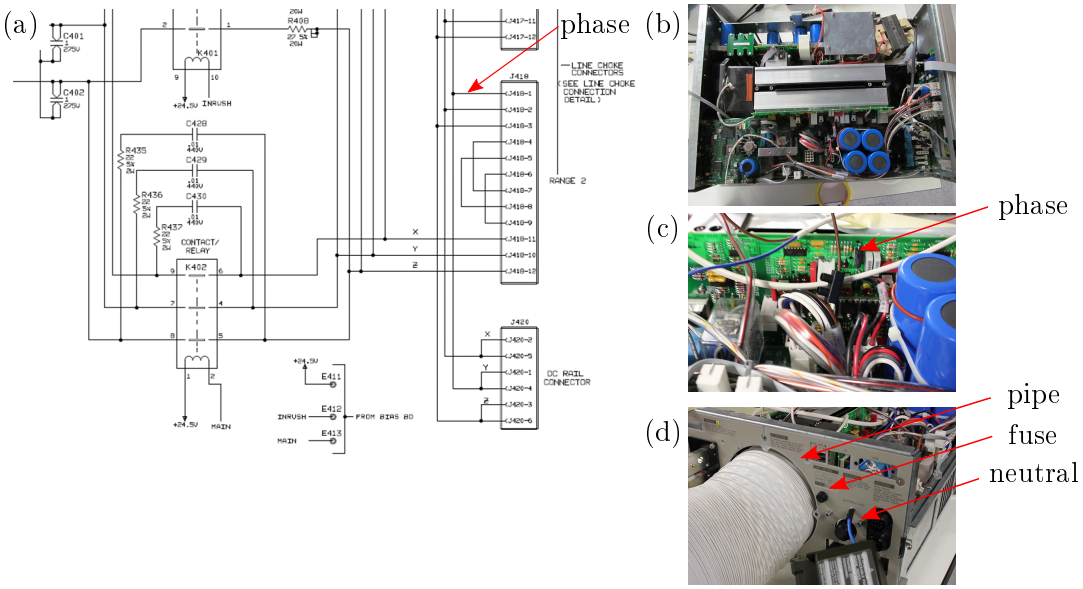

Figure C.1: Power connection of external fan. (a) Part of AC input board schematics taken from the Agilent 6682A manual (figure 6-12. A4). The fan phase power connection is made at J418-1 as shown on the schematic. In addition the open power supply is shown in (b) while (c) zooms in onto the phase power connection. (d) Connection of neutral line, additional fuse and pipe installation.

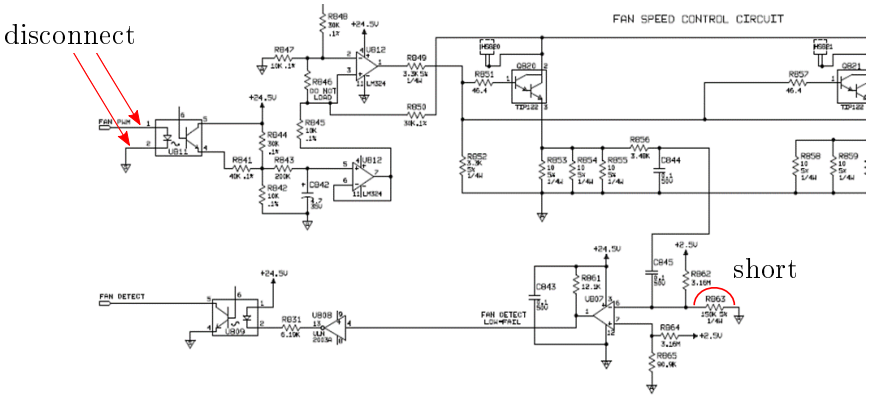

Figure C.2: Bridging of the fan interlock. Part of "figure 6-16. A6 Bias Board, Schematic Diagram (Sheet 2 of 2)" from the Agilent manual. The fan PWM is disconnected and shorting of the resistor R863 leads to a constantly high (bridged) interlock signal.

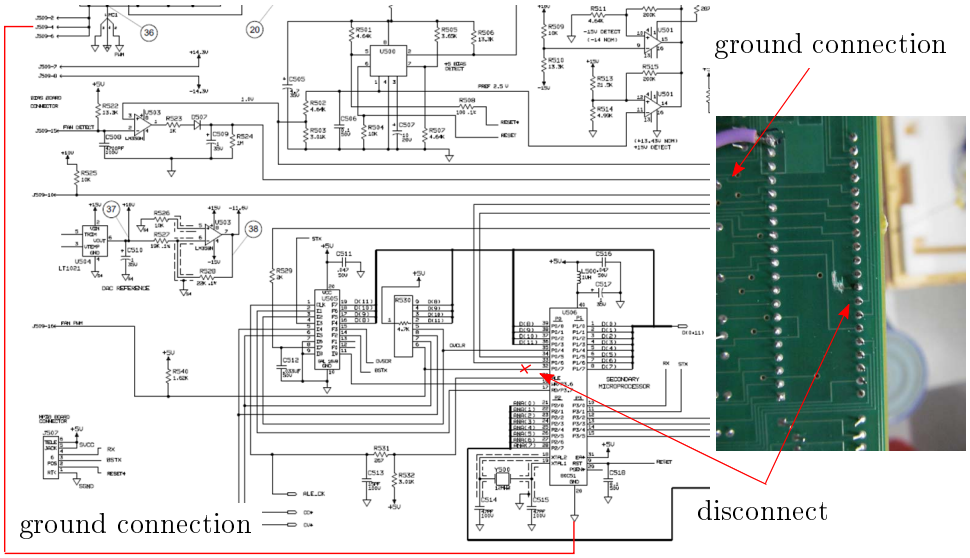

Figure C.3: Removal of the PWM coupling into the current output. Part of "Figure 6-26. A10 Control Board, Schematic Diagram (Sheet 1 of 4)" from the Agilent manual. The indicated track 32 is cut, which can be seen also in the photograph and the additional ground wire is introduced.

C.2 DC stabilization noise characterization

Figure C.4 shows a photograph of the measurement setup used for the characterization of noise in the slow magnetic field stabilization electronics. Results of the measurements were given in figure 4.5 of the main text.

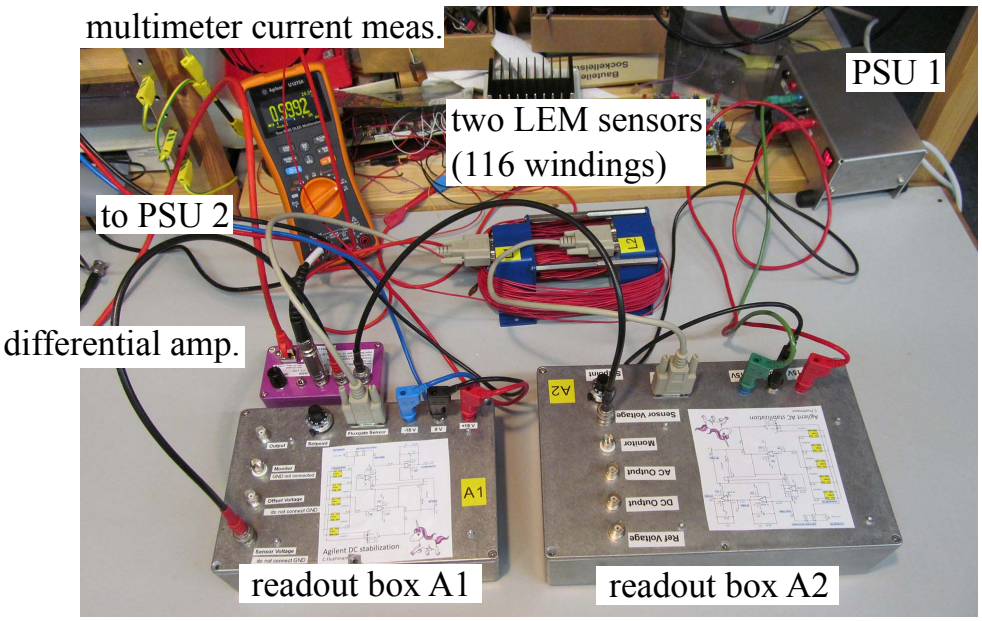

Figure C.4: Setup used for the characterization of noise in the slow current stabilization. Not shown on the picture is the used current source as well as PSU2. LEM sensors denote the two fluxgate sensors.

D Motional state interferometry

D.1 Qubit-motion entangled states

The TIQI group work published in [37] probed how far squeezed initial oscillator wave packets $|\psi_0\rangle = \hat{\mathcal{S}}(r \approx 1.13)\,|0\rangle$ could be separated and recombined using two SDF pulses. The poor internal state qubit coherent time, which was around 150 μs has been modeled as shot to shot noise and was able to explain the observed reduction in internal state revivals height after two SDF pulses. Therefore a substantial improvement for this experiment is expected due to the longer qubit coherence time. Figure D.1 show a reproduction of the old experiment by intentionally reducing the qubit coherence time. In addition the same experiment was performed using the current qubit coherence level.

Additional experiments were used to check that the second SDF pulse phase $\overline{\phi}$ (see equation 3.21) is set correctly. The results indicated an offset of $\delta\overline{\phi}$=24 deg compared to the phase calculated by the control system, which was used for both scans. Nevertheless sensitivity to such a constant phase offset is not very high for example a mistake of this size leads only to a reduction of the revival probability of about $P(\downarrow) = (1 + \cos(\delta\overline{\phi}))/2 \approx 0.95$.

Shown in figure D.1 is the final revival height of the probability $P(\downarrow)$

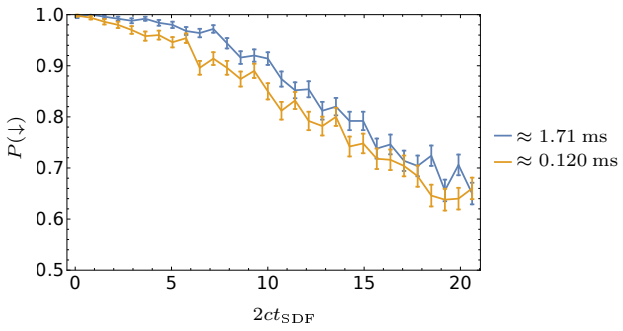

Figure D.1: Qubit-oscillator interferometer with squeezed wave packets [37]. The initially squeezed oscillator state $|r\rangle = \hat{\mathcal{S}}(r)\,|0\rangle$ with $r \approx 0.984 \pm 0.03$ together with the qubit in $|\downarrow\rangle$ is transformed by a first SDF of duration t_{SDF} to a state $|+\rangle\,\hat{\mathcal{D}}(\alpha/2)\,|r\rangle + |-\rangle\,\hat{\mathcal{D}}(\alpha/2)\,|r\rangle$. Ideally $\alpha = 2ct_{SDF}$. The used coupling was $c = (36.8 \pm 0.5) \cdot 10^{-3}\,\mathrm{s}^{-1}$. A second SDF pulse of equal duration and strength but with the phase $\Delta\phi$ (see equation 3.21) changed by π is applied. Ideally the qubit population would be fully returned to $|\downarrow\rangle$. The experiment is shown in case of qubit coherence given by 120 μs (yellow) and by 1.71 ms (blue). An improvement is seen for smaller α while larger separations are limited by other noise sources.

when both SDF durations are scanned jointly. The old data is qualitatively reproduced, while the longer coherence leads to a small improvement in the revivals. At larger separations the qubit coherence seems not to be the dominating factor. Further studies are required to unravel the dominating mechanism of decoherence here.

D.2 Large cat interferometer

Figure D.2 shows an extension of the squeezed qubit-motional interferometer discussed in [37]. First squeezed cat superpositions $|\psi\rangle \propto [\hat{\mathcal{D}}(-\alpha/2) + \hat{\mathcal{D}}(\alpha/2)]\,|r\rangle\,|\downarrow\rangle$ are prepared solely in the oscillator degree of freedom using the symmetric modular measurement (SDF + post selected fluorescence readout, see chapter 7). In this case the separation is determined by the duration of the SDF pulse and the coupling strength c: $\alpha = 2ct_{\mathrm{SDF}}$. After a free evolution time T a second modular measurement is then used to probe the created superposition. Comparable to the other interferometer experiments the superposition components are re-interfered using an SDF of the same strength but with opposite phase. Column (i) in figure D.2 shows the measured revivals $M_X(t) = \mathrm{Re}[\hat{\mathcal{D}}(2ct_{SDF2})]$ as a function of the second SDF time for 4 different durations of the first SDF pulse. column (ii) then shows the decay of these revivals as a function of free evolution time in case of identical SDF times i.e. $t_{SDF} = t_{SDF2}$. The data is fitted to an exponential decay but due to the small revival contrast the fitted timescales show poor quality and therefore are not quoted here. Nevertheless the revival in column (i) is still clearly visible for the longest SDF time i.e 300 μs.

In addition to confirm the separation of the created superposition an analysis SDF pulse perpendicular to the the initial separation is used. In this case $M_Z(t) = \mathrm{Re}[\hat{\mathcal{D}}(i2ct_{SDF2})]$ is measured. Results for three different wait time durations are shown in column (iii) these were $T = 0$ ms black, $T = 0.5$ ms blue and $T =$ ms purple. Fourier transform of this signal provides an estimate of the position probability density P(q) of the state, which is shown in column (iv). The envelope of the oscillations in column (iii) shows the extent of the squeezed wave packet along the anti-squeezed axis, which is clearly increasing in case of the larger states. The scans at these longer times do not contain the full envelope any more and therefore zero padding creates a sharp edge in the data. As a consequence the Fourier transformed wave packet shape gets distorted, nevertheless the oscillation frequency components should provide information about the size of the separation.

Multiple decoherence mechanisms and calibrations influence the results of these experiments. For example miscalibration in the motional frequency lead to mismatch between oscillator superposition and the SDF pulse direction. Constant detunings could be probed by scanning the latter. Accumulation of relative phase between the two wave packets could be checked by scanning

the modular variable phase φ. Similar to a qubit Ramsey this would lead to oscillations of the revival probability where the contrast probes the coherence of the superposition. Note that furthermore the larger states in this experiment are no longer properly described by the Lamb-Dicke approximation. Unraveling the dominant error source in such experiment is left for future studies.

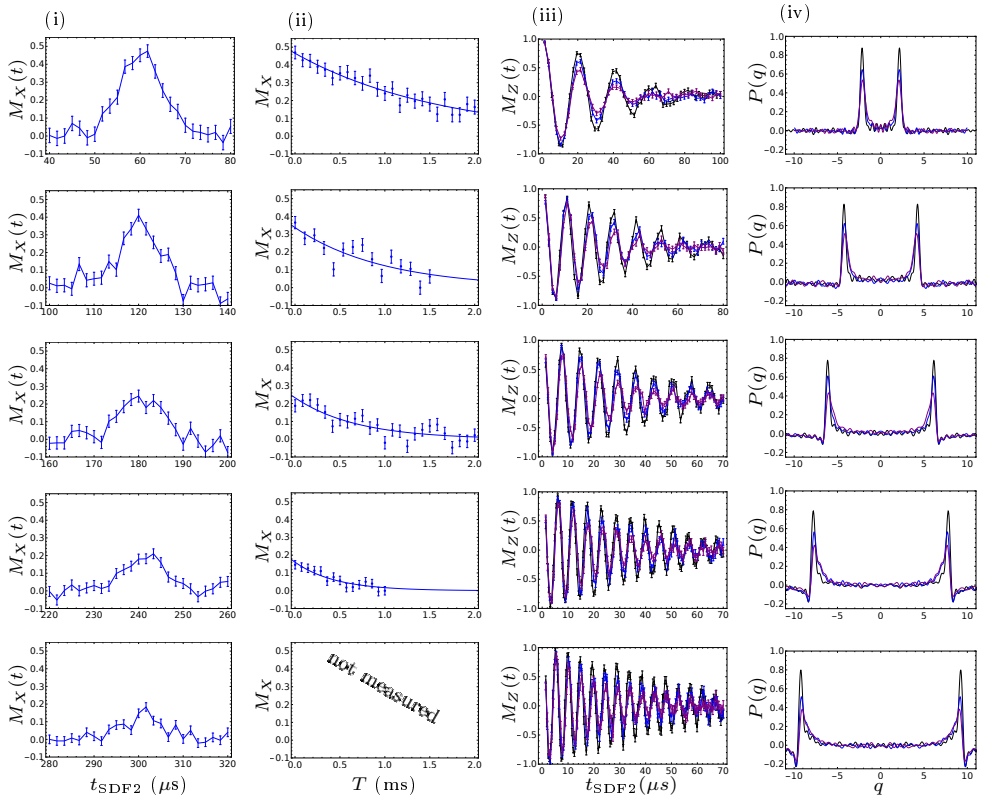

Figure D.2: Squeezed cat interferometer. A first modular measurement creates states $[\hat{\mathcal{D}}(-\alpha/2)+\hat{\mathcal{D}}(\alpha/2)]\,|r\rangle$ with $r \approx 0.98$ and $\alpha \approx 2ct_{\mathrm{SDF}}$. Where the coupling strength $c \approx 35.5\,\mathrm{ms}^{-1}$. After a free evolution time T these are probed by a second modular measurement. column (i) shows the revival in the signal $M_X(t) = \mathrm{Re}[\hat{\mathcal{D}}(2ct_{SDF2})]$ for $t_{\mathrm{SDF}} \in [60, 120, 180, 240, 300]$ (μs). column (ii) shows the decay of this revival as function of wait time T. For the largest separation this measurement was no longer performed. column (iii) shows analysis along the perpendicular direction $M_Z(t) = \mathrm{Re}[\hat{\mathcal{D}}(i2ct_{SDF2})]$. Here the wait time T was set to 0 ms (black), 0.5 ms (blue) and 1 ms (purple). (iv) Fourier transform of the signal in column (iii) leads to a measure of the position probability density. For the longer SDF times not all relevant signal is captured in column (iii). This leads to unphysical negative values in the simple discrete Fourier transform given in column (iv).

E Sequential measurement probabilities

In this section we describe how to calculate the signaling in time parameter $\mathscr{S}$ as well as the correlator $\mathcal{C}$ between sequential modular measurement.

E.1 Measurements in the density matrix formalism

Our description of indirect measurement in section 1.4.1 was in terms of pure input states. For mixed input state $\hat{\rho}_{\text{in}}$ the measurement properties can be written as:

- measurement probabilities: $P(\pm 1) = \text{Tr}(\hat{\rho}_{\text{in}} \hat{E}_{\pm}^{\dagger} \hat{E}_{\pm})$
- system post-measurement state: $\hat{\rho}_{\pm 1} = \hat{E}_{\pm} \hat{\rho}_{\text{in}} \hat{E}_{\pm}^{\dagger} / P(\pm 1)$
- system observable (unchanged): $\hat{E}_{+}^{\dagger} \hat{E}_{+} - \hat{E}_{-}^{\dagger} \hat{E}_{-} = \hat{O}$

E.2 Calculation of measurement probabilities

The analytic calculation is based on few basic principles which can be used for any number and implementation of modular measurements with a wide variety of input states including mixed thermal states. These few principles we automated using Mathematica and are summarized in the following. First we note that by combining displacement operators using equation 2.8, any measurement probability can be expressed as a summation over terms of the same type. These can be simplified using the cyclicity of the trace, that $\hat{\mathcal{D}}(\gamma)^{\dagger} = \hat{\mathcal{D}}(-\gamma)$ and evaluation in a suitable basis. For example:

$$\begin{aligned} P_A(a) =& \text{Tr}\left\{ \hat{E}_a^{\dagger}(\phi, \alpha) \hat{E}_a(\phi, \alpha) \hat{\rho}_{\text{in}} \right\} \\ =& \sum_{i,j} d_{i,j} \text{Tr}\left\{ \hat{\mathcal{D}}(\beta_i) \hat{\rho}_0 \hat{\mathcal{D}}(\gamma_j)^{\dagger} \right\} \\ =& \sum_{i,j} d_{i,j} e^{-i\text{Im}(\gamma_j \beta_i^*)} \sum_{n=0}^{\infty} \langle n | \, \hat{\mathcal{D}}(\delta_{ij}) \hat{\rho}_0 \, | n \rangle \end{aligned}$$

The measurement input state $\hat{\rho}_{\text{in}}$ can be the post-measurement state of previous experiments. Thus we inserted $\hat{\rho}_{\text{in}} = \sum_{i,j} d_{i,j} \hat{\mathcal{D}}(\beta_i) \hat{\rho}_0 \hat{\mathcal{D}}(\gamma_j)^{\dagger}$, with $d_{i,j} \in \mathbb{C}$ and $\hat{\rho}_0$ the input state to the first measurement. Further we define $\delta_{ij} = \beta_i - \gamma_j$. For the states considered in chapter 7 $\hat{\rho}_0$ is given by either (i): ground state $|0\rangle\langle 0|$, (ii): first excited state $|1\rangle\langle 1|$, (iii): thermal state $\hat{\rho}_{\text{th}} = \sum_{k=0}^{\infty} \frac{\overline{n}^k}{(1+\overline{n})^{k+1}} |k\rangle\langle k|$ or (iv): squeezed vacuum state $\hat{\mathcal{S}}(\xi)|0\rangle$. For the states $(i) - (iii)$ the probabilities can be evaluated using

$$\langle n | \hat{\mathcal{D}}(\alpha) | n \rangle = e^{-\frac{1}{2}|\alpha|^2} L_n^0(|\alpha|^2) \tag{E.1}$$

where for (iii) the additional thermal sum is calculated with the relation:

$$\sum_{n=0}^{\infty} L_n^{\lambda}(z) w^n = (1-w)^{-\lambda-1} e^{\frac{wz}{w-1}}, |w| < 1. \tag{E.2}$$

Here L denote the Laguerre polynomials. For the squeezed vacuum state we evaluate the trace in the corresponding squeezed Fock state basis and interchange squeezing and displacement operator with the relation equation 2.15.

$$\begin{aligned} P_A(a) &= \sum_{i,j} d_{i,j} e^{-i\mathrm{Im}(\gamma_j \beta_i^*)} \sum_{n=0}^{\infty} \langle n|\hat{\mathcal{S}}(\xi)^\dagger \hat{\mathcal{D}}(\delta_{ij}) \hat{\mathcal{S}}(\xi)|0\rangle\langle 0|n\rangle \\ &= \sum_{i,j} d_{i,j} e^{-i\mathrm{Im}(\gamma_j \beta_i^*)} \sum_{n=0}^{\infty} \langle n|\hat{\mathcal{D}}(\delta'_{ij})|n\rangle \end{aligned}$$

E.3 Calculation of signaling in time and correlators

In order to calculate $\mathscr{S}$ and $\mathcal{C}$ for the symmetric as well as the asymmetric implementation, we first expand the expression for $P_B(b)$, which is identical for the two implementations due to their connection via an unitary i.e. $\hat{U}\hat{F}_\pm = \hat{E}_\pm$ with $\hat{F}_\pm(\varphi,\alpha) = \frac{1}{2}(\mathbb{1} \pm e^{i\varphi}\hat{\mathcal{D}}(\alpha))$ the measurement operators of the asymmetric implementation, $\hat{E}_\pm(\varphi,\alpha) = \frac{1}{2}(\hat{\mathcal{D}}(-\alpha/2) \pm e^{i\varphi}\hat{\mathcal{D}}(\alpha/2))$ the measurement operators of the symmetric implementation and $\hat{U} = \hat{\mathcal{D}}(-\alpha/2)$.

$$\begin{aligned} P_B(b) =& \langle\psi_{\mathrm{in}}| \hat{E}_b^\dagger \hat{E}_b |\psi_{\mathrm{in}}\rangle \\ =& \frac{1}{4} \langle\psi_{\mathrm{in}}| 2\cdot\mathbb{1} + be^{-i\varphi_B}\hat{\mathcal{D}}(-\alpha_B) + be^{i\varphi_B}\hat{\mathcal{D}}(\alpha_B) |\psi_{\mathrm{in}}\rangle \\ =& \frac{1}{2} \{1 + b|\chi_{\alpha_B}| \cos(\varphi_B + \arg(\chi_{\alpha_B}))\} \end{aligned}$$

where $\chi_\alpha = \chi(\alpha) = \langle\psi_{\mathrm{in}}| \hat{\mathcal{D}}(\alpha) |\psi_{\mathrm{in}}\rangle = |\chi_\alpha| e^{i\arg(\chi_\alpha)}$ is the characteristic function and we used its polar representation. Further we expand $P_{BA}(b,a)$, which depends on the post-measurement state of A and thus on the implementation we choose:

$$P_{BA}(b,a) = \langle\psi_{\mathrm{in}}| \hat{F}_a^\dagger \hat{U}^\dagger \hat{F}_b^\dagger \hat{F}_b \hat{U} \hat{F}_a |\psi_{\mathrm{in}}\rangle .$$

Defining the geometric phase as $\Phi = \mathrm{Im}(\alpha_B \alpha_A^*)$ we find for the symmetric P and asymmetric $\widetilde{P}$ implementations:

$$\begin{aligned}
\widetilde{P}_{BA}(b,a) =& \frac{1}{16}(4 + \langle\psi_{\mathrm{in}}| \\
& (b\hat{\mathcal{D}}(-\alpha_B)e^{-i\varphi_B}(1+e^{-2i\Phi}) \\
& +b\hat{\mathcal{D}}(\alpha_B)e^{i\varphi_B}(1+e^{2i\Phi}) \\
& +2a(\hat{\mathcal{D}}(-\alpha_A)e^{-i\varphi_A} + \hat{\mathcal{D}}(\alpha_A)e^{i\varphi_A}) \\
& +ab\hat{\mathcal{D}}(\alpha_A - \alpha_B)e^{i(\varphi_A-\varphi_B-\Phi)} \\
& +ab\hat{\mathcal{D}}(\alpha_A + \alpha_B)e^{i(\varphi_A+\varphi_B+\Phi)} \\
& +ab\hat{\mathcal{D}}(-\alpha_A - \alpha_B)e^{i(-\varphi_A-\varphi_B-\Phi)} \\
& +ab\hat{\mathcal{D}}(-\alpha_A + \alpha_B)e^{i(\varphi_B-\varphi_A+\Phi)}) \\
& |\psi_{\mathrm{in}}\rangle)
\end{aligned}$$

$$\begin{aligned}
P_{BA}(b,a) =& \frac{1}{16}(4 + \langle\psi_{\mathrm{in}}| \\
& (b(\hat{\mathcal{D}}(-\alpha_B)e^{-i\varphi_B}(e^{i\Phi}+e^{-i\Phi}) \\
& +b(\hat{\mathcal{D}}(\alpha_B)e^{i\varphi_B}(e^{i\Phi}+e^{-i\Phi}) \\
& +2a(\hat{\mathcal{D}}(-\alpha_A)e^{-i\varphi_A} + \hat{\mathcal{D}}(\alpha_A)e^{i\varphi_A}) \\
& +ab\hat{\mathcal{D}}(\alpha_A - \alpha_B)e^{i(\varphi_A-\varphi_B)} \\
& +ab\hat{\mathcal{D}}(\alpha_A + \alpha_B)e^{i(\varphi_A+\varphi_B)} \\
& +ab\hat{\mathcal{D}}(-\alpha_A - \alpha_B)e^{i(-\varphi_A-\varphi_B)} \\
& +ab\hat{\mathcal{D}}(-\alpha_A + \alpha_B)e^{i(\varphi_B-\varphi_A)}) \\
& |\psi_{\mathrm{in}}\rangle)
\end{aligned}$$

The dependence on the measurement outcomes a, b are of the form:

$$P_{BA}(b,a) = ac_1 + bc_2 + abc_3 + c_4.$$

Using this we find

$$\begin{aligned}
\mathcal{C}_{AB} &= \sum_{a,b} abP_{BA}(b,a) = 4c_3, \\
\mathscr{S} &= P_B(b=+1) - P_{B(A)}(b=+1) \\
&= P_B(b=+1) - \sum_a P_{BA}(b,a) \\
&= P_B(b=+1) - 2c_2 - 2c_4.
\end{aligned}$$

From which the formula of section 7.2 follow. The analogous is true for $\widetilde{P}_{BA}(b,a)$ from which $\widetilde{\mathcal{C}}_{AB}$ and $\widetilde{\mathscr{S}}_{AB}$ follow.

F State preparation infidelity

If we model state preparation as not completely pumping populations into the $|\downarrow\rangle \equiv \left|^2S_{1/2}, m_j = 1/2\right\rangle$ level, leaving populations in $\left|^2S_{1/2}, m_j = -1/2\right\rangle$ then we find for the true expectation value $\langle\hat{Z}\rangle_t$ and the measured value $\langle\hat{Z}\rangle_m$:

$$\begin{aligned} 1 &= P(\downarrow) + P(\uparrow) + P(f) \qquad \text{(F.1)} \\ \langle\hat{Z}\rangle_t &= (P(\downarrow) - P(\uparrow))/(1 - P(f)) = (-2P(\uparrow) + 1 - P(f))/(1 - P(f)) \\ \langle\hat{Z}\rangle_m &= -2P(\uparrow) + 1 = \langle\hat{Z}\rangle_t(1 - P(f)) + P(f) \end{aligned}$$

Here $P(f)$ is the amount of population remaining in $\left|^2S_{1/2}, m_j = -1/2\right\rangle$.

However sometimes we associate the variable for convenience (i.e. in some pulse sequences it is more natural to start with an initial $|\uparrow\rangle$ instead of $|\downarrow\rangle$) with $\langle\hat{Z}\rangle_t = (P(\uparrow) - P(\downarrow))$ in this case

$$\langle\hat{Z}'\rangle_m = 2P(\uparrow) - 1 = \langle\hat{Z}\rangle_t(1 - P(f)) - P(f) \qquad \text{(F.2)}$$

Thus it is best to allow for $P(f)$ being positive or negative and using the model:

$$\langle\hat{Z}\rangle_m = \langle\hat{Z}\rangle_t(1 - |P(f)|) + P(f) \qquad \text{(F.3)}$$

Acronyms

AOM acousto optic modulator. viii, 36, 56, 61, 62, 66, 67, 68, 81, 92

App. Appendix. 1, 20, 22, 44, 48, 74, 75, 102, 108, 109, 160

AR anti-reflection. 63, 64

CV continuous-variable. 4

DC direct current (constant). xi, 46, 48, 49, 53, 54, 55, 61, 62, 95, 184

DDS direct digital synthesis. 81

e-SWAP exponential-SWAP gate. 151

EIT Electromagnetically Induced Transparency. 26, 29

EOM electro optic modulator. 57, 58

FF feedforward. viii, 42, 43, 51, 52, 54, 55

FNC fiber noise cancellation. 56, 57, 61, 63

FP Fabry-Pérot. 56, 57, 63, 64

FPGA field-programmable gate array. 29, 102, 153

GHZ Greenberger–Horne–Zeilinger. 172

GKP Gottesman, Kitaev and Preskill. ix, 11, 12, 123, 124, 125, 126, 127, 129, 131, 151, 163, 169, 170, 171, 172, 173

LGI Leggett-Garg inequality. ix, 111, 112, 114, 115, 116, 118, 119, 120, 121, 122, 170, 171, 172

MR macroscopic realism. 7, 110, 122, 172

NIM non-invasive measurement. 7, 110, 111, 114, 115, 116, 118, 119, 171, 172

NSIT non signaling in time. 102, 103, 104, 105, 106, 107, 108, 115, 116, 120, 122

Op. Amp. operational amplifier. 45, 46, 47

PBS polarizing beam splitter. 63, 65

PCB printed circuit board. 45, 46, 47, 62

PD photodiode. 58, 61

PDH Pound-Drever-Hall. 56, 57, 58, 59, 62, 63, 64, 65, 67, 69

PMT photo multiplier tube. 27

PSU power supply unit. 47, 48, 184

PWM pulse-width modulated. 44, 181, 182, 183

r.m.s root mean square. 107

RF radio frequency. 36, 61, 81, 150

s.e.m. standard error of the mean. 75, 86, 90, 94, 103, 106, 114, 136, 141, 143, 160

SDF state-dependent force. viii, 37, 38, 39, 40, 59, 66, 74, 75, 77, 79, 80, 81, 82, 83, 99, 100, 112, 116, 131, 133, 137, 150, 151, 153, 155, 156, 158, 159, 161, 164, 165, 169, 171, 185, 186, 188

SIT signaling in time. ix, 101, 102, 103, 105, 106, 108, 114, 116, 118, 119, 120, 121, 122, 170, 171, 172, 189

TA tapered amplifier. 56, 57, 64, 65

TIQI trapped ion quantum information. v, 25, 56, 60, 61, 63, 151, 172, 185

ULE ultra low expansion. 56, 57, 59, 65

VCO voltage-controlled-oscillator. 58, 62

List of used symbols

general symbols

P:	measurement probability
$\hat{U}$:	unitary
$\wp$:	populations
$\left\|\psi\right\rangle, \hat{\rho}$:	generic quantum state
c_r:	reduced chi square
p_f:	error probability
σ:	standard deviation
Δ:	variance
L:	Lindblad operator

harmonic oscillator

$\hat{q}_r$:	position operator
$\hat{q}$:	dimensionless position operator
$\hat{q}^\lambda$:	quadrature operator
q^λ	quadrature variable
$\hat{p}_r$:	momentum operator
$\hat{p}$:	dimensionless momentum operator
m:	oscillator mass
ω:	oscillator angular frequency
$\hbar$:	reduced Planck constant
$\hat{a}^\dagger, (\hat{a})$:	oscillator quanta creation (destruction) operator
$\hat{N}$:	number operator
$\left\|n\right\rangle$:	Fock state n
$\hat{\mathcal{D}}(\alpha)$:	phase space shift operator
Φ:	phase due to non-commuting shifts
$\hat{\mathcal{S}}(\xi = re^{i\vartheta})$:	squeezing operator
φ:	phase between separated wave packets
$\hat{O}$:	measurement observable
$\mathcal{W}(\gamma)$:	Wigner function
$\chi(\beta)$:	symmetric characteristic function
$\mathcal{Q}$:	Q function
$\hat{\mathcal{P}}$:	parity operator
$\left\|\alpha\right\rangle$:	coherent state
c_n, b_{mn}:	basis expansion coefficient
$\hat{K}$:	displaced squeezed destruction operator
$\left\|n\right\rangle_{\alpha,\xi}$:	squeezed displaced Fock state
$\langle n\rangle$:	mean number of quanta
δn:	standard deviation of quanta

internal states and qubit

$\|\downarrow\rangle$:	internal qubit down level
$\|\uparrow\rangle$:	internal qubit up level
$\|a\rangle$:	additional internal state level
$\hat{X}, \hat{Y}, \hat{Z}$:	Pauli operators
$\boldsymbol{\sigma}$	vector of Pauli operations
$\hat{\sigma}_+$:	qubit creation operator
ω_a:	internal qubit angular transition frequency
θ	qubit rotation angle, polar coordinates
ϕ:	qubit rotation, laser phase and other phases
$\hat{R}(\theta, \phi)$:	qubit rotation
$\hat{H}$:	Hadamard operation
$\hat{T}$:	T gate
τ:	magnetic field sensitivity

laser interactions

ω_l:	laser angular frequency
η:	Lamb-dicke paramter
Ω:	Rabi frequency
δ:	laser detuning
$\hat{H}_I$:	Hamiltonian in interaction picture
$\hat{H}_-$:	displaced squeezed red sideband Hamiltonian
$\hat{H}_+$:	Anti-Hamiltonian, displaces squeezed blue sideband Hamiltonian
$\hat{H}_{\mathrm{SDF}}$:	SDF Hamiltonian
T:	free evolution time
C:	Ramsey contrast
T_π:	π-time
g:	tickling strength
L_n^a:	generalized Laguerre polynomials
$\mathcal{F}$:	cavity finesse

modular measurement

$\hat{E}_\pm$:	Kraus operators
$\hat{O}$:	observable
$\|\psi_{\mathrm{in}}\rangle$:	oscillator input state
$\|\psi_\pm\rangle$:	oscillator post-meas. state

measurement sequences

$\mathscr{S}$:	signaling in time
$\mathcal{C}$:	measurement correlator

$\mathcal{L}$:	Leggett-Garg inequality parameter

logical qubit

$\|\psi\rangle_L$:	logical qubit state
$\hat{X}_L, \hat{Y}_L, \hat{Z}_L$:	logical Pauli operators
$\hat{S}_X, \hat{S}_Z$:	logical qubit stabilizer operators
$\|0\rangle_L, \|1\rangle_L$:	approximate eigenstates of $\hat{Z}_L$
$\|\pm\rangle_L$	approximate eigenstates of $\hat{X}_L$
$\|\phi_+\rangle_L, \|\phi_-\rangle_L$:	approximate eigenstates of $\hat{Y}_L$
Ξ	process matrix

Bibliography

[1] P. W. Shor. "Polynomial-time algorithms for prime factorisation and discrete logarithms on a quantum computer". *SIAM Rev.* 41.2 (1999), pp. 303–332. DOI: 10.1137/S0036144598347011 (cit. on p. 1).

[2] L. K. Grover. "Quantum Mechanics Helps in Searching for a Needle in a Haystack". *Phys. Rev. Lett.* 79.2 (1997), pp. 325–328. DOI: 10.1103/PhysRevLett.79.325 (cit. on p. 1).

[3] J. Preskill. "Quantum Computing in the NISQ era and beyond". *Quantum* 2 (2018), p. 79. DOI: 10.22331/q-2018-08-06-79 (cit. on p. 1).

[4] A. P. Lund et al. "Quantum sampling problems, BosonSampling and quantum supremacy". *npj Quantum Inf.* 3.15 (2017). DOI: 10.1038/s41534-017-0018-2 (cit. on p. 1).

[5] M. Reiher et al. "Elucidating reaction mechanisms on quantum computers". *PNAS* 114.29 (2017), pp. 7555–7560. DOI: 10.1073/pnas.1619152114 (cit. on p. 1).

[6] P. A. M. Dirac. "A new notation for quantum mechanics". *Math. Proc. Camb. Philos. Soc.* 35.3 (1939), pp. 416–418. DOI: 10.1017/S0305004100021162 (cit. on pp. 1, 177).

[7] M. A. Nielsen and I. L. Chuang. *Quantum Computation and Quantum Information*. Cambridge University Press, 2000 (cit. on pp. 2, 8, 134).

[8] W. H. Zurek. "Decoherence and the Transition from Quantum to Classical — Revisited". In: *Quantum Decoherence*. Ed. by B. Duplantier et al. Birkhäuser Basel, 2007, pp. 1–31. DOI: 10.1007/978-3-7643-7808-0_1 (cit. on p. 2).

[9] C. H. Bennett et al. "Teleporting an unknown quantum state via dual classical and Einstein-Podolsky-Rosen channels". *Phys. Rev. Lett.* 70.13 (1993), pp. 1895–1899. DOI: 10.1103/PhysRevLett.70.1895 (cit. on pp. 3, 133).

[10] D. Gottesman. "Stabilizer codes and quantum error correction". PhD Thesis. Caltech, 1997 (cit. on pp. 3, 8).

[11] J. I. Cirac and P. Zoller. "Quantum Computations with Cold Trapped Ions". *Phys. Rev. Lett.* 74.20 (1995), pp. 4091–4094. DOI: 10.1103/PhysRevLett.74.4091 (cit. on pp. 4, 5).

[12] M. Saffman. "Quantum computing with neutral atoms". *Natl. Sci. Rev.* (2018). DOI: 10.1093/nsr/nwy088 (cit. on p. 4).

[13] N. A. Gershenfeld and I. L. Chuang. "Bulk Spin-Resonance Quantum Computation". *Science* 275.5298 (1997), pp. 350–356. DOI: 10.1126/science.275.5298.350 (cit. on p. 4).

[14] M. H. Devoret and R. J. Schoelkopf. "Superconducting Circuits for Quantum Information: An Outlook". *Science* 339.6124 (2013), pp. 1169–1174. DOI: 10.1126/science.1231930 (cit. on pp. 4, 124).

[15] G Wendin. "Quantum information processing with superconducting circuits: a review". *Rep. Prog. Phys.* 80.10 (2017), p. 106001. DOI: 10.1088/1361-6633/aa7e1a (cit. on p. 4).

[16] P. van Loock. "Optical hybrid approaches to quantum information". *Laser Photonics Rev.* 5.2 (2011), pp. 167–200. DOI: 10.1002/lpor.201000005 (cit. on pp. 4, 123).

[17] E. Knill et al. "A scheme for efficient quantum computation with linear optics". *Nature* 409 (2001), pp. 46–52. DOI: 10.1038/35051009 (cit. on pp. 4, 123).

[18] R. Raussendorf and H. J. Briegel. "A One-Way Quantum Computer". *Phys. Rev. Lett.* 86.22 (2001), pp. 5188–5191. DOI: 10.1103/PhysRevLett.86.5188 (cit. on pp. 4, 123).

[19] D. Gottesman et al. "Encoding a qubit in an oscillator". *Phys. Rev. A* 64 (2001), p. 012310. DOI: 10.1103/PhysRevA.64.012310 (cit. on pp. 4, 11, 122, 123, 125–129).

[20] C. Weedbrook et al. "Gaussian quantum information". *Rev. Mod. Phys.* 84.2 (2012), pp. 621–669. DOI: 10.1103/RevModPhys.84.621 (cit. on p. 4).

[21] C. Hamsen et al. "Strong coupling between photons of two light fields mediated by one atom". *Nat. Phys.* 14.9 (2018), pp. 885–889. DOI: 10.1038/s41567-018-0181-1 (cit. on pp. 4, 123).

[22] S. Lloyd and S. L. Braunstein. "Quantum Computation over Continuous Variables". *Phys. Rev. Lett.* 82.8 (1999), pp. 1784–1787. DOI: 10.1103/PhysRevLett.82.1784 (cit. on p. 4).

[23] M. Reagor et al. "Reaching 10 ms single photon lifetimes for superconducting aluminum cavities". *Appl. Phys. Lett.* 102.19 (2013), p. 192604. DOI: 10.1063/1.4807015 (cit. on pp. 4, 124).

[24] K. Mølmer and A. Sørensen. "Multiparticle Entanglement of Hot Trapped Ions". *Phys. Rev. Lett.* 82.9 (1999), pp. 1835–1838. DOI: 10.1103/PhysRevLett.82.1835 (cit. on pp. 5, 38).

[25] E. T. Jaynes and F. W. Cummings. "Comparison of quantum and semiclassical radiation theories with application to the beam maser". *Proc. IEEE* 51.1 (1963), pp. 89–109. DOI: 10.1109/PROC.1963.1664 (cit. on p. 5).

[26] D. J. Wineland et al. "Experimental issues in coherent quantum-state manipulation of trapped atomic ions". *J. Res. Natl. Inst. Stand. Technol.* 103 (1998), pp. 259–328. DOI: 10.6028/jres.103.019 (cit. on pp. 5, 29, 31, 33).

[27] F. Diedrich et al. "Laser Cooling to the Zero-Point Energy of Motion". *Phys. Rev. Lett.* 62.4 (1989), pp. 403–406. DOI: 10.1103/PhysRevLett.62.403 (cit. on p. 5).

[28] C. Monroe et al. "Resolved-Sideband Raman Cooling of a Bound Atom to the 3D Zero-Point Energy". *Phys. Rev. Lett.* 75.22 (1995), pp. 4011–4014. DOI: 10.1103/PhysRevLett.75.4011 (cit. on p. 5).

[29] D. Leibfried et al. "Experimental Determination of the Motional Quantum State of a Trapped Atom". *Phys. Rev. Lett.* 77.21 (1996), pp. 4281–4285. DOI: 10.1103/PhysRevLett.77.4281 (cit. on pp. 5, 34, 83, 84, 92, 95, 155).

[30] D. M. Meekhof et al. "Generation of nonclassical motional states of a trapped atom". *Phys. Rev. Lett.* 76 (1996), p. 1796. DOI: 10.1103/PhysRevLett.76.1796 (cit. on p. 5).

[31] C. Monroe et al. "A Schrödinger cat superposition state of an atom". *Science* 272.5265 (1996), pp. 1131–1136. DOI: 10.1126/science.272.5265.1131 (cit. on pp. 5, 84, 116, 117).

[32] S. Deléglise et al. "Reconstruction of non-classical cavity field states with snapshots of their decoherence". *Nature* 455 (2008), pp. 510–514. DOI: 10.1038/nature07288 (cit. on pp. 5, 6).

[33] E. Schrödinger. "Die gegenwärtige Situation in der Quantenmechanik". *Naturwissenschaften* 23.48 (1935), pp. 807–812. DOI: 10.1007/BF01491891 (cit. on pp. 5, 7).

[34] M. Brune et al. "Quantum Rabi Oscillation: A Direct Test of Field Quantization in a Cavity". *Phys. Rev. Lett.* 76.11 (1996), pp. 1800–1803. DOI: 10.1103/PhysRevLett.76.1800 (cit. on pp. 5, 84).

[35] Q. A. Turchette et al. "Heating of trapped ions from the quantum ground state". *Phys. Rev. A* 61.6 (2000), p. 063418. DOI: 10.1103/PhysRevA.61.063418 (cit. on pp. 5, 71, 91).

[36] Q. A. Turchette et al. "Decoherence and decay of motional quantum states of a trapped atom coupled to engineered reservoirs". *Phys. Rev. A* 62.5 (2000), p. 053807. DOI: 10.1103/PhysRevA.62.053807 (cit. on pp. 5, 72, 73, 91).

[37] H.-Y. Lo et al. "Spin-motion entanglement and state diagnosis with squeezed oscillator wavepackets". *Nature* 521 (2015), pp. 336–339. DOI: doi:10.1038/nature14458 (cit. on pp. 5, 74, 84, 103, 116, 185, 186).

[38] K. G. Johnson et al. "Ultrafast creation of large Schrödinger cat states of an atom". *Nat. Commun.* 8.697 (2017). DOI: 10.1038/s41467-017-00682-6 (cit. on pp. 5, 116).

[39] D. Kienzler et al. "Quantum Harmonic Oscillator State Control in a Squeezed Fock Basis". *Phys. Rev. Lett.* 119.3 (2017), p. 033602. DOI: 10.1103/PhysRevLett.119.033602 (cit. on pp. 5, 37).

[40] D. Kienzler et al. "Quantum harmonic oscillator state synthesis by reservoir engineering". *Science* 347.6217 (2015), pp. 53–56. DOI: 10.1126/science.1261033 (cit. on pp. 5, 35–37, 79, 80, 131, 153).

[41] M. Arndt and K. Hornberger. "Testing the limits of quantum mechanical superpositions". *Nat. Phys.* 10 (2014), pp. 271–277. DOI: 10.1038/nphys2863 (cit. on p. 6).

[42] M. Aspelmeyer et al. "Cavity optomechanics". *Rev. Mod. Phys.* 86.4 (2014), pp. 1391–1452. DOI: 10.1103/RevModPhys.86.1391 (cit. on p. 6).

[43] F. Fröwis et al. "Macroscopic quantum states: Measures, fragility, and implementations". *Rev. Mod. Phys.* 90.2 (2018), p. 025004. DOI: 10.1103/RevModPhys.90.025004 (cit. on p. 6).

[44] S. Gerlich et al. "Quantum interference of large organic molecules". *Nat. Commun.* 2.263 (2011). DOI: 10.1038/ncomms1263 (cit. on p. 6).

[45] A. J. Leggett. "Realism and the physical world". *Rep. Prog. Phys.* 71.2 (2008), p. 022001. DOI: 10.1088/0034-4885/71/2/022001 (cit. on pp. 6, 111).

[46] A. Bassi et al. "Models of wave-function collapse, underlying theories, and experimental tests". *Rev. Mod. Phys.* 85.2 (2013), pp. 471–527. DOI: 10.1103/RevModPhys.85.471 (cit. on p. 6).

[47] M. Born. "Statistical Interpretation of Quantum Mechanics". *Science* 122.3172 (1955), pp. 675–679. DOI: 10.1126/science.122.3172.675 (cit. on p. 6).

[48] H. M. Wiseman and G. J. Milburn. *Quantum Measurement and Control*. Cambridge University Press, 2009 (cit. on pp. 6, 9).

[49] J. von Neumann. *Mathematical Foundations of Quantum Mechanics*. Investigations in physics. Princeton University Press, 1955 (cit. on pp. 6, 148).

[50] B. Vlastakis et al. "Deterministically Encoding Quantum Information Using 100-Photon Schrödinger's Cat States". *Science* 342 (2013), pp. 607–610. DOI: 10.1126/science.1243289 (cit. on pp. 6, 84).

[51] A. J. Leggett and A. Garg. "Quantum mechanics versus macroscopic realism: Is the flux there when nobody looks?" *Phys. Rev. Lett.* 54.9 (1985), pp. 857–860. DOI: 10.1103/PhysRevLett.54.857 (cit. on pp. 6, 7, 97, 110, 114).

[52] C.-M. Li et al. "Witnessing Quantum Coherence: from solid-state to biological systems". *Sci. Rep.* 2 (2012), p. 885. DOI: 10.1038/srep00885 (cit. on pp. 7, 101, 116).

[53] J. Kofler and Č. Brukner. "Condition for macroscopic realism beyond the Leggett-Garg inequalities". *Phys. Rev. A* 87.5 (2013), p. 052115. DOI: 10.1103/PhysRevA.87.052115 (cit. on pp. 7, 101, 115, 116, 122, 172).

[54] F. Palacios-Laloy Agustinand Mallet et al. "Experimental violation of a Bell's inequality in time with weak measurement". *Nat. Phys.* 6 (2010), pp. 442–447. DOI: 10.1038/nphys1641 (cit. on pp. 7, 111).

[55] J. P. Groen et al. "Partial-Measurement Backaction and Nonclassical Weak Values in a Superconducting Circuit". *Phys. Rev. Lett.* 111.9 (2013), p. 090506. DOI: 10.1103/PhysRevLett.111.090506 (cit. on pp. 7, 111, 171).

[56] G. Waldherr et al. "Violation of a Temporal Bell Inequality for Single Spins in a Diamond Defect Center". *Phys. Rev. Lett.* 107.9 (2011), p. 090401. DOI: 10.1103/PhysRevLett.107.090401 (cit. on pp. 7, 111, 171).

[57] R. E. George et al. "Opening up three quantum boxes causes classically undetectable wavefunction collapse". *PNAS* 110.10 (2013), pp. 3777–3781. DOI: 10.1073/pnas.1208374110 (cit. on pp. 7, 111, 171).

[58] V. Athalye et al. "Investigation of the Leggett-Garg Inequality for Precessing Nuclear Spins". *Phys. Rev. Lett.* 107.13 (2011), p. 130402. DOI: 10.1103/PhysRevLett.107.130402 (cit. on pp. 7, 111, 171).

[59] A. M. Souza et al. "A scattering quantum circuit for measuring Bell's time inequality: a nuclear magnetic resonance demonstration using maximally mixed states". *New J. Phys.* 13.5 (2011), p. 053023. DOI: 10.1088/1367-2630/13/5/053023 (cit. on pp. 7, 111, 171).

[60] H. Katiyar et al. "Violation of entropic Leggett-Garg inequality in nuclear spins". *Phys. Rev. A* 87.5 (2013), p. 052102. DOI: 10.1103/PhysRevA.87.052102 (cit. on pp. 7, 111, 171).

[61] G. C. Knee et al. "Violation of a Leggett-Garg inequality with ideal non-invasive measurements". *Nat. Commun.* 3.606 (2012). DOI: 10.1038/ncomms1614 (cit. on pp. 7, 111, 171).

[62] Z.-Q. Zhou et al. "Experimental Detection of Quantum Coherent Evolution through the Violation of Leggett-Garg-Type Inequalities". *Phys. Rev. Lett.* 115.11 (2015), p. 113002. DOI: 10.1103/PhysRevLett.115.113002 (cit. on pp. 7, 111, 171).

[63] M. E. Goggin et al. "Violation of the Leggett–Garg inequality with weak measurements of photons". *PNAS* 108.4 (2011), pp. 1256–1261. DOI: 10.1073/pnas.1005774108 (cit. on pp. 7, 111, 171).

[64] J. Dressel et al. "Experimental Violation of Two-Party Leggett-Garg Inequalities with Semiweak Measurements". *Phys. Rev. Lett.* 106.4 (2011), p. 040402. DOI: 10.1103/PhysRevLett.106.040402 (cit. on pp. 7, 111, 171).

[65] Y. Suzuki et al. "Violation of Leggett–Garg inequalities in quantum measurements with variable resolution and back-action". *New J. Phys.* 14.10 (2012), p. 103022. DOI: 10.1088/1367-2630/14/10/103022 (cit. on pp. 7, 111, 171).

[66] C. Robens et al. "Ideal Negative Measurements in Quantum Walks Disprove Theories Based on Classical Trajectories". *Phys. Rev. X* 5.1 (2015), p. 011003. DOI: 10.1103/PhysRevX.5.011003 (cit. on pp. 7, 111, 118, 171, 172).

[67] A. Asadian et al. "Probing Macroscopic Realism via Ramsey Correlation Measurements". *Phys. Rev. Lett.* 112.19 (2014), p. 190402. DOI: 10.1103/PhysRevLett.112.190402 (cit. on pp. 7, 100, 111, 116, 122).

[68] E. P. Wigner. "Remarks on the Mind-Body Question". In: *Philosophical Reflections and Syntheses*. Ed. by J. Mehra. Springer Berlin Heidelberg, 1995, pp. 247–260. DOI: 10.1007/978-3-642-78374-6_20 (cit. on p. 7).

[69] D. Frauchiger and R. Renner. "Quantum theory cannot consistently describe the use of itself". *Nat. Commun.* 9.3711 (2018). DOI: 10.1038/s41467-018-05739-8 (cit. on p. 7).

[70] F. J. MacWilliams and N. J. A. Sloane. *The theory of error correcting codes*. North-Holland Pub. Co., 1977 (cit. on p. 7).

[71] W. K. Wootters and W. H. Zurek. "A single quantum cannot be cloned". *Nature* 299.5886 (1982), pp. 802–803. DOI: 10.1038/299802a0 (cit. on p. 7).

[72] S. J. Devitt et al. "Quantum error correction for beginners". *Rep. Prog. Phys.* 76.7 (2013), p. 076001. DOI: 10.1088/0034-4885/76/7/076001 (cit. on pp. 7, 126).

[73] P. W. Shor. "Scheme for reducing decoherence in quantum computer memory". *Phys. Rev. A* 52.4 (1995), R2493–R2496. DOI: 10.1103/PhysRevA.52.R2493 (cit. on p. 7).

[74] A. M. Steane. "Error Correcting Codes in Quantum Theory". *Phys. Rev. Lett.* 77.5 (1996), pp. 793–797. DOI: 10.1103/PhysRevLett.77.793 (cit. on p. 7).

[75] P. W. Shor. "Fault-tolerant Quantum Computation". In: *Proceedings of the 37th Annual Symposium on Foundations of Computer Science*. IEEE Computer Society, 1996, pp. 56–65. DOI: 10.1109/SFCS.1996.548464 (cit. on p. 7).

[76] A. Y. Kitaev. "Quantum computations: algorithms and error correction". *Russian Mathematical Surveys* 52 (1997), pp. 1191–1249. DOI: 10.1070/RM1997v052n06ABEH002155 (cit. on p. 7).

[77] E. Knill et al. "Resilient quantum computation: error models and thresholds". *Proc. Royal Soc. A* 454.1969 (1998), pp. 365–384. DOI: 10.1098/rspa.1998.0166 (cit. on pp. 7, 133).

[78] J. Preskill. "Reliable quantum computers". *Proc. Royal Soc. A* 454.1969 (1998), pp. 385–410. DOI: 10.1098/rspa.1998.0167 (cit. on p. 7).

[79] A. R. Calderbank et al. "Quantum Error Correction and Orthogonal Geometry". *Phys. Rev. Lett.* 78.3 (1997), pp. 405–408. DOI: 10.1103/PhysRevLett.78.405 (cit. on p. 8).

[80] C. H. Bennett et al. "Mixed-state entanglement and quantum error correction". *Phys. Rev. A* 54.5 (1996), pp. 3824–3851. DOI: 10.1103/PhysRevA.54.3824 (cit. on pp. 8, 10, 11).

[81] E. Knill and R. Laflamme. "Theory of quantum error-correcting codes". *Phys. Rev. A* 55.2 (1997), pp. 900–911. DOI: 10.1103/PhysRevA.55.900 (cit. on pp. 8, 10).

[82] M. D. Reed et al. "Realization of three-qubit quantum error correction with superconducting circuits". *Nature* 482 (2012), pp. 382–385. DOI: 10.1038/nature10786 (cit. on p. 10).

[83] O. Moussa et al. "Demonstration of Sufficient Control for Two Rounds of Quantum Error Correction in a Solid State Ensemble Quantum Information Processor". *Phys. Rev. Lett.* 107.16 (2011), p. 160501. DOI: 10.1103/PhysRevLett.107.160501 (cit. on p. 10).

[84] M. Lassen et al. "Quantum optical coherence can survive photon losses using a continuous-variable quantum erasure-correcting code". *Nat. Photonics* 4 (2010), pp. 700–705. DOI: 10.1038/nphoton.2010.168 (cit. on pp. 10, 11).

[85] J Cramer et al. "Repeated quantum error correction on a continuously encoded qubit by real-time feedback". *Nat. Commun.* 7.11526 (2016). DOI: 10.1038/ncomms11526 (cit. on p. 10).

[86] N. Ofek et al. "Extending the lifetime of a quantum bit with error correction in superconducting circuits". *Nature* 536.7617 (2016), pp. 441–445. DOI: 10.1038/nature18949 (cit. on pp. 10, 11, 124).

[87] C. J. Axline et al. "On-demand quantum state transfer and entanglement between remote microwave cavity memories". *Nat. Phys.* 14.7 (2018), pp. 705–710. DOI: 10.1038/s41567-018-0115-y (cit. on pp. 10, 11, 124, 125).

[88] P. Schindler et al. "Experimental Repetitive Quantum Error Correction". *Science* 332.6033 (2011), pp. 1059–1061. DOI: 10.1126/science.1203329 (cit. on p. 10).

[89] M. Müller et al. "Iterative Phase Optimization of Elementary Quantum Error Correcting Codes". *Phys. Rev. X* 6.3 (2016), p. 031030. DOI: 10.1103/PhysRevX.6.031030 (cit. on p. 10).

[90] V Negnevitsky et al. "Repeated multi-qubit readout and feedback with a mixed-species trapped-ion register". *Nature* 563.7732 (2018), pp. 527–531. DOI: 10.1038/s41586-018-0668-z (cit. on pp. 10, 25, 82).

[91] D. Nigg et al. "Quantum computations on a topologically encoded qubit". *Science* 345.6194 (2014), pp. 302–305. DOI: 10.1126/science.1253742 (cit. on p. 10).

[92] C. Langer et al. "Long-Lived Qubit Memory Using Atomic Ions". *Phys. Rev. Lett.* 95.6 (2005), p. 060502. DOI: 10.1103/PhysRevLett.95.060502 (cit. on pp. 10, 26, 43).

[93] T. P. Harty et al. "High-Fidelity Preparation, Gates, Memory, and Readout of a Trapped-Ion Quantum Bit". *Phys. Rev. Lett.* 113.22 (2014), p. 220501. DOI: 10.1103/PhysRevLett.113.220501 (cit. on p. 10).

[94] C. J. Ballance et al. "High-Fidelity Quantum Logic Gates Using Trapped-Ion Hyperfine Qubits". *Phys. Rev. Lett.* 117.6 (2016), p. 060504. DOI: 10.1103/PhysRevLett.117.060504 (cit. on p. 10).

[95] A. Bermudez et al. "Assessing the Progress of Trapped-Ion Processors Towards Fault-Tolerant Quantum Computation". *Phys. Rev. X* 7.4 (2017), p. 041061. DOI: 10.1103/PhysRevX.7.041061 (cit. on p. 11).

[96] I. L. Chuang et al. "Bosonic quantum codes for amplitude damping". *Phys. Rev. A* 56.2 (1997), pp. 1114–1125. DOI: 10.1103/PhysRevA.56.1114 (cit. on pp. 11, 125).

[97] M. H. Michael et al. "New Class of Quantum Error-Correcting Codes for a Bosonic Mode". *Phys. Rev. X* 6.3 (2016), p. 031006. DOI: 10.1103/PhysRevX.6.031006 (cit. on pp. 11, 125, 170).

[98] Z. Leghtas et al. "Hardware-Efficient Autonomous Quantum Memory Protection". *Phys. Rev. Lett.* 111.12 (2013), p. 120501. DOI: 10.1103/PhysRevLett.111.120501 (cit. on pp. 11, 124, 170).

[99] P. T. Cochrane et al. "Macroscopically distinct quantum-superposition states as a bosonic code for amplitude damping". *Phys. Rev. A* 59.4 (1999), pp. 2631–2634. DOI: 10.1103/PhysRevA.59.2631 (cit. on pp. 11, 124).

[100] S. L. Braunstein. "Error Correction for Continuous Quantum Variables". *Phys. Rev. Lett.* 80.18 (1998), pp. 4084–4087. DOI: 10.1103/PhysRevLett.80.4084 (cit. on p. 11).

[101] S. L. Braunstein. "Quantum error correction for communication with linear optics". *Nature* 394 (1998), p. 47. DOI: 10.1038/27850 (cit. on p. 11).

[102] S. Lloyd and J.-J. E. Slotine. "Analog Quantum Error Correction". *Phys. Rev. Lett.* 80.18 (1998), pp. 4088–4091. DOI: 10.1103/PhysRevLett.80.4088 (cit. on p. 11).

[103] J. Niset et al. "Experimentally Feasible Quantum Erasure-Correcting Code for Continuous Variables". *Phys. Rev. Lett.* 101.13 (2008), p. 130503. DOI: 10.1103/PhysRevLett.101.130503 (cit. on p. 11).

[104] M. Mirrahimi et al. "Dynamically protected cat-qubits: a new paradigm for universal quantum computation". *New J. Phys.* 16.4 (2014), p. 045014. DOI: 10.1088/1367-2630/16/4/045014 (cit. on pp. 11, 124, 170, 173).

[105] T. Aoki et al. "Quantum error correction beyond qubits". *Nat. Phys.* 5 (2009), pp. 541–546. DOI: 10.1038/nphys1309 (cit. on p. 11).

[106] J. Niset et al. "No-Go Theorem for Gaussian Quantum Error Correction". *Phys. Rev. Lett.* 102.12 (2009), p. 120501. DOI: 10.1103/PhysRevLett.102.120501 (cit. on pp. 11, 123).

[107] C. Vuillot et al. "Quantum error correction with the toric Gottesman-Kitaev-Preskill code". *Phys. Rev. A* 99 (3 2019), p. 032344. DOI: 10.1103/PhysRevA.99.032344 (cit. on pp. 11, 123, 126, 128, 153).

[108] R. W. Heeres et al. "Implementing a universal gate set on a logical qubit encoded in an oscillator". *Nat. Commun.* 8.94 (2017). DOI: 10.1038/s41467-017-00045-1 (cit. on pp. 11, 152).

[109] V. V. Albert et al. "Performance and structure of single-mode bosonic codes". *Phys. Rev. A* 97.3 (2018), p. 032346. DOI: 10.1103/PhysRevA.97.032346 (cit. on pp. 11, 125).

[110] K. Noh et al. "Quantum capacity bounds of Gaussian thermal loss channels and achievable rates with Gottesman-Kitaev-Preskill codes". *IEEE Trans. Inf. Theory* (2018), pp. 1–1. DOI: 10.1109/TIT.2018.2873764 (cit. on pp. 11, 125, 129).

[111] K. Fukui et al. "High-Threshold Fault-Tolerant Quantum Computation with Analog Quantum Error Correction". *Phys. Rev. X* 8.2 (2018), p. 021054. DOI: 10.1103/PhysRevX.8.021054 (cit. on pp. 11, 153).

[112] D. Kienzler et al. "Observation of Quantum Interference between Separated Mechanical Oscillator Wave Packets". *Phys. Rev. Lett.* 116.14 (2016), p. 140402. DOI: 10.1103/PhysRevLett.116.140402 (cit. on pp. 12, 83, 85, 102, 155).

[113] C. Flühmann et al. "Sequential Modular Position and Momentum Measurements of a Trapped Ion Mechanical Oscillator". *Phys. Rev. X* 8.2 (2018), p. 021001. DOI: 10.1103/PhysRevX.8.021001 (cit. on pp. 12, 97).

[114] C. Flühmann et al. "Encoding a qubit in a trapped-ion mechanical oscillator". *Nature* 566.7745 (2019), pp. 513–517. DOI: 10.1038/s41586-019-0960-6 (cit. on pp. 12, 123).

[115] S. H. Haroche and J.-M. Raimond. *Exploring the Quantum: Atoms and Cavities and Photons*. Oxford University Press, 2006 (cit. on pp. 13, 14, 71, 85, 93, 124).

[116] W. P. Schleich. "WKB and Berry Phase". In: *Quantum Optics in Phase Space*. Wiley-VCH Verlag GmbH & Co. KGaA, 2005, pp. 171–188. DOI: 10.1002/3527602976.ch6 (cit. on pp. 14, 20).

[117] R. Ozeri. "The trapped-ion qubit tool box". *Contemp. Phys.* 52.6 (2011), pp. 531–550. DOI: 10.1080/00107514.2011.603578 (cit. on pp. 14, 38).

[118] H. Goldstein et al. *Classical Mechanics: 3rd edition*. Addison-Wesley, 2001 (cit. on p. 14).

[119] E. Wigner. "On the Quantum Correction For Thermodynamic Equilibrium". *Phys. Rev.* 40.5 (1932), pp. 749–759. DOI: 10.1103/PhysRev.40.749 (cit. on p. 15).

[120] D. J. Griffiths and D. F. Schroeter. *Introduction to Quantum Mechanics*. 3rd ed. Cambridge University Press, 2018. DOI: 10.1017/9781316995433 (cit. on pp. 16, 177).

[121] H. P. Robertson. "The Uncertainty Principle". *Phys. Rev.* 34.1 (1929), pp. 163–164. DOI: 10.1103/PhysRev.34.163 (cit. on p. 16).

[122] S. M. Barnett and P. M. Radmore. *Methods in Theoretical Quantum Optics*. Oxford University Press Inc., 2002. DOI: 10.1093/acprof:oso/9780198563617.001.0001 (cit. on pp. 20, 21, 35, 157, 163).

[123] D. Kienzler. "Quantum Harmonic Oscillator State Synthesis by Reservoir Engineering". PhD Thesis. ETH Zürich, 2015 (cit. on pp. 25, 26, 35–37, 41, 43, 72, 73).

[124] H.-Y. Lo. "Creation of Squeezed Schrödinger's Cat States in a Mixed-Species Ion Trap". PhD Thesis. ETH Zürich, 2015 (cit. on pp. 25–27, 43).

[125] W. Paul. "Electromagnetic traps for charged and neutral particles". *Rev. Mod. Phys.* 62.3 (1990), pp. 531–540. DOI: 10.1103/RevModPhys.62.531 (cit. on p. 25).

[126] D. V. F. James. "Quantum dynamics of cold trapped ions with application to quantum computation". *Appl. Phys. B* 66 (1998), pp. 181–190. DOI: 10.1007/s003400050373 (cit. on p. 26).

[127] V. Negnevitsky. "Feedback-stabilised quantum states in a mixed-species ion system". PhD Thesis. ETH Zürich, 2018 (cit. on pp. 25, 26, 38, 51, 81, 151).

[128] M. D. Barrett et al. "Sympathetic cooling of $^{9}Be^{+}$ and $^{24}Mg^{+}$ for quantum logic". *Phys. Rev. A* 68.4 (2003), p. 042302. DOI: 10.1103/PhysRevA.68.042302 (cit. on p. 25).

[129] H. J. Metcalf and P. van der Straten. *Laser cooling and trapping*. Springer-Verlag, 1999 (cit. on p. 25).

[130] C. F. Roos et al. "Experimental Demonstration of Ground State Laser Cooling with Electromagnetically Induced Transparency". *Phys. Rev. Lett.* 85.26 (2000), pp. 5547–5550. DOI: 10.1103/PhysRevLett.85.5547 (cit. on p. 26).

[131] J. D. Jackson. *Classical electrodynamics*. 3rd ed. Wiley, 1999 (cit. on p. 30).

[132] C. Roos. "Controlling the quantum state of trapped ions". PhD Thesis. Universität Innsbruck, 2000 (cit. on p. 30).

[133] S. Haroche. "Nobel Lecture: Controlling photons in a box and exploring the quantum to classical boundary". *Rev. Mod. Phys.* 85.3 (2013), pp. 1083–1102. DOI: 10.1103/RevModPhys.85.1083 (cit. on pp. 32, 84).

[134] K. C. McCormick et al. "Quantum-enhanced sensing of a mechanical oscillator". *arXiv:1807.11934 [physics.atom-ph]* (2018). arXiv: 1807.11934 (cit. on pp. 34, 71, 150).

[135] C. Wunderlich et al. "Robust state preparation of a single trapped ion by adiabatic passage". *J. Mod. Opt.* 54.11 (2007), pp. 1541–1549. DOI: 10.1080/09500340600741082 (cit. on p. 34).

[136] Y. Aharonov and J. Anandan. "Phase change during a cyclic quantum evolution". *Phys. Rev. Lett.* 58.16 (1987), pp. 1593–1596. DOI: 10.1103/PhysRevLett.58.1593 (cit. on p. 38).

[137] P. C. Haljan et al. "Spin-Dependent Forces on Trapped Ions for Phase-Stable Quantum Gates and Entangled States of Spin and Motion". *Phys. Rev. Lett.* 94.15 (2005), p. 153602. DOI: 10.1103/PhysRevLett.94.153602 (cit. on p. 38).

[138] A. Sørensen and K. Mølmer. "Quantum Computation with Ions in Thermal Motion". *Phys. Rev. Lett.* 82.9 (1999), pp. 1971–1974. DOI: 10.1103/PhysRevLett.82.1971 (cit. on p. 38).

[139] G. Milburn et al. "Ion Trap Quantum Computing with Warm Ions". *Fortschr. Phys.* 48.9-11 (2000), pp. 801–810 (cit. on p. 38).

[140] D. Leibfried et al. "Experimental demonstration of a robust and high-fidelity geometric two ion-qubit phase gate". *Nature* 422 (2003), pp. 412–415. DOI: 10.1038/nature01492 (cit. on p. 38).

[141] G. Kirchmair et al. "Deterministic entanglement of ions in thermal states of motion". *New J. Phys.* 11.2 (2009), p. 023002. DOI: 10.1088/1367-2630/11/2/023002 (cit. on p. 38).

[142] C. F. Roos. "Ion trap quantum gates with amplitude-modulated laser beams". *New J. Phys.* 10.1 (2008), p. 013002. DOI: 10.1088/1367-2630/10/1/013002 (cit. on p. 38).

[143] J. Home. "Entanglement of Two Trapped-Ion Spin Qubits". PhD Thesis. Linacre College, Oxford, 2016 (cit. on p. 42).

[144] L. Viola and S. Lloyd. "Dynamical suppression of decoherence in two-state quantum systems". *Phys. Rev. A* 58.4 (1998), pp. 2733–2744. DOI: 10.1103/PhysRevA.58.2733 (cit. on p. 42).

[145] E. L. Hahn. "Spin Echoes". *Phys. Rev.* 80.4 (1950), pp. 580–594. DOI: 10.1103/PhysRev.80.580 (cit. on p. 42).

[146] M. J. Biercuk et al. "Dynamical decoupling sequence construction as a filter-design problem". *J. Phys. B* 44.15 (2011), p. 154002. DOI: 10.1088/0953-4075/44/15/154002 (cit. on p. 42).

[147] C. Flühmann. "Stabilizing lasers and magnetic fields for quantum information experiments". Masters Thesis. ETH Zürich, 2014 (cit. on pp. 43, 44, 51, 63).

[148] B. Merkel et al. "Magnetic field stabilization system for atomic physics experiments". *Rev. Sci. Instrum.* 90.4 (2019), p. 044702. DOI: 10.1063/1.5080093 (cit. on p. 49).

[149] S. Kotler et al. "Nonlinear Single-Spin Spectrum Analyzer". *Phys. Rev. Lett.* 110.11 (2013), p. 110503. DOI: 10.1103/PhysRevLett.110.110503 (cit. on p. 50).

[150] D. R. Leibrandt et al. "Spherical reference cavities for frequency stabilization of lasers in non-laboratory environments". *Opt. Express* 19.4 (2011), pp. 3471–3482. DOI: 10.1364/OE.19.003471 (cit. on p. 56).

[151] M. A. Sepiol. "Frequency stabilization of a 729 nm diode laser to an external high finesse reference cavity". Masters Thesis. ETH Zürich, 2012 (cit. on pp. 56, 57, 59).

[152] L. Gerster. "Spectral filtering and laser diode injection for multi-qubit trapped ion gates". Masters Thesis. ETH Zürich, 2015 (cit. on pp. 56, 60, 63, 64).

[153] N. D. Oppong. "Cancellation of optical phase noise induced by an optical fiber". Semester Thesis. ETH Zürich, 2015 (cit. on pp. 56, 62).

[154] S. Seel et al. "Cryogenic Optical Resonators: A New Tool for Laser Frequency Stabilization at the 1 Hz Level". *Phys. Rev. Lett.* 78.25 (1997), pp. 4741–4744. DOI: 10.1103/PhysRevLett.78.4741 (cit. on p. 57).

[155] T. L. Nicholson et al. "Comparison of Two Independent Sr Optical Clocks with 1×10^{-17} Stability at 10^3 s". *Phys. Rev. Lett.* 109.23 (2012), p. 230801. DOI: 10.1103/PhysRevLett.109.230801 (cit. on p. 57).

[156] E. D. Black. "An introduction to Pound–Drever–Hall laser frequency stabilization". *Am. J. Phys.* 69.1 (2001), pp. 79–87. DOI: 10.1119/1.1286663 (cit. on p. 57).

[157] I. Ito et al. "Stable CW laser based on low thermal expansion ceramic cavity with 4.9 mHz/s frequency drift". *Opt. Express* 25.21 (2017), pp. 26020–26028. DOI: 10.1364/OE.25.026020 (cit. on p. 63).

[158] S. Häfner et al. "fractional laser frequency instability with a long room-temperature cavity". *Opt. Lett.* 40.9 (2015), pp. 2112–2115. DOI: 10.1364/OL.40.002112 (cit. on p. 63).

[159] S. Saner. "Diode injection stability: Comparison between a Fabry-Perot diode and an anti-reflective coated diode". Semester Thesis. ETH Zürich, 2018 (cit. on p. 64).

[160] D. A. Hite et al. "Measurements of trapped-ion heating rates with exchangeable surfaces in close proximity". *MRS Advances* 2.41 (2017), pp. 2189–2197. DOI: 10.1557/adv.2017.14 (cit. on p. 71).

[161] K. C. McCormick et al. "Coherently displaced oscillator quantum states of a single trapped atom". *Quantum. Sci. Technol.* 4.2 (2019), p. 024010. DOI: 10.1088/2058-9565/ab0513 (cit. on p. 71).

[162] P. C. Haljan et al. "Entanglement of trapped-ion clock states". *Phys. Rev. A* 72.6 (2005), p. 062316. DOI: 10.1103/PhysRevA.72.062316 (cit. on p. 84).

[163] M. J. McDonnell et al. "Long-Lived Mesoscopic Entanglement outside the Lamb-Dicke Regime". *Phys. Rev. Lett.* 98.6 (2007), p. 063603. DOI: 10.1103/PhysRevLett.98.063603 (cit. on p. 84).

[164] U. Poschinger et al. "Observing the Phase Space Trajectory of an Entangled Matter Wave Packet". *Phys. Rev. Lett.* 105.26 (2010), p. 263602. DOI: 10.1103/PhysRevLett.105.263602 (cit. on p. 84).

[165] D. J. Wineland. "Nobel Lecture: Superposition, entanglement, and raising Schrödinger's cat". *Rev. Mod. Phys.* 85.3 (2013), pp. 1103–1114. DOI: 10.1103/RevModPhys.85.1103 (cit. on p. 84).

[166] M. S. Kim et al. "Properties of squeezed number states and squeezed thermal states". *Phys. Rev. A* 40.5 (1989), pp. 2494–2503. DOI: 10.1103/PhysRevA.40.2494 (cit. on p. 89).

[167] C. Shen et al. "Optimized tomography of continuous variable systems using excitation counting". *Phys. Rev. A* 94.5 (2016), p. 052327. DOI: 10.1103/PhysRevA.94.052327 (cit. on pp. 95, 156).

[168] D. Lv et al. "Reconstruction of the Jaynes-Cummings field state of ionic motion in a harmonic trap". *Phys. Rev. A* 95.4 (2017), p. 043813. DOI: 10.1103/PhysRevA.95.043813 (cit. on p. 95).

[169] J. F. Poyatos et al. "Motion tomography of a single trapped ion". *Phys. Rev. A* 53.4 (1996), R1966–R1969. DOI: 10.1103/PhysRevA.53.R1966 (cit. on p. 95).

[170] M. Ozawa. "Universally valid reformulation of the Heisenberg uncertainty principle on noise and disturbance in measurement". *Phys. Rev. A* 67.4 (2003), p. 042105. DOI: 10.1103/PhysRevA.67.042105 (cit. on p. 97).

[171] M. Ozawa. "Uncertainty relations for joint measurements of noncommuting observables". *Phys. Lett. A* 320.5–6 (2004), pp. 367–374. DOI: 10.1016/j.physleta.2003.12.001 (cit. on p. 97).

[172] M. J. W. Hall. "Prior information: How to circumvent the standard joint-measurement uncertainty relation". *Phys. Rev. A* 69.5 (2004), p. 052113. DOI: 10.1103/PhysRevA.69.052113 (cit. on p. 97).

[173] O. Gühne et al. "Compatibility and noncontextuality for sequential measurements". *Phys. Rev. A* 81.2 (2010), p. 022121. DOI: 10.1103/PhysRevA.81.022121 (cit. on p. 97).

[174] B. M. Terhal and D. Weigand. "Encoding a qubit into a cavity mode in circuit QED using phase estimation". *Phys. Rev. A* 93.1 (2016), p. 012315. DOI: 10.1103/PhysRevA.93.012315 (cit. on pp. 98, 126, 129, 131, 151, 152).

[175] Y. Aharonov et al. "Modular variables in quantum theory". *Int. J. of Theor. Phys.* 2.3 (1969), pp. 213–230. DOI: 10.1007/BF00670008 (cit. on p. 98).

[176] S. Popescu. "Dynamical quantum non-locality". *Nat. Phys.* 6.3 (2010), pp. 151–153. DOI: 10.1038/nphys1619 (cit. on p. 98).

[177] Y. Aharonov and D. Rohrlich. "Modular Variables". In: *Quantum paradoxes: Quantum theory for the perplexed*. Wiley-VCH, 2005, pp. 61–75 (cit. on p. 98).

[178] B.-G. Englert et al. "Periodic and discrete Zak bases". *J. Phys. A* 39 (2006), pp. 1669–1682. DOI: 10.1088/0305-4470/39/7/011 (cit. on p. 104).

[179] S. Kochen and E. P. Specker. "The Problem of Hidden Variables in Quantum Mechanics". *J. Appl. Math. Mech.* 17 (1967), pp. 59–87. DOI: 10.1512/iumj.1968.17.17004 (cit. on p. 110).

[180] B. Hensen et al. "Loophole-free Bell inequality violation using electron spins separated by 1.3 kilometres". *Nature* 526.7575 (2015), pp. 682–686. DOI: 10.1038/nature15759 (cit. on p. 110).

[181] J. S. Bell. "On the Einstein Podolsky Rosen paradox". *Physics* 1.3 (1964), pp. 195–200. DOI: 10.1103/PhysicsPhysiqueFizika.1.195 (cit. on p. 110).

[182] J. F. Clauser et al. "Proposed Experiment to Test Local Hidden-Variable Theories". *Phys. Rev. Lett.* 23.15 (1969), pp. 880–884. DOI: 10.1103/PhysRevLett.23.880 (cit. on p. 110).

[183] J. P. Paz and G. Mahler. "Proposed test for temporal Bell inequalities". *Phys. Rev. Lett.* 71.20 (1993), pp. 3235–3239. DOI: 10.1103/PhysRevLett.71.3235 (cit. on p. 110).

[184] M. M. Wilde and A. Mizel. "Addressing the Clumsiness Loophole in a Leggett-Garg Test of Macrorealism". *Found. Phys.* 42.2 (2012), pp. 256–265. DOI: 10.1007/s10701-011-9598-4 (cit. on p. 111).

[185] C. D. Tesche. "Can a noninvasive measurement of magnetic flux be performed with superconducting circuits?" *Phys. Rev. Lett.* 64.20 (1990), pp. 2358–2361. DOI: 10.1103/PhysRevLett.64.2358 (cit. on p. 111).

[186] A. Peres. "Quantum Limitations on Measurement of Magnetic Flux". *Phys. Rev. Lett.* 61.18 (1988), pp. 2019–2021. DOI: 10.1103/PhysRevLett.61.2019 (cit. on p. 111).

[187] A. J. Leggett and A. Garg. "Comment on "Quantum limitations on measurement of magnetic flux"". *Phys. Rev. Lett.* 63.19 (1989), pp. 2159–2159. DOI: 10.1103/PhysRevLett.63.2159 (cit. on p. 111).

[188] L. E. Ballentine. "Realism and quantum flux tunneling". *Phys. Rev. Lett.* 59.14 (1987), pp. 1493–1495. DOI: 10.1103/PhysRevLett.59.1493 (cit. on p. 111).

[189] A. Elby and S. Foster. "Why SQUID experiments can rule out non-invasive measurability". *Phys. Lett. A* 166.1 (1992), pp. 17 –23. DOI: 10.1016/0375-9601(92)90867-L (cit. on p. 111).

[190] C. Emary et al. "Leggett–Garg inequalities". *Rep. Prog. Phys.* 77.1 (2014), p. 016001. DOI: 10.1088/0034-4885/77/1/016001 (cit. on pp. 111, 114, 116, 118).

[191] R. Rivière et al. "Optomechanical sideband cooling of a micromechanical oscillator close to the quantum ground state". *Phys. Rev. A* 83.6 (2011), p. 063835. DOI: 10.1103/PhysRevA.83.063835 (cit. on p. 112).

[192] R. Diehl et al. "Optical levitation and feedback cooling of a nanoparticle at subwavelength distances from a membrane". *Phys. Rev. A* 98.1 (2018), p. 013851. DOI: 10.1103/PhysRevA.98.013851 (cit. on p. 112).

[193] J. J. Halliwell. "Comparing conditions for macrorealism: Leggett-Garg inequalities versus no-signaling in time". *Phys. Rev. A* 96.1 (2017), p. 012121. DOI: 10.1103/PhysRevA.96.012121 (cit. on pp. 115, 122).

[194] J. V. Kujala et al. "Necessary and Sufficient Conditions for an Extended Noncontextuality in a Broad Class of Quantum Mechanical Systems". *Phys. Rev. Lett.* 115.15 (2015), p. 150401. DOI: 10.1103/PhysRevLett.115.150401 (cit. on pp. 119, 121, 172).

[195] A. Ketterer. "Modular variables in quantum information". PhD Thesis. Université Sorbonne Paris cité, Université Paris Diderot, 2016 (cit. on p. 122).

[196] A. R. Plastino and A. Cabello. "State-independent quantum contextuality for continuous variables". *Phys. Rev. A* 82.2 (2010), p. 022114. DOI: 10.1103/PhysRevA.82.022114 (cit. on pp. 122, 170, 172).

[197] A. Asadian et al. "Contextuality in Phase Space". *Phys. Rev. Lett.* 114.25 (2015), p. 250403. DOI: 10.1103/PhysRevLett.114.250403 (cit. on pp. 122, 170, 172).

[198] A. S. Arora and A. Asadian. "Proposal for a macroscopic test of local realism with phase-space measurements". *Phys. Rev. A* 92.6 (2015), p. 062107. DOI: 10.1103/PhysRevA.92.062107 (cit. on pp. 122, 170, 172).

[199] S. Massar and S. Pironio. "Greenberger-Horne-Zeilinger paradox for continuous variables". *Phys. Rev. A* 64.6 (2001), p. 062108. DOI: 10.1103/PhysRevA.64.062108 (cit. on pp. 122, 170, 172).

[200] M. Bergmann and P. van Loock. "Quantum error correction against photon loss using multicomponent cat states". *Phys. Rev. A* 94.4 (2016), p. 042332. DOI: 10.1103/PhysRevA.94.042332 (cit. on p. 124).

[201] L. Hu et al. "Quantum error correction and universal gate set operation on a binomial bosonic logical qubit". *Nat. Phys.* 15.5 (2019), pp. 503–508. DOI: 10.1038/s41567-018-0414-3 (cit. on p. 125).

[202] S. Glancy and E. Knill. "Error analysis for encoding a qubit in an oscillator". *Phys. Rev. A* 73.1 (2006), p. 012325. DOI: 10.1103/PhysRevA.73.012325 (cit. on pp. 125, 128).

[203] N. C. Menicucci. "Fault-Tolerant Measurement-Based Quantum Computing with Continuous-Variable Cluster States". *Phys. Rev. Lett.* 112.12 (2014), p. 120504. DOI: 10.1103/PhysRevLett.112.120504 (cit. on p. 125).

[204] B. C. Travaglione and G. J. Milburn. "Preparing encoded states in an oscillator". *Phys. Rev. A* 66.5 (2002), p. 052322. DOI: 10.1103/PhysRevA.66.052322 (cit. on pp. 126, 129, 131).

[205] S. Pirandola et al. "Continuous variable encoding by ponderomotive interaction". *Eur. Phys. J. D* 37.2 (2006), pp. 283–290. DOI: 10.1140/epjd/e2005-00306-3 (cit. on p. 126).

[206] H. M. Vasconcelos et al. "All-optical generation of states for "Encoding a qubit in an oscillator"". *Opt. Lett.* 35.19 (2010), pp. 3261–3263. DOI: 10.1364/OL.35.003261 (cit. on p. 126).

[207] K. R. Motes et al. "Encoding qubits into oscillators with atomic ensembles and squeezed light". *Phys. Rev. A* 95.5 (2017), p. 053819. DOI: 10.1103/PhysRevA.95.053819 (cit. on p. 126).

[208] D. F. V. James et al. "Measurement of qubits". *Phys. Rev. A* 64.5 (2001), p. 052312. DOI: 10.1103/PhysRevA.64.052312 (cit. on p. 146).

[209] R. Bhandari and N. A. Peters. "On the general constraints in single qubit quantum process tomography". *Sci. Rep.* 6 (2016), p. 26004. DOI: 10.1038/srep26004 (cit. on p. 146).

[210] K. Duivenvoorden et al. "Single-mode displacement sensor". *Phys. Rev. A* 95.1 (2017), p. 012305. DOI: 10.1103/PhysRevA.95.012305 (cit. on pp. 148, 150, 170, 173).

[211] W. H. Zurek. "Sub-Planck structure in phase space and its relevance for quantum decoherence". *Nature* 412 (2001), p. 712. DOI: 10.1038/35089017 (cit. on p. 150).

[212] S. C. Burd et al. "Quantum amplification of mechanical oscillator motion". *arXiv:1812.01812 [quant-ph]* (2018). arXiv: 1812.01812 (cit. on p. 150).

[213] F. Wolf et al. "Motional Fock states for quantum-enhanced amplitude and phase measurements with trapped ions". *arXiv:1807.01875 [physics.atom-ph]* (2018). arXiv: 1807.01875 (cit. on p. 150).

[214] K. R. Brown et al. "Coupled quantized mechanical oscillators". *Nature* 471 (2011), pp. 196–199. DOI: 10.1038/nature09721 (cit. on p. 151).

[215] M. Harlander et al. "Trapped-ion antennae for the transmission of quantum information". *Nature* 471 (2011), pp. 200–203. DOI: 10.1038/nature09800 (cit. on p. 151).

[216] K. Toyoda et al. "Hong–Ou–Mandel interference of two phonons in trapped ions". *Nature* 527 (2015), pp. 74–77. DOI: 10.1038/nature15735 (cit. on p. 151).

[217] Y. Y. Gao et al. "Entanglement of bosonic modes through an engineered exchange interaction". *Nature* 566.7745 (2019), pp. 509–512. DOI: 10.1038/s41586-019-0970-4 (cit. on p. 151).

[218] T. Sägesser. "Fast dynamic exchange cooling of trapped ions". Masters Thesis. ETH Zürich, 2018 (cit. on p. 151).

[219] L. De Clercq. "Transport Quantum Logic Gates for Trapped Ions". PhD Thesis. ETH Zürich, 2015 (cit. on p. 151).

[220] A. S. Parkins and H. J. Kimble. "Quantum state transfer between motion and light". *J. Opt. B* 1.4 (1999), pp. 496–504. DOI: 10.1088/1464-4266/1/4/323 (cit. on p. 151).

[221] H. Zeng and F. Lin. "Quantum conversion between the cavity fields and the center-of-mass motion of ions in a quantized trap". *Phys. Rev. A* 50.5 (1994), R3589–R3592. DOI: 10.1103/PhysRevA.50.R3589 (cit. on p. 151).

[222] D. Crow et al. "Improved Error Thresholds for Measurement-Free Error Correction". *Phys. Rev. Lett.* 117.13 (2016), p. 130503. DOI: 10.1103/PhysRevLett.117.130503 (cit. on p. 152).

[223] C. Rutkowski. "Exploring optimized preparation schemes for logical qubit states encoded in the trapped ion motional oscillator". Semester Thesis. ETH Zürich, 2018 (cit. on pp. 152, 171).

[224] O. Landon-Cardinal et al. "Quantitative Tomography for Continuous Variable Quantum Systems". *Phys. Rev. Lett.* 120.9 (2018), p. 090501. DOI: 10.1103/PhysRevLett.120.090501 (cit. on p. 156).

[225] R. Gerritsma et al. "Quantum Simulation of the Klein Paradox with Trapped Ions". *Phys. Rev. Lett.* 106.6 (2011), p. 060503. DOI: 10.1103/PhysRevLett.106.060503 (cit. on p. 157).

[226] F. Zähringer et al. "Realization of a Quantum Walk with One and Two Trapped Ions". *Phys. Rev. Lett.* 104.10 (2010), p. 100503. DOI: 10.1103/PhysRevLett.104.100503 (cit. on p. 157).

[227] R. Gerritsma et al. "Quantum simulation of the Dirac equation". *Nature* 463 (2010), pp. 68–71. DOI: 10.1038/nature08688 (cit. on p. 157).

[228] K. G. Johnson et al. "Sensing Atomic Motion from the Zero Point to Room Temperature with Ultrafast Atom Interferometry". *Phys. Rev. Lett.* 115.21 (2015), p. 213001. DOI: 10.1103/PhysRevLett.115.213001 (cit. on p. 157).

[229] E. Bradley and J. T. Robert. *An Introduction to the Bootstrap*. Monographs on Statistics and Applied Probability 57. Chapman & Hall/CRC, 1993 (cit. on p. 158).

[230] R. S. Anderssen and P. Bloomfield. "Numerical differentiation procedures for non-exact data". *Numer. Math.* 22.3 (1974), pp. 157–182. DOI: 10.1007/BF01436965 (cit. on p. 163).

[231] J. Cullum. "Numerical Differentiation and Regularization". *SIAM Journal on Numerical Analysis* 8.2 (1971), pp. 254–265. DOI: 10.1137/0708026 (cit. on p. 163).

[232] M. S. Kim et al. "Scheme for direct observation of the Wigner characteristic function in cavity QED". *Phys. Rev. A* 58.1 (1998), R65–R68. DOI: 10.1103/PhysRevA.58.R65 (cit. on p. 166).

[233] M. V. Satyanarayana. "Generalized coherent states and generalized squeezed coherent states". *Phys. Rev. D* 32.2 (1985), pp. 400–404. DOI: 10.1103/PhysRevD.32.400 (cit. on p. 180).

[234] G. S. Agarwal. *Quantum Optics*. Cambridge University Press, 2012. DOI: 10.1017/CBO9781139035170 (cit. on p. 180).